Heterostructures from Chemical Vapour Deposition. The Synthesis and Characterisation of Tungsten and Tin Chalcogenides on Graphene Substrates

Rushworth, Andrew

Award date:
2017

Awarding institution:
University of Bath

Heterostructures from Chemical Vapour Deposition. The Synthesis and Characterisation of Tungsten and Tin Chalcogenides on Graphene Substrates.

Andrew James Rushworth

A thesis submitted for the degree of Doctor of Philosophy

University of Bath

Department of Chemistry

April 2017

.....

Andrew J. Rushworth

Contents

Abstract

This thesis ‘’**Heterostructures from Chemical Vapour Deposition. The Synthesis and Characterisation of Tungsten and Tin Chalcogenides on Graphene Substrates.’’** encompasses a range of research areas, all under the umbrella of chemical vapour deposition (CVD). Within this report, two types of deposition techniques are compared, high temperature CVD and aerosol assisted CVD (AA-CVD).

Chapter 1 presents an up-to-date review of the literature landscape pertaining to graphene and graphene-like materials, including their history, synthesis and properties. Additionally, the various CVD techniques and growth mechanisms are presented.

In Chapter 2 we describe the design and use of a CVD reactor to produce graphene. It was found through optimisation of reaction conditions, graphene could be grown on cm length scales on copper foil. Graphene samples were then successfully transferred onto SiO_2 substrates, onto which tin sulphides and tungsten disulphide could be grown. An atomic layer deposition (ALD) technique was also used to deposit graphitic carbon films onto copper foil at temperatures as low as 250 ^{o}C, which could be transferred to SiO_2 without the need of a polymer support.

Chapter 3 explores the CVD of tungsten disulphide (WS_2) on various substrates including CVD grown graphene. The first example of the AACVD of WS_2 onto graphene is reported, where it was shown films as thin as 5 nm could be grown. Using high temperature CVD of tungsten oxide and sulphur, monolayer WS_2 was also successfully grown on silicon dioxide and graphene. The characteristic photoluminescent response of monolayer WS_2 could be observed on graphene. Materials were analysed using microscopy and spectroscopic techniques such as scanning electron microscopy (SEM), atomic force microscopy (AFM), Raman spectroscopy and powder x-ray diffraction (PXRD). These techniques identified the increased orientation of WS_2 deposited onto graphene versus amorphous substrates.

Chapter 4 presents findings on how depositing onto graphene substrates may affect the growth and behaviour of tin sulphide materials. Using high temperature CVD, the largest tin sulphide single crystals grown to date from CVD are reported. At lower deposition temperatures, we report the first examples of tin and sulphides deposited onto graphene using an AA-CVD approach. The photoactivity of the tin sulphide-graphene heterostructures has been successfully analysed using photoelectrochemical techniques, where it was found the quality of the graphene substrate had a large effect on device performance. Additionally, bandgaps of the tin sulphides were affected when deposited onto graphene, indicating graphene substrates effect strain in heterostructure materials. As with WS_2 depositing onto graphene altered the orientation of tin disulphide, which could be observed by SEM, AFM and PXRD.

Declaration

The work described in this thesis was conducted by the author at the University of Bath between October 2013 and April 2017. It represents the author's original and independent work, except where specific reference is made to the contrary. Neither the whole nor part of this thesis has been submitted previously in support of a degree at this or any other university. It does not exceed the prescribed limit including tables, references and appendices.

Acknowledgments

Firstly, I would like to thank Dr Andrew Johnson. I would not have completed this work without having a supervisor who was so invested my development in and out of the lab. I cannot commend enough his scientific ability and talent for creating such a positive research group culture. I would also like to thank Prof. Paul Raithby. He went above and beyond the call of duty in ensuring my project received the best possible support and supervision. Also thanks to Prof Simon Bending and Dr Dan Wolverson whose guidance in aspects of physics was vital to the work contained in this report.

Thanks also goes to my office colleagues, who now will be friends for life, with whom I learnt new phases such as ‘snaking’ and discussed the merits of laying chocolate eggs. In a strange way, I think these crazy moments have been a reason I have managed to stay sane through the last three years. These gems include Joe, Jamie, Jeff, Prem, Hannah, Jerome, Pete, Ibbi, Dave and Sam.

Shout out to Niall, Mat, Hollie and big V. It has been a privilege to be able to surround myself with people outside of work who have such a positive outlook on life. I hope to recreate the many happy times I have spent in Parade bar with the resident tutor gang with you guys in the future, wherever we end up. A big thank you goes to Yimini. From holding my hand all night in A&E when I had a disagreement with a wall, to having a caring face to look forward to seeing after a hard day’s work.

I would finally like to thank my parents, for their continual love and support for the past four years.

List of Abbreviations

Abbreviation		Abbreviation	
AA-CVD	Aerosol Assisted CVD	**MG**	Monolayer Graphene
AFM	Atomic Force Microscopy	**PCE**	Power Conversion Efficiency
ALD	Atomic Layer Deposition	**PCBM**	[6, 6]-phenyl C61 butyric acid methyl ester
AP-CVD	Atmospheric Pressure CVD	**PE-ALD**	Plasma enhanced ALD
BBG	Bernal-stacked Bilayer Graphene	**PE-CVD**	Plasma Enhanced CVD
CBD	Chemical Bath Deposition	**PL**	Photoluminescence
CIS	Copper Indium Selenide	**PMMA**	Poly Methyl Methacrylate
CIGS	Copper Indium Gallium Selenide	**PXRD**	Powder X-Ray Diffraction
Ch	Chalcogenide	**P3HT**	Poly(3-hexylthiophene-2,5-diyl)
CMOS	Complementary Metal Oxide Semiconductor	**QHE**	Quantum Hall Effect
CNT	Carbon Nanotube	**r-GO**	Reduced- Graphene Oxide
CVD	Chemical Vapour Deposition	**RMS**	Root Mean Squared Roughness
DI	De-ionised	**SEM**	Scanning Electron Microscopy
DSC	Differential Scanning Microscopy	**S-K**	Stransky-Krastanov
EDS	Energy-dispersive X-ray spectroscopy	**TBG**	Twisted Bilayer Graphene
EQE	External quantum efficieny	**TE**	Transparent Electrode
FET	Field Effect Transistor	**TEM**	Tunnelling Electron Microscopy
FETT	Field-effect tunnelling transistor	**TMD**	Transition Metal Chalcogenide
F-M	Frank–van der Merwe	**TGA**	Thermo-Gravimetric Analysis
FTO	Fluorine doped Tin Oxide	**THF**	Tetra Hydro Furan
FWHM	Full Width Half Maximum	**UHV-CVD**	Ultra-High Vacuum CVD
GNR	Graphene Nanoribbon	**UV**	Ultraviolet
GO	Graphene Oxide	**V-W**	Volmer-Weber
GTE	Graphene Transparent Electrode	**ZnPc:C60**	zinc phthalocyanine:fullerene
HOPG	Highly Oriented Pyrolytic Graphite	**0D**	0 Dimensional
ITO	Indium doped Tin Oxide	**1D**	1 Dimensional
IPA	Isopropyl Alcohol	**2D**	2 Dimensional
IR	Infrared	**3D**	3 Dimensional
LED	Light Emitting Diode	**α-DD**	α,α- dithiobisformamidinium dinitrate
LP-CVD	Low Pressure CVD		

Chapter 1. Introduction

The development of new materials has led to a drastic change in many societies around the world. One standout example is the miniaturisation, cost reduction and thus dissemination of computational technologies.[1] This has led to an unprecedented level of access to information for billions of people. This has however come at a cost, the global reserves of many rare metals required for this change are running low, and thus the continued spread of computational technologies is widely deemed unsustainable. Therefore there is a need to reduce the reliance of computational technologies on unsustainable materials.

Tackling climate change is also a major global challenge. All the major industrialised nations agree that climate change is directly linked to CO_2 produced by human activities.[2] In the United States, energy generation contributes the largest amount of CO_2 produced annually at 33%.[3] Currently high purity silicon or cadmium telluride are the materials of choice for photovoltaic cells, which offer a low carbon producing energy generation technique. An issue with using silicon is it is an indirect semiconductor, so large amounts of material are needed for sufficient light adsorption. The tellurium in cadmium telluride solar cells is very rare so a problem similar to that facing computational technologies arises.

These two challenges have been a key driver in the development of new materials. Despite its simple structure, graphene was first electronically isolated and probed in 2004 in the landmark paper by Novoselov and Geim.[4] Since then it has often been touted as a 'wonder material', with many properties that are useful in a whole raft of applications.

Graphene is sheet of sp^2 bonded carbon that is one atom thick. It has the potential to create high performance transistors of that also require less power than conventional devices which could reduce the need for rare metals. It also has the potential be used as an electrode in lighter, more efficient, flexible solar cells. Graphene is just one member of a family of so called graphene-like materials. Graphene-like materials can have vastly different chemical and physical properties compared to graphene. Additionally they present the opportunity to alter graphene's properties by stacking them with graphene, further widening its potential application.

There are still many hurdles to overcome however, before the properties of graphene and graphene-like materials can be harnessed. Probably the main hurdle is large scale production at the desired level of quality. One potential technique to realise this is chemical vapour deposition (CVD), another

is atomic layer deposition (ALD). Whether these techniques are employed at low or high temperatures often affects the quality of the materials produced. This thesis involves the exploration of CVD and ALD of graphene and graphene-like materials at 'low' and 'high' temperatures. Firstly the history and properties of graphene and related materials will be discussed, then the current pathways to manufacturing them. The current progress with integrating these materials into devices will then be considered. After this, three distinct bodies of work will be discussed: Firstly, the scalable growth of graphene via CVD and ALD, secondly the growth of WS_2 on and off graphene via CVD and finally the growth of tin chalcogenides on and off graphene via CVD.

1.1 History of graphene

The story of graphene could be considered to begin as early as 1859 when Benjamin Brodie isolated a 'peculiar crystalline substance', now called graphite oxide, by treating graphite with potassium chlorate and nitric acid.[5] By 1948 the first tunnelling electron microscopy (TEM) images of few layer-graphene were published.[6] In 2002, Nanotek filed a patent for the production of graphene platelets from chemically exfoliated carbonised polymers.[7] Geim and Novoselov published the famous scotch tape technique for producing graphene flakes from graphite in 2004, and a year later with researchers from Russia and the Netherlands showed that as predicted, quasiparticles in graphene were massless Dirac fermions.[8] Since then, effort has been placed into finding avenues for the commercialisation of the material; companies such as IBM and Samsung have been demonstrating the integration of graphene into some of their electronic products.[9] However a graphene containing product closer to commercialisation is 'graphene ink' which is conducting and can be printed onto a flexible surface. Graphene currently has a part to play in new products entering the market, however for it to be as disruptive as many predicted, significant developments need to be made.

1.2 Properties of graphene

The following section will discuss graphene's properties with respect to perfect crystalline graphene, usually obtained by exfoliation. How manufacture affects graphene's properties will be discussed in the relevant section. For example, large sheets of graphene grown by CVD tend to be polycrystalline, as different orientations of graphene domains stitch together during the growth phase of the CVD process. This polycrystallinity tends to degrade the properties of graphene and reduce the lifetime of graphene in devices, as localised heating effects can occur at crystal grain boundaries.[10]

1.2.1 Structure

Graphene is a sheet of carbon atoms that is one atom thick. It belongs to a family of allotropes of carbon for which it is sp^2 hybridised and forms 3 bonds with adjacent carbon atoms to from a planar array. It is a two-dimensional (2D) building block of zero-dimensional (0D) fullerenes, one-dimensional (1D) carbon nanotubes and three-dimensional (3D) graphite.[11] The structures of which are shown in figure 1.1.

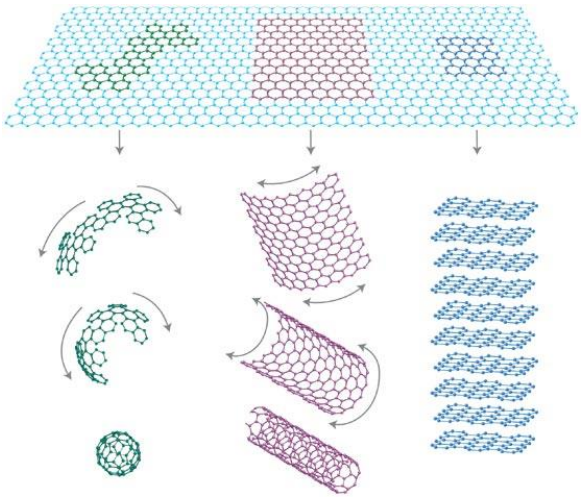

Figure 1.1 Graphene is the building block for fulerenes (left) nanotubes (center) and graphite (right). Reproduced from ref 10.

1.2.2 Physical properties

Using atomic force microscopy (AFM) measurements, graphene has been shown to exhibit a breaking strength of ca. 42 Nm^{-1}, with theory and experiment in good agreement.[12,13] Additionally graphene's Young's modulus was measured to be 1.0 TPa, establishing it as the strongest material ever measured.[14] Room temperature values of thermal conductivity of 4840-5300 $Wm^{-1}K^{-1}$ were extracted for single-layer graphene using Raman microscopy experiments, outperforming even carbon nanotubes which are known for their exceptional heat conducting properties. These thermal conduction properties are valuable for proposed electronic applications, where heat dissipation is vital and additionally places graphene as a potential material for thermal management.[15] Graphene is highly elastic, and can be stretched up to 20%, more than any other crystal. [13,14] Interestingly, even though graphene is highly pliable, with folds often observed, it also exhibits brittle behaviour at high strains, breaking like glass.[16] Additionally, unlike any other material, graphene shrinks with increasing temperature because membrane phonons dominate in 2D.[17] Also unlike any other material, a single layer of graphene is impermeable to common gases, including helium.[18]

The melting temperature of graphene is unknown, although it is predicted to be ca. 5000 K where it is initiated by the formation of 1D carbon chains.[19] A schematic of the predicted process is shown in figure 1.2. The thermodynamics of 2D crystals in a 3D environment could be very different to thin films, and may be better described by the physics of soft membranes.

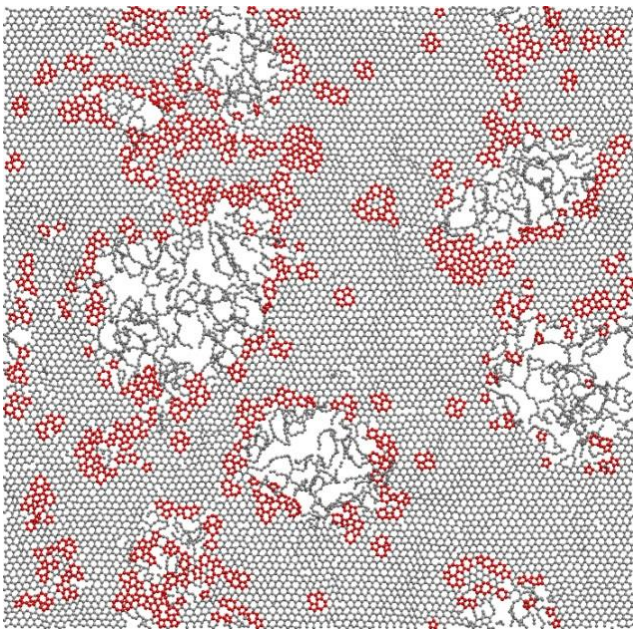

Figure 1.2 Theoretical result of graphene melting and forming 1D chains at ~5000 K. Reproduced from ref 19.

1.2.3 Electronic properties

Since the isolation of graphene, charge carrier mobility's of up to ca. 200,000 $cm^2V^{-1}s^{-1}$ in suspended graphene, and ca. 15,000 $cm^2V^{-1}s^{-1}$ have been reported when mounted on a silicon substrate.[20,21] Fast graphene devices would work in the ballistic transport regime, where carrier mobility is limited by elastic scattering, where the elastic carrier mean free path is greater than the inelastic mean free path. Devices showing the mean free path in the order of microns at room temperature have been reported.[22] Therefore ballistic devices at similar or even larger scales to the current complementary metal–oxide–semiconductor (CMOS) technology seem feasible.[23] Carbon nanotubes have a similar potential however graphene is planar, allowing for easier integration into CMOS compatible systems.

In order to understand the electronic properties of graphene, it is important to discuss its band structure. Figure 1.3 displays simple band structure diagrams for different electronic types of materials.

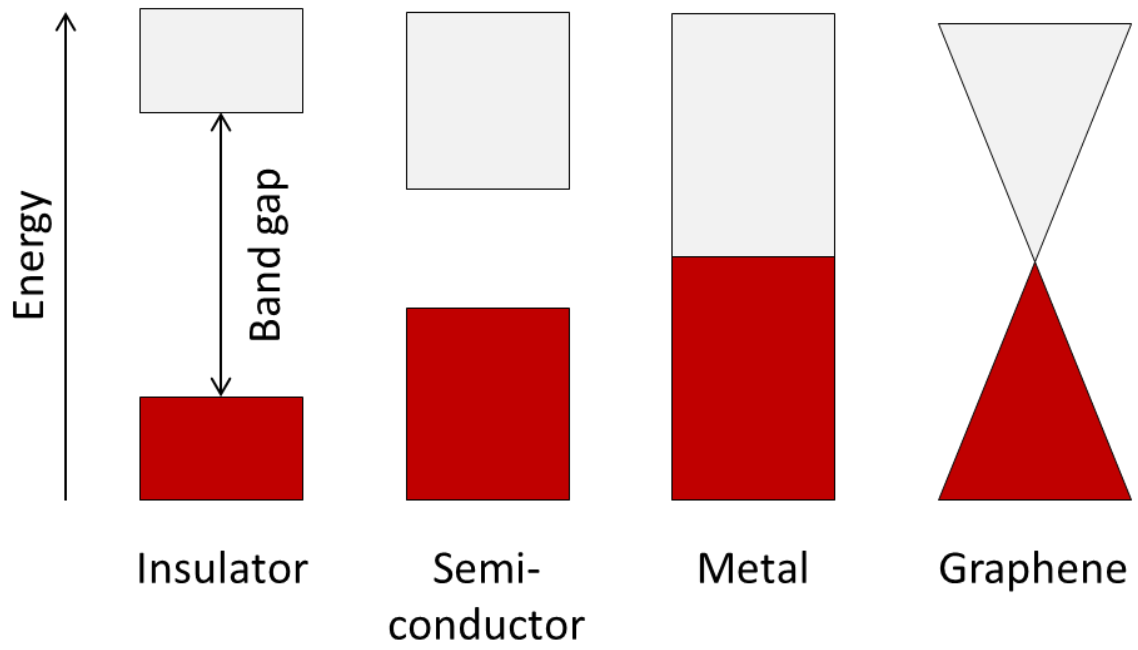

Figure 1.3 Bandgaps of the different electronic classes of material. The red shaded areas are the occupied states.

Graphene has been referred to as a semi-metal, as it does not possess a bandgap. However unlike metals, the density of states vanishes to zero at the fermi level. This means even though graphene is highly conductive, like a metal, due to charge carriers not having to be thermally or optically excited into the conduction band, charge transport involves ballistic conduction. These conductive properties are down the sp^2 hybridisation of all the carbon atoms in the honeycomb lattice. The p orbitals that are perpendicular to the sp^2 orbitals form π bonding/antibonding orbitals which correspond to the conduction and valence band with a zero bandgap.

1.2.4 Quantum Hall effect

The quantum Hall effect (QHE), is a quantum phenomenon that manifests on macroscopic length scales, and has been the subject of research since its discovery in 1980. The QHE has deepened our understanding of many areas of quantum physics and has led to the metrological standard, quantum resistance, being established. Graphene is the only material to display the QHE effect at room temperature.[24] This is due to another special property of graphene, its charge carriers cannot be described by Shrödinger's equation but rather are described by Dirac's relativistic equation. In fact they can be described as Dirac fermions, which behave as massless relativistic particles which undergo little scattering, even at room temperature.[8]

1.2.5 Chemical reactivity

The chemistry of graphene is rather limited due to its chemical inertness and the difficulty encountered in controlling stoichiometry of the functionalised graphene. However, there is still a large body of work involving functionalising graphene which aims to give graphene new properties and thus applications.[25] The chemistry of graphene can be split into two sections, covalent and non-covalent chemistry.

Then most common covalent chemistry carried out on graphene is to functionalise it with carboxyl, epoxy and hydroxyl groups to form graphene oxide.[26] One of the oldest and most famous methods of doing so is called the Hummers' method, where a mixture of $KMnO_4$, $NaNO_3$ and H_2SO_4 is heated at ca. 45 ^oC with graphite to produce graphite oxide. The negatively charged oxygenated species then help to disperse the graphite oxide into monolayers of graphene oxide (GO). Recently it has been found that using a 9:1 mixture of H_2SO_4/H_3PO_4 improves the efficiency of the oxidation process.[27] This method results in a greater amount of GO that is more completely oxidised compared to Hummers' method without producing toxic dinitrogen tetraoxide and nitrogen dioxide. It is also possible to functionalise graphene with oxygen by exposing it to oxygen plasma for short periods of time.[28] In addition to the formation of C-O covalent bonds, work has been undertaken in producing direct C-C bonds with graphene,[29] although most work involves nucleophilic substitution, electrophilic addition as well as condensation, additions with GO have also been demonstrated.[26] Figure 1.4 shows an example covalent functionalization route for graphene via GO.

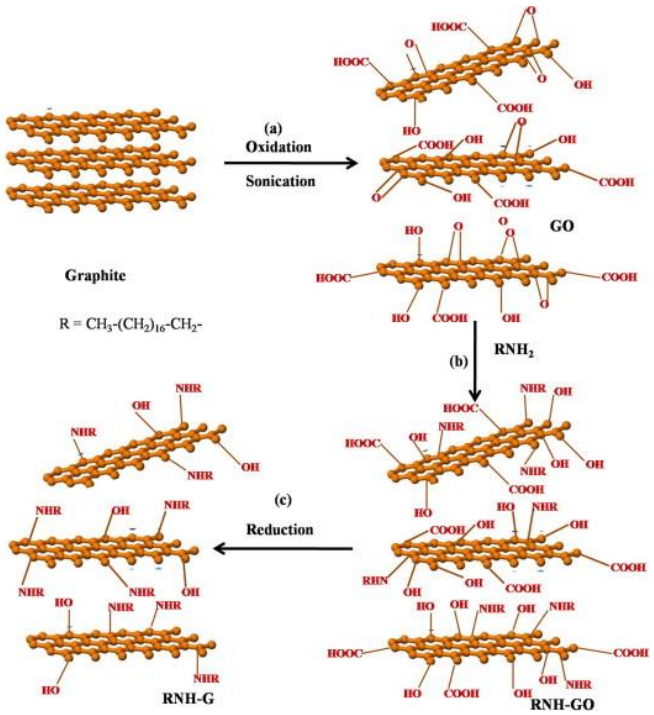

Figure 1.4 Schematic of how graphene can be functionalised via GO Reproduced from ref 26.

The non-covalent chemistry is based on van der Waals interactions, or π–π stacking of aromatic molecules on the graphene plane. The benefit of this type of interaction is it does not interrupt the π-conjugation of the graphene surface as it does not introduce sp^3 sites. It has been shown pyrene has a strong affinity for a graphene surface, which can be useful for increasing its solubility.[30] Perylene tetracarboxylic acid (PTCA) has been shown to interact with graphene and has been used to provide a seed layer for the growth of metal oxides onto graphene via ALD.[31]

1.2.6 Toxicity

Before finishing reviewing the properties of graphene, it is important to discuss the new but important field of graphene toxicity, especially if it is going to be produced on a large scale. One of the key areas of concern is the sharp, strong edges of graphene which have the potential to cut into living cells.[32] Although very few studies have been done in this area the initial results cause pause for thought. One computational report suggests even micron sized flakes of graphene could enter into cells.[33] Other reports suggest that graphene oxide nanoparticles are stable and mobile in surface water such as lakes or rivers.[34]

1.3 Synthetic routes to graphene

Synthetic routes to high quality graphene remain one of the largest hurdles to its uptake on a commercial scale. There are two separate approaches to synthesising graphene, 'top down' and 'bottom up', with top down approaches sacrificing scale for quality and bottom up quality for scale. Techniques using both these approaches will be discussed in the introduction to chapter 2.

1.3.1 Giving graphene a bandgap

To improve the versatility of graphene, it is highly desirable to be able to open up its zero bandgap. Zero bandgap graphene is difficult to switch off in devices. Opening the bandgap is achieved in two main ways, quantum confinement effects and doping.

Quantum confinement effects in graphene can be accessed by creating graphene nanoribbons (GNRs) with one of their dimensions in the order of nanometres. These can be 'top-down' synthesised, by unzipping nanotubes, i.e. through sonication in an organic solvent, or through the 'bottom-up' technique of surface assisted polymerisation.[35,36] Other methods include patterning where the GNRs are created through ion implementation and lithography techniques.[37,38] These techniques have allowed functioning graphene containing field-effect transistor (FET) devices to be demonstrated.

Another, and more common route to achieving a bandgap in graphene is through doping. The elements boron and nitrogen are the natural candidates for doping in graphene and thus have been the main focus. They have a similar atomic size to that of carbon, and have hole acceptor and electron donor characteristics for substitutional p and n doping, respectively. An issue however with doping graphene is it degrades its conductive properties as scattering increases.

CVD has proven to be a powerful tool for doping graphene due to its bottom up synthetic approach. The most common way of creating nitrogen doped graphene via CVD is to add NH_3 into the mix of CH_4 and H_2, where the relative concentration of NH_3 can control the amount of nitrogen incorporation into the graphene sheet.[39] More recently it has been shown that other precursors such as pyridine can also be used to create nitrogen doped graphene.[40] P-type doping using boron has been achieved using CVD techniques using molecules such as B_2H_6 as the boron source.[41]

1.4 Graphene-like materials

In addition to graphene, materials that have a similar hexagonal structure are being explored. One reason is they have the potential to have some of the interesting electronic properties of graphene whilst having a different chemical reactivity. They can also have different and interesting electronic phenomena to graphene. The desire to find materials that have some of graphene's properties, but also have a bandgap, is a big driver for their study. Finally they are good candidates for materials to be combined with graphene where there is potential to combine graphene's properties with their own.

1.4.1 Silicene and Germanene

Silicene is the Si analogue of graphene, where silicon replaces the carbon atoms. Similarly to graphene it is a zero bandgap semimetal, however it is much more chemically reactive as silicon-silicon double bonds are weaker.[42] Silicene has been synthesised by molecular beam epitaxy onto silver, where the study of its properties is still in an early stage.[43] Similar to graphene, hydrogen and fluorine can be added to silicene to modulate the bandgap,[44] whilst introducing defects and doping silicene can also alter its electronic properties.[45] Germanene, a hexagonal network of germanium atoms and graphene like tin networks has been studied theoretically but have not been physically isolated.[46] Studies of binary phases of graphene like group IV elements such as GeC and SnC, have remained theoretical.

1.4.2 Hexagonal boron nitride

Hexagonal boron nitride (h-BN) is an isoelectronic and isostructural analogue of graphene. It is a wide bandgap semiconductor and thus, due to its optical properties, is sometimes called white graphene.[47] The layered structure of its parent material boron nitride is shown in figure 1.5. Interactions between graphene and h-BN have been extensively studied. Graphene layered with h-BN changes graphene's behaviour, turning it into an insulator.[48]

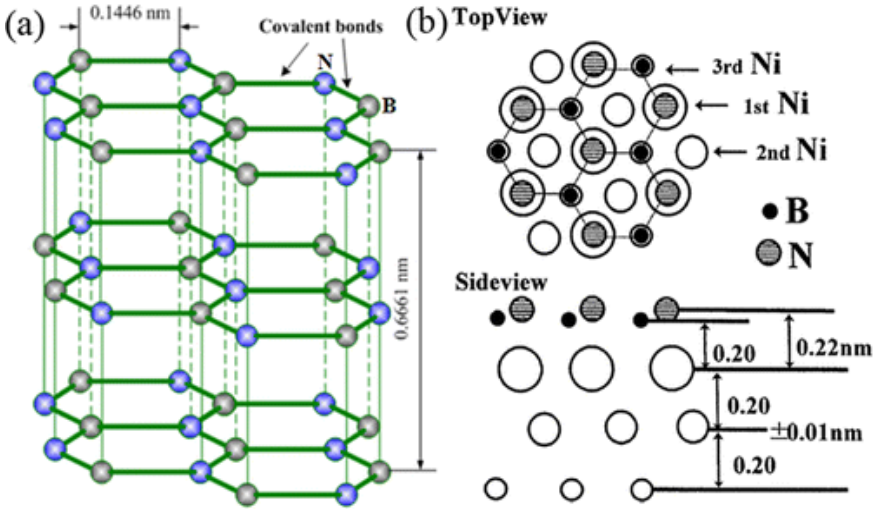

Figure 1.5 a) Structure and key lengths associated with bulk h-BN. **b)** Diagram of h-BN deposited on Ni. Reproduced from ref 47.

As well as being a useful substrate material for graphene, h-BN has received attention due to its own interesting properties. Its parent material has a high chemical stability and has traditionally been used as a lubricant. Due to its large bandgap of ca. 5.9 eV it has insulating properties and thus has seen application as a charge leakage barrier in electronic equipment.[49]

Functionalising h-BN has been a route to modifying its properties. For example, when covered with oxygen, h-BN becomes ferromagnetic with a small band gap.[50] Substituting boron or nitrogen with carbon in h-BN has been achieved by electron beam radiation; whereupon it was found that h-BN could be made conducting.[51]

The synthetic methods for producing 2D h-BN are similar to those for graphene, which include mechanical exfoliation, chemical exfoliation and CVD. Currently exfoliation techniques produce the highest quality sheets of h-BN, however, as with graphene, these techniques do not produce large sheets and would be difficult to scale. CVD, however, has the potential to be scalable, but work still needs to be done to increase the quality of the h-BN produced. Precursors used in the CVD process include multi source precursors, such as BCl_3/NH_3 and single source precursors, such as BH_3NH_3. An advantage of a single source precursor is that the stoichiometry of B:N is easier to control.

1.4.3 Graphene-like $A^{II}B^{VI}$ phases

Theoretical studies have shown that materials such as ZnO and BeO can form graphene-like phases when the thickness of the materials reaches a few monolayers.[52] The transition of the wurtzite to graphene-like structure is shown in figure 1.6. This has now been experimentally confirmed for ZnO on Ag(111) and Pd(111).[52-53] The bandgaps of these materials vary with the number of layers, the more layers, the smaller the bandgap.

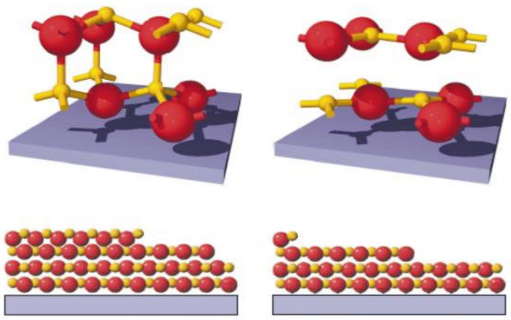

Figure 1.6 Schematic of wurtzite structured ZnO (top left) converting to graphene-like (top right) as the number of layers decrease (bottom). Reproduced from ref 52.

1.4.4 Metal Carbides

Theoretically, there are two types of graphene-like metal carbides. Graphene with regularly arranged metal adatoms has never been synthesised due to problems with metal aggregation.[54] The other type of graphene-like metal carbide is synthesised from the isolation of single layers of metal carbide from nanolaminates also known as MAX phases.[55] These $M_{n+1}AX_n$ (n = 1, 2 or 3) where M is an early transition metal, A is usually a group 13 or 14 element and X is carbon or nitrogen, form laminated structures. Around 60 are known, figure 1.7 shows how the individual layers in a MAX phase can be separated.

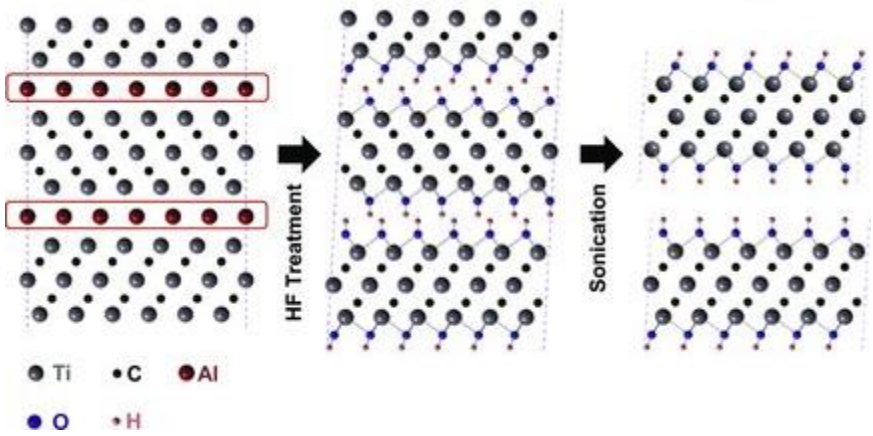

Figure 1.7 Schematic of how MAX phases can be separated to produce metal carbides. Reproduced from ref 55.

1.4.5 Layered transition metal dichalogenides

A transition metal dichalogenide (TMD) is made up of layers of a transition metal sandwiched between two chalcogen (Ch) atoms (O, S, Se and Te), with the layers held together by van der Waals interactions.[56] TMDs therefore share some similar physical properties with graphite and individual layers can be isolated by exfoliation in a similar manner to graphene.[56] Interest in these materials is wide ranging, from studying superconductivity, lubrication and water splitting properties. Going down the group of chalcogens, the ionic component of the M-Ch bond gets weaker, making any isolated monolayers increasingly unstable. In general, it can be said that the structural properties and stability of TMDs are governed by the chalcogenides, whereas the electronic properties are governed by the metal. TMDs containing niobium and tantalum exhibit metal-like properties, however, TMDs containing molybdenum and tungsten are semiconducting.[45] The properties of several TMDs are presented in figure 1.8.

Similarly to graphene, TMDs have been synthesised by top down and bottom up approaches. To achieve 2D graphene-like layers, CVD, often involving the metal oxide and sulphur, has been successfully employed.[57] Additionally exfoliation of bulk crystals has also been successful.[58]

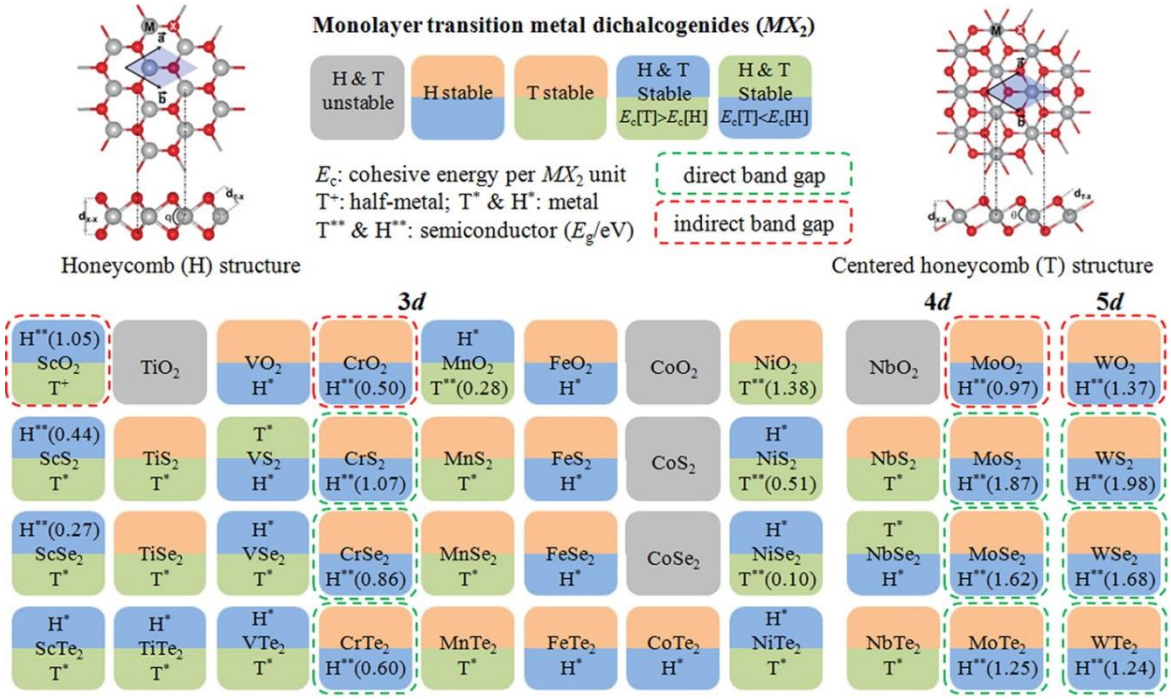

Figure 1.8 Summary of stability, conformation and semiconducting properties of selected TMDs. Reproduced from ref 56.

1.5 Transparent electrodes

Transparent electrodes (TEs) are already very important in many technologies that couple light and electricity. They are already used in touch screens, displays, solar panels, light emitting diodes (LEDs) and functional glass, among others.[59] Conventional transparent electrodes include indium tin oxide (ITO) and fluorine tin oxide (FTO). These conducting metal oxides however have several drawbacks. They lack transparency in the near-infrared, lack stability in acid and base and are too brittle to be used in flexible devices.[60] Additionally indium is scarce. To overcome these challenges other materials as well as graphene are being explored. These include conducting polymers, nanostructured metals and carbon nanotubes (CNTs).

1.5.1 Conducting polymers

Conducting polymers are the most mature technology looking to tackle some of the challenges faced by ITO and FTO. Polythiophene and polyaniline came to the fore as the most promising conducting polymers due to their solubility in common solvents and relative stability. Much work has been undertaken to enhance their properties.[61, 62] Doping has been key to enhancing the conductivity. These polymers conduct through a conjugated backbone, and removing delocalised electrons via oxidative doping increases the mobility of the remaining delocalised electrons. Positive charges can also be added to the conjugated backbone via dissolution in acids. The choice of solvent was also found to be important, with the control over polymer morphology being key. Although conducting polymers have matched many of the properties of FTO and ITO whilst also being flexible, they have been held back by stability. Exposure to high temperatures, humidity, or UV light has been shown to be particularly problematic.[63]

1.5.2 Metallic nanostructures

Metals are very good conductors due to their high density of free electrons. Although this is obviously useful in an electrode, it also means they are very reflective. To circumnavigate this problem, metals can be made very thin (ca. 10 nm or less). There is a trade-off between the film thickness (which affects transparency) and conductivity. Devices such as solar cells have been demonstrated using ultrathin metals.[64] Although ultrathin metals do not outperform other alternative materials, they are comparatively transmittive to infra-red (IR) and ultra-violet (UV) light. Another advantage is thin metals tend to be flexible. Patterning the metal, which exposes parts of the material beneath the metal, can also be used to increase transmission at the cost of conductivity. Nanopatterned metal gratings can achieve this, however current manufacturing techniques make this cost prohibitive. Networks of metal nanowires can be used as an alternative.

An advantage over ultrathin metals is they can be deposited from solution. Exemplar devices that substitute metal oxides with metallic nanostructures as TEs include solar cells.[65]

1.5.3 Carbon nanotubes (CNTs)

CNTs are a more mature technology compared to metal nanostructures and graphene. The first report of 'helical microtubules of graphitic carbon' was made in 1991 and their properties, which relate to the wrapping angle and diameter of the tube, were elucidated over the following decade. Individual CNTs were found to have mobilities greater than 100 000 $cm^2/V^{-1}s^{-1}$ and fracture strengths of over 100 GPa.[66,67,68] Despite this, CNTs have only recently seen commercial application. This is largely due to the difficulties involved in producing large quantities of high purity CNTs. Synthetic techniques can leave contamination in the form of catalyst particles and a mixture of allotropes of carbon.[59] However progress is being made in this area, with CVD providing a route to large scale production.[69] This has led to CNTs being employed in a range of areas such as energy storage and high strength composite materials.

Due to their flexibility and electronic properties, CNTs are also being explored for the next generation of TEs. However, in this area, replacement of ITO and FTO has yet to be realised. This is largely due to the length of which carbon nanotubes can be grown, which limit their electrical performance over large length scales. Progress is being made in this area with CNTs of up to half a meter long being reported, although producing these in large quantities remains a challenge that still needs to be overcome.[70]

Although currently unable to match ITO or FTO based devices, CNTs films have been employed as a TE in various devices. These include organic photovoltaic devices, light emitting devices and electrocatalysts.[71,72,73]

1.5.4 Graphene

Graphene has been regarded as an ideal candidate material to substitute for ITO for the preparation of TEs due to its unique thermal conductivity, mechanical strength, chemical stability, high electron mobility low sheet resistance and high optical transmittance.[74] Graphene can be directly used as a TE, or can through integration, improve other TEs such as metal nanowires.[75] Figure 1.9 shows potential applications for graphene-based transparent electrodes (GTEs) and the growth in GTE publications in recent years.

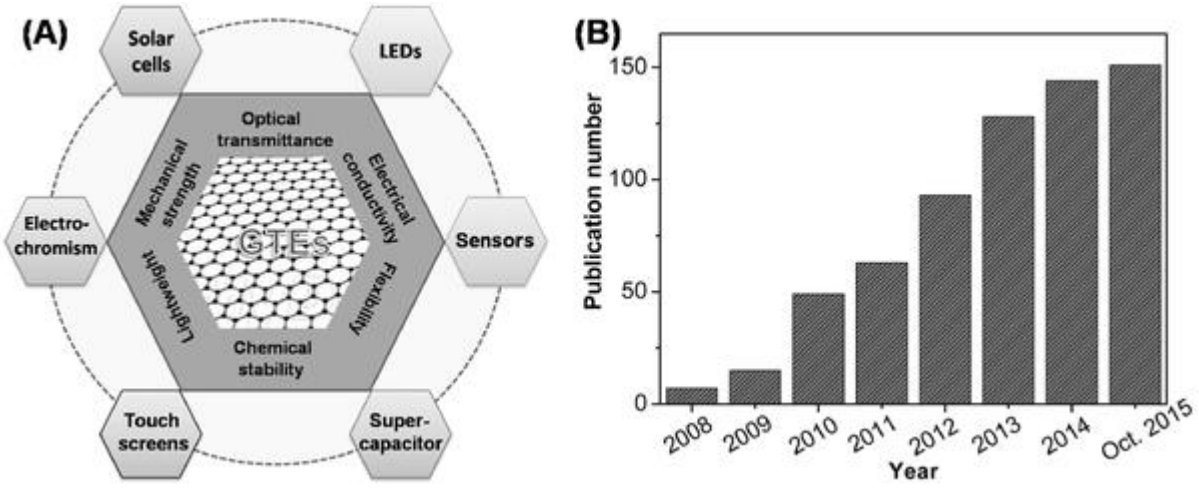

Figure 1.9 A) Characteristics and thus potential applications of GTEs **B)** Number of GTE related publications since 2008. Reproduced from ref 74.

1.5.5 Synthesising graphene transparent electrodes

Methods for synthesising graphene on a scale large enough for TEs will be discussed in chapter 2. Due to the large scale of high quality graphene produced, CVD seems to be the most desirable technique for producing GTEs. However copper and nickel, the most common and effective growth substrates for the CVD of graphene are clearly not transparent. Therefore processes that transfer graphene onto desirable substrates need to be developed.

1.5.6 CVD graphene transfer

Transfer methods for CVD graphene either involve polymer assisted transfer or mechanical exfoliation. Although the growth and transfer of graphene films has yet to be optimised, various functioning devices using GTEs have been made. The techniques for CVD graphene transfer will be discussed in depth in chapter 2.

1.5.7 Applications of graphene transparent electrodes - solar cells

State of the art mono-crystalline solar cells have a PCE of 25%.[76] At the time of writing the record reported power conversion efficiency (PCE) of a solar cell using a GTE is 15.6 % by Kong et al.[77] The Shottky type solar cell used the Shottky contact between graphene and silicon to separate charges whilst also using graphene as a TE. Monolayer CVD graphene was transferred onto a silicon window using a polymethylmethacrylate (PMMA) mediated wet transfer method. A Ga–In eutectic was used as the back silicon contact. The graphene was p-doped by spin-coating $AuCl_3$. [77]

A 15.6 % efficiency perovskite based solar cell containing graphene has also been reported by Nicholas et al., however in this case a graphene/TiO_2 composite is mounted on FTO, not replacing

it.[78] A flexible organic solar cell reported by Gradečak et al. had a PCE of 6.1 % when using graphene as an anode and 7.1 % as a cathode, showing no performance change over 100 flexing cycles and approaching equivalent non flexible FTO based devices.[79]

Diagrams of the mentioned Shottky type solar cell and the flexible solar cell, with graphene as the anode is shown in Figure 1.10.

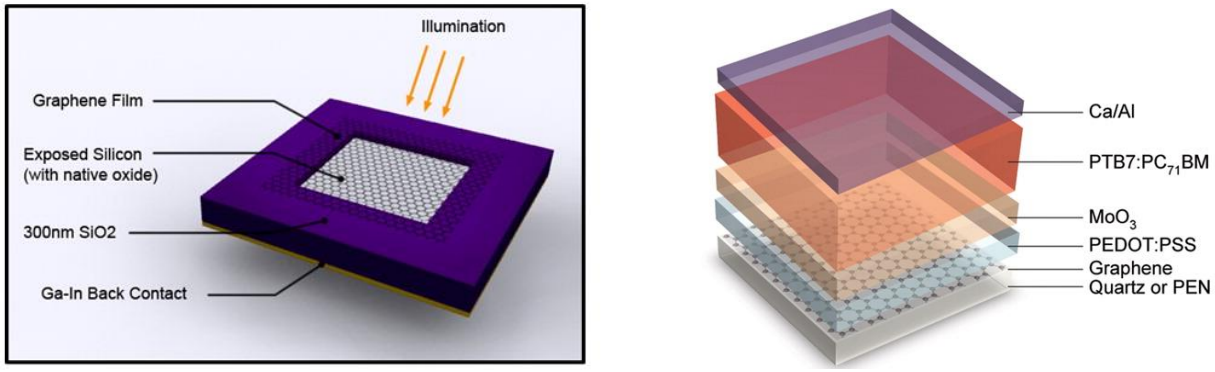

Figure 1.10 Left: Graphene in a Shottky solar cell.(Ref 76). Right: Graphene in a flexible organic cell. Reproduced from ref 79.

Although the obvious application of graphene in a solar cell is as a TGE, it can also be used as an intermediate layer in tandem cells. Tandem solar cell designs can increase device efficiency by stacking single-junction cells with different band gaps.[80] This means the total absorption window of the solar cell is increased. An intermediate layer allows the stacked cells to harvest complementary absorption spectra, without significant optical and electronic losses. An efficient intermediate layer have three properties: (i) act as a good recombination layer for electron and holes, (ii) be transparent to the required wavelengths (iii) be continuous to prevent intermixing of two subcells.[81]

Due to graphene being highly conductive, transparent and impermeable,[82] it is a strong candidate for an intermediate layer. A tandem cell using Poly(3-hexylthiophene-2,5-diyl) (P3HT) and [6, 6]-phenyl C61 butyric acid methyl ester (PCBM) (P3HT) as an active layer, zinc phthalocyanine:fullerene (ZnPc:C60) as the other active layer and graphene as the intermediate layer has been reported.[83] Even without the photocurrents of the subcells being matched, the tandem cell had a PCE of 2.3 %, 88% of the sum of the individual PCEs of the cells.

1.5.8 Applications of graphene transparent electrodes - organic light emitting diodes

Organic light emitting diodes (OLEDs) have seen vast improvements in recent years. Due to their vibrant colours, thin and lightweight form factor, efficiency and mechanical flexibility they and are now starting to be incorporated into the latest commercial displays. OLEDs are also considered for lighting applications. Due to their thinness and transparency they can fulfil niche applications such as head up displays. ITO is the current TE of choice however the scarceness of In and ITO's lack of flexibility, is holding back OLED development. Additionally Indium is known to diffuse into the active components of OLEDs, degrading their performance over time.[84] As discussed previously, GTEs have significant advantages over ITO that are also relevant for OLEDs, such as flexibility, chemical inertness, and being comprised of solely carbon. Until recently GTE based OLEDs have at best matched conventional ITO based OLEDs. However Lee et al. report graphene/TiO_2 layers as a TE for an OLED which possessed very high external quantum efficiencies (EQEs).[85]

To further increase the performance and miniaturise OLEDs materials, Novoselov et al. report LEDs using van der Waals heterostructures of 2D materials with graphene as the TE with high efficiencies.[86] Van der Waals heterostructures are an important class of material that is currently receiving a lot of attention. These heterostructures often involve graphene and will be discussed in the next section.

1.5.9 Van der Waals heterostructures

Van der Waals heterostructures involve layers of 2D materials held together by van der Waals interactions. As research on graphene sheets in isolation is now well established, researchers are increasingly devoting efforts to studying other 2D materials. Some of these have already been mentioned in the graphene-like materials section. The motivation behind layering these materials is driven by the ability to have fine control over the material properties, by stacking the 2D materials with the required properties in the desired order. 2D materials have been referred to as 'Lego blocks' in heterostructures, with figure 1.11 visualising the concept.[87]

Due to the large library of 2D materials to choose from, many different functionalities have been proposed and studied for these materials.

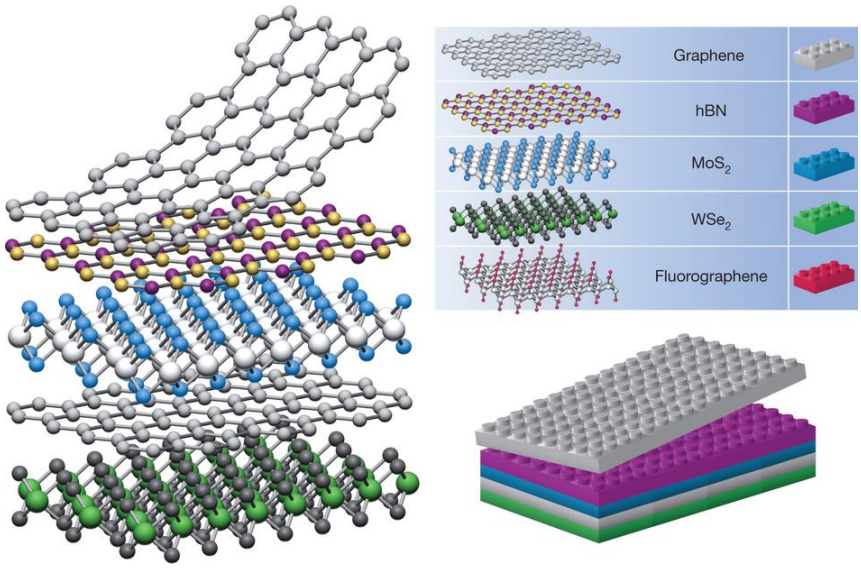

Figure 1.11 Diagram of a potential van der Waals heterostructure and its visualisation as Lego blocks. Reproduced from ref 87.

1.5.10 Heterostructures devices

A graphene-based field-effect tunnelling transistor (FETT) using a graphene/WS_2/graphene heterostructure on a multilayer BN substrate has recently been reported by Mishchenko et al.[88] As it has a relatively small bandgap, WS_2 provides a method to increase the ON/OFF ratio of the FET due to the changes in the Fermi level of the graphene being large compared to the barrier height. WS_2 offers an advantage over MoS_2 because it allows for switching between tunnelling and thermionic transport regimes. This allows for much higher ON/OFF ratios and larger ON current, increasing transistor performance.

Nonvolatile memory cells based upon graphene/MoS_2 with a floating 'few' (less than 10 layers) layer graphene gate have also been demonstrated by Kis et al.[89] MoS_2 acts as a channel which is in intimate contact with graphene electrodes in a FET geometry. This FET is then integrated with a multilayer graphene charge trapping floating gate that can be operated as a nonvolatile memory cell. Due to the electronics of 2D MoS_2, it is highly sensitive to the presence of charges in the charge trapping layer. Figure 1.12 depicts the FETT and non-volatile memory devices made from heterostructures of 2D materials.

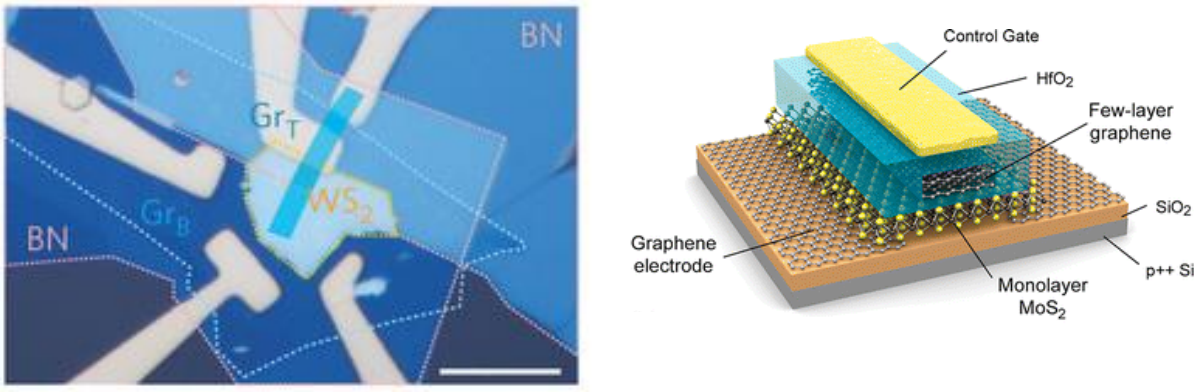

Figure 1.12 Left: FETT device involving a graphene/WS_2/graphene heterostructure. Right: Graphene/MoS_2 heterostructure non-volatile memory cell. Reproduced from refs 88 (left) and 89 (right).

Although the devices mentioned, as well as a growing number of examples in the literature,[87] have demonstrated some of the impressive properties of 2D heterostructure devices, they are almost exclusively based on exfoliating 2D flakes of material from 3D crystals. To achieve manufacturing techniques that are compatible with large scale production bottom up synthetic approaches need to be considered. As with growing individual layers of 2D materials such as graphene or WS_2, CVD is one of the most promising bottom up approaches available.

CVD techniques will now be given a general overview with specific techniques used in this thesis given more attention. Then the CVD work towards depositing various materials onto graphene will be reviewed.

1.6 Chemical vapour deposition

CVD involves the adsorption of precursor molecules from the vapour phase onto a heated substrate where they break down to form a desired material. These precursor species may have already begun thermal breakdown in the vapour phase, or been activated by a plasma. A generalised process is shown in figure 1.13.[90]

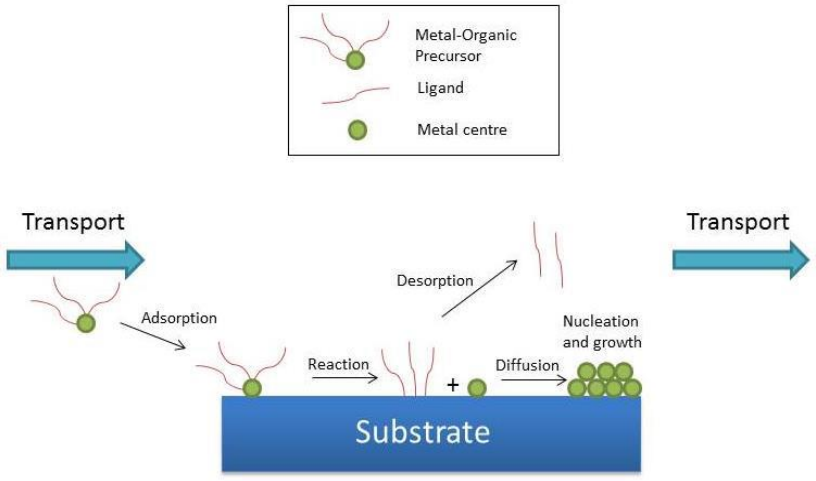

Figure 1.13 Diagram of processes involved in CVD. Reproduced from ref 90.

The precursor molecules are often volatile, and are delivered to the heated substrate by an inert carrier gas, typically nitrogen or argon. However, reactive gases such as oxygen or ammonia can also be used if oxidising or reducing conditions are required. Precursors can either be single source, where all the elements of the desired material are contained within one molecule, or multisource where different precursor molecules react together to produce the required material. Volatile by-products produced by the decomposing precursors are removed by vacuum and/or carrier gas. An advantage of CVD is it is often a scalable process.[91]. Additionally thin films are easy to produce and purity and stoichiometry is often easy to control.[90] However, high temperatures are often required and precursors can be difficult to design.[92] CVD can also be sensitive to a wide range of parameters such as flow rates, gas purities, and pressure. These parameters can also vary locally, so depositions even over length scales less than 1 cm can vary considerably. This multi parameter sensitivity means depositions are highly reactor specific, making the repeatability and comparability of results reported in different publications difficult. This often leads to the need for extensive optimisation of a process whenever a new CVD reactor is built.

Although all CVD reactors have individual design considerations depending on scale, the type of CVD process and the desired material they all have three basic design features outlined in figure 1.14.

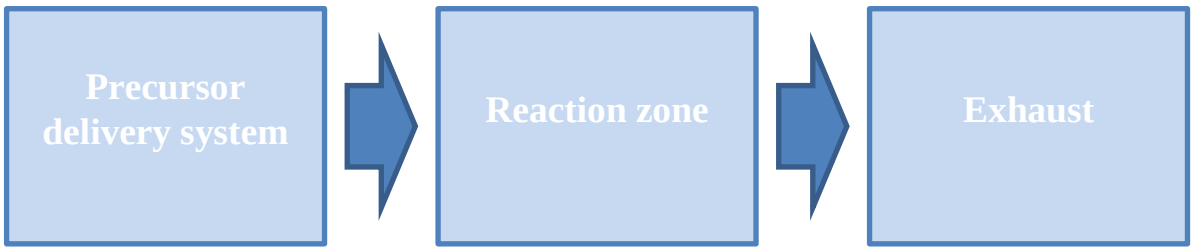

Figure 1.14 Basic design features of all CVD reactors.

There are a number of different CVD techniques that have different strengths and weaknesses:

- Atmospheric pressure CVD (AP-CVD).[93]
- Low pressure CVD (LP-CVD) and Ultra high vacuum CVD (UHV-CVD).[94]
- Aerosol assisted CVD (AA-CVD) and direct liquid injection.[95]
- Plasma enhanced CVD (PE-CVD).[96]

1.6.1 AP-CVD

AP-CVD utilises the volatility of precursors at atmospheric pressure and a carrier gas flow to deliver them to the reaction zone of the furnace. To increase their volatility they can be heated, this allows good control over the concentration of the precursor in the reaction zone. The residency time of the precursor can also be adjusted by changing the carrier gas flow. AP-CVD can either be run as true AP-CVD, where a pump balances the carrier gas input to create a flow at atmospheric pressure, or more commonly without a pump which creates an overpressure which depends on the carrier gas flowrate and the reactor geometries. This deviation from atmospheric pressure will affect depositions but is rarely mentioned in the literature and highlights the possible difficulties in repeating published results as home built reactors are all different. An advantage of working above atmospheric pressure is it helps exclude oxygen from the system as any leaks will have a flow of carrier gas out rather than a diffusion of oxygen in.

1.6.2 LP-CVD

LP-CVD and UHV-CVD operate in a similar manner to AP-CVD but are used when less volatile precursors are being employed. Additionally, due to the more homogeneous concentration of precursor over the reaction zone, a greater control over film uniformity can sometimes be achieved. It can be more expensive than AP-CVD however and the temperatures inside the reactor can be harder to control.

1.6.3 AA-CVD

AA-CVD is a method for getting non-volatile precursors into the vapour phase. AA-CVD usually employs ultrasonication or nebulisation to create a liquid/gas aerosol of precursor, usually in a solvent. A big advantage of AA-CVD is the range of precursors that can be used is large as volatility is not a limiting factor. Other advantages of AA-CVD include high deposition rates, flexible reaction environments (AA-CVD can be run at high or low pressures) and low cost of equipment. All these benefits make it an attractive technique to produce materials on a large scale. Due to the range of precursors, many different materials have been successfully deposited by AA-CVD. Precursors range from metal salts to complex organometallic molecules.[97,98] Due to the range of the materials produced at scales desirable for industry, materials produced by AA-CVD have been proposed for use in gas sensors, electronics, window coatings and solar cells amongst others.[99,100] Although AA-CVD offers access to a great range of materials, care has to be taken over material quality, especially contamination. One of the reasons for this is the solvent used in the aerosol can break down and be incorporated into the material rather than evaporating as desired. Additionally, more complex precursors often contain elements that are undesired in the final product, particularly carbon and

nitrogen. Therefore it is of great importance to select solvents that do not incorporate into the film and precursors that have clean decomposition pathways. If AA-CVD is going to be used to create microelectronics in the future, one final challenge is producing films with control over morphology at the nanometre scale. Due to the relatively fast deposition rates and turbulent conditions on the substrate due to evaporation of solvent, flat ultra-thin films on the scale of nm produced by AA-CVD have yet to be realised.

1.6.4 PE-CVD

PE-CVD allows the temperature required for precursor decomposition to be reduced. This is useful when the film is temperature sensitive, or the precursors are thermally stable. Microwave or radiowave radiation is often used to generate the plasma, which interacts with the precursor on the substrate. An advantage of PE-CVD is more uniform films can be generated, and due to lower temperatures, amorphous films can be produced. However, due to the increased reactive conditions it is harder to control the level of impurities within the film, also some substrates may not be plasma compatible[92]. This technique can be combined with AA-CVD to activate aerosolised precursors.[101]

1.7 Atomic layer deposition

Atomic layer deposition (ALD) is a type of CVD, however a precursor is chemisorbed onto and saturates the substrate surface which self-limits the film thickness. Any excess precursor is then purged out of the system before another layer is added. ALD also differs from CVD in that different precursors are introduced at different stages. An example process can be seen in figure 1.15.[102]

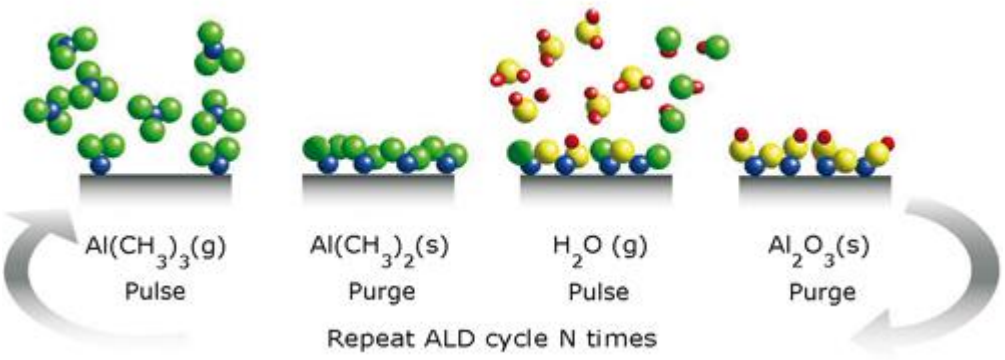

Figure 1.15 Schematic of a typical ALD cycle. Reproduced from ref 102.

One advantage of ALD over conventional CVD is that it limits potentially problematic gas phase reactions in CVD. Also, there is typically greater control over film thickness and less pinhole defects are created. Additionally unlike CVD, high aspect ratio materials can also be deposited as layers build up on a surface evenly, regardless of the angle of the surface with respect to the flow of the precursor. Electronic grade films are also easier to access as each pulse tends to have well defined surface reactions. Due to this, ALD is currently used by groups such as NASA and Intel to produce very high quality components. A disadvantage with ALD is the scope of materials that can be made is less than CVD, films take longer to grow due to the purging cycles, and only multisource precursors can be used.[102] Material scope is much reduced due to a smaller precursor space available as the requirements on precursors are much more stringent. Precursors need to be volatile and highly reactive to get a reasonable growth rate. Therefore the discovery of new ALD precursors is an active field of research. The other way to increase reactivity is to use plasma to activate the desired precursor.[103]

1.8 Chemical vapour deposition mechanisms

Apart from ALD, which has one growth mechanism, CVD has three distinct mechanisms by which deposited materials grow; these mechanisms depend on the substrate, the deposited material and the deposition conditions.

In a system where material **A** is going to be grown onto material **B**, and the interface between the two is atomically flat, defect free and only surface energies of materials are considered, there are two possible growth mechanisms. If the surface energy of **A** is higher than **B** it will prefer to deposit on itself and form islands. If the surface energy of **A** is less than **B** then **B** 'wets' **A** and **A** grows monolayer by monolayer. These two mechanisms of growth are called Frank van der Merwe (F-M) and Volmer-Weber (V-W)respectively.[104]

However, realistically **A** and **B** will have different atomic spacings, which introduce strain into the system. Theoretically, it has been shown at equilibrium layer by layer growth of a strained system is not possible.[105] However, kinetic constraints on mass transport can result in layer by layer growth of materials, which although are metastable, can last for a long time.[104]

The concept of strain can be used to explain the third growth mechanism, Stranski–Krastanov (S-K) growth, which is the initial growth of monolayers of material followed by island growth. As the number of monolayers increases, the amount of strain in material **A** increases, pushing it further from equilibrium. At a critical thickness, which is a function of the lattice mismatch of the materials, island growth will start to occur in order to relieve strain.[104] Figure 1.16 depicts the three growth mechanisms, the grey material is **B** and the coloured materials are **A.**

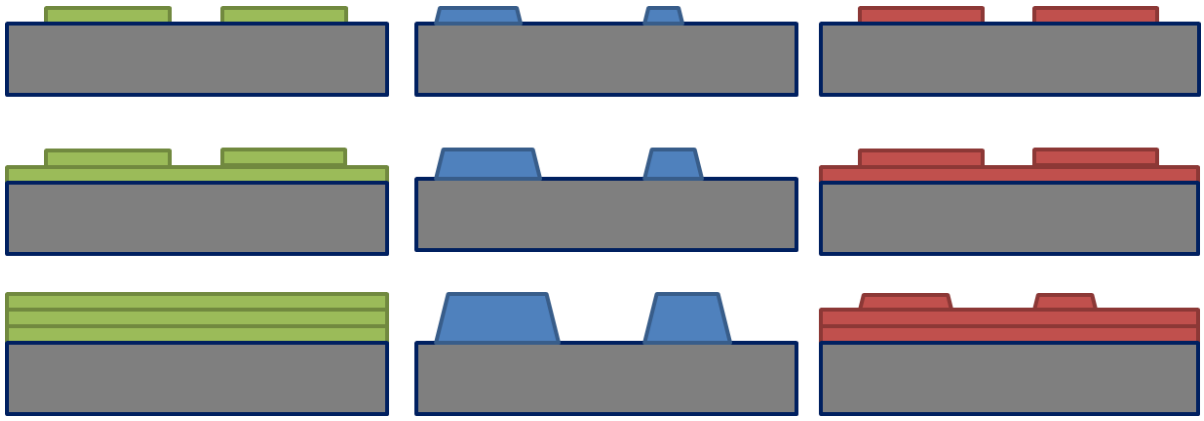

Figure 1.16 Left: Volmer-Webber growth Middle: Frank van der Merwe growth Right: Stranski–Krastanov growth.

1.9 Aims and Objectives

Graphene is well placed to contribute to the next generation of TCEs. One of the main barriers to realising this contribution is scalable routes to graphene and heterostructures devices. CVD and ALD are promising techniques that can deposit high quality materials on large scales, whether this be graphene or materials on graphene. Tungsten disulphide and tin sulphides have been suggested as materials that could find applications in the next generation of electronics and photovoltaic devices. Reliable scalable routes to these materials however have yet to be realised. The body of work presented in the next three chapters will focus on employing CVD and ALD to produce graphene, tungsten disulphide and tin sulphides. The aims of this thesis are to demonstrate the growth of graphene on a large scale, with the study of relevant materials deposited onto it also by scalable techniques. Throughout the work presented, the differences between the growth of materials on common substrates and graphene will be highlighted, and whether these differences are beneficial, will be explored.

1.10 References

1. Brock, D. C., *Understanding Moore's Law: Four Decades of Innovation*. Chemical Heritage Foundation: 2006.
2. *Joint science academies' statement: Global response to climate change.*; 2005.
3. EPA Sources of Greenhouse Gas Emissions. http://www.epa.gov/climatechange/ghgemissions/sources.html (accessed 08/09/2013).
4. Novoselov, K. S., Electric field effect in atomically thin carbon films. *Science* **2004,** *306*, 666-669.
5. Brodie, B., On the Atomic Weight of Graphite. *Proceedings of the Royal Society of London (1854-1905)* **1859,** *10*, 2.
6. Ruess, G.; Vogt, F., Höchstlamellarer Kohlenstoff aus Graphitoxyhydroxyd. *Monatshefte für Chemie und verwandte Teile anderer Wissenschaften* **1948,** *78* (3), 222-242.
7. Jang, B. Z.; Huang, W. C., Nano-scaled graphene plates. Google Patents: 2006.
8. Novoselov, K. S., Two-dimensional atomic crystals. *Proc. Natl Acad. Sci. USA* **2005,** *102*, 10451-10453.
9. Ryu, J.; Kim, Y.; Won, D.; Kim, N.; Park, J. S.; Lee, E.-K.; Cho, D.; Cho, S.-P.; Kim, S. J.; Ryu, G. H.; Shin, H.-A. S.; Lee, Z.; Hong, B. H.; Cho, S., Fast Synthesis of High-Performance Graphene Films by Hydrogen-Free Rapid Thermal Chemical Vapor Deposition. *ACS Nano* **2013,** *8* (1), 950-956.
10. Grosse, K. L.; Dorgan, V. E.; Estrada, D.; Wood, J. D.; Vlassiouk, I.; Eres, G.; Lyding, J. W.; King, W. P.; Pop, E., Direct observation of resistive heating at graphene wrinkles and grain boundaries. *Applied Physics Letters* **2014,** *105* (14), 143109.
11. Geim, A. K.; Novoselov, K. S., The rise of graphene. *Nat Mater* **2007,** *6* (3), 183-191.
12. Lee, C.; Wei, X.; Kysar, J. W.; Hone, J., Measurement of the Elastic Properties and Intrinsic Strength of Monolayer Graphene. *Science* **2008,** *321* (5887), 385-388.
13. Liu, F.; Ming, P.; Li, J., Ab initio calculation of ideal strength and phonon instability of graphene under tension. *Physical Review B* **2007,** *76* (6), 064120.
14. Dato, A.; Radmilovic, V.; Lee, Z.; Phillips, J.; Frenklach, M., Substrate-free gas-phase synthesis of graphene sheets. *Nano Letters* **2008,** *8* (7), 2012-2016.
15. Balandin, A. A.; Ghosh, S.; Bao, W. Z.; Calizo, I.; Teweldebrhan, D.; Miao, F.; Lau, C. N., Superior thermal conductivity of single-layer graphene. *Nano Letters* **2008,** *8* (3), 902-907.
16. Booth, T. J.; Blake, P.; Nair, R. R.; Jiang, D.; Hill, E. W.; Bangert, U.; Bleloch, A.; Gass, M.; Novoselov, K. S.; Katsnelson, M. I.; Geim, A. K., Macroscopic Graphene Membranes and Their Extraordinary Stiffness. *Nano Letters* **2008,** *8* (8), 2442-2446.
17. Bao, W.; Miao, F.; Chen, Z.; Zhang, H.; Jang, W.; Dames, C.; Lau, C. N., Controlled ripple texturing of suspended graphene and ultrathin graphite membranes. *Nat Nano* **2009,** *4* (9), 562-566.
18. Bunch, J. S.; Verbridge, S. S.; Alden, J. S.; van der Zande, A. M.; Parpia, J. M.; Craighead, H. G.; McEuen, P. L., Impermeable atomic membranes from graphene sheets. *Nano Letters* **2008,** *8* (8), 2458-2462.
19. Zakharchenko, K. V.; Fasolino, A.; Los, J. H.; Katsnelson, M. I., Melting of graphene: from two to one dimension. *Journal of Physics-Condensed Matter* **2011,** *23* (20).
20. Du, X.; Skachko, I.; Barker, A.; Andrei, E. Y., Approaching ballistic transport in suspended graphene. *Nature Nanotechnology* **2008,** *3* (8), 491-495.
21. Morozov, S. V.; Novoselov, K. S.; Katsnelson, M. I.; Schedin, F.; Elias, D. C.; Jaszczak, J. A.; Geim, A. K., Giant Intrinsic Carrier Mobilities in Graphene and Its Bilayer. *Physical Review Letters* **2008,** *100* (1), 016602.
22. Baringhaus, J.; Ruan, M.; Edler, F.; Tejeda, A.; Sicot, M.; Taleb, I.; Li, A.-P.; Jiang, Z.; Conrad, E. H.; Berger, C.; Tegenkamp, C.; de Heer, W. A., Exceptional ballistic transport in epitaxial graphene nanoribbons. *Nature* **2014,** *506* (7488), 349-354.
23. Tse, W. K.; Hwang, E. H.; Sarma, D. S., Ballistic hot electron transport in graphene. *Applied Physics Letters* **2008,** *93* (2).

24. Novoselov, K. S.; Jiang, Z.; Zhang, Y.; Morozov, S. V.; Stormer, H. L.; Zeitler, U.; Maan, J. C.; Boebinger, G. S.; Kim, P.; Geim, A. K., Room-Temperature Quantum Hall Effect in Graphene. *Science* **2007,** *315* (5817), 1379.
25. Loh, K. P.; Bao, Q.; Ang, P. K.; Yang, J., The chemistry of graphene. *Journal of Materials Chemistry* **2010,** *20* (12), 2277-2289.
26. Kuila, T.; Bose, S.; Mishra, A. K.; Khanra, P.; Kim, N. H.; Lee, J. H., Chemical functionalization of graphene and its applications. *Progress in Materials Science* **2012,** *57* (7), 1061-1105.
27. Marcano, D. C.; Kosynkin, D. V.; Berlin, J. M.; Sinitskii, A.; Sun, Z.; Slesarev, A.; Alemany, L. B.; Lu, W.; Tour, J. M., Improved Synthesis of Graphene Oxide. *ACS Nano* **2010,** *4* (8), 4806-4814.
28. Nourbakhsh, A.; Cantoro, M.; Vosch, T.; Pourtois, G.; Clemente, F.; van der Veen, M. H.; Hofkens, J.; Heyns, M. M.; De Gendt, S.; Sels, B. F., Bandgap opening in oxygen plasma-treated graphene. *Nanotechnology* **2010,** *21* (43).
29. Bekyarova, E.; Itkis, M. E.; Ramesh, P.; Berger, C.; Sprinkle, M.; de Heer, W. A.; Haddon, R. C., Chemical Modification of Epitaxial Graphene: Spontaneous Grafting of Aryl Groups. *Journal of the American Chemical Society* **2009,** *131* (4), 1336-+.
30. Xu, Y. X.; Bai, H.; Lu, G. W.; Li, C.; Shi, G. Q., Flexible graphene films via the filtration of water-soluble noncovalent functionalized graphene sheets. *Journal of the American Chemical Society* **2008,** *130* (18), 5856-+.
31. Wang, X. R.; Tabakman, S. M.; Dai, H. J., Atomic layer deposition of metal oxides on pristine and functionalized graphene. *Journal of the American Chemical Society* **2008,** *130* (26), 8152-+.
32. Li, Y.; Yuan, H.; von dem Bussche, A.; Creighton, M.; Hurt, R. H.; Kane, A. B.; Gao, H., Graphene microsheets enter cells through spontaneous membrane penetration at edge asperities and corner sites. *Proceedings of the National Academy of Sciences* **2013,** *110* (30), 12295-12300.
33. Li, Y.; Yuan, H.; von dem Bussche, A.; Creighton, M.; Hurt, R. H.; Kane, A. B.; Gao, H., Graphene microsheets enter cells through spontaneous membrane penetration at edge asperities and corner sites. *Proceedings of the National Academy of Sciences* **2013**.
34. Chowdhury, I.; Duch, M. C.; Mansukhani, N. D.; Hersam, M. C.; Bouchard, D., Colloidal Properties and Stability of Graphene Oxide Nanomaterials in the Aquatic Environment. *Environmental Science & Technology* **2013,** *47* (12), 6288-6296.
35. Jiao, L.; Wang, X.; Diankov, G.; Wang, H.; Dai, H., Facile synthesis of high-quality graphene nanoribbons. *Nat Nano* **2010,** *5* (5), 321-325.
36. Ruffieux, P.; Wang, S.; Yang, B.; Sánchez-Sánchez, C.; Liu, J.; Dienel, T.; Talirz, L.; Shinde, P.; Pignedoli, C. A.; Passerone, D.; Dumslaff, T.; Feng, X.; Müllen, K.; Fasel, R., On-surface synthesis of graphene nanoribbons with zigzag edge topology. *Nature* **2016,** *531* (7595), 489-492.
37. Tongay, S.; Lemaitre, M.; Fridmann, J.; Hebard, A. F.; Gila, B. P.; Appleton, B. R., Drawing graphene nanoribbons on SiC by ion implantation. *Applied Physics Letters* **2012,** *100* (7).
38. Hwang, W. S.; Zhao, P.; Tahy, K.; Nyakiti, L. O.; Wheeler, V. D.; Myers-Ward, R. L.; Eddy, C. R., Jr.; Gaskill, D. K.; Robinson, J. A.; Haensch, W.; Xing, H.; Seabaugh, A.; Jena, D., Graphene nanoribbon field-effect transistors on wafer-scale epitaxial graphene on SiC substrates. *APL Materials* **2015,** *3* (1).
39. Koos, A. A.; Murdock, A. T.; Nemes-Incze, P.; Nicholls, R. J.; Pollard, A. J.; Spencer, S. J.; Shard, A. G.; Roy, D.; Biro, L. P.; Grobert, N., Effects of temperature and ammonia flow rate on the chemical vapour deposition growth of nitrogen-doped graphene. *Phys. Chem. Chem. Phys.* **2014,** *16* (36), 19446-19452.
40. Jin, Z.; Yao, J.; Kittrell, C.; Tour, J. M., Large-Scale Growth and Characterizations of Nitrogen-Doped Monolayer Graphene Sheets. *ACS Nano* **2011,** *5* (5), 4112-4117.
41. Cattelan, M.; Agnoli, S.; Favaro, M.; Garoli, D.; Romanato, F.; Meneghetti, M.; Barinov, A.; Dudin, P.; Granozzi, G., Microscopic View on a Chemical Vapor Deposition Route to Boron-Doped Graphene Nanostructures. *Chemistry of Materials* **2013,** *25* (9), 1490-1495.
42. Röthlisberger, U.; Andreoni, W.; Parrinello, M., Structure of nanoscale silicon clusters. *Physical Review Letters* **1994,** *72* (5), 665-668.

43. Kara, A.; Leandri, C.; Davila, M.; Padova, P.; Ealet, B.; Oughaddou, H.; Aufray, B.; Lay, G., Physics of Silicene Stripes. *Journal of Superconductivity and Novel Magnetism* **2009,** *22* (3), 259-263.
44. Voon, L. C. L. Y.; Sandberg, E.; Aga, R. S.; Farajian, A. A., Hydrogen compounds of group-IV nanosheets. *Applied Physics Letters* **2010,** *97* (16), 163114-3.
45. Ivanovskii, A. L., Graphene-based and graphene-like materials. *Russian Chemical Reviews* **2012,** *81* (7), 571-605.
46. Houssa, M.; Scalise, E.; Sankaran, K.; Pourtois, G.; Afanas'ev, V. V.; Stesmans, A., Electronic properties of hydrogenated silicene and germanene. *Applied Physics Letters* **2011,** *98* (22), 223107-3.
47. Rokuta, E.; Hasegawa, Y.; Suzuki, K.; Gamou, Y.; Oshima, C.; Nagashima, A., Phonon Dispersion of an Epitaxial Monolayer Film of Hexagonal Boron Nitride on Ni(111). *Phys. Rev. Lett.* **1997,** *79* (23), 4609-4612.
48. Ponomarenko, L. A.; Geim, A. K.; Zhukov, A. A.; Jalil, R.; Morozov, S. V.; Novoselov, K. S.; Grigorieva, I. V.; Hill, E. H.; Cheianov, V. V.; Fal/'ko, V. I.; Watanabe, K.; Taniguchi, T.; Gorbachev, R. V., Tunable metal-insulator transition in double-layer graphene heterostructures. *Nat Phys* **2011,** *7* (12), 958-961.
49. Kubota, Y.; Watanabe, K.; Tsuda, O.; Taniguchi, T., Deep Ultraviolet Light-Emitting Hexagonal Boron Nitride Synthesized at Atmospheric Pressure. *Science* **2007,** *317* (5840), 932-934.
50. Xu, M.; Liang, T.; Shi, M.; Chen, H., Graphene-Like Two-Dimensional Materials. *Chemical Reviews* **2013,** *113* (5), 3766-3798.
51. Wei, X.; Wang, M.-S.; Bando, Y.; Golberg, D., Electron-Beam-Induced Substitutional Carbon Doping of Boron Nitride Nanosheets, Nanoribbons, and Nanotubes. *ACS Nano* **2011,** *5* (4), 2916-2922.
52. Tusche, C.; Meyerheim, H. L.; Kirschner, J., Observation of Depolarized ZnO(0001) Monolayers: Formation of Unreconstructed Planar Sheets. *Physical Review Letters* **2007,** *99* (2), 026102.
53. Weirum, G.; Barcaro, G.; Fortunelli, A.; Weber, F.; Schennach, R.; Surnev, S.; Netzer, F. P., Growth and Surface Structure of Zinc Oxide Layers on a Pd(111) Surface. *The Journal of Physical Chemistry C* **2010,** *114* (36), 15432-15439.
54. Bai, H.; Li, C.; Shi, G., Functional Composite Materials Based on Chemically Converted Graphene. *Advanced Materials* **2011,** *23* (9), 1089-1115.
55. Naguib, M.; Kurtoglu, M.; Presser, V.; Lu, J.; Niu, J.; Heon, M.; Hultman, L.; Gogotsi, Y.; Barsoum, M. W., Two-Dimensional Nanocrystals Produced by Exfoliation of Ti3AlC2. *Advanced Materials* **2011,** *23* (37), 4248-4253.
56. Chhowalla, M.; Shin, H. S.; Eda, G.; Li, L. J.; Loh, K. P.; Zhang, H., The chemistry of two-dimensional layered transition metal dichalcogenide nanosheets. *Nat. Chem.* **2013,** *5* (4), 263-275.
57. Shi, Y.; Li, H.; Li, L.-J., Recent advances in controlled synthesis of two-dimensional transition metal dichalcogenides via vapour deposition techniques. *Chemical Society Reviews* **2015,** *44* (9), 2744-2756.
58. Chhowalla, M.; Shin, H. S.; Eda, G.; Li, L.-J.; Loh, K. P.; Zhang, H., The chemistry of two-dimensional layered transition metal dichalcogenide nanosheets. *Nat Chem* **2013,** *5* (4), 263-275.
59. Hecht, D. S.; Hu, L.; Irvin, G., Emerging Transparent Electrodes Based on Thin Films of Carbon Nanotubes, Graphene, and Metallic Nanostructures. *Advanced Materials* **2011,** *23* (13), 1482-1513.
60. Sierros, K. A.; Morris, N. J.; Kukureka, S. N.; Cairns, D. R., Dry and wet sliding wear of ITO-coated PET components used in flexible optoelectronic applications. *Wear* **2009,** *267* (1–4), 625-631.
61. Jaymand, M.; Hatamzadeh, M.; Omidi, Y., Modification of polythiophene by the incorporation of processable polymeric chains: Recent progress in synthesis and applications. *Prog. Polym. Sci.* **2015,** *47*, 26-69.
62. Crispin, X.; Jakobsson, F. L. E.; Crispin, A.; Grim, P. C. M.; Andersson, P.; Volodin, A.; van Haesendonck, C.; Van der Auweraer, M.; Salaneck, W. R.; Berggren, M., The Origin of the High Conductivity of Poly(3,4-ethylenedioxythiophene)−Poly(styrenesulfonate) (PEDOT−PSS) Plastic Electrodes. *Chemistry of Materials* **2006,** *18* (18), 4354-4360.

63. Nardes, A. M.; Kemerink, M.; de Kok, M. M.; Vinken, E.; Maturova, K.; Janssen, R. A. J., Conductivity, work function, and environmental stability of PEDOT:PSS thin films treated with sorbitol. *Organic Electronics* **2008,** *9* (5), 727-734.
64. O'Connor, B.; Haughn, C.; An, K.-H.; Pipe, K. P.; Shtein, M., Transparent and conductive electrodes based on unpatterned, thin metal films. *Applied Physics Letters* **2008,** *93* (22), 223304.
65. Lee, J.-Y.; Connor, S. T.; Cui, Y.; Peumans, P., Solution-Processed Metal Nanowire Mesh Transparent Electrodes. *Nano Letters* **2008,** *8* (2), 689-692.
66. Dürkop, T.; Getty, S. A.; Cobas, E.; Fuhrer, M. S., Extraordinary Mobility in Semiconducting Carbon Nanotubes. *Nano Letters* **2004,** *4* (1), 35-39.
67. Wilder, J. W. G.; Venema, L. C.; Rinzler, A. G.; Smalley, R. E.; Dekker, C., Electronic structure of atomically resolved carbon nanotubes. *Nature* **1998,** *391* (6662), 59-62.
68. Peng, B.; Locascio, M.; Zapol, P.; Li, S.; Mielke, S. L.; Schatz, G. C.; Espinosa, H. D., Measurements of near-ultimate strength for multiwalled carbon nanotubes and irradiation-induced crosslinking improvements. *Nat Nano* **2008,** *3* (10), 626-631.
69. De Volder, M. F. L.; Tawfick, S. H.; Baughman, R. H.; Hart, A. J., Carbon Nanotubes: Present and Future Commercial Applications. *Science* **2013,** *339* (6119), 535-539.
70. Wu, Z.; Chen, Z.; Du, X.; Logan, J. M.; Sippel, J.; Nikolou, M.; Kamaras, K.; Reynolds, J. R.; Tanner, D. B.; Hebard, A. F.; Rinzler, A. G., Transparent, Conductive Carbon Nanotube Films. *Science* **2004,** *305* (5688), 1273-1276.
71. Tyler, T. P.; Brock, R. E.; Karmel, H. J.; Marks, T. J.; Hersam, M. C., Electronically Monodisperse Single-Walled Carbon Nanotube Thin Films as Transparent Conducting Anodes in Organic Photovoltaic Devices. *Advanced Energy Materials* **2011,** *1* (5), 785-791.
72. Zhang, D.; Ryu, K.; Liu, X.; Polikarpov, E.; Ly, J.; Tompson, M. E.; Zhou, C., Transparent, Conductive, and Flexible Carbon Nanotube Films and Their Application in Organic Light-Emitting Diodes. *Nano Letters* **2006,** *6* (9), 1880-1886.
73. Yu, X.; Hua, T.; Liu, X.; Yan, Z.; Xu, P.; Du, P., Nickel-Based Thin Film on Multiwalled Carbon Nanotubes as an Efficient Bifunctional Electrocatalyst for Water Splitting. *ACS Applied Materials & Interfaces* **2014,** *6* (17), 15395-15402.
74. Park, H.; Brown, P. R.; Bulović, V.; Kong, J., Graphene As Transparent Conducting Electrodes in Organic Photovoltaics: Studies in Graphene Morphology, Hole Transporting Layers, and Counter Electrodes. *Nano Letters* **2012,** *12* (1), 133-140.
75. Zhu, Z.; Mankowski, T.; Balakrishnan, K.; Shikoh, A. S.; Touati, F.; Benammar, M. A.; Mansuripur, M.; Falco, C. M., Ultrahigh Aspect Ratio Copper-Nanowire-Based Hybrid Transparent Conductive Electrodes with PEDOT:PSS and Reduced Graphene Oxide Exhibiting Reduced Surface Roughness and Improved Stability. *ACS Applied Materials & Interfaces* **2015,** *7* (30), 16223-16230.
76. Saga, T., Advances in crystalline silicon solar cell technology for industrial mass production. *Npg Asia Materials* **2010,** *2* (3), 96-102.
77. Song, Y.; Li, X.; Mackin, C.; Zhang, X.; Fang, W.; Palacios, T.; Zhu, H.; Kong, J., Role of Interfacial Oxide in High-Efficiency Graphene–Silicon Schottky Barrier Solar Cells. *Nano Letters* **2015,** *15* (3), 2104-2110.
78. Wang, J. T.-W.; Ball, J. M.; Barea, E. M.; Abate, A.; Alexander-Webber, J. A.; Huang, J.; Saliba, M.; Mora-Sero, I.; Bisquert, J.; Snaith, H. J.; Nicholas, R. J., Low-Temperature Processed Electron Collection Layers of Graphene/TiO2 Nanocomposites in Thin Film Perovskite Solar Cells. *Nano Letters* **2014,** *14* (2), 724-730.
79. Park, H.; Chang, S.; Zhou, X.; Kong, J.; Palacios, T.; Gradečak, S., Flexible Graphene Electrode-Based Organic Photovoltaics with Record-High Efficiency. *Nano Letters* **2014,** *14* (9), 5148-5154.
80. Ameri, T.; Dennler, G.; Lungenschmied, C.; Brabec, C. J., Organic tandem solar cells: A review. *Energy & Environmental Science* **2009,** *2* (4), 347-363.
81. Loh, K. P.; Tong, S. W.; Wu, J., Graphene and Graphene-like Molecules: Prospects in Solar Cells. *Journal of the American Chemical Society* **2016,** *138* (4), 1095-1102.

82. Morrow, W. K.; Pearton, S. J.; Ren, F., Review of Graphene as a Solid State Diffusion Barrier. *Small* **2016,** *12* (1), 120-134.
83. Tong, S. W.; Wang, Y.; Zheng, Y.; Ng, M.-F.; Loh, K. P., Graphene Intermediate Layer in Tandem Organic Photovoltaic Cells. *Advanced Functional Materials* **2011,** *21* (23), 4430-4435.
84. Lee, S. T.; Gao, Z. Q.; Hung, L. S., Metal diffusion from electrodes in organic light-emitting diodes. *Applied Physics Letters* **1999,** *75* (10), 1404-1406.
85. Lee, J.; Han, T.-H.; Park, M.-H.; Jung, D. Y.; Seo, J.; Seo, H.-K.; Cho, H.; Kim, E.; Chung, J.; Choi, S.-Y.; Kim, T.-S.; Lee, T.-W.; Yoo, S., Synergetic electrode architecture for efficient graphene-based flexible organic light-emitting diodes. *Nat Commun* **2016,** *7*.
86. Withers, F.; Del Pozo-Zamudio, O.; Mishchenko, A.; Rooney, A. P.; Gholinia, A.; Watanabe, K.; Taniguchi, T.; Haigh, S. J.; Geim, A. K.; Tartakovskii, A. I.; Novoselov, K. S., Light-emitting diodes by band-structure engineering in van der Waals heterostructures. *Nat Mater* **2015,** *14* (3), 301-306.
87. Geim, A. K.; Grigorieva, I. V., Van der Waals heterostructures. *Nature* **2013,** *499* (7459), 419-425.
88. Georgiou, T.; Jalil, R.; Belle, B. D.; Britnell, L.; Gorbachev, R. V.; Morozov, S. V.; Kim, Y.-J.; Gholinia, A.; Haigh, S. J.; Makarovsky, O.; Eaves, L.; Ponomarenko, L. A.; Geim, A. K.; Novoselov, K. S.; Mishchenko, A., Vertical field-effect transistor based on graphene-WS_2 heterostructures for flexible and transparent electronics. *Nat Nano* **2013,** *8* (2), 100-103.
89. Bertolazzi, S.; Krasnozhon, D.; Kis, A., Nonvolatile Memory Cells Based on MoS2/Graphene Heterostructures. *ACS Nano* **2013,** *7* (4), 3246-3252.
90. Jairath, R.; Jain, A.; Tolles, R. D.; Hampden-Smith, M. J.; Kodas, T. T., Introduction. In *The Chemistry of Metal CVD*, Wiley-VCH Verlag GmbH: 2007; pp 1-43.
91. Schwarz, S.; Rosiwal, S. M.; Frank, M.; Breidt, D.; Singer, R. F., Dependence of the growth rate, quality, and morphology of diamond coatings on the pressure during the CVD-process in an industrial hot-filament plant. *Diamond and Related Materials* **2002,** *11* (3-6), 589-595.
92. Pierson, H. O., 1 - Introduction and General Considerations. In *Handbook of Chemical Vapor Deposition (CVD) (Second Edition)*, William Andrew Publishing: Norwich, NY, 1999; pp 25-35.
93. Drosos, C.; Vernardou, D., Perspectives of energy materials grown by APCVD. *Sol. Energy Mater. Sol. Cells* **2015,** *140*, 1-8.
94. Maeda, K., CVD (Part 1): Atmospheric Pressure/Low-Pressure CVD. In *Ultraclean Surface Processing of Silicon Wafers: Secrets of VLSI Manufacturing*, Hattori, T., Ed. Springer Berlin Heidelberg: Berlin, Heidelberg, 1998; pp 317-330.
95. Alghamdi, Y.; O'Brien, P.; Chemistry, U. o. M. S. o., *Deposition of Semiconductor Thin Films Via AACVD from Single-source Precursors*. University of Manchester: 2008.
96. Kern, W., *Thin film processes II*. Academic press: 2012; Vol. 2.
97. Ponja, S. D.; Sehmi, S. K.; Allan, E.; MacRobert, A. J.; Parkin, I. P.; Carmalt, C. J., Enhanced Bactericidal Activity of Silver Thin Films Deposited via Aerosol-Assisted Chemical Vapor Deposition. *ACS Applied Materials & Interfaces* **2015,** *7* (51), 28616-28623.
98. Ahmet, I. Y.; Hill, M. S.; Johnson, A. L.; Peter, L. M., Polymorph-Selective Deposition of High Purity SnS Thin Films from a Single Source Precursor. *Chemistry of Materials* **2015,** *27* (22), 7680-7688.
99. Marchand, P.; Hassan, I. A.; Parkin, I. P.; Carmalt, C. J., Aerosol-assisted delivery of precursors for chemical vapour deposition: expanding the scope of CVD for materials fabrication. *Dalton Transactions* **2013,** *42* (26), 9406-9422.
100. Hou, X.; Choy, K. L., Processing and Applications of Aerosol-Assisted Chemical Vapor Deposition. *Chemical Vapor Deposition* **2006,** *12* (10), 583-596.
101. Wang, H. B.; Meng, G. Y.; Peng, D. K., Aerosol and plasma assisted chemical vapor deposition process for multi-component oxide La0.8Sr0.2MnO3 thin film. *Thin Solid Films* **2000,** *368* (2), 275-278.

102. Pakkala, A.; Putkonen, M., Chapter 8 - Atomic Layer Deposition. In *Handbook of Deposition Technologies for Films and Coatings (Third Edition)*, Peter, M. M., Ed. William Andrew Publishing: Boston, 2010; pp 364-391.
103. Kim, H.; Oh, I. K., Review of plasma-enhanced atomic layer deposition: Technical enabler of nanoscale device fabrication. *Japanese Journal of Applied Physics* **2014,** *53* (3).
104. Venables, J., *Introduction to surface and thin film processes*. Cambridge University Press: 2000.
105. Humphreys, C., SURFACE PHYSICS - CONTROLLING CRYSTAL-GROWTH. *Nature* **1989,** *341* (6244), 689-689.

Chapter 2. Chemical Vapour Deposition and Atomic Layer deposition of Graphitic Materials

2.1 Introduction

This chapter focuses on the growth and transfer of graphitic and graphene films, grown using chemical vapour deposition (CVD) and atomic layer deposition (ALD) techniques, for use as transparent conducting electrodes (TCEs). Current progress in top down and bottom up routes to graphene will be discussed, focussing on CVD routes to graphene. Transferring CVD graphene onto relevant substrates for integration into devices will be considered, followed by a discussion of Raman spectroscopy, a key analytical technique in graphene science. Efforts to produce graphene on cm length scales using a home built CVD reactor will then be presented, followed by transferring the graphene films onto desired substrates. Finally, graphitic films produced by plasma enhanced ALD (PE-ALD) through efforts to reduce the deposition temperatures, will be presented.

2.1.1 Synthetic routes to graphene

2.1.1.1 Exfoliation

The two top down approaches to obtain graphene involve exfoliation of graphene from graphite. This can be achieved by micromechanical or chemical exfoliation.

Micromechanical exfoliation is the simplest and one of the oldest techniques for producing graphene.[1] One method is the 'Scotch tape method' that is still currently used by researchers, where a sample of highly oriented pyrolitic graphite (HOPG) is repeatedly thinned down using tape, until monolayer and few layer graphene flakes are obtained.[2] Another method is to use AFM tips to physically manipulate graphite into single sheets of graphene.[3] These techniques still tend to produce the highest quality samples with the least defects, however a drawback is there is little potential for scaling the process. A recent development in this area was Paton et al. reporting using a kitchen blender to shear off sheets of graphene from graphite.[4] This provides a route for the upscaling of the mechanical exfoliation technique for use in products such as conducting inks, however it will be of limited use for applications requiring continuous sheets.

Graphite can also be exfoliated chemically. One method involves intercalating alkali metals into graphite, whereupon it is heated, breaking it apart into individual sheets.[5] Solvents with a high enough

affinity with a graphene surface so as to overcome the energetic penalty for separating the graphite sheets can also be used to exfoliate graphite. Solvents that have proven effective include N-methylpyrrolidone (NMP) and N,N-Dimethylacetamide (DMA).[6]

2.1.1.2 Reduction of graphene oxide (GO)

The physics and chemistry of GO will be discussed later, however its reduction is an important route to the production of graphene, which will be discussed below.

Once graphite has been oxidised to graphene oxide, it can be exfoliated by a variety of thermal and mechanical methods, with sonicating and/or stirring GO in water being the most common. Sonicating in water or in a polar organic media is much faster than mechanical stirring, but causes damage on top of that introduced by the oxidation process. The mean size of the platelets is reduced from the order of several microns per side, to several hundred nanometers per side, with the distribution of sizes increasing. Once platelets of GO have been obtained, different reduction techniques can be used to generate graphene flakes. These include, chemical, thermal and electrochemical reductions.[7]

The most common, and one of the first reported chemicals, used to reduce GO was hydrazine monohydrate.[8] While most strong reductants have reactivity issues with water, hydrazine monohydrate does not, making it an attractive approach for reducing aqueous dispersions of graphene oxide. More recently, sodium borohydride has been shown to produce graphene sheets of higher quality than hydrazine, with less heteroatom inclusion.[9] Hydroquinone and highly alkaline solutions have also been used although they seem to be less effective than hydrazine and sodium borohydride.

The thermal reduction of GO involves the loss of CO_2 at temperatures of ~1050 ^{o}C. This method has the advantage of exfoliating graphite oxide due to the large pressures involved, as well as reducing it in one step. However, due to the loss of carbon from the GO, this technique tends to generate far more defects.[10]

Electrochemical reduction is probably the least developed technique for producing graphene flakes from GO. It generally involves depositing a thin film of GO onto a substrate with electrodes attached at either end and a voltage is then swept across.[11] The advantages of this method include the mild conditions required, with no toxic chemicals needed. However, it has yet to be demonstrated this can be achieved on a large scale.

2.1.1.3 Chemical vapour deposition

For the synthesis of graphene by chemical vapour deposition, the metals which the graphene is grown on have been dominated by copper and nickel. The mechanisms by which graphene grows on these two metals is different, which leads to differences in how many layers of graphene are formed.

For graphene grown on nickel, generally polycrystalline nickel films are initially annealed in an Ar/H_2 atmosphere at 900-1000 ^oC. This increases grain size and helps flatten the nickel. The nickel is then typically exposed to a H_2/CH_4 gas mixture. In this step, CH_4 breaks down and carbon atoms dissolve into the nickel film to form a solid solution. Finally, samples are cooled down under Ar gas. Unlike copper, nickel has relatively high carbon solubility at high temperatures.[12] During the 'cooling down' process, carbon atoms diffuse out of the bulk of the nickel and precipitate on the surface to form graphene films. The Ni(111) surface has a lattice geometry similar to the hexagonal lattice of graphene and also has a similar lattice constant, providing a good lattice matched substrate for graphene growth. Since the graphene growth on nickel is a carbon segregation and precipitation process, control over the precipitation process by varying the rate at which the substrate is cooled leads to differences in the number of layers of graphene produced.[13]

Unlike nickel, copper has low carbon solubility at all temperatures.[15] Most of the carbon for graphene formation is catalytically decomposed on the copper surface. After the first layer of graphene is fully covering the copper surface, there is no catalyst exposed to decompose the hydrocarbon and thus growth of a second graphene layer is quenched. This means graphene growth on a copper surface is self-limiting. This mechanism has been proven experimentally by isotopic labelling of hydrocarbon precursors combined with Raman mapping.[14] The growth conditions for graphene on copper are similar to those of nickel, with an initial annealing step of ca. 1000 ^oC in an Ar/H_2 atmosphere to increase grain size and remove any surface oxides. A CH_4/H_2 mixture is then passed over the copper, at which time carbon nucleates and graphene domains grow, which eventually stitch together to form a graphene sheet.[15] A schematic of this process can be seen in figure 2.1.

Although CVD graphene currently looks to be the most viable technique for producing large quantities of single layer graphene, there are still some hurdles that need to be overcome. The three main issues are: i) the temperatures required, ii) the polycrystallinity of the graphene produced and iii) the limited substrates graphene can be formed on. Temperature is obviously tied up with cost for large scale production, but is also important when considering sensitive components in whole device manufacture. Polycrystallinity affects the working lifetime of the graphene sheets in devices and their electronic properties.[16] Limited growth substrates also affects cost, as an extra step has to be added to the manufacture process to transfer graphene onto desirable substrates (which can also degrade

the graphene). Researchers therefore have been studying different substrates, hydrocarbon precursors and processing conditions to try to address these problems.

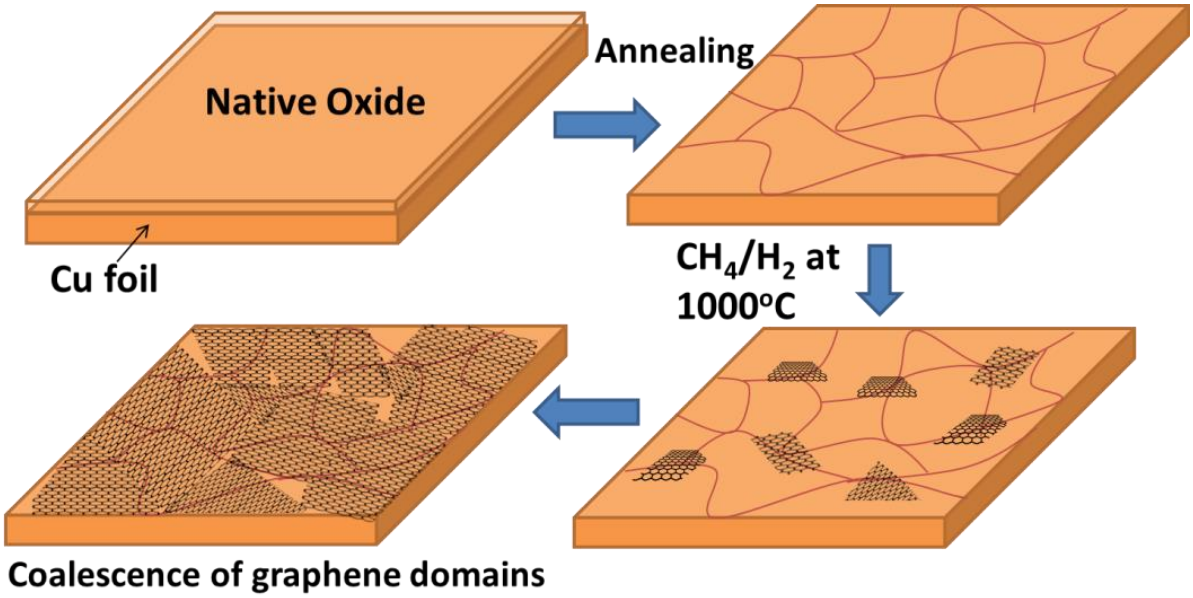

Figure 2.1 Diagram of the general CVD process for synthesising graphene onto copper. From ref 15.

Recently, it was shown that monocrystalline graphene could be grown on an oriented germanium wafer. As the germanium was hydrogen terminated, the graphene could be peeled off by a small layer of gold and the expensive germanium could be reused.[17] Whilst this is a exciting development, the process uses low pressures of 10^{-6} Torr, GeH_4 and processing temperatures are still rather high at 930 °C.

Another route to producing moncrystaline graphene, using cheaper copper substrates, involves minimising the graphene nucleation points during the process. This is achieved by flattening the copper as much as possible by melting it at ca. 1100 °C and using methane gas diluted in an Ar/H_2 mix.[18] The major issues with this technique involve the long growth times of ca. 24 h and the high temperatures required. Additionally wafer length scales of cm have yet to be achieved.

In an attempt to achieve lower deposition temperatures, precursor sources other than methane have been studied. The current lowest temperature reported that produces high quality monolayer graphene is 300 °C, using benzene as a precursor source.[19] Many other alternate precursors have been studied, which have significantly reduced the temperatures required, however there is still a lot of scope for designing bespoke precursors that have an even lower decomposition energy than benzene.

One alternative way in which the lower temperatures can be achieved is to break down the hydrocarbons using a plasma. Whilst this area of research is still relatively small compared to conventional CVD approaches, there has been success at lowering the reaction temperatures required to produce graphene, although the quality of the graphene produced tends to suffer. One example involved a CH_4/H_2 plasma generated by radiofrequency waves. Growth temperatures as low as 600 ^oC were achieved, although quality did decrease.[20] Another method used a high energy microwave generated plasma to activate CH_4 to decomposition on an aluminium substrate. For this method was a low temperature of 300 ^oC was used, along with a non-catalytic substrate.[21]

In summary, CVD is currently the most promising avenue of research for the realisation of the large scale manufacture of graphene. Recent developments have shown there is still a lot of scope for developing the process to overcome key challenges that remain, such as growth temperatures, choice of growth substrate and polycrystallinity.

2.1.2 CVD graphene transfer

Methods for synthesising graphene on a scale large enough for TCEs has been discussed in the previous section. Due to the large scale of high quality graphene produced, CVD seems to be the most desirable technique for producing graphene transparent electrodes (GTEs). However copper and nickel, the most common and effective growth substrates for the CVD of graphene, are obviously not transparent. Additionally, for many devices, it is necessary to have graphene supported by an insulating substrate. Therefore processes that transfer graphene onto desirable substrates need to be developed. Transfer methods for CVD graphene either involve polymer assisted transfer, or mechanical exfoliation.

Polymer assisted transfer involves 4 general steps:

1) Etching away unwanted graphene on the underside of the growth substrate, either by plasma or an oxidising acid such as HNO_3.
2) Graphene on the growth substrate has to be coated with a supportive polymer layer such as poly(methylmethacrylate) (PMMA).
3) The growth substrate then needs to be etched away. A typical etchant for copper is $FeCl_3$.
4) The graphene/polymer stack can then be transferred to a desired flat substrate. The polymer can then be dissolved in a solvent such as acetone.

Although this process can transfer graphene sheets onto target substrates large enough to use as TCEs, there are issues with the process that have yet to be fully solved. These issues can be split into problems with polymer residues and discontinuities in the transferred film.

Polymer residues can inhibit the transparency of the GTE, limiting performance. They can also prevent an intimate contact between the GTE and the active material deposited onto it, leading to limitations in performance. The persistence of polymer residues on transferred graphene has been a long standing problem. Attempts to overcome this issue include annealing the films, using different solvents for polymer removal, more soluble polymers and alternate 'dry transfer' techniques. With all these techniques, there is a trade-off between polymer removal and damage to the graphene film.

It is generally agreed that annealing graphene films in a reducing atmosphere or vacuum after dissolving the polymer away produces the most residue free films. Chiu et al. used tunnelling electron microscopy (TEM) to demonstrate PMMA is lost in a two-step process under annealing at 200 ^{o}C in H_2, with the second loss event involving PMMA tightly bound to the graphene surface.[22] However residues still remained and even annealing in air, which made the surface cleaner, did not completely remove residues. Annealing in air also increased the damage to the graphene film and is often incompatible with some plastic substrates. Chiu et al. mention even annealing at 700 ^{o}C in a TEM vacuum left films 'far from satisfactory'.

Some evidence has been put forward suggesting cleaning graphene sheets in acetic acid rather than acetone reduces residues.[23] However with little quantitative data, such as X-ray photoemission spectroscopy (XPS) produced to support this assertion, it is difficult to confirm that acetone cleans graphene to a greater degree without annealing.[24] Supporting polymers other than PMMA such as poly(bisphenol A carbonate) have been reported to produce less residue,[25] although similarly to alternate chemical PMMA removal techniques, there are reports claiming PMMA can produce graphene films with a similar amount of residue.[26]

Removal of residues produced during transfer is still a problem that needs to be overcome, with even very recent papers exploring whether the supporting polymer can be left on after transfer to avoid this step completely.[27]

Dry transfer techniques give the advantage of not having to use metal etchants, polymers with a strong adherence to graphene such as PMMA, more accuracy of graphene placement on substrate and the ability to reuse the growth substrate. However, the major drawback of manipulating graphene in this way leads to more physically damaged graphene films. Cho et al. demonstrated graphene could be directly exfoliated from copper using an epoxy adhesion layer.[28] Lipomi et al. show various metals can be evaporated onto graphene, thermal release tape applied and the graphene exfoliated from the growth substrate. The thermal release tape is then removed and the metal etched away.[29] Figure 2.2 displays a diagram showing the process.

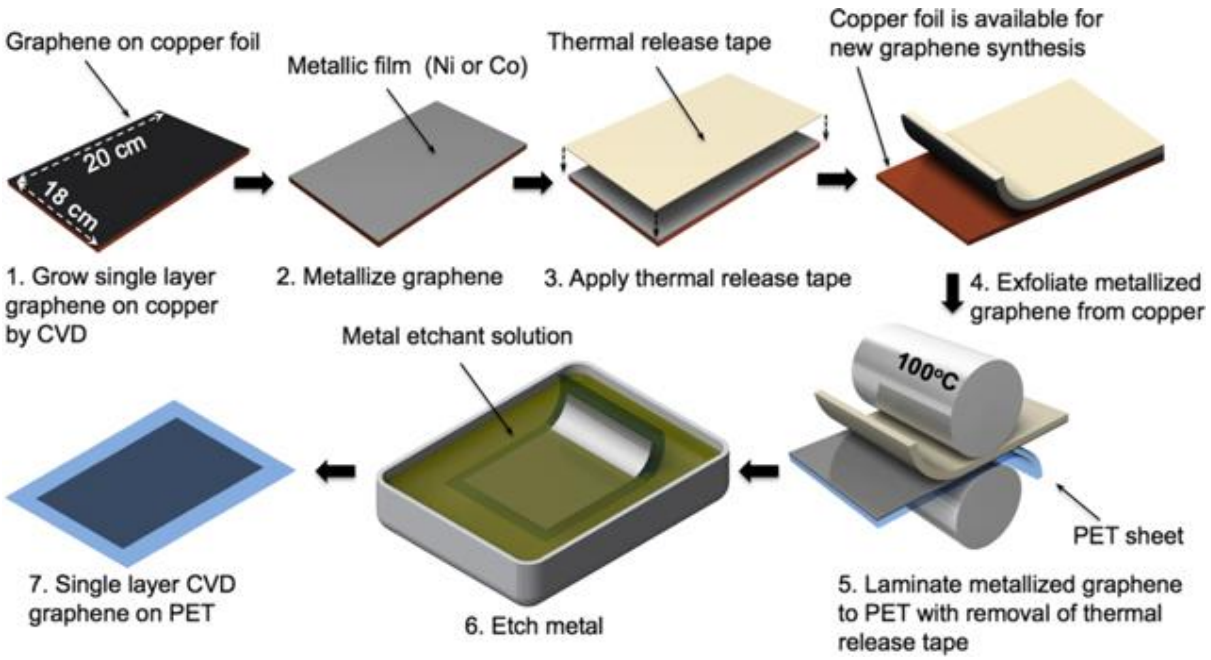

Figure 2.2 Process for dry transfer of graphene films from growth substrate. Reproduced from ref 29.

Discontinuities and wrinkles in the graphene film created during the transfer process are the other significant factor limiting GTEs performance. Due to the different thermal expansion coefficients between growth substrates and graphene, metals contract more on cooling, causing the graphene to wrinkle and crack. Wrinkles have been shown to reduce graphene's conductivity.[30] To minimise wrinkling of the graphene film, several methods have been proposed. Yoon et al. coat a glass substrate with a sub 10 nm coating of titanium, which increases adhesion with the graphene film. As the titanium is thin, it does not affect the transmittance of the glass.[31] Cho et al. demonstrated that a thin layer of organic solvent decreases the surface tension on the substrate, reducing wrinkling.[32] Decreasing the growth substrate's roughness also has been shown to reduce some of the wrinkling. [33]Partially melting the PMMA stack in a baking step relaxes the graphene and adheres it strongly to the substrate surface.[24]

Although the growth and transfer of graphene films has yet to be optimised, various functioning devices using GTEs have been made, which have been discussed in chapter 1.

2.1.3 Raman spectroscopy

Due to graphene being a very thin material (between 1-10 atomic layers), techniques that rely on bulk material such as powder x-ray diffraction (PXRD) are often ineffective. Fortunately, graphene has a strong Raman signal and as such, Raman spectroscopy is probably the leading technique for

characterising graphene. Due to Raman spectroscopy's importance to graphene research, a short overview will now be given.

Raman spectroscopy is similar to IR spectroscopy in that vibrational information from molecules and materials can be acquired, however the types of vibrations that can be detected depend on the technique. IR spectroscopy measures absorption of IR waves that result in vibrational changes in molecules or materials and detects vibrations that involve a change in dipole moment. Raman spectroscopy relies on the inelastic scattering of monochromatic light, usually provided by a laser. The initial absorption involves an electronic rather than vibrational transition (as in IR spectroscopy). The frequency of the re-emitted photons are shifted 'up' or 'down' compared with the original monochromatic frequency through changes in the vibrational state of the molecule or material, which is called the Raman effect.[34] The shift in frequency provides information about vibrational, rotational and other low frequency transitions in samples. Raman spectroscopy can detect vibrations that involve a change in polarisability. As IR and Raman spectroscopy can detect different types of vibrations, the techniques are complementary. One of the strengths of Raman and IR spectroscopy is they can be used to study solid, liquid and gaseous samples.

In Raman spectroscopy, only about 0.0001% of incident photons produce inelastic scattering. This means special measures need to be taken to distinguish it from the predominant Rayleigh scattering. Instruments therefore use devices such as notch filters and laser stop apertures, to obtain high-quality Raman spectra. Even so, signal strength can still be a major problem for Raman spectroscopy and there is currently an active research field attempting to overcome this problem, although this is not a problem for the Raman spectroscopy of graphene.

Overall, Raman spectroscopy has a number of benefits, it is non-destructive and local areas on micrometre length scales can be analysed, in addition to large area maps being possible. The technique is usually fast, with no vacuum or cooling required and solids, liquids and gases can be studied. There is however the possibility for laser damage to delicate samples and some samples do not have significant Raman spectra. Graphene is not the only carbon material that can be characterised by Raman spectroscopy. Carbon nanotubes, even down to their chirality, number of layers and quality can be analysed. Figure 2.3 shows example Raman spectra for a variety of carbon based materials.

The G and D peaks are the main features in the Raman spectra of carbon materials, which appear around 1560 and 1360 cm^{-1}, respectively, when a visible laser is used for excitation. In amorphous carbon a peak at around 1060 cm^{-1} (T peak) is seen under UV excitation.[35] Unless a UV laser is being used, the spectra are dominated by the sp^2 sites, because visible wavelengths are close in energy to transitions in π states. Even for highly sp^3 amorphous carbon samples, the visible Raman spectra are due to sp^2 sites. The G peak arises from in plane stretching of sp^2 C-C bonds. Only for diamond or samples containing a significant fraction of diamond phase, is the diamond sp^3 peak at 1332cm^{-1} seen.[36]

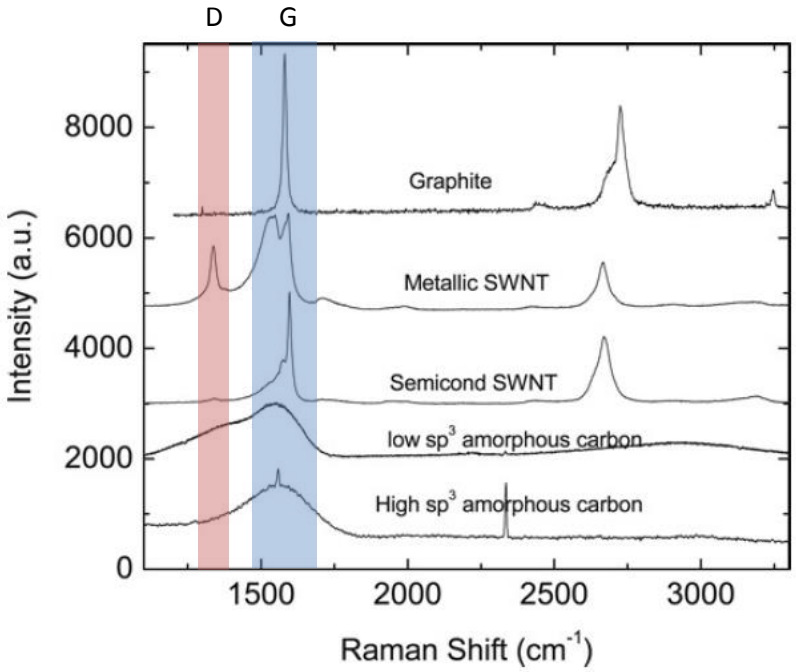

Figure 2.3 Example Raman spectra of various carbon materials. Reproduced from ref 35.

A typical Raman spectrum of graphene compared with graphite obtained with a green laser line can be seen in figure 2.4. The two most important peaks in the Raman spectrum of graphene are the G and the historically although inaccurately named G' peak (now more commonly known as the 2D peak). In pristine graphene, the G peak is the only first order peak present, as it arises from the only electron–single vibrational mode (phonon) energy exchange with no wavevector variation (so momentum is conserved). If disorder is present within the graphene film D and D' peaks will be present at ~ 1350 and 1620 cm^{-1} respectively. For a D or D' peak to occur, a charge carrier must be excited and scattered inelastically by a phonon, then recombination must occur which can happen due to a second elastic scattering at a defect or edge. The difference between the peaks is the D peak evolves from an inter-valley scattering process which involves large momentum phonons, whereas the D' peak evolves from an intra-valley process which involves low momentum phonons, these processes can be seen in figure 2.5.[37] It has recently been found that the nature of the defect sites in graphene relate to the ratio of intensities between the D and D' peak.[38]

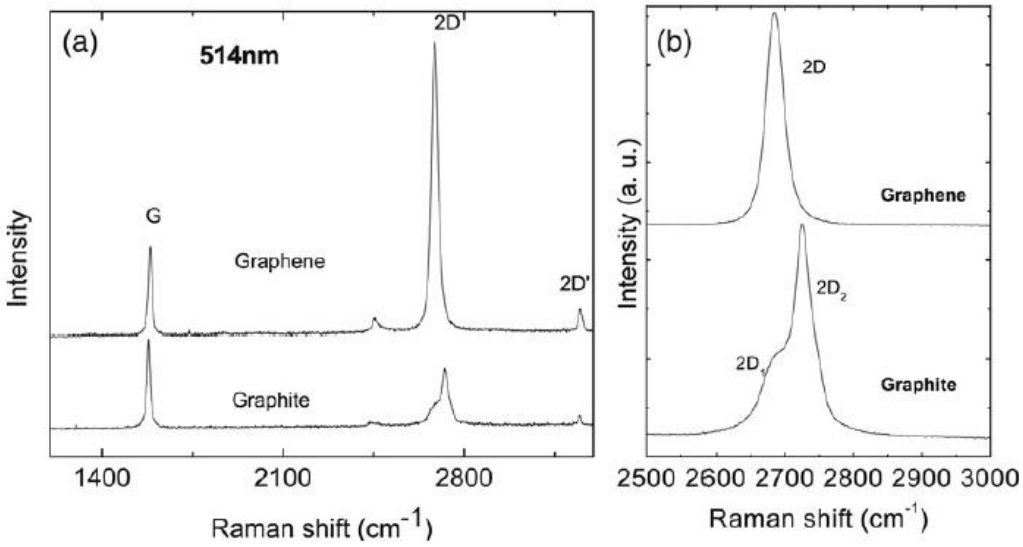

Figure 2.4 Typical Raman spectra of graphene compared with graphite. Reproduced from ref 35.

Vacancy defects produce a relatively higher D' peak compared to sp^3 defects. Figure 2.5 shows all the phonon scattering processes that the Raman peaks discussed so far arise from. The cones are the electronic states in the hexagonal Brillouin zone. The 2D peak results from a second order scattering process. In second order processes, incident photons produce two phonons rather than one, thus resulting in a Raman shift twice the size of the corresponding first order process. The corresponding process of the 2D peak is the D peak which, as discussed, is not present in pristine graphene. The 2D peak is always allowed, as recombination can happen due to the second phonon in the process.

The 2D peak also gives important information on how many layers of graphene are present. Figure 2.6 shows the evolution of a single Lorentzian peak as the number of graphene layers increase at two different laser wavelengths. Additionally, the ratio of heights between the G and 2D peaks indicates the number of layers present, for single layer graphene as shown in figure 2.4, the 2D is over two times the height of the G peak, for bilayer graphene the heights are roughly equal, and for more layers the G peak is higher than the 2D peak.

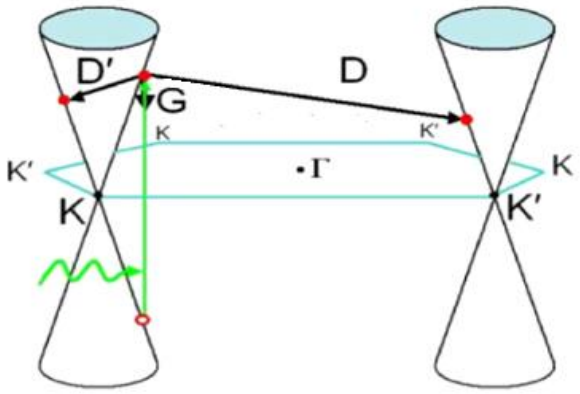

Figure 2.5 Green arrow depicts the initial excitation of the electron. The black arrows depict the transitions of the excited electron that produce the various Raman shifts. Adapted from ref 37.

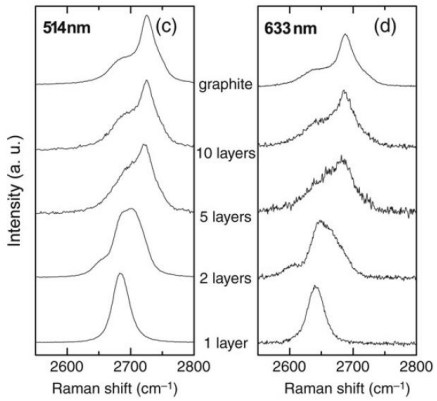

Figure 2.6 Raman spectra showing the evolution of a single Lorentzian peak as the number of graphene layers decreases for two different laser excitations. Reproduced from ref 35.

2.2 Results and discussion – reactor design and process development

2.2.1 Reactor design

The first choice when considering the design of a reactor that will produce graphene is whether it will operate under low or atmospheric pressure. As previously discussed, there are advantages and disadvantages to both systems. Atmospheric pressure systems tend to involve an easier set up as parts required to hold an acceptable vacuum are not needed. Additionally, it has been reported that growth on copper substrates is not self-limiting in an AP-CVD setup, with the flow of methane allowing control over the number of layers produced.[11] However, according to various studies low pressure systems tend to produce higher quality graphene samples.[39]

For the purposes of our research, creating a low pressure based system was chosen due to the potential to create higher quality graphene. In addition the vacuum system could be more easily modified to run at atmospheric pressure and use a larger range of precursors, including liquid and inorganic precursors such as ammonia borane. Due to its ability to withstand high temperatures and moderate vacuums, quartz was chosen to house the substrate used to grow the graphene on. The quartz tube was made sufficiently long enough that a tube furnace could be moved away from the catalyst without interfering with temperature sensitive components of the reactor for rapid cooling of the catalyst if desired. A liquid nitrogen trap was fitted to protect the pump and to help achieve a lower vacuum, particularly by trapping water vapour. Figure 2.7 displays a diagram of the complete reactor, with a picture of it functioning.

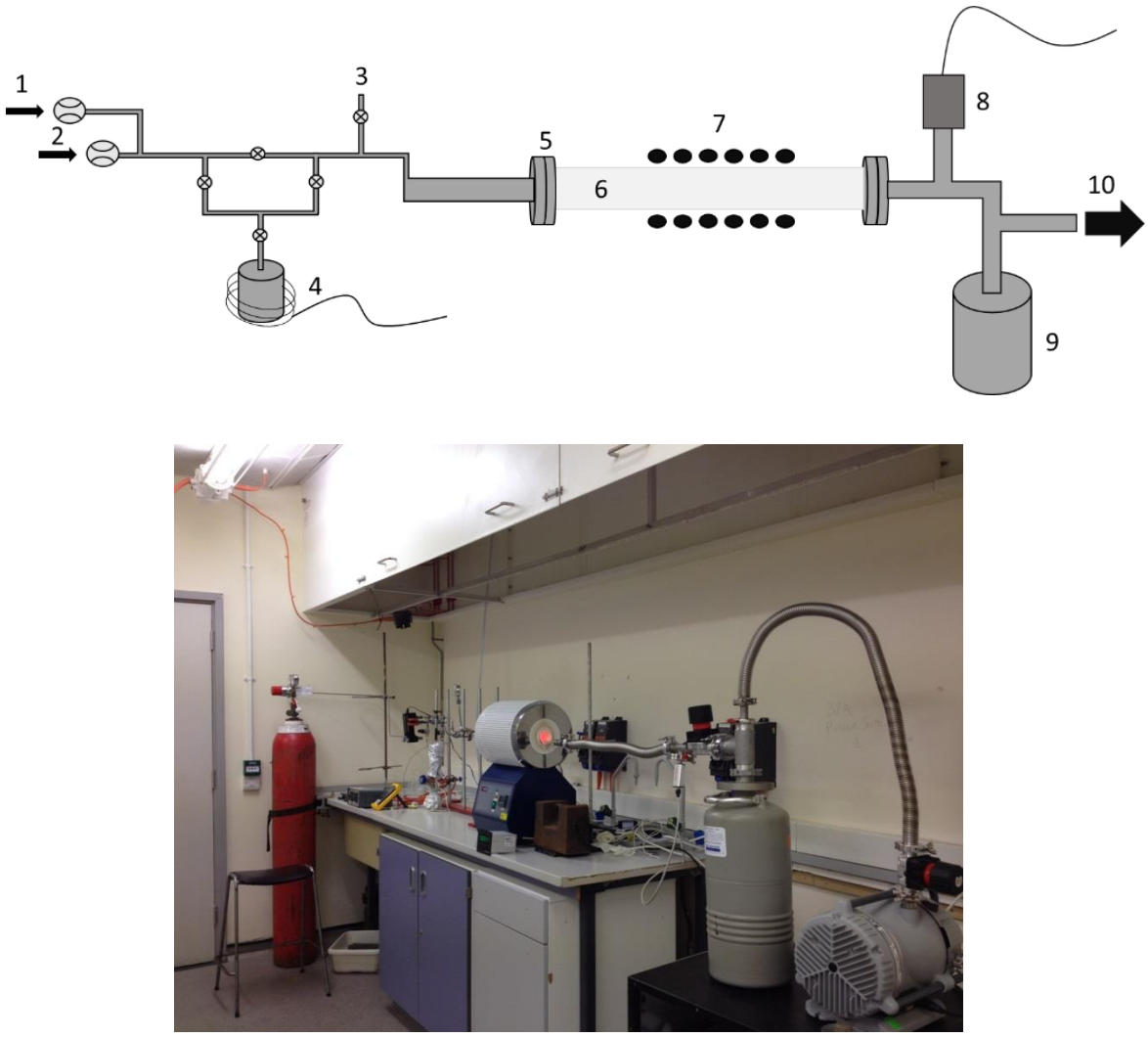

Figure 2.7 Diagram and picture of designed reactor. 1. Inlet flow for H_2 2.Inlet flow for CH_4 3.Valve to atmosphere to release pressure or used for additional process gas. 4.Solid/liquid precursor pot with electrical heating tape. 5. Ultra-torr fitting 6.Quartz tube 7.Tube furnace 8.Pressure sensor 9.Liquid N_2 trap 10.To scroll pump.

After the CVD system had been designed, a choice had to be made as to what substrate to grow the graphene on. As discussed in the introduction, many different metals have been shown to catalyse the growth of high quality graphene. The most commonly discussed metals in the literature are nickel and copper due to their availability and the quality of graphene produced. Copper was chosen due to its ability to produce exclusively single layer, high quality graphene.

2.1.2 Graphene CVD process development

Before graphene can be grown on copper, its pre-treatment needs to be considered, without which the quality of graphene produced is drastically altered. Although there is no clear consensus in the literature as to the optimum pre-treatment process it generally involves two major steps: substrate cleaning and substrate annealing. It has been shown both of these steps can affect the quality of the graphene produced. It is generally agreed flatter copper substrates, with few impurities, produce higher quality graphene.[40] However, even though the quality of graphene produced correlates with copper purity and flatness is reported as being important in some papers, there seems to be little consistency between different publications. This highlights one of the main weaknesses in the CVD graphene literature; there is no established universal method on how to report graphene quality. Some authors produce Raman maps whilst others take a series of individual measurements. Even the maps presented tend to be on a very small scale compared to the size of the graphene on copper. Therefore, one of the aims of this section of work is to appreciate the quality of graphene produced on the entirety of a copper substrate, primarily by large scale Raman mapping.

2.1.2.1 Pre-treatment process

There are two main ways to reduce the level of impurities on the copper substrate. First and most obviously, higher purity copper can be used. One of the main limitations of higher purity materials is cost. A common source of copper foil is Alfa Aesar™, who offer a range of purities and thicknesses. Table 2.1 gives some examples of purities and thicknesses available and the associated cost at the time of writing. As the purity increases so does the cost.

Table 2.1 Purities, thicknesses and cost of copper foil.

Cu foil purity (%)	Thickness (in)	Cost per cm^2 (£/cm^2)
99.8	0.001	0.027
99.9	0.005	0.070
99.999	0.001	8.5

All these purities have been reported to produce high quality graphene, [41] however some papers have argued 99.999% purity produces higher quality graphene.[42]

Taking into consideration that 99.8% purity copper has been shown to produce high quality graphene and its relative cost compared to 99.999% purity, it was chosen as the main copper foil to be studied. 99.8% purity was chosen over 99.9% purity partly due to cost, however the only available thickness

for 99.9% purity was 0.0005 in. This was too thick for the copper etching process when the graphene was being transferred off the copper.

After the desired purity of copper had been established, pre-cleaning treatments were explored. This pre-treatment is used to achieve three goals: removal of the native copper oxide layer, removal of any organic impurities on the copper surface and flattening of the copper. There is generally good agreement in the literature that nitric acid based cleaning methods most effectively clean copper and produce the highest quality graphene.[43] Reasoning for this involves the oxidising power of nitric acid that can remove organic impurities, whilst also acting as an acid to etch the metal. Additionally, nitric acid cleaning produces bubbles, which are said to drive impurities from the surface. In this work acetic acid, also used in literature reports, was compared to nitric acid.[43] Figure 2.8 shows example AFM images, with corresponding root mean squared roughness (RMS), taken of copper foil cleaned by acetic acid for 5 mins and a 10% solution of nitric acid for 30s for comparison. If the copper is etched for longer in the nitic acid, the surface roughness increases, as the acid etches unevenly further into the copper. Both were rinsed with isopropanol (IPA) and water after etching. It can be seen the copper that underwent nitric acid cleaning has been more extensively etched. The acetic acid washed copper still possesses the ridges produced when copper foil is rolled.

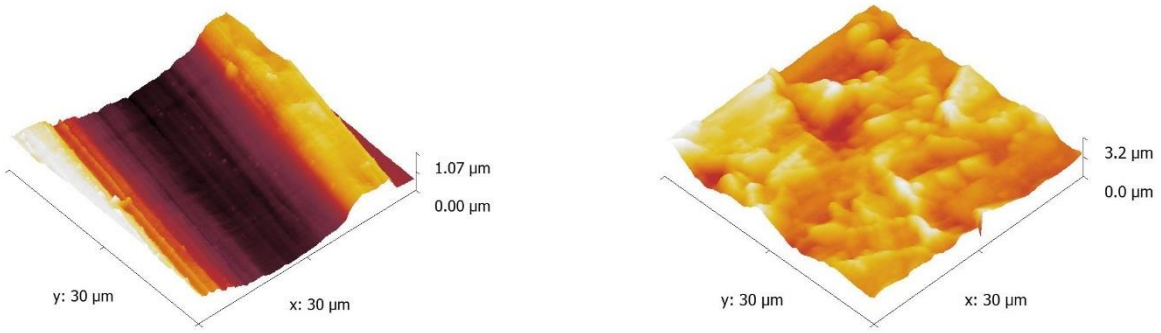

RMS: 0.301 µm RMS: 0.302 µm

Figure 2.8 AFM images of acetic acid washed copper (left) and nitric acid washed copper (right).

Graphene was then grown on the copper washed by the different techniques after annealing to see if any difference in graphene quality is observed. Figure 2.9 compares two typical Raman spectra of approximately bi-layer graphene grown under the same conditions except for a different pre-cleaning method of the copper substrate using the homebuilt reactor. This is in agreement with previous reports in the literature, which show surface impurities and roughness caused by ineffective cleaning lead to a greater defect density in the graphene produced.[43,44]

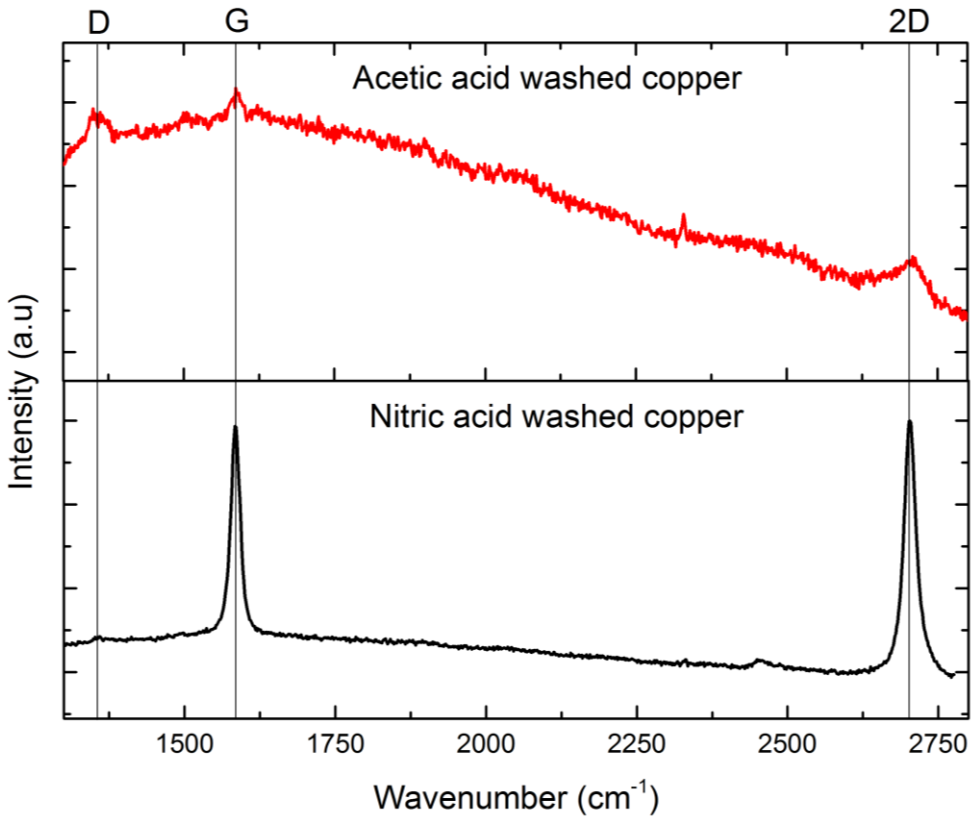

Figure 2.9 Raman spectra of Graphene grown on acetic acid and nitric acid washed copper.

The final pre-treatment process to be explored was the annealing of the copper foil. The main goal of this process was to increase the copper crystallographic grain size and further flatten the copper to produce the highest quality graphene. It was found there was a balance between the time required for annealing and surface roughness. At temperatures higher than 1050 °C copper grains expanded quickly. However, due to low pressure conditions the copper surface began to bubble, increasing its roughness. Figure 2.10 shows a series of AFM images taken of copper foils annealed at various temperatures for 6 hours. Little can be said about the RMS values from the AFM scans as the values are dominated by the broad undulations of the copper substrate, however it is evident on the AFM scan of the copper annealed at 1070 °C the surface is rougher due to bubbles in the copper film.

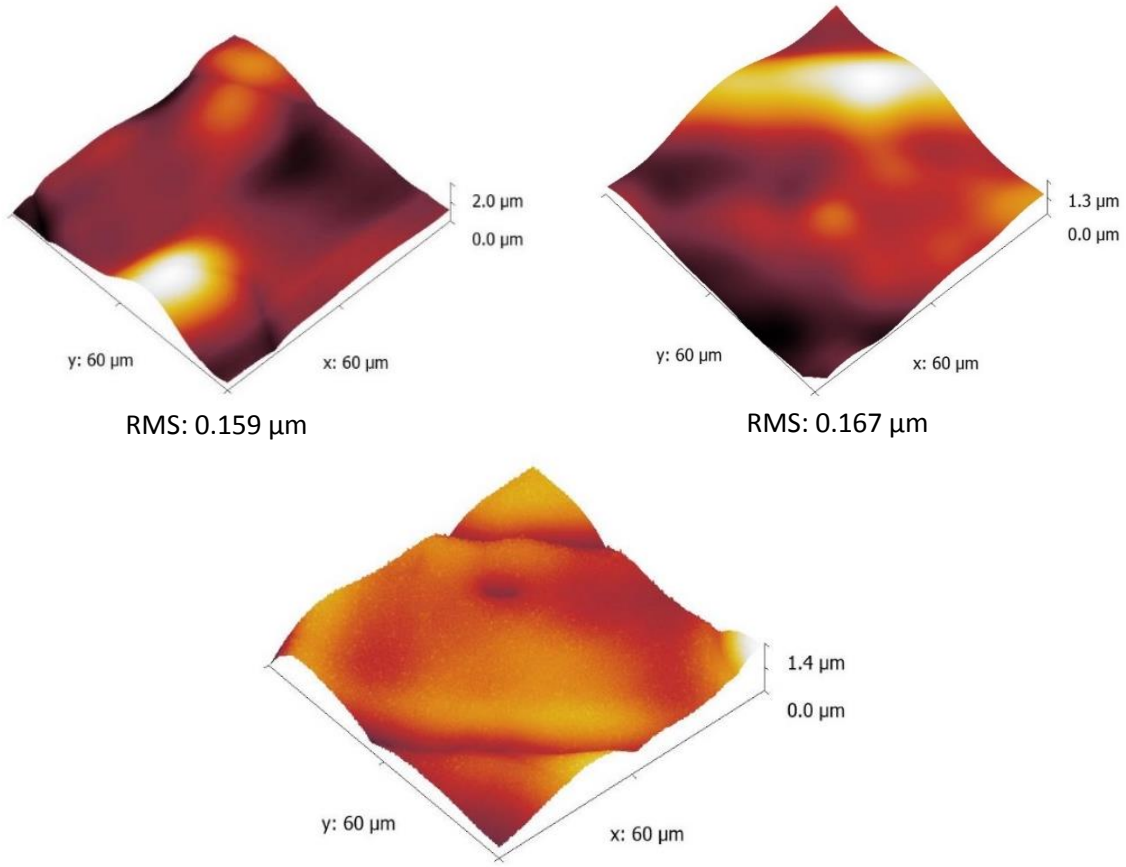

Figure 2.10 Clockwise from top left: AFM of copper annealed at 1020 °C, AFM of copper annealed at 1050 °C, AFM of copper annealed at 1070 °C.

Once the copper pre-treatment had been fully explored, the CVD of graphene via different carbon precursors, liquid and gaseous, was studied.

2.3 Results and discussion – CVD graphene from benzene precursor

Benzene was chosen as a liquid graphene precursor for several reasons. Firstly, there was already literature precedent for using it as a graphene precursor, where it had been shown benzene can produce graphene at a lower temperature than more conventional methane.[45] This makes production of graphene more industrially relevant due to lower processing temperatures and the handling of liquids rather than gases, whilst also potentially widening the range of materials that could be deposited with graphene. Secondly, it was desired to explore graphene deposition via PEALD. As benzene seemed a good choice for this, due to potential π surface interactions with substrates, it was deposited via conventional CVD to provide a contrast between ALD and CVD processes.

The general CVD process as a function of time and temperature is shown in figure 2.11. Although graphene growth conditions are reactor specific, papers by Hofmann et al.[46] and Zeng et al.[19] were used as a starting guide for our CVD process. Before placing the copper substrate in the reactor, it had undergone the previously discussed pre-treatment process. First it was washed with 10% nitric acid for 30 s followed by rinsing with DI water and IPA. It was then annealed under a flow of 30 cubic centimetres per min (ccm) of H_2 at ca. 1 mbar at 1020 ^{o}C for 6 h. A problem we encountered was the introduction of H_2 to the system meant the electronic pressure sensor no longer gave accurate readings. The reading slowly climbed until it read atmospheric pressure. The introduction of a physical pressure gauge however confirmed the pressure was still low, although accurate pressure readings could not be taken when hydrogen gas was present in the system. After the introduction of H_2, the tube furnace was heated to 1020 ^{o}C to remove any copper oxide that had regrown during storage of the foil and to flatten any areas where oxide formation had caused roughness.[47] After annealing, the tube furnace temperature was adjusted to 950 ^{o}C, as this seemed to produce the highest quality graphene and a small, but undefined, flow of benzene was introduced to the reactor and graphene was grown on the copper foil. Finally, the benzene flow was stopped and the copper substrate rapidly cooled by sliding the tube furnace away from the substrate.

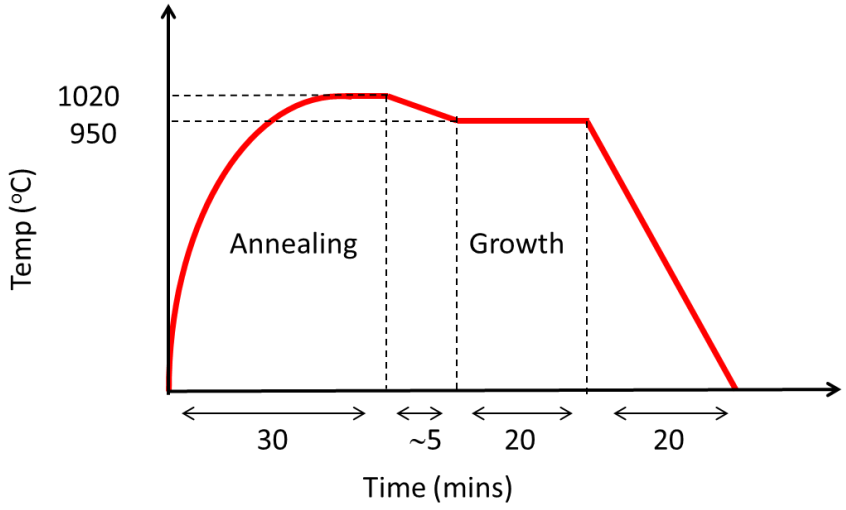

Figure 2.11 Diagram of general graphene CVD process.

Initially, graphene growth without H_2 present was attempted, as had been demonstrated by Hofmann et al.[46] However, it was found without hydrogen gas present, residual oxygen in the system oxidised the copper substrate, quenching any potential graphene growth. An ultra-high vacuum system would be needed to produce graphene this way.

Although groups had reported using an undefined amount of benzene to produce graphene,[19] it was found graphene growth was very sensitive to the flow of benzene into the reactor. Initially the flow of benzene was too high, producing amorphous carbon rather than graphene. An example Raman

spectra is shown in figure 2.22. A high concentration of carbon in the reactor during growth seems to promote disordered growth, however the films were still very thin and were not optically visible on the copper substrate. As graphene has been shown to grow by a nucleation and subsequent growth mechanism on copper, a high carbon concentration would cause very fast nucleation and quenching of the copper surface, preventing graphene from crystalising, explaining the thin amorphous carbon films.

One complication of using Raman spectroscopy to interrogate thin carbon based materials on a copper substrate is that copper heavily fluoresces in the visible region, where the peaks of interest are. This effect can distort the carbon signals. However, the peaks can usually be distinguished from the background. An example Raman spectra of a blank copper substrate used in this project is also shown in figure 2.12.

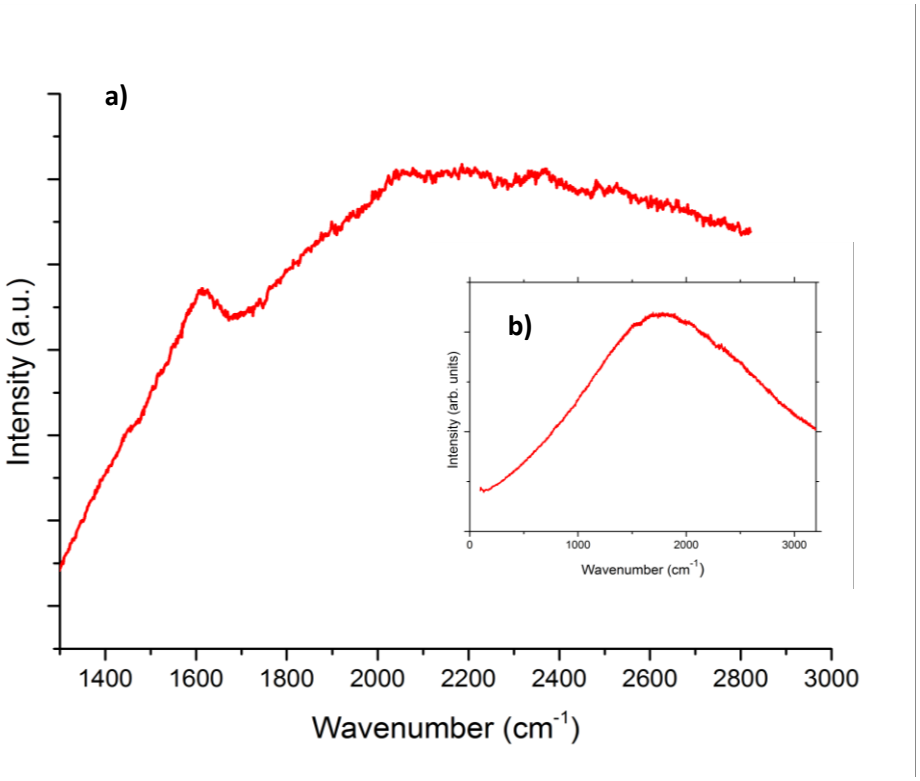

Figure 2.12 a) Sample Raman spectrum of amorphous carbon grown with a high flow rate of benzene **b)** Spectrum of fluorescent background of copper.

Success was first found when the benzene flow rate was kept very low, with a flow of 50 ccm of H_2 and a growth time of 25 mins. However, there were issues with repeatability, due to the lack of control the valve on the benzene source afforded. The Raman spectra for this result can be seen in figure 2.13. The G and 2D peaks are clearly viable above the fluorecence of the copper. Due to the fluorecence, it is difficult to judge the number of layers of graphene produced, the best estimate was a mixture of 1 and 2 layers. Importantly, the lack of the D peak in the Raman spectra indicated the graphene produced was free of defects.

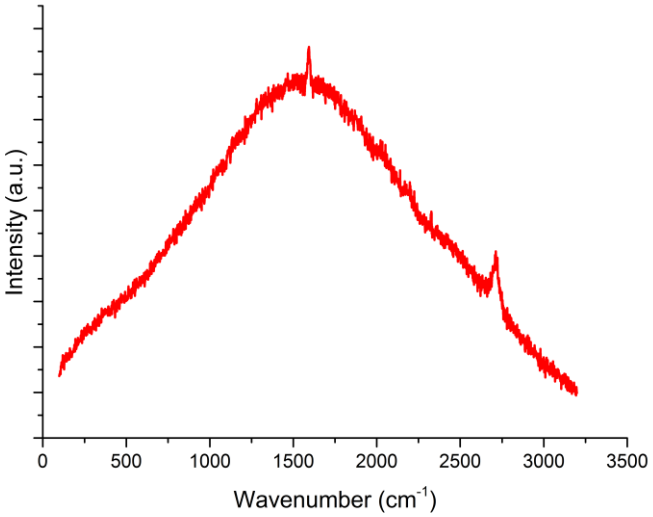

Figure 2.13 Raman spectrum of a successfully deposited graphene film.

To further characterise the graphene film produced, it was analysed by scanning electron microscopy (SEM). As graphene is extremely thin, it is hard to analyse without using very low accelerating voltages. Due to the equipment available, images of individual graphene layers could not be obtained. However meaningful data could still be acquired. Figure 2.14 shows a gap in the graphene film where the copper substate is in focus, whereas the image is blurred around it.

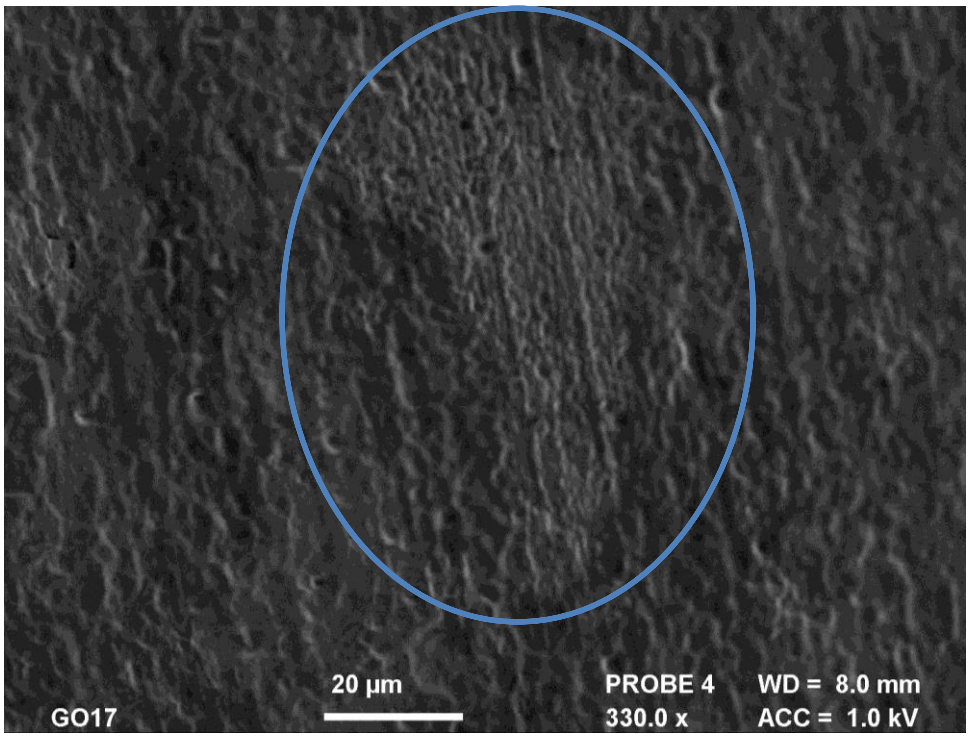

Figure 2.14 SEM image taken of graphene film on copper. A gap in the film, highlighted by blue ovoid, brings the copper into focus whereas it is blurred where covered by the copper.

Figure 2.15 shows an SEM image of graphene on copper grown using benzene as the carbon source. A SEM image from the literature is also displayed for comparison.[46] 'Terraces' can clearly be seen in in the image, which correspond to structure of the copper underneath the graphene. The darker regions in both images correspond to thicker regions of graphene. Interestingly the thicker regions seem to correspond to different copper grains. There is some discussion in the literature of how graphene grows on different copper orientations, with copper (111) grains most likely to form high quality monolayer graphene due to high diffusion, improved adsorption and epitaxial growth.[48]

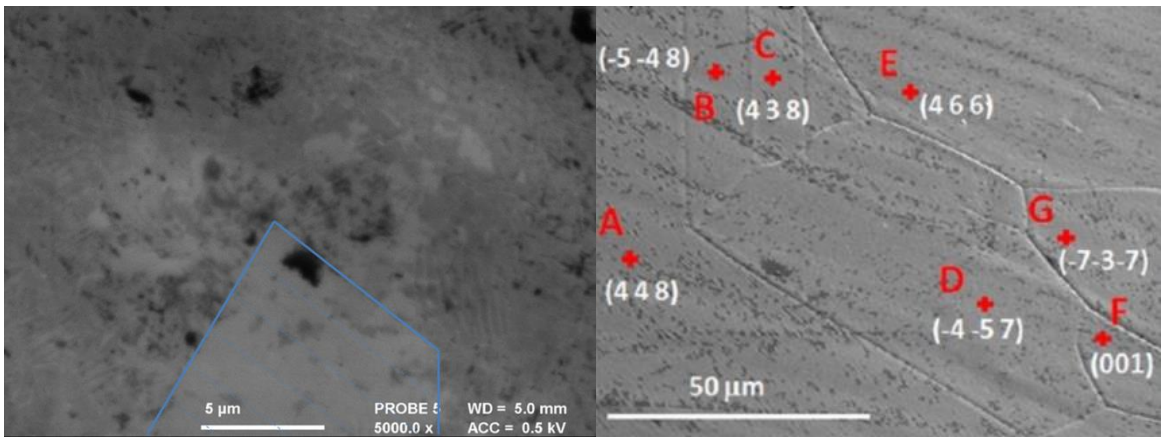

Figure 2.15 Left: SEM image of monolayer graphene where ripples corresponding to scattered electrons can be seen. Right: SEM image from ref 46 for comparison.

Although it was shown to be possbile to produce graphene films with the current apparatus, repeatability was an issue. The main problem was with the control over the flow of benzene. The replacement of the original valve with a needle valve allowed far greater control over the small amounts of benzene required. This greater contol allowed for better reliability and films to be produced with varying thicknesses.

2.3.1 Optimising benzene CVD

Once it was established, using the designed reactor, that graphene could be grown via CVD using benzene as the required precursor, an attempt was made to find relationships between the various growth parameters. This proved challenging due to the many parameters involved, as well as issues with repeatability. However a series of experiments were run and some quantifiable results were obtained. All the data points presented in this section are results averaged from at least 3 experiments.

2.3.1.1 Benzene flow rate

It was found the thicknesses of the graphene films was strongly dependant on the flow rate of benzene, with the results not strongly affected by changing other parameters. Figure 2.16 presents G/2D values at various flow rates. It must be noted other parameters also vary between data points.

It can be seen the graphene films deposited are at a minimum thickness when the needle valve controlling the benzene flow is turned to a value of 20. The value corresponds to value that the SS-SS4-VH Swagelock™ metering valve was set to, which is assumed to be linearly related to flow rate. At higher flow rates the thickness increases before appearing to level off. A higher benzene concentration will logically encourage the growth of thicker films, however a faster growth rate will lead to a quick covering of the copper substrate, limiting the maximum thicknesses achievable. The reason the thickness increases at lower pressure is likely due to incomplete growth on the copper substrate, coupled with benzene being used a precursor. The π-π interactions between benzene molecules are reasonably strong, leading to likelihood of them being able to stack. As the growth rate will be relatively low due to low benzene flux, there will be sites on the copper catalyst to activate the benzene molecules for a long period of time.

The defect density did not seem to depend on the benzene flow rate and no trends could be found. Therefore a valve value of 20 for the flow rate was kept constant for further experiments.

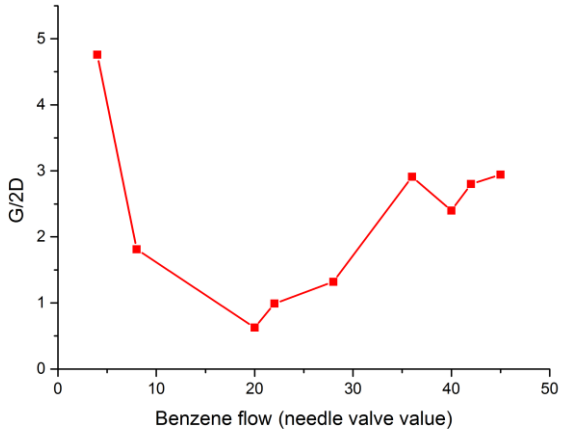

Figure 2.16 G/2D ratio of Raman peaks for graphene films grown with various flows of benzene precursor.

2.3.1.2 H_2 flow rate

Two different flow rates of 50 ccm and 100 ccm of H_2 were tested. The graphene thickness did not seem to depend on the H_2 flow strongly, however a 100 ccm flow of H_2 more reliably produced lower defect graphene. This implies H_2 does not play a strong role in the process of growing graphene, which is backed up by the reported successful synthesis of graphene without using H_2.[46] However H_2 is known to prevent the copper surface oxidising due to residual oxygen, which is likely why a higher flow of H_2 produces higher quality graphene.[49]

2.3.1.3 Reactor temperature.

With a H_2 flow rate of 100 ccm set, the reactor temperature was varied. Figure 2.17 plots how the D/G and the G/2D ratios vary with temperature. At increasing temperatures, the defect density decreases. This could be due to more complete breakdown of the benzene precursor, allowing a more ordered graphene structure to crystallise. Additionally, at increased temperatures the thickness of graphene increases, a more rapid conversion of benzene molecules into graphene is likely to encourage the growth of multilayers. However, quenching of the copper surface is likely to limit the possible thicknesses reached by increasing temperatures. These results highlight an issue that could not be overcome using benzene to produce graphene with the reactor used for these experiments. Single layer graphene was found to contain the most defects, whereas higher quality graphene was multilayer. To try and overcome these issues, benzene was substituted for methane. The results for the CVD of graphene using methane will be discussed below

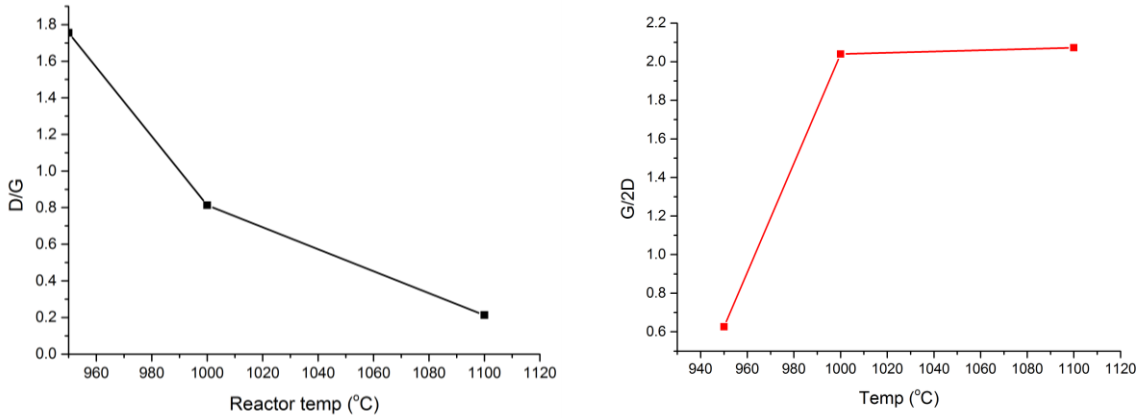

Figure 2.17 D/G and G/2D ratio of Raman peaks for graphene films grown at various reactor temperatures.

2.4 Results and discussion – CVD graphene from methane precursor

Methane is the most commonly used precursor to produce graphene.[50,15] Depositing graphene using methane allows a good comparison with graphene produced via benzene. To optimise the deposition conditions the whole of the parameter space had to be explored. The key parameters are CVD growth time, temperature, H_2 flow rate and CH_4 flow rate.

2.4.1 Optimising methane CVD

2.4.1.1 Methane flow rate

As with benzene CVD growth, it was found the methane flow rate strongly affected the thickness of the graphene formed. In figure 2.18 data points are averages taken from at least five experiments, at a constant run time of 15 minutes, with a reactor temperature between 1000 and 1070 °C. It shows at methane flows less than 10 ccm, increasing the reactor temperature decreased the thickness of the graphene films produced. However, at methane flows higher than 10 ccm, increasing the reactor temperature increased the graphene film thickness, displaying behaviour similar to benzene.

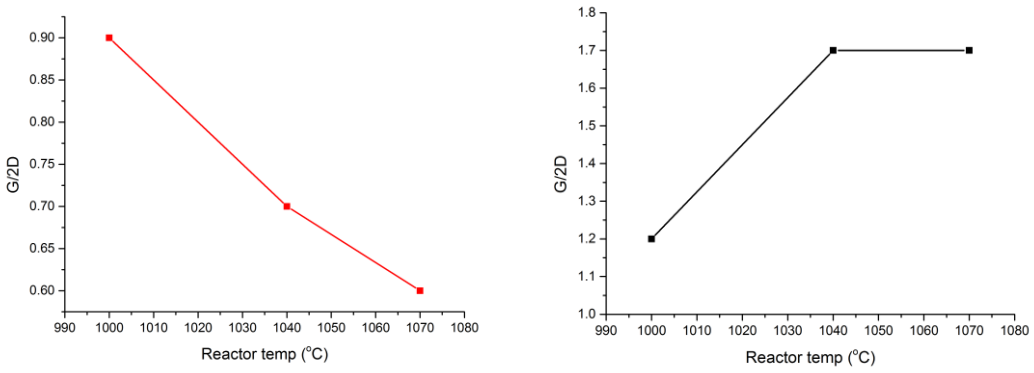

Figure 2.18 Left: G/2D ratio vs reactor temperature when methane flows are less than 10 ccm. Right: G/2D ratio vs reactor temperature when methane flows are greater than 10 ccm.

2.4.1.2 H_2 flow rate

It was found flow rates of H_2 below 5 ccm produced highly defective graphene, whilst flow rates above 50 ccm tended to restrict graphene growth. A 15 ccm flow of H_2 seemed to produce the most consistent low defect results so was chosen for all further experiments. 15 ccm is close to a 1/6 of the 100 ccm used for benzene experiments, which indicates the ratio of H_2 to C is important.

2.4.1.3 Reactor temperature

Regardless of the flow of methane used, it was found the defect density of the graphene produced decreased with increasing temperature, in line with the benzene experiments. A similar reasoning for this trend is likely to be relevant. A more complete breakdown of the methane molecule would allow a more ordered structure to crystallise. Figure 2.19 displays a plot of D/G peak ratio against reaction temperature.

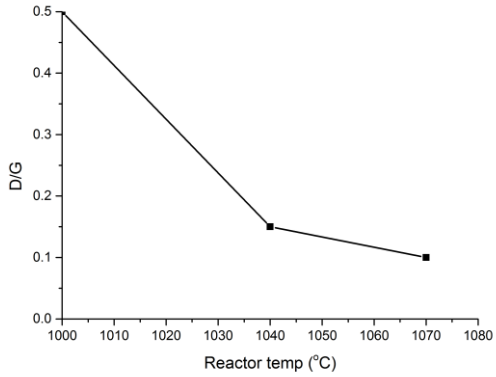

Figure 2.19 D/G peak ratio for graphene films deposited from methane at various reaction temperatures.

Overall, a flowrate of 10 ccm or less of methane at a reactor temperature of 1070 °C most reliably produced single layer graphene with the fewest number of defects. A final sweep of methane flow rates at 1070 °C, with results displayed in figure 2.20, show the lowest flow rate of methane possible with the experimental set up used produced the thinnest graphene films with the least damage. As with the benzene experiments, no relationship between the flow of methane and the defect density could be established.

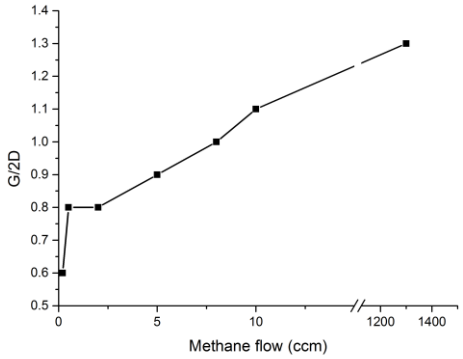

Figure 2.20 G/2D peak ratio for graphene films deposited at 1070°C at various methane flow rates.

2.5 Results and discussion - Benzene vs methane depositions

Overall it was found, using the home built reactor, greater control could be obtained over the deposition of graphene using methane rather than benzene as the carbon source. At higher methane concentrations, the control over the number of layers of graphene produced seems to follow a similar

pattern to benzene. However, at low concentrations, thickness monotonically decreased with temperature and increased with methane flow. This could be due the deposition of graphene from benzene being more thermodynamically favourable, causing the faster seeding of multilayers causing thicker growth across all temperature ranges. Similarly, it was found the maximum thickness of graphene produced using benzene was higher than for methane.

It was also found that graphene could not be grown at temperatures below 950 ^{o}C using benzene. This was lower than was possible using methane, although not as low as has been reported previously.[19] This is likely due to limitations with control of the benzene flow and the experimental setup used.

2.6 Results and discussion - Transferring graphene films from growth substrate

Once an effective method of growing graphene had been established, it was important to transfer the graphene produced from the copper substrate. Transfering graphene from its metallic growth substrate onto an insulator is desireable for a number of reasons. Firstly, it is easier to characterise, both optically and by Raman spectroscopy. Silicon, for example, provides a better optical contrast, particularly with a thermal oxide layer of 200-300 nm and does not as heavily fluoresce in the Raman spectrum. Secondly, if graphene's electronic properties are going to be measured, it needs to be electronically isolated from the substrate. Similarly, any devices incorporating graphene are most likely to be built on an insulating or perhaps semiconducting substrate.

The general transfer process followed procedures outlined in the introduction to the chapter, which involved spincoating a layer of polymethylmethacrylate (PMMA) onto the graphene layer on copper. This provided structural support as the graphene was transferred. Next, the copper substrate was briefly floated on dilute nitirc acid to remove any graphene that had grown on the underside of the copper. The copper was then floated on an aqueous solution of $FeCl_3$ which dissolved it. The remaining graphene-PMMA stack was then transfered onto a silicon substrate, whereupon the PMMA was dissolved in an acetone bath. It was found the choice of copper thickness was crucial, as copper that was too thick required a higher concentration of etchant and thus more impurities could be observed on the resulting graphene film.

Issues with graphene transfer can be divided into two general areas:

1. Damage to the graphene film, including wrinkles, folds and tears.
2. Impurities left on the graphene film from the transfer process, including incomplete removal of PMMA support.

What was found to cause these issues and how they were rectified will be discussed below.

2.6.1 Issues with transfer - Damage to the graphene film

It was found tears in the graphene film could be caused by bubbles produced during the etching process, which then get trapped under the film whilst it is floating. These interfere when the film is lowered onto the substrate. Using a more dilute etching solution than was reccomended in the literature rectified this. Rapid dissolution of the polymer layer also caused tears, so if it was desired to have the solvent used to dissolve the PMMA hot, the graphene film had to be added whilst it was at room temperature. Tears and folds were also caused when the graphene was insufficiently adhered to the substrate after transfer. To overcome this, firstly the graphene film was allowed to completely dry at room temperature to remove any water between it and the substrate. If this was not carried out when the substrate was heated, the water could boil, causing damage to the film. Once the graphene film was dry, it was heated to 150 ^{o}C for 30 mins to help adhere it to the substrate and relax the polymer support. As the poylmer was spun onto the graphene whilst it was still on the copper foil, it retained some of the foil's structure during transfer. Heating it to around its glass transisition temperature allowed it to relax, reducing the strain on the graphene on a flat substrate minimising the chance for structural damage. Some tears in the graphene were found to be unavoidable, but were minimised by mechanically manipulating the graphene as little as possible.

2.6.2 Issues with transfer – Impurities on graphene film

A source of impurities on the graphene film was the incomplete removal of the etchant solution. Even with a thorough washing with deionised (DI) water, particles could be observed. Including a dilute HCl wash similar to that found published by Liang et al. facilitated the removal of these particles.[24] It was also found if sodium persulfate was used as an etching solution, fewer impurities were present. Complete removal of the PMMA support proved to be more challenging. To date, there has been no process found which completely removes the polymer whilst maintaining graphene quality. However, in spite of this, steps can be taken to remove as much of the polymer as possible. It was found solvent selection to remove the polymer was important. Althought the standard solvent used is acetone, even under reflux conditons it was found dichloromethane more effectively removed PMMA. The chain length of the PMMA was also important. Even though both 495K and 950K molecular weight (M_w) chains of PMMA have been reported for graphene transfer, it was found 495 K M_w PMMA produced less residues. This could be a result of the shorter chain lengths being easier to 'untangle' and thus dissolve.

2.6.3 Optical analysis of transferred graphene films

Figure 2.21 displays various optical images of graphene films on silicon, with different levels of impurities and types of structural damage present. **a)** shows the presence of impurties left from the etching solution, in this case $FeCl_3$. Additionally holes in the graphene film created during the transfer process are also visible. **b)** shows the presence of PMMA residue rather than etchant. It also shows a large fold in the graphene film that was likely to have been formed where the previous geometry of the graphene on copper collapsed when it was transferred onto a flat substrate. **c)** Shows a relatively clean graphene film, with only minor wrinkles present. **d)** displays a Raman spectrum of the PMMA residue. **e)** shows a clean graphene film, with the prescence of double layer islands. It is interesting to note that the double layer islands clearly follow the grain boundaries of the copper. This provides evidence that copper grain boundaries can act as nucleation points for graphene growth.[51] **e)** shows a clean graphene film where the majority of the film is tri-layer. Here it is important to note due to the size of the laser spot used during Raman spectroscopy, the detector 'sees' an average of the area excited by the laser, **f)** also shows the general size of a laser spot used to collect spectra. Therefore if a Raman spectra is taken of graphene on copper foil, where there is insufficient contrast to detect changes in thickness, the spectrum suggesting tri-layer graphene does not mean the trilayer sections of the graphene are continuous.

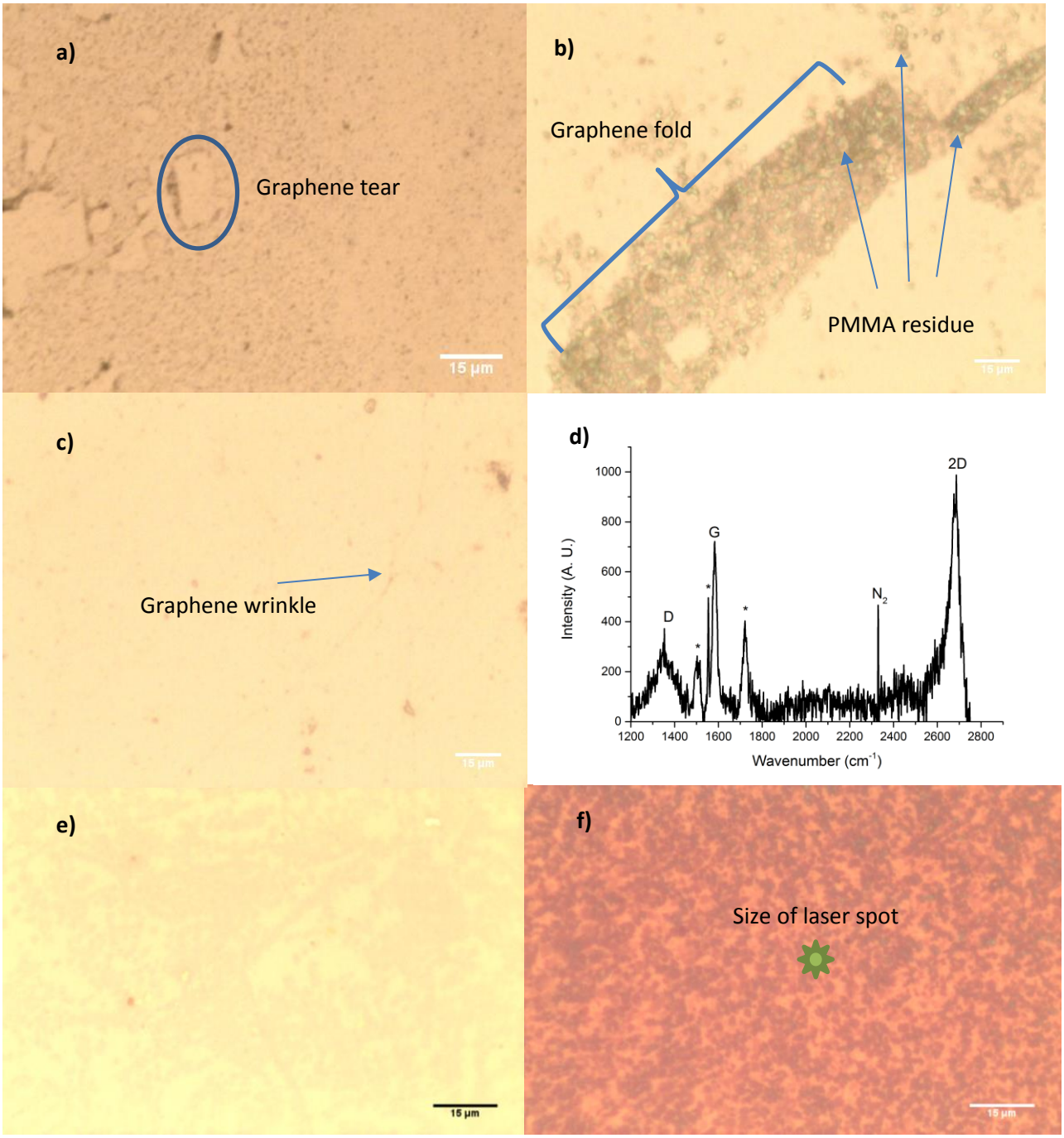

Figure 2.21 a) Optical image of graphene film on silicon with $FeCl_3$ impurities. **b)** Optical image of graphene film on silicon with fold and PMMA residue. **c)** Optical image of graphene film on silicon with small wrinkles. **d)** Raman spectrum of PMMA residue. **e)** Optical image of graphene film on silicon with double layer islands. **f)** Optical image of graphene film on silicon with tri-layer islands.

2.6.4 SEM analysis of transferred films

SEM analysis of transferred films gave a more detailed view of some of the effects of the transfer process. SEM images of various transferred graphene films are shown in figure 2.22. **a)** shows PMMA residue left on a graphene film whilst **b)** shows etchant residue. EDS analysis (figure S.1 and S.2) found the needle-like etchant residues contained sulphur, that was likely to be the result of the use of sodium persulfate. **c)** Shows a much cleaner graphene film where wrinkles introduced by the transferred processes are evident. **d)** is an image of a graphene film with multilayer islands

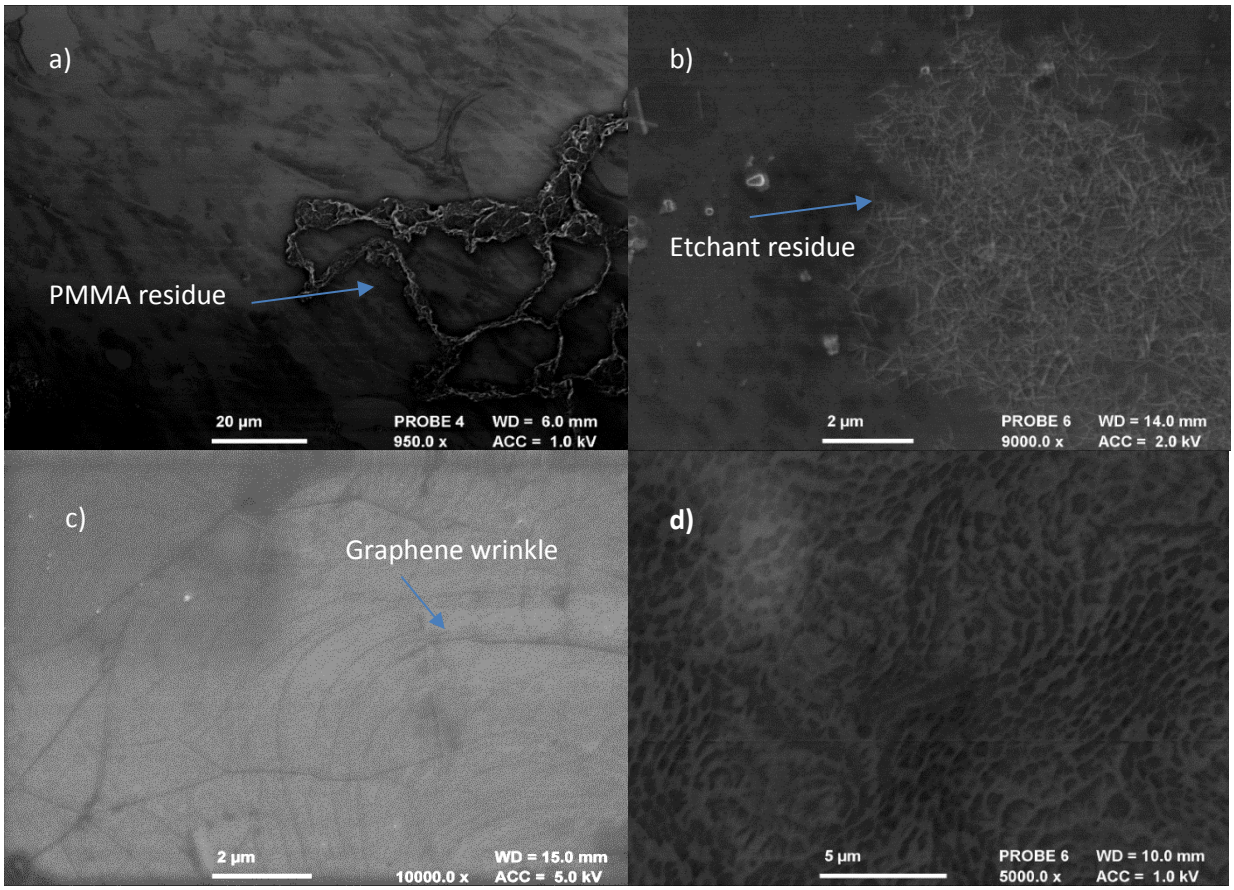

Figure 2.22 SEM images of: **a)** Graphene film on Si with PMMA residue. **b)** Graphene film on Si with etchant residue. **c)** Clean graphene film on Si with small wrinkles. **d)** Graphene film on Si with tri-layer islands.

2.6.5 AFM analysis of transferred films

AFM analysis revealed areas of graphene that were featureless on length scales greater than 30 µm. It also revealed areas of damaged graphene such as wrinkles and tears. AFM examples of featureless and wrinkled and cracked graphene are displayed in figure 2.23.

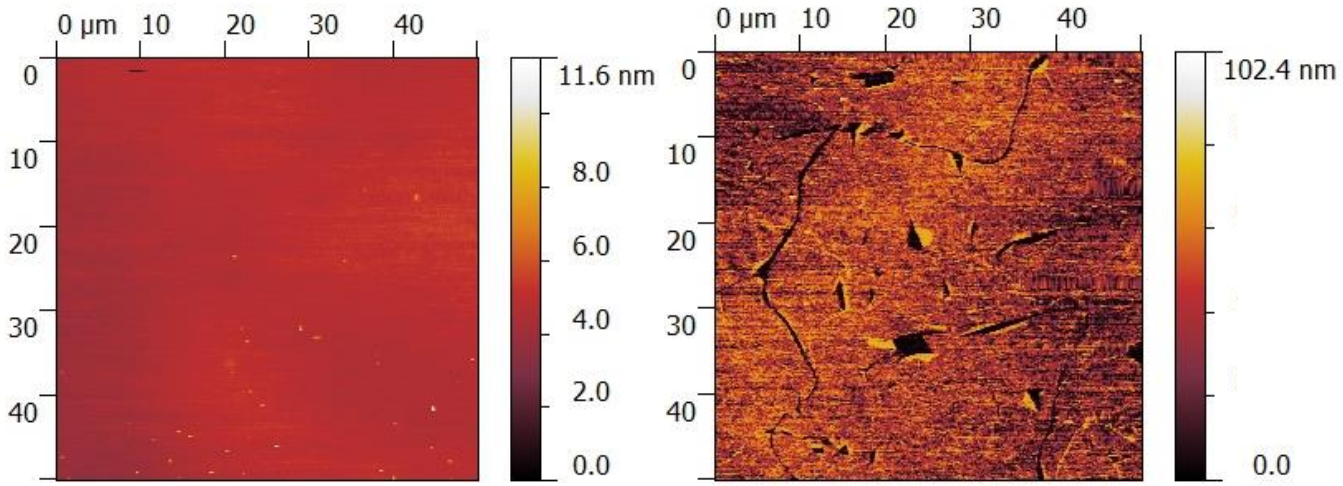

Figure 2.23 Left: AFM of flat featureless graphene on silicon. Right: Area of wrinkled and cracked graphene, colour mapping is nonlinear to highlight features.

2.6.6 Raman mapping analysis of transferred films

Figure 2.25 shows an optical and a Raman map of a graphene film transferred onto an SiO_2 substrate. **a)** Reveals defects in the transferred film visible optically. The blue box corresponds to the area of the film that was selected for Raman mapping. It includes a tear in the graphene film likely produced by a trapped air bubble during the transfer process. **b)** displays a map of the ratio of the G/2D Raman peaks to give an indication of the variations in the graphene films thickness. The lighter colours indicating thinner parts of the film. The crystallographic grain morphologies of the copper are clearly present in the map of the transfered film. This builds on the discussion in section 2.3, that different crystallographic copper grains have an effect on the growth of graphene films. The darker colours indicate thicker areas of graphene. The darkest points occur around the hole in the graphene that is visible optically. This is likely due to wrinkling of the film around wheree a bubble formed and eventually escaped by creating a hole in the graphene. **c)** displays a map of the ratio of the D/G Raman peaks to highlight variations in the defect density of the graphene film. The lighter colours indicate areas of fewer defects. It can be seen that as well as thickness, the quality of graphene films is affected by the crystallographic grain it has been grown on. Additionally, it can be seen wrinkling in the graphene film visible in **b)** and **d)**, does not introduce any more defects into the graphene lattice. **d)** displays a map of the shift of the 2D Raman

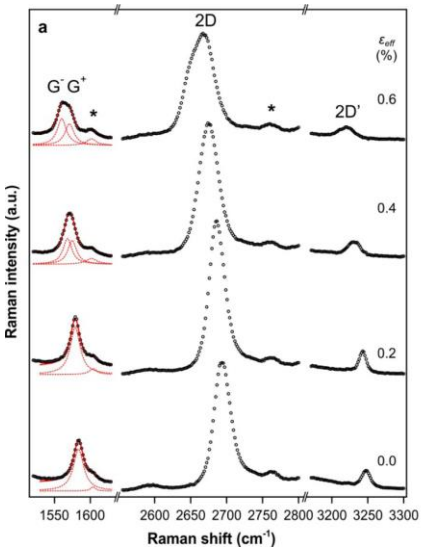

Figure 2.24 Plots of the graphene 2D peak at various strains reported by Frank et al.[52]

peak. Darker colours correspond to the 2D peak occuring at lower wavenumbers, which is indicative of strain in the graphene film. Figure 2.24 displays the shift in 2D peak with strain reported by Frank et al.[52] As expected, the greatest regions of strain appear around the wrinkles caused by the hole in the graphene sheet. All these maps highlight the fact that although the graphene films are homogeneous over mm lengthscales, care has to be taken not to assume they are consistant over a whole sample.

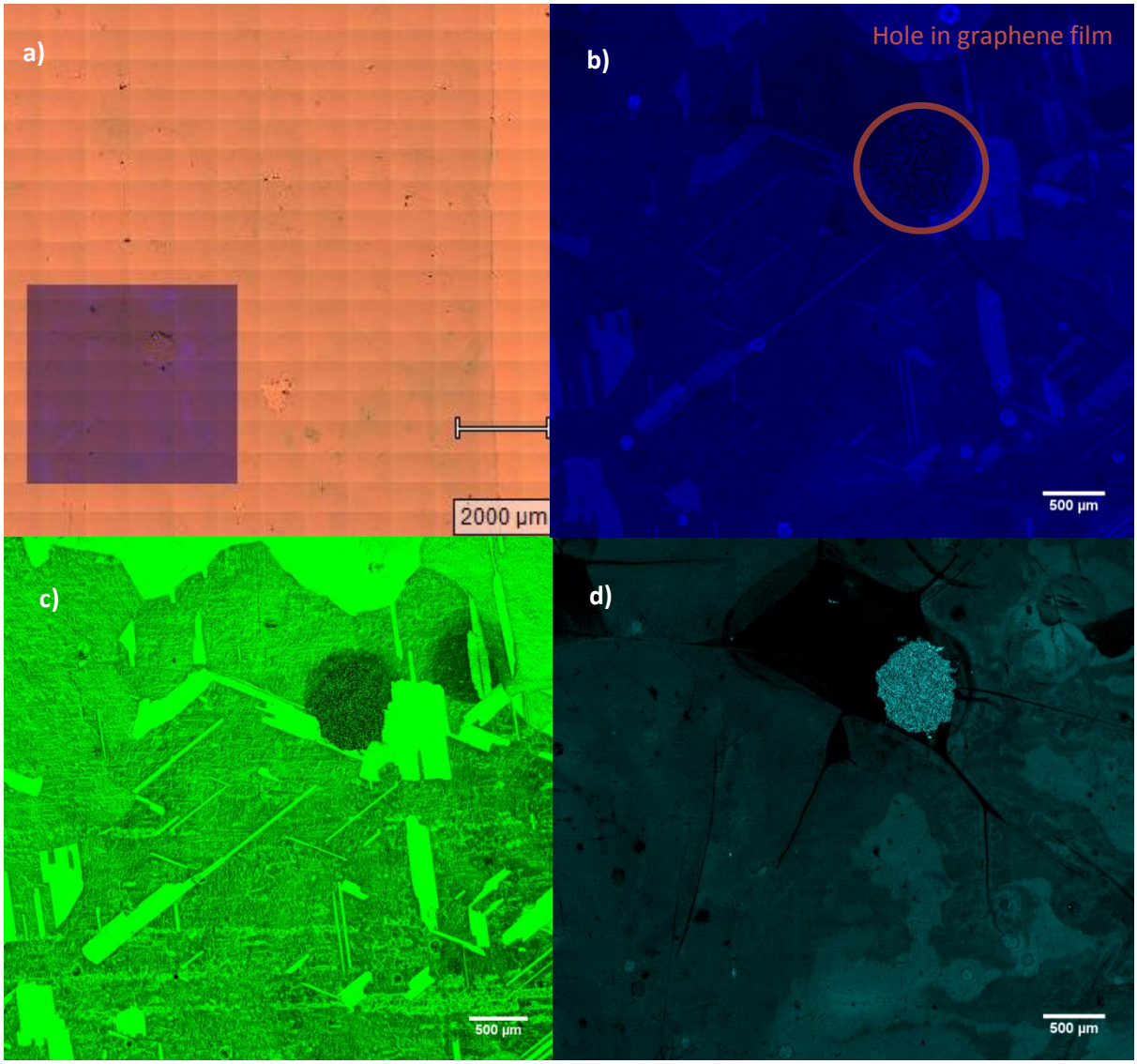

Figure 2.25 a) Optical image of graphene film transferred onto SiO_2 substrate. Coloured area indicates where Raman maps were taken from. **b)** Map of the ratio of the G/2D Raman peaks to give an indication of the variations in the graphene films thickness. The lighter colours indicating thin parts of the film. **c)** Map of the ratio of the D/G Raman peaks to highlight variations in the defect density of the graphene film. The lighter colours indicate areas of fewer defects. **d)** Displays a map of the shift of the 2D Raman peak. Darker colors correspond to higher strain in the graphene film.

2.7 ALD of graphitic materials

After the high temperature growth of graphene had been explored, the question was raised whether graphene could be grown at lower temperatures using ALD techniques. At the time of writing, only one paper has been published synthesising graphene using ALD.[53] Using PE-ALD, Zhang et al. have demonstrated the deposition of graphene sheets at 400 °C onto copper with a 2.5 kW remote plasma. However, there are some drawbacks with the process used. Firstly a 2.5 kW plasma power is very high, far out of the range of any industrial ALD tool. Secondly 400 °C is not a low enough temperature to truly justify the use of plasma, as the record for producing graphene without plasma from benzene is 300 °C. [54] Finally, the graphene produced is discontinuous; figure 3.26 is an SEM of the discontinuous graphene film produced by Zhang et. al.

Therefore the aim was to produce graphitic films below 400 °C that do not use the high plasma energies, or copper that has been annealed at 1000 °C, which is often still necessary in low temperature CVD of graphene publications.

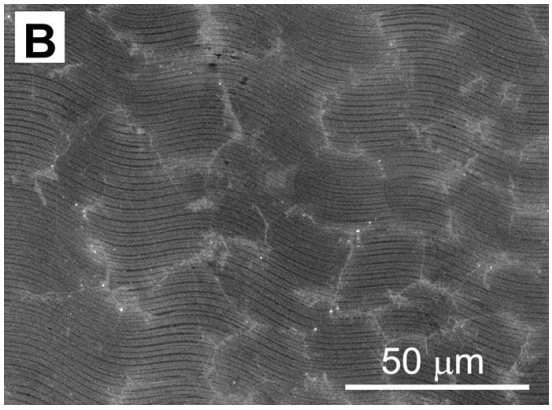

Figure 2.26 Literature example of only graphene film previously deposited by ALD, SEM highlights the lack of continuity. Reproduced from ref 53.

All the following processes were run on a commercially available Beneq TFS 200 ALD rig. Initially experiments were run where a H_2/Ar plasma was used to activate benzene molecules physisorbed onto the copper surface, the general processing conditions were as follows:

- Once the substrate was at the desired temperature, hydrogen plasma was introduced for ~10 mins to clean away any surface oxide on the copper substrates used.
- A pulse of benzene was introduced to the reactor.
- The excess benzene not physisorbed was then pumped out of the reactor and a plasma of H_2 and Ar was ignited.
- After a few seconds, the radio frequency (RF) wave delivering energy to the plasma was turned off and gases present pumped out of the reactor.
- The previous three steps were then repeated as many times as desired

It was found at 250 °C, regardless of changing any other conditions, only amorphous carbon could be produced on copper. Although if the H_2/Ar plasma was not present, no film was found on the copper. Interestingly, amorphous films were also found on other metallic substrates such as gold, however no carbon films were present on glass or silicon. This indicates the substrate still has a role in breaking down the benzene molecule, even when plasma is being used.

Increasing the reactor temperatures to 350 °C, amorphous carbon films could be produced on annealed copper in the absence or presence of H_2/Ar plasma. However, if the benzene molecule was itself incorporated into the plasma, ordered graphitic films could be produced. Figure 2.27 displays general process schemes for producing the carbon films via ALD.

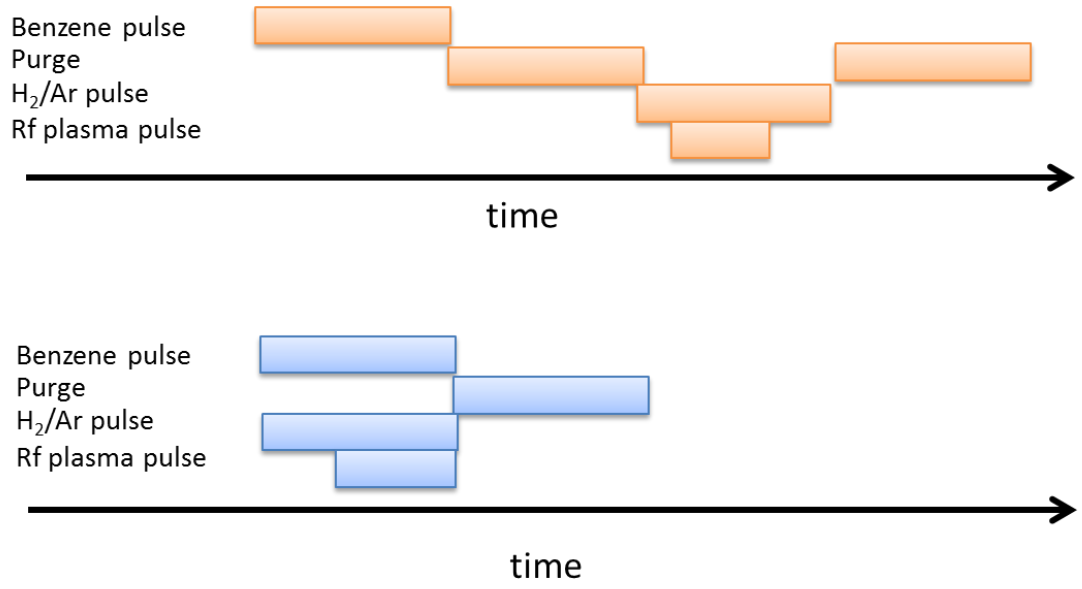

Figure 2.27 General process schemes for producing the carbon films via ALD.

The difference between the Raman spectra of carbon films deposited on copper at 250 °C with H_2/Ar plasma (**1**), 250 °C with H_2/Ar/benzene plasma (**2**), 350 °C with H_2/Ar/ plasma (**3**) and 350 °C with H_2/Ar/benzene plasma (**4**) is shown in figure 2.28. Deposition parameters for **1**-**4** are presented in table 2.2. It can be observed that an increase in the reactor temperature increases the degree of graphitisation whilst introducing bezene into the plasma creates the most graphene-like carbon films. Indeed their spectra closely resemble those recently published where graphene was deposited by a hot filament thermal CVD method,[55,56] which involves activating carbon molecules using a hot filament, also in an attempt to reduce temperatures and producue a scaleable process. Spectra from refs 55 and 56 can be seen in figure 2.30 for comparison. This supports the idea that direct activation of the benzene molecule allows more ordered films to be grown.

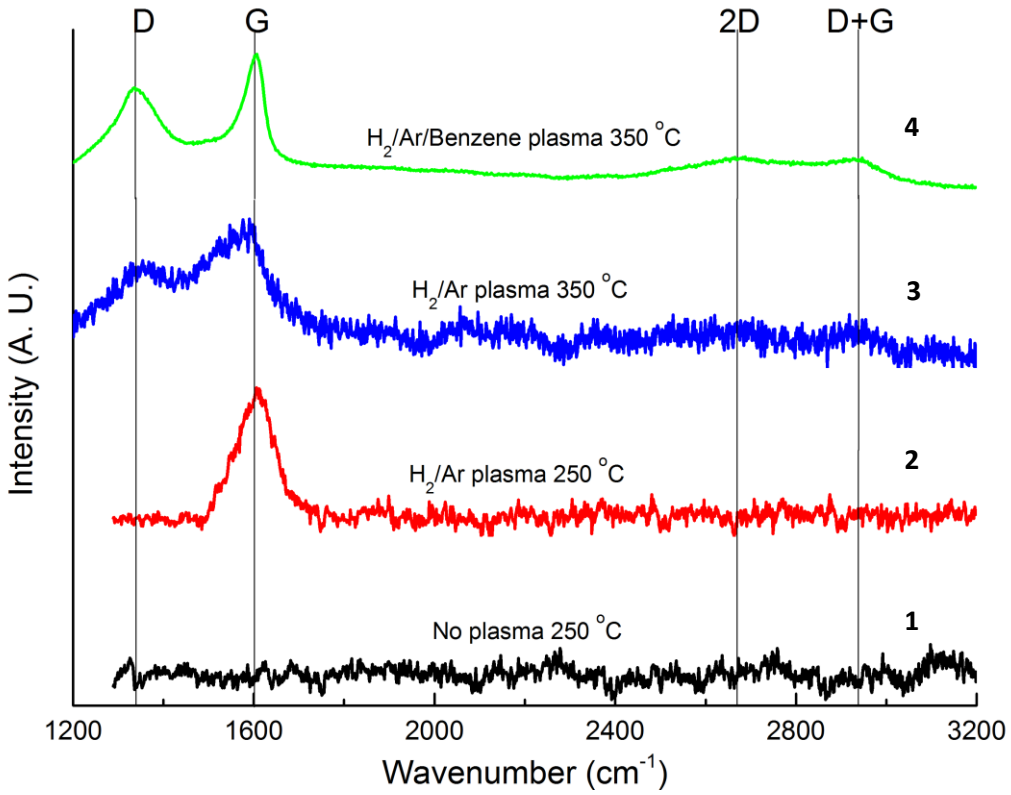

Figure 2.28 Raman spectra of **1-4.**

Table 2.2 deposition parameters for **1-4.**

Deposition	Reactor temperature (°C)	Process gas flow (ccm)	Benzene pulse (s)	Purge (s)	H_2/Ar pulse (s)	RF plasma pulse (s)
1	250	100	2	10	2	None
2	250	100	2	10	2	5 (300 W)
3	350	100	2	10	2	5 (300 W)
4	350	100	2	10	2	5 (300 W)

A film deposited using activated benzene was thicker than a monolayer, allowing it to be transferred onto SiO_2 without the need of a PMMA support. Figure 2.29 shows an optical image of the film still on copper and a SEM with Raman spectra after transfer. These images show the film, although thicker than monolayer graphene, is still transparent, with the copper substrate clearly visible in the optical image. The SEM image shows the film retained its structure after transfer; displaying the ridges and terraces of the now etched copper substrate. Raman spectroscopy revealed the transferred film retained all the peaks present pre-transfer.

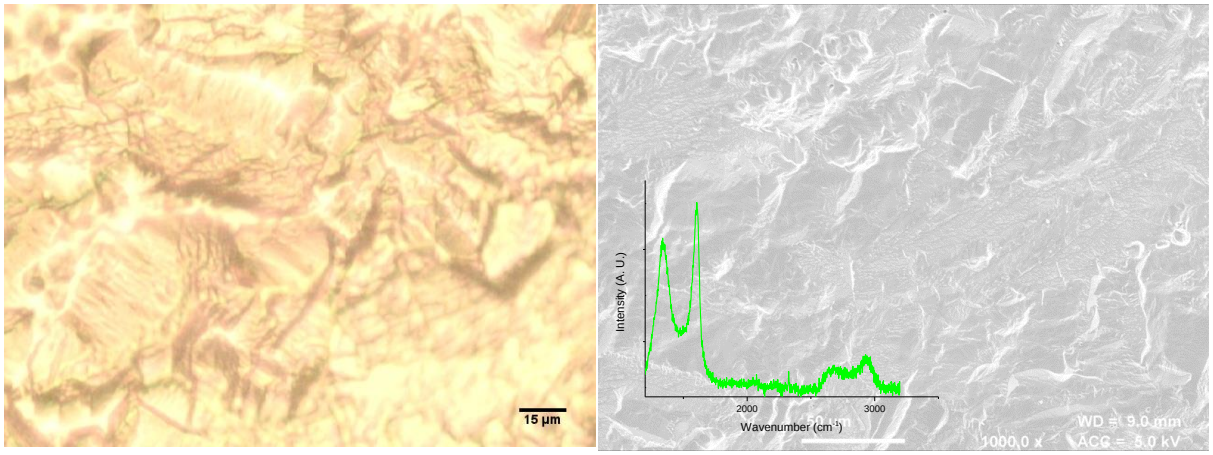

Figure 2.29 Left: Optical image of graphitic film on copper. Right: SEM image and Raman of film post-transfer.

It was found that increasing the number of ALD cycles increased the thicknesses of the films produced, which could be witnessed by the decreasing fluorescent background from the copper substrate. This indicates although copper still plays a role in the initial growth of the graphitic films, the growth process was no longer self-limiting.

2.7.1 ALD or CVD?

Although up to this point the graphitic films have been referred to as deposited by ALD, with ALD processes being used, it is not clear whether the process can truly be called ALD. Firstly, as only one precursor molecule is being pulsed, the cycle of two self limiting processes is not occuring, one of the key tenets of ALD. Secondly, to produce graphitic films, benzene could not be activated by plasma once it had 'saturated' the copper surface, but had to be activated in the vapour phase. Even the one publication claiming to produce graphene via ALD had to employ 10 cycles to produce a monolayer. However, the transferred films closely followed the morphology of the copper substrate and the films produced appeared homogeneous across the substrate up to 5 " in size, even when bent. Producing such uniformity is a big challenge for CVD as flow effects are important. Additionally, even classic ALD processes do not produce a true monolayer of material per pulse.[57] All things considered, even though this process could not be called true ALD, it produced continuous graphitic films at low temperatures with no annealing of the copper films. Additionally, the films did not require a polymer support to transfer.

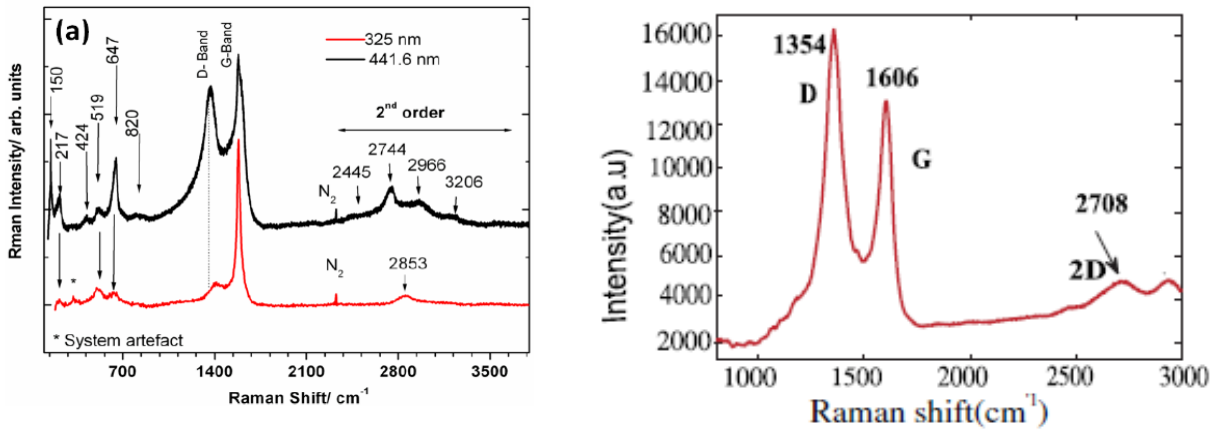

Figure 2.30 Raman spectra of graphene like carbon films from refs 55 (left) and 56 (right).

2.8 Large area graphene synthesis and transfer conclusions

This chapter has presented work on the large area synthesis and transfer of graphene films using CVD or ALD and wet transfer techniques. The graphene CVD precursors methane and benzene have been compared. It was found that although the benzene precursor allowed depositions at lower temperatures, methane afforded greater control probably because of its decreased reactivity which leads to slower more controlled growth. It has been shown although CVD onto copper substrates is a route to large area graphene, there are some limitations that still need to be addressed. Large area Raman mapping revealed the inhomogeneity that multiple different copper crystallographic grains can create in graphene films, through the introduction of defects and thicker areas. Although roll to roll processes of CVD graphene using copper foils have been developed,[58] it is likely that work on other growth substrates or single domain copper will have to mature before true industrial scale CVD graphene can be achieved. Nevertheless the growth and transfer techniques developed in this chapter produced graphene of sufficient quality to be studied as a substrate for other materials. Large area graphitic carbon films were grown at temperatures as low as 250 ^{o}C by ALD, which did not require a polymer support to transfer to an insulating substrate. In the following two chapters, depositions of WS_2, SnS and SnS_2 on to CVD graphene grown and transferred using techniques presented in this chapter will be discussed.

2.9 References

1. Novoselov, K. S.; Geim, A. K.; Morozov, S. V.; Jiang, D.; Zhang, Y.; Dubonos, S. V.; Grigorieva, I. V.; Firsov, A. A., Electric field effect in atomically thin carbon films. *Science* **2004,** *306* (5696), 666-669.
2. Stadler, J.; Schmid, T.; Zenobi, R., Nanoscale Chemical Imaging of Single-Layer Graphene. *ACS Nano* **2011,** *5* (10), 8442-8448.
3. Lu, X. K.; Yu, M. F.; Huang, H.; Ruoff, R. S., Tailoring graphite with the goal of achieving single sheets. *Nanotechnology* **1999,** *10* (3), 269-272.
4. Paton, K. R.; Varrla, E.; Backes, C.; Smith, R. J.; Khan, U.; O'Neill, A.; Boland, C.; Lotya, M.; Istrate, O. M.; King, P.; Higgins, T.; Barwich, S.; May, P.; Puczkarski, P.; Ahmed, I.; Moebius, M.; Pettersson, H.; Long, E.; Coelho, J.; O'Brien, S. E.; McGuire, E. K.; Sanchez, B. M.; Duesberg, G. S.; McEvoy, N.; Pennycook, T. J.; Downing, C.; Crossley, A.; Nicolosi, V.; Coleman, J. N., Scalable production of large quantities of defect-free few-layer graphene by shear exfoliation in liquids. *Nat Mater* **2014,** *13* (6), 624-630.
5. Viculis, L. M.; Mack, J. J.; Kaner, R. B., A chemical route to carbon nanoscrolls. *Science* **2003,** *299*, 1361.
6. Hernandez, Y.; Nicolosi, V.; Lotya, M.; Blighe, F. M.; Sun, Z.; De, S.; McGovern, I. T.; Holland, B.; Byrne, M.; Gun'Ko, Y. K.; Boland, J. J.; Niraj, P.; Duesberg, G.; Krishnamurthy, S.; Goodhue, R.; Hutchison, J.; Scardaci, V.; Ferrari, A. C.; Coleman, J. N., High-yield production of graphene by liquid-phase exfoliation of graphite. *Nat Nano* **2008,** *3* (9), 563-568.
7. Dreyer, D. R.; Park, S.; Bielawski, C. W.; Ruoff, R. S., The chemistry of graphene oxide. *Chemical Society Reviews* **2010,** *39* (1), 228-240.
8. Stankovich, S.; Dikin, D. A.; Piner, R. D.; Kohlhaas, K. A.; Kleinhammes, A.; Jia, Y.; Wu, Y.; Nguyen, S. T.; Ruoff, R. S., Synthesis of graphene-based nanosheets via chemical reduction of exfoliated graphite oxide. *Carbon* **2007,** *45* (7), 1558-1565.
9. Shin, H.-J.; Kim, K. K.; Benayad, A.; Yoon, S.-M.; Park, H. K.; Jung, I.-S.; Jin, M. H.; Jeong, H.-K.; Kim, J. M.; Choi, J.-Y.; Lee, Y. H., Efficient Reduction of Graphite Oxide by Sodium Borohydride and Its Effect on Electrical Conductance. *Advanced Functional Materials* **2009,** *19* (12), 1987-1992.
10. Schniepp, H. C.; Li, J.-L.; McAllister, M. J.; Sai, H.; Herrera-Alonso, M.; Adamson, D. H.; Prud'homme, R. K.; Car, R.; Saville, D. A.; Aksay, I. A., Functionalized Single Graphene Sheets Derived from Splitting Graphite Oxide. *The Journal of Physical Chemistry B* **2006,** *110* (17), 8535-8539.
11. Zhou, M.; Wang, Y.; Zhai, Y.; Zhai, J.; Ren, W.; Wang, F.; Dong, S., Controlled Synthesis of Large-Area and Patterned Electrochemically Reduced Graphene Oxide Films. *Chemistry – A European Journal* **2009,** *15* (25), 6116-6120.
12. Baker, H.; Okamoto, H., ASM Handbook, Volume 03 - Alloy Phase Diagrams. ASM International.
13. Reina, A.; Thiele, S.; Jia, X.; Bhaviripudi, S.; Dresselhaus, M. S.; Schaefer, J. A.; Kong, J., Growth of Large-Area Single- and Bi-Layer Graphene by Controlled Carbon Precipitation on Polycrystalline Ni Surfaces. *Nano Research* **2009,** *2* (6), 509-516.
14. Li, X. S.; Cai, W. W.; Colombo, L.; Ruoff, R. S., Evolution of Graphene Growth on Ni and Cu by Carbon Isotope Labeling. *Nano Letters* **2009,** *9* (12), 4268-4272.
15. Mattevi, C.; Kim, H.; Chhowalla, M., A review of chemical vapour deposition of graphene on copper. *Journal of Materials Chemistry* **2011,** *21* (10), 3324-3334.
16. Van Tuan, D.; Kotakoski, J.; Louvet, T.; Ortmann, F.; Meyer, J. C.; Roche, S., Scaling Properties of Charge Transport in Polycrystalline Graphene. *Nano Letters* **2013,** *13* (4), 1730-1735.
17. Lee, J. H.; Lee, E. K.; Joo, W. J.; Jang, Y.; Kim, B. S.; Lim, J. Y.; Choi, S. H.; Ahn, S. J.; Ahn, J. R.; Park, M. H.; Yang, C. W.; Choi, B. L.; Hwang, S. W.; Whang, D., Wafer-Scale Growth of Single-Crystal Monolayer Graphene on Reusable Hydrogen-Terminated Germanium. *Science* **2014,** *344* (6181), 286-289.

18. Wu, Y. M. A.; Fan, Y.; Speller, S.; Creeth, G. L.; Sadowski, J. T.; He, K.; Robertson, A. W.; Allen, C. S.; Warner, J. H., Large Single Crystals of Graphene on Melted Copper Using Chemical Vapor Deposition. *Acs Nano* **2012,** *6* (6), 5010-5017.
19. Li, Z. C.; Wu, P.; Wang, C. X.; Fan, X. D.; Zhang, W. H.; Zhai, X. F.; Zeng, C. G.; Li, Z. Y.; Yang, J. L.; Hou, J. G., Low-Temperature Growth of Graphene by Chemical Vapor Deposition Using Solid and Liquid Carbon Sources. *Acs Nano* **2011,** *5* (4), 3385-3390.
20. Kato, T.; Hatakeyama, R., Direct Growth of Doping-Density-Controlled Hexagonal Graphene on SiO2 Substrate by Rapid-Heating Plasma CVD. *ACS Nano* **2012,** *6* (10), 8508-8515.
21. Yamada, T.; Kim, J.; Ishihara, M.; Hasegawa, M., Low-temperature graphene synthesis using microwave plasma CVD. *Journal of Physics D-Applied Physics* **2013,** *46* (6).
22. Lin, Y.-C.; Lu, C.-C.; Yeh, C.-H.; Jin, C.; Suenaga, K.; Chiu, P.-W., Graphene Annealing: How Clean Can It Be? *Nano Letters* **2012,** *12* (1), 414-419.
23. Her, M.; Beams, R.; Novotny, L., Graphene transfer with reduced residue. *Physics Letters A* **2013,** *377* (21–22), 1455-1458.
24. Liang, X.; Sperling, B. A.; Calizo, I.; Cheng, G.; Hacker, C. A.; Zhang, Q.; Obeng, Y.; Yan, K.; Peng, H.; Li, Q.; Zhu, X.; Yuan, H.; Hight Walker, A. R.; Liu, Z.; Peng, L.-m.; Richter, C. A., Toward Clean and Crackless Transfer of Graphene. *ACS Nano* **2011,** *5* (11), 9144-9153.
25. Joshua, D. W.; Gregory, P. D.; Enrique, A. C.; Justin, C. K.; Joshua, A. K.; Isha, D.; Ashkan, B.; Jayan, H.; Basil, A.; Yaofeng, C.; Hefei, D.; Richard, T. H.; Joseph, W. L.; Eric, P., Annealing free, clean graphene transfer using alternative polymer scaffolds. *Nanotechnology* **2015,** *26* (5), 055302.
26. Liang, X. L.; Sperling, B. A.; Calizo, I.; Cheng, G. J.; Hacker, C. A.; Zhang, Q.; Obeng, Y.; Yan, K.; Peng, H. L.; Li, Q. L.; Zhu, X. X.; Yuan, H.; Walker, A. R. H.; Liu, Z. F.; Peng, L. M.; Richter, C. A., Toward Clean and Crackless Transfer of Graphene. *Acs Nano* **2011,** *5* (11), 9144-9153.
27. Cai, C.; Jia, F.; Li, A.; Huang, F.; Xu, Z.; Qiu, L.; Chen, Y.; Fei, G.; Wang, M., Crackless transfer of large-area graphene films for superior-performance transparent electrodes. *Carbon* **2016,** *98*, 457-462.
28. Yoon, T.; Shin, W. C.; Kim, T. Y.; Mun, J. H.; Kim, T.-S.; Cho, B. J., Direct Measurement of Adhesion Energy of Monolayer Graphene As-Grown on Copper and Its Application to Renewable Transfer Process. *Nano Letters* **2012,** *12* (3), 1448-1452.
29. Aliaksandr, V. Z.; Herad, M.; Casey, K.; Eric, J. S.; Suchol, S.; Eduardo, V.; Timothy, F. O. C.; Adam, D. P.; Darren, J. L., Metal-assisted exfoliation (MAE): green, roll-to-roll compatible method for transferring graphene to flexible substrates. *Nanotechnology* **2015,** *26* (4), 045301.
30. Zhu, W. J.; Low, T.; Perebeinos, V.; Bol, A. A.; Zhu, Y.; Yan, H. G.; Tersoff, J.; Avouris, P., Structure and Electronic Transport in Graphene Wrinkles. *Nano Letters* **2012,** *12* (7), 3431-3436.
31. Park, B.-J.; Choi, J.-S.; Kim, H.-S.; Kim, H.-Y.; Jeong, J.-R.; Choi, H.-J.; Jung, H.-J.; Jung, M.-W.; An, K.-S.; Yoon, S.-G., Realization of Large-Area Wrinkle-Free Monolayer Graphene Films Transferred to Functional Substrates. *Scientific Reports* **2015,** *5*, 9610.
32. Kim, H. H.; Lee, S. K.; Lee, S. G.; Lee, E.; Cho, K., Wetting-Assisted Crack- and Wrinkle-Free Transfer of Wafer-Scale Graphene onto Arbitrary Substrates over a Wide Range of Surface Energies. *Advanced Functional Materials* **2016,** *26* (13), 2070-2077.
33. Mun, J. H.; Cho, B. J., Synthesis of Monolayer Graphene Having a Negligible Amount of Wrinkles by Stress Relaxation. *Nano Letters* **2013,** *13* (6), 2496-2499.
34. American Chemical Society International Historic Chemical Landmarks. The Raman Effect. http://www.acs.org/content/acs/en/education/whatischemistry/landmarks/ramaneffect.html (accessed 01/11/16).
35. Ferrari, A. C.; Robertson, J., Resonant Raman spectroscopy of disordered, amorphous, and diamondlike carbon. *Physical Review B* **2001,** *64* (7), 075414.
36. Ferrari, A. C., Raman spectroscopy of graphene and graphite: Disorder, electron–phonon coupling, doping and nonadiabatic effects. *Solid State Communications* **2007,** *143* (1–2), 47-57.

37. Ado, J.; Marcia, M. L.; Fernando, S.; Erlon, H. M. F.; Marcus, V. O. M.; Rodrigo, B. C.; Carlos, A. A., Raman study of ion-induced defects in N -layer graphene. *Journal of Physics: Condensed Matter* **2010,** *22* (33), 334204.
38. Eckmann, A.; Felten, A.; Mishchenko, A.; Britnell, L.; Krupke, R.; Novoselov, K. S.; Casiraghi, C., Probing the Nature of Defects in Graphene by Raman Spectroscopy. *Nano Letters* **2012,** *12* (8), 3925-3930.
39. Loh, K. P.; Bao, Q.; Ang, P. K.; Yang, J., The chemistry of graphene. *Journal of Materials Chemistry* **2010,** *20* (12), 2277-2289.
40. (a) Jeon, K.-J.; Lee, Z.; Pollak, E.; Moreschini, L.; Bostwick, A.; Park, C.-M.; Mendelsberg, R.; Radmilovic, V.; Kostecki, R.; Richardson, T. J.; Rotenberg, E., Fluorographene: A Wide Bandgap Semiconductor with Ultraviolet Luminescence. *ACS Nano* **2011,** *5* (2), 1042-1046; (b) Delphine, S. M.; Jayachandran, M.; Sanjeeviraja, C., Review of material properties of (Mo/W)Se-2-layered compound semiconductors useful for photoelectrochemical solar cells. *Crystallography Reviews* **2011,** *17* (4), 281-301.
41. (a) Vlassiouk, I.; Smirnov, S.; Regmi, M.; Surwade, S. P.; Srivastava, N.; Feenstra, R.; Eres, G.; Parish, C.; Lavrik, N.; Datskos, P.; Dai, S.; Fulvio, P., Graphene Nucleation Density on Copper: Fundamental Role of Background Pressure. *J. Phys. Chem. C* **2013,** *117* (37), 18919-18926; (b) Kim, S. M.; Hsu, A.; Lee, Y.-H.; Dresselhaus, M.; Palacios, T.; Kim, K. K.; Kong, J., The effect of copper pre-cleaning on graphene synthesis. *Nanotechnology* **2013,** *24* (36).
42. Liu, Y.; Bhowmick, S.; Yakobson, B. I., BN White Graphene with "Colorful" Edges: The Energies and Morphology. *Nano Letters* **2011,** *11* (8), 3113-3116.
43. Soo Min, K.; Allen, H.; Yi-Hsien, L.; Mildred, D.; Tomás, P.; Ki Kang, K.; Jing, K., The effect of copper pre-cleaning on graphene synthesis. *Nanotechnology* **2013,** *24* (36), 365602.
44. Kim, M.-S.; Woo, J.-M.; Geum, D.-M.; Rani, J. R.; Jang, J.-H., Effect of copper surface pre-treatment on the properties of CVD grown graphene. *AIP Advances* **2014,** *4* (12), 127107.
45. Li, Z.; Wu, P.; Wang, C.; Fan, X.; Zhang, W.; Zhai, X.; Zeng, C.; Li, Z.; Yang, J.; Hou, J., Low-Temperature Growth of Graphene by Chemical Vapor Deposition Using Solid and Liquid Carbon Sources. *ACS Nano* **2011,** *5* (4), 3385-3390.
46. Kidambi, P. R.; Ducati, C.; Dlubak, B.; Gardiner, D.; Weatherup, R. S.; Martin, M.-B.; Seneor, P.; Coles, H.; Hofmann, S., The Parameter Space of Graphene Chemical Vapor Deposition on Polycrystalline Cu. *The Journal of Physical Chemistry C* **2012,** *116* (42), 22492-22501.
47. Yu, Y.; Gan, L.; Wan, X.; Zhai, T., Breakdown of self-limiting growth on oxidized copper substrates: a facile method for large-size high-quality bi- and trilayer graphene synthesis. *RSC Adv.* **2015,** *5* (69), 56293-56298.
48. Wood, J. D.; Schmucker, S. W.; Lyons, A. S.; Pop, E.; Lyding, J. W., Effects of Polycrystalline Cu Substrate on Graphene Growth by Chemical Vapor Deposition. *Nano Letters* **2011,** *11* (11), 4547-4554.
49. Poulston, S.; Parlett, P. M.; Stone, P.; Bowker, M., Surface Oxidation and Reduction of CuO and Cu_2O Studied Using XPS and XAES. *Surface and Interface Analysis* **1996,** *24* (12), 811-820.
50. Zhang, Y.; Zhang, L.; Zhou, C., Review of Chemical Vapor Deposition of Graphene and Related Applications. *Accounts of Chemical Research* **2013,** *46* (10), 2329-2339.
51. Huang, P. Y.; Ruiz-Vargas, C. S.; van der Zande, A. M.; Whitney, W. S.; Levendorf, M. P.; Kevek, J. W.; Garg, S.; Alden, J. S.; Hustedt, C. J.; Zhu, Y.; Park, J.; McEuen, P. L.; Muller, D. A., Grains and grain boundaries in single-layer graphene atomic patchwork quilts. *Nature* **2011,** *469* (7330), 389-392.
52. del Corro, E.; Kavan, L.; Kalbac, M.; Frank, O., Strain Assessment in Graphene Through the Raman 2D' Mode. *The Journal of Physical Chemistry C* **2015,** *119* (45), 25651-25656.
53. Zhang, Y.; Ren, W.; Jiang, Z.; Yang, S.; Jing, W.; Shi, P.; Wu, X.; Ye, Z.-G., Low-temperature remote plasma-enhanced atomic layer deposition of graphene and characterization of its atomic-level structure. *Journal of Materials Chemistry C* **2014,** *2* (36), 7570-7574.
54. Jang, J.; Son, M.; Chung, S.; Kim, K.; Cho, C.; Lee, B. H.; Ham, M.-H., Low-temperature-grown continuous graphene films from benzene by chemical vapor deposition at ambient pressure. *Scientific Reports* **2015,** *5*, 17955.

55. Stojanović, D.; Woehrl, N.; Buck, V., Synthesis and characterization of graphene films by hot filament chemical vapor deposition. *Physica Scripta* **2012,** *2012* (T149), 014068.
56. Hawaldar, R.; Merino, P.; Correia, M. R.; Bdikin, I.; Grácio, J.; Méndez, J.; Martín-Gago, J. A.; Singh, M. K., Large-area high-throughput synthesis of monolayer graphene sheet by Hot Filament Thermal Chemical Vapor Deposition. *Scientific Reports* **2012,** *2*, 682.
57. Aliofkhazraei, M.; Ali, N.; Milne, W. I.; Ozkan, C. S.; Mitura, S.; Gervasoni, J. L., *Graphene Science Handbook: Mechanical and Chemical Properties*. CRC Press: 2016.
58. Bae, S.; Kim, H.; Lee, Y.; Xu, X.; Park, J.-S.; Zheng, Y.; Balakrishnan, J.; Lei, T.; Ri Kim, H.; Song, Y. I.; Kim, Y.-J.; Kim, K. S.; Ozyilmaz, B.; Ahn, J.-H.; Hong, B. H.; Iijima, S., Roll-to-roll production of 30-inch graphene films for transparent electrodes. *Nat Nano* **2010,** *5* (8), 574-578.

Chapter 3. Chemical vapour deposition of Tungsten disulphide

3.1 Introduction

This chapter focuses on the graphene-like material tungsten disulphide (WS_2). It is part of the family of transition metal dichalgogenides (TMDs) discussed in chapter 1. TMDs such as WS_2 have the potential to form van der Waals heterostructures with graphene. As will be discussed in greater depth in the introduction to this chapter, WS_2 has properties that make it desirable to combine with graphene. Chapter 1 gives an example of a graphene/WS_2/graphene field-effect tunnelling transistor (FETT).[1] Producing WS_2 on a large scale is an important challenge to overcome. As with graphene, chemical vapour deposition (CVD) is a promising technology for meeting this challenge. In particular, aerosol assisted CVD (AA-CVD) is an under-researched area in producing large areas of high quality WS_2. This chapter will explore the deposition of WS_2 on and off graphene via CVD. Therefore, a detailed consideration will be given to WS_2's synthesis and properties. Current progress on creating graphene/WS_2 heterostructures will also be discussed. The experimental results of depositing WS_2 thin films by AA-CVD from this piece of work will then be presented. This will be contrasted against WS_2 deposited by AA-CVD onto CVD graphene, produced by the techniques developed in the previous chapter. It will be shown that WS_2 deposits in a significantly different way onto graphene compared to more classic AA-CVD target substrates such as glass and silicon. Due to the different growth mechanisms involved when depositing onto graphene, greater control could be afforded over WS_2 film thickness. This allowed films as thin as 5 nm to be grown, by far the thinnest continuous films ever produced by AA-CVD. Due to the success of producing ultrathin, continuous WS_2 at relatively low temperatures, using an industrially relevant technique, it was of interest to see if high temperature CVD techniques could afford WS_2 on graphene. Following literature precedent of producing WS_2 monolayers on SiO_2, from WO_3 and sulphur, it was found, as with AA-CVD, WS_2 grew readily on graphene and monolayer thickness could be achieved, creating a large-scale WS_2/graphene heterostructure.

3.1.1 WS_2 properties

In its bulk form WS_2 is a grey, inert material which is industrially relevant in lubrication. As with many other TMDs, its layered bulk structure is formed from the stacking of monolayers, bound by weak van

der Waals interactions. The in plane stability of monolayers of WS_2 derives from the strong covalent bonding. More recently, its catalytic properties have been of interest for use in water splitting and it is actively being studied for this purpose today.[2] Additionally, with the advent of the isolation of graphene and graphene-like materials, it is increasingly being studied for use in applications related to graphene such as microelectronics. Like graphene, WS_2 exists in 1D, 2D and 3D forms. In fact, WS_2 was the first inorganic nanotube to be discovered.[3]

3.1.1.1 WS_2 structure

WS_2, like closely related molybdenum disulphide (MoS_2) and other TMDs, can exist in the 1T, 2H (or 1H in the case of a monolayer) and 3R phases. The difference between the 2H and 3R phase is the stacking order of the WS_2 layers, as both can be thought of as made up of stacked 1H layers. 2H has a hexagonal symmetry and stacks ABAB whereas 3R has a rhombohedral symmetry and stacks ABCABC.[4] Calculations have shown that 2H stacking is more stable than 3R stacking and thin films of TMDs exfoliated from a natural crystal are mostly 2H although 3R stacking is possible, albeit rare.[5] The difference between the 1H and the 1T phase is the coordination of individual tungsten atoms. In the 1H phase the tungsten atom is in a trigonal prismatic environment whereas the 1T phase is in a octahedral environment. Figure 3.1 displays the various phases WS_2 can assume.

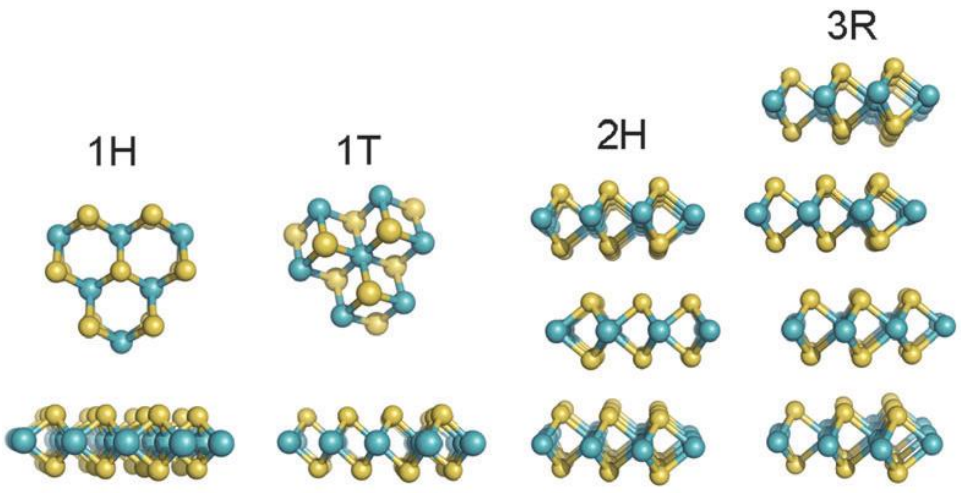

Figure 3.1 Top down and side on images of the various phases WS_2 can assume. Blue atoms are tungsten and yellow atoms are sulphur. Reproduced from ref 4.

3.1.1.2 WS_2 electrical properties

For the different phases of WS_2 the d-orbital splitting determines whether it behaves as a semiconductor or a metal. The p-orbitals of sulphur are far lower in energy than the Fermi level, so their electrons have a negligible influence on the electronics of WS_2. The d orbitals of tungsten in the 1T phase split into two degenerate states, dxy,yz,zx (t_{2g}) and dx^2y^2,z^2 (e_g). For the 1H phase the d orbitals split into the degenerate states dz^2, dx^2-y^2,xy and dxy,yz, where the bandgap is between the dz^2 and the dx^2-y^2,xy states.[4] Partly filled orbitals of the 1T phase leads to metallic behaviour, whereas completely filled orbitals of the 1H phase leads to semiconducting behavour. These unpaired electrons also lead to paramagnetism in the 1T phase. Figure 3.2 displays the molecular orbital diagrams for the 1T and 1H phase.

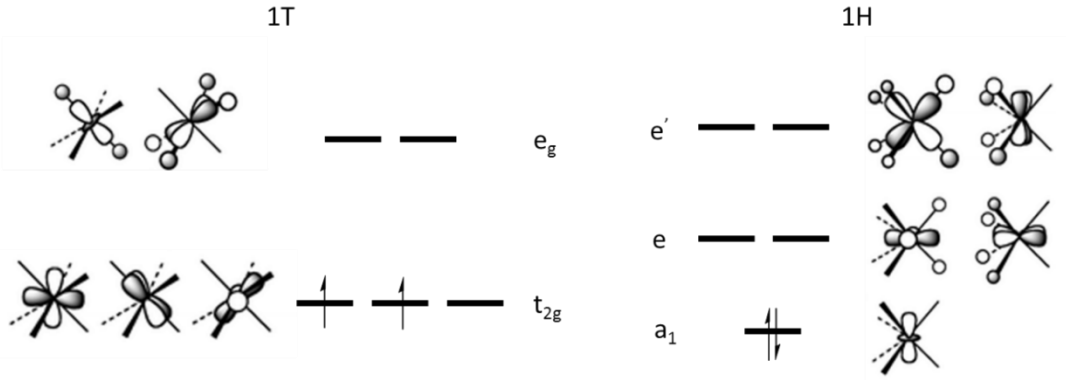

Figure 3.2 Molecular orbital diagram of the 1T and 1H phase of WS_2.

Bulk 2H WS_2 has a relatively small indirect bandgap of 1.4 eV. This increases to a larger direct bandgap for a monolayer. The exact value has been controversial, due to the strong exciton binding energy in monolayer WS_2, with reported values ranging from 2.14 to 3.11 eV.[6] This change in bandgap is relatively common among the TMDs, with quantum confinement effects shifting the positions of the valence and conduction bands. This in turn allows for tuning of the bandgap of the material, depending on the number of layers.[7] A unique electronic property of WS_2 is that its monolayer conduction band aligns with the Dirac point of graphene.[8] This means the current between WS_2 and graphene can easily be switched on and off as only a small change in the fermi level of graphene is needed. This can be achieved by using a gate voltage that is sufficiently small to avoid dielectric breakdown.[1,6]

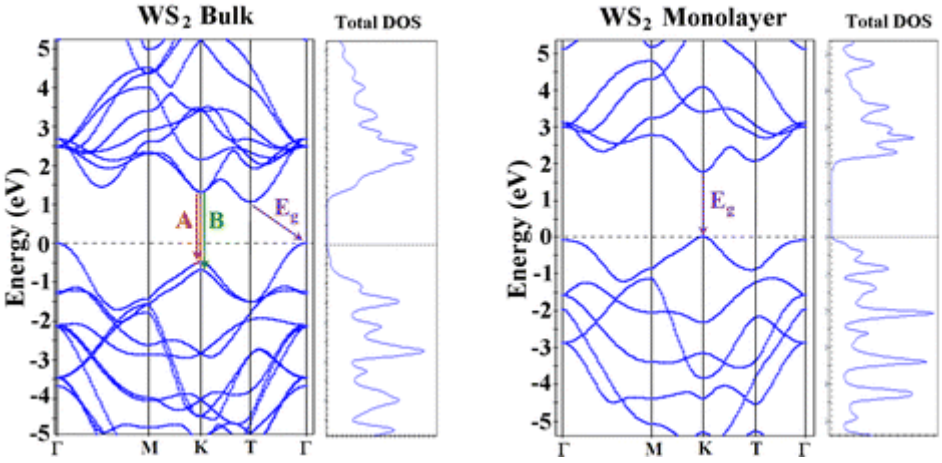

Figure 3.3 Band structure diagrams and density of states for bulk and monolayer WS_2. Reproduced from ref 9.

3.1.1.3 WS_2 photoluminescence

Compared to monolayer MoS_2, WS_2 exhibits a very strong photoluminescence (PL) peak corresponding to a direct excitonic transition at the bandgap. However, for bulk WS_2 there is valence band splitting which creates two separate transitions (labelled A and B in figure 3.3) where the lowest energy transition (the band gap) is indirect.

Terrones et al. were the first to report this strong PL related to monolayer WS_2.[9] They found from their CVD grown monolayers, PL intensity was greatest around the edges of the crystals. However if the crystals were then manually broken, no higher intensity was found at the broken edges. The mechanism for the increased PL intensity is still unknown, however there is speculation it could be related to PL redshift near the grown crystal edges. Xu et al. later demonstrated similar findings and also found the PL intensity varied over a monolayer flake of WS_2, although it was not always greatest at its edges. They postulate that defects quench the PL intensity, as the centre of a CVD grown flake has been exposed to high temperatures for longer it will be the most defective.[10]

3.1.3 WS_2 applications

It has been shown that heterostructures of monolayer graphene, WS_2 and MoS_2 can achieve power conversion efficiencies of ca. 1 %, an order of magnitude higher than the current state of the art ultrathin solar cell technologies such as GaAs and silicon.[11] WS_2 has also been shown to be effective as a catalyst in the hydrogen evolution reaction.[12] A high responsivity UV-vis photodetector has also been created using a 'nanofilm' of WS_2.[13] The authors acknowledge the need to produce WS_2 films on a large scale and achieve this by magnetron sputtering. However, they have to include an annealing

step at 800 °C. Due to its layered structure WS_2 is also being studied as a super capacitor and WS_2 films deposited on graphene oxide by hydrothermal synthesis have been made.[14]

3.1.4 WS_2 synthesis

In a similar manner to graphene, WS_2 can be synthesised through top down or bottom up approaches. If thin layers of WS_2 are desired, bulk crystals can be exfoliated either mechanically or by intercalation. Although this method can produce high quality flakes of WS_2 and can be used to isolate the less stable 1T phase, it is not well suited to producing WS_2 films on a large scale.[15]

Due to issues with scalability of top down techniques, several bottom up techniques are being developed. These include hydrothermal synthesis, magnetron sputtering, pulsed laser deposition and CVD. Hydrothermal synthesis typically involves heating a tungsten salt, such as WCl_6, with a sulphur source such as thioacetamide, in a solvent at temperatures up to 300 °C.[14,16] Magnetron sputtering has been reported to produce WS_2 films, which although uses relatively low temperatures of 300-400 °C uses high vacuum systems of ca. 10^{-7} mbar.[17] Pulsed laser deposition involves ablating a WS_2 target with a laser, which again is under high vacuum (HV) conditions, produces few layer WS_2.[18] Although the bottom-up routes mentioned so far may offer promising routes to the large-scale manufacture of WS_2 thin films, a rapidly increasing area of research is in producing monolayer WS_2 thin films by what shall be called high temperature CVD.

3.1.4.1 High temp CVD

The CVD of monolayer TMD crystallites was first reported for MoS_2 in 2012.[19] It involved growing crystals of MoS_2 from a vapour of MoO_3 and sulphur on a SiO_2 substrate, seeded by reduced graphene oxide. Since then well-defined MoS_2 monolayer, triangular crystals have been synthesised. Different molybdenum salts have been used and the growth substrates varied, but the general principles have remained the same.[20] The deposition of monolayer WS_2 triangular crystals soon followed in 2013 with the evaporation of WO_3 thin films onto a SiO_2 substrate followed by subsequent sufurisation at 800 °C. The growth mechanism of the crystals is currently not completely understood and will be discussed in more detail in a later section. Complete monolayer coverage of substrates have also been achieved on gold foils, an advantage of this method is that the gold foil is reusable.[21]

3.1.4.2 AA-CVD

As discussed in chapter 1, AA-CVD offers a scalable, cost effective route to thin films of many materials. Using AA-CVD, pre-made WS_2 nanoparticles have been incorporated into Cr_2O_3,[22] however to date there have been no examples in the literature of depositing WS_2 films by AA-CVD. O'Brien has shown

MoS_2 can be deposited via AA-CVD using a molybdenum dithiocarbamate precursor in a tetrahydrofuran (THF) solvent. The general structure of a metal dithiocarbamate is shown in figure 3.4.

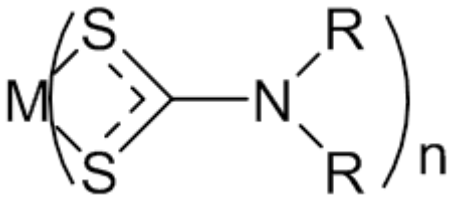

Figure 3.4 General structure of metal dithiocarbamate precursor.

Due to the limited volatility of molybdenum dithiocarbamate systems, ultra-high vacuum (UHV) systems have been used previously to produce densely packed MoS_2 platelets on nickel.[23] The success of depositing MoS_2 by AA-CVD demonstrates a precedent for exploring AA-CVD of WS_2 using a tungsten dithiocarbamate precursor. O'Brien has shown metal dithiocarbamates can be deposited via AA-CVD to produce a series of metal sulphides. These materials include but are not limited to: tin sulphide, cadmium sulphide and iron sulphide.[24,25,26] With this precedent in mind, we used tungsten dithiocarbamate as a precursor for the attempted deposition of WS_2 via CVD, and the results are described later in this chapter.

3.1.5 WS_2 on graphene

The most obvious way of creating a WS_2/graphene heterostructure is to stack exfoliated layers of WS_2 onto graphene. This gives the advantage of producing high quality heterostructures with well-established techniques for manipulating exfoliated flakes. This has led to the creation of devices such as a vertical field-effect transistor, tunnel barrier and a solar device.[8,27,28]

Although these devices point to some of the exciting applications of WS_2/graphene heterostructures, methods used to produce these structures on a large scale need to be developed. As with producing WS_2 films in isolation, CVD is a promising technique to meet this challenge. Currently, it has been demonstrated that WS_2 crystals may he grown directly onto graphite using WO_3 and sulphur as precursors.[29] Miyata et al. observed a sharpening of the PL peak for WS_2 on graphite compared to on SiO_2 from a full width half maximum (FWHM) of 61 meV to 21 meV. Additionally the peak on graphite could by fitted by a single Lorentzian function whereas on SiO_2 two Voigt functions had to be used. They assign the lower and higher energy Voigt peaks to trion and neutral free excitons respectively, which indicates local charge doping. They also observe quenching of the PL signal on graphene compared to SiO_2. This is attributed to fast non-radiative recombination processes of WS_2 on graphite.

Finally, they find an increase in PL peak energy for WS_2 on graphite. This is likely to be due to the graphite surface being ultra-flat, reducing strain on the WS_2 crystals. It has been shown tensile strain reduces the bandgap for TMDs.[30] SiO_2 and graphite have similar and small thermal expansion coefficients; therefore, on cooling any strain introduced into WS_2 is likely to be tensile. The lower energy PL spectra of WS_2 on SiO_2 is therefore likely to be caused by greater tensile strain. Figure 3.5 shows WS_2 crystal domains on graphite and PL spectra of monolayer WS_2 on various substrates.

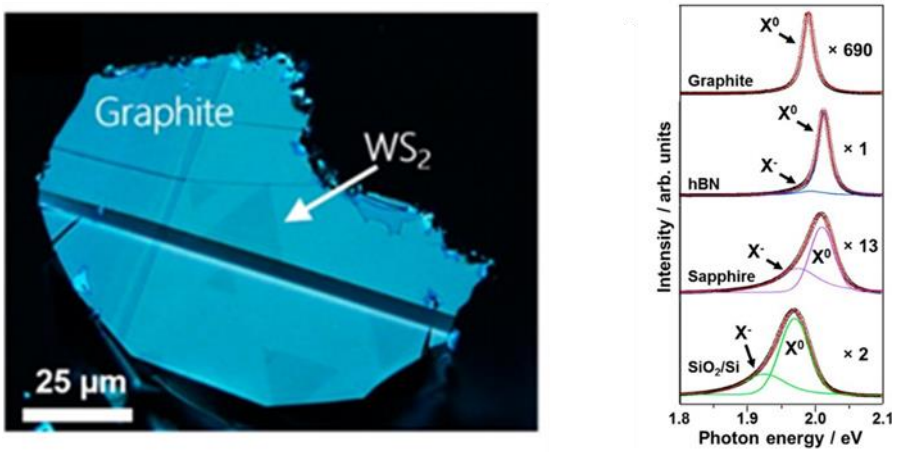

Figure 3.5 WS_2 crystal domains on graphite and various PL spectra. Adapted from ref 29.

To date, there have been only two reported examples of WS_2 being directly grown onto graphene. Bianco et al., using $W(CO)_6$ and sulphur as precursors, deposited WS_2 on graphene grown from SiC and CVD onto copper at 600 ^oC.[31] Similarly to Miyata et al. they show it is possible to grown triangular WS_2 crystals on graphene. They find WS_2 crystals are more likely to grow at grain boundaries of the graphene and on bilayer graphene. They find that they achieve a PL response for the triangles grown on graphene but give no comparison with WS_2 grown on SiO_2. However, when they increase growth times to achieve complete coverage of the graphene, the PL peak is absent. They attributed this to multilayer coverage. Figure 3.6 shows an SEM image of the WS_2 crystals growing on monolayer graphene (MG), Bernal-stacked bilayer graphene (BBG) and twisted bilayer graphene (TBG). The twisted bilayer graphene come from a rip in the graphene film, revealing the SiO_2 substrate underneath.

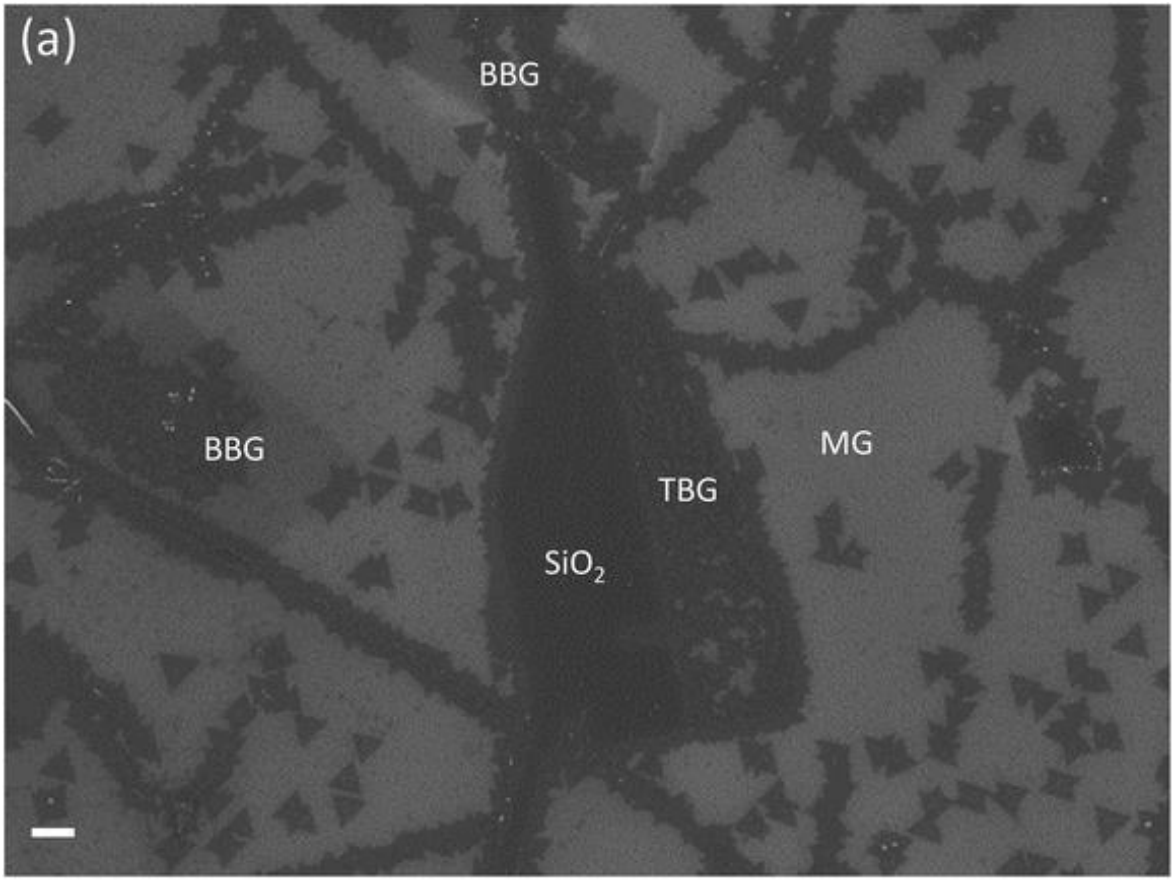

Figure 3.6 WS_2 crystals growing on various types of graphene: monolayer graphene (MG) Bernal-stacked bilayer graphene (BBG) and twisted bilayer graphene (TBG). Scale bar 500 nm. Image adapted from ref 31.

3.2 Results and discussion - AA-CVD of WS_2 on glass and silicon

As discussed previously, $W(S_2CNEt_2)_4$ was selected as the precursor to deposit WS_2. It was synthesised and isolated by Joseph Thompson as part of a study of various novel AA-CVD precursors. $W(S_2CNEt_2)_4$ was chosen for further study for several reasons:

- It followed naturally on from work previously carried within the group and in the literature, depositing analogous Mo carbamates to produce MoS_2.
- It has never been explored as a WS_2 precursor before.
- Due to its relative stability and ease of synthesis it provided a good gateway into exploring AA-CVD onto graphene substrates, which to the best of our knowledge has never been reported before.

The synthetic route and molecular structure of $W(S_2CNEt_2)_4$ can be seen in figure 3.7.

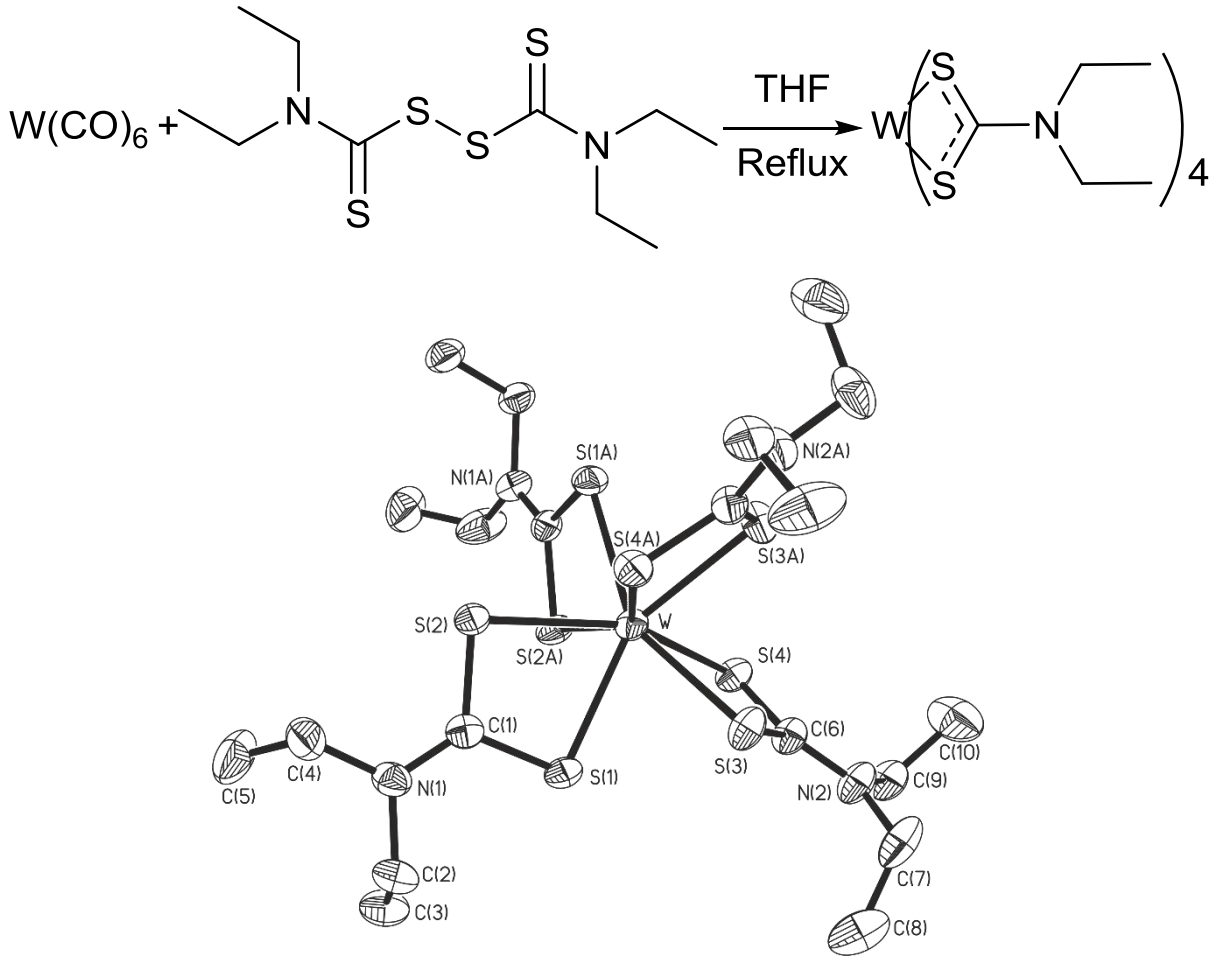

Figure 3.7 Synthetic route and molecular structure of $W(S_2CNEt_2)_4$

3.2.1 Thermogravimetric Analysis (TGA) of $W(S_2CNEt_2)_4$

To explore decomposition pathways and potential CVD process temperatures $W(S_2CNEt_2)_4$ was subjected to a thermal-gravimetric analysis (TGA) in a nitrogen atmosphere. In this method, the mass of a material is measured as temperature is ramped over a set period of time. Figure 3.8 is a plot of % weight remaining of the precursor at a certain temperature. A summary of the data obtained is displayed in table 3.1.

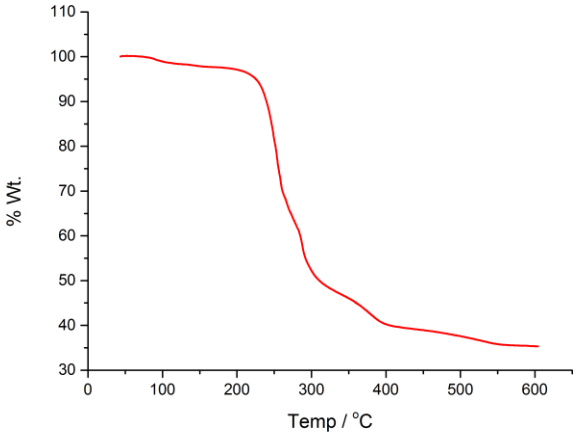

Figure 3.8 TGA trace of $W(S_2CNEt_2)_4$.

Table 3.1 Summary of TGA data for $W(S_2CNEt_2)_4$.

Onset / ^{O}C	Endpoint / ^{O}C	% wt. expected for WS_2	Final % wt.
200	400	31.9	35.3

The final % weight remaining of 35.3% is close to the theoretical weight expected if the precursor decomposed entirely into WS_2. It is likely that the theoretical weight was not exactly reached due to impurities left in the final product. This could be due to incomplete breakdown of the carbamate, which there is some precedent for other metal carbamates in the literature.[32] Additionally as a 'closed' pan was used to contain the precursor to eliminate reactions with atmospheric oxygen, the narrow bore of the pinhole has been known to hinder escape of decomposition products.

Between 100 and 200 ^{o}C there is a slight mass loss of 5 %. After this there is a larger mass loss of ~26 % up to 263 °C which could be attributed to the loss of ethene. A Further mass loss at 280 °C (~7 % loss) and 305 °C (~11 %) could be due to the loss of HCN. The final weight loss of ~11% to the decomposition end point at 400 °C could be due to the loss of excess sulphur.

TGA therefore indicates CVD process temperatures should be run close to or above 400 ^{o}C to ensure full decomposition of the precursor.

3.2.2 Depositions of WS_2 on glass and Si

Firstly WS_2 was deposited onto glass and silicon, commonly available substrates often used in CVD processes, at a range of temperatures to assess its growth potential.

Under an inert atmosphere a saturated solution (ca. 15mmol) of $W(S_2CNEt_2)_4$ dissolved in toluene was delivered into the precursor pot. The AA-CVD apparatus was then purged with argon gas for 15 mins. Once the furnace had reached the desired temperature, the precursor pot was opened to the argon flow for 90 mins. After deposition, the precursor vessel was stoppered and the substrates were cooled to room temperature under a flow of argon. Depositions were run at 350, 400, 450 and 500 °C.

3.2.3 Analysis of WS_2 on glass and silicon - Powder X-Ray Diffraction (PXRD)

Apart from the deposition at 350 °C on silicon, all the PXRD patterns of the WS_2 films are dominated by the major peak at ca. 14.4 °, which corresponds to either the 2H (14.320° = (002))[33] and 3R (14.359° = (003))[34]phases. This indicates films are highly orientated, with thin crystallites orientated with their basal planes parallel to the substrate surface.[35,36] Peaks at ca. 33 ° for the films on the silicon substrates correspond to the (100) reflection of the underlying silicon. The small peak at 32.6 ° on the PXRD pattern for the film deposited on silicon at 450 °C likely corresponds to the (100) peak of the 2H phase, indicating at least the presence of the 2H phase.

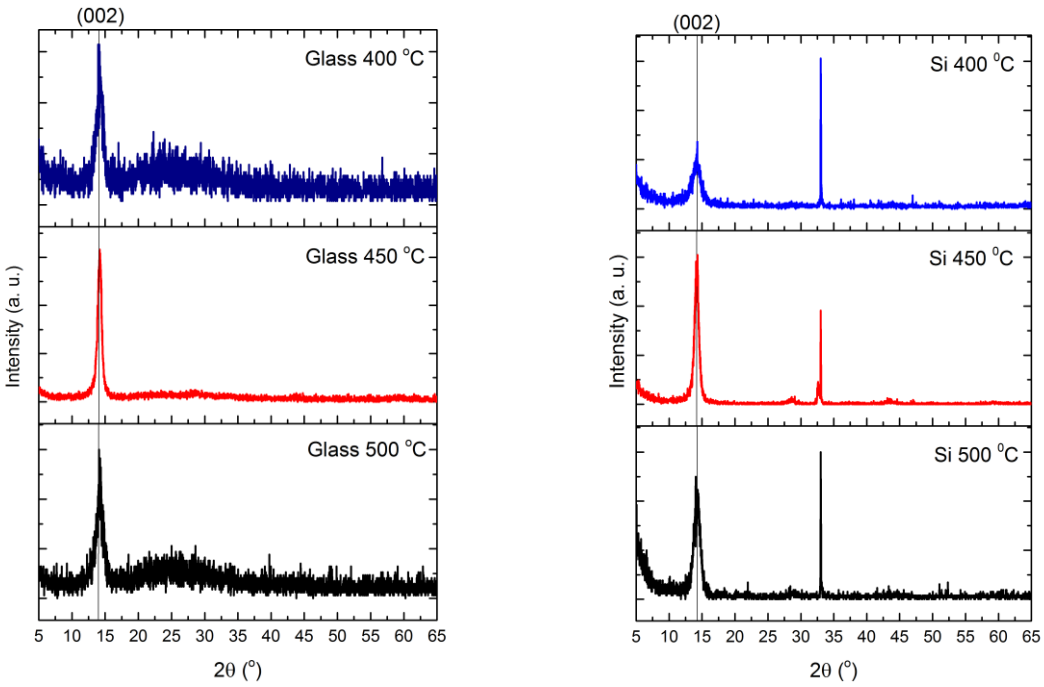

Figure 3.9 PXRD spectra of WS_2 on glass and silicon.

The broadening of a diffraction peak can be the result of the crystallite dimensions perpendicular to the planes that produced the diffraction peak decreasing, which can be shown mathematically by the Scherrer formula[37] :

$$\beta(2\Theta) = \frac{k\lambda}{Lcos(\Theta)} \qquad \text{Equation 3.1}$$

Where L is a volume average of the crystal thickness in the direction normal to the reflecting planes, λ is the wavelength of X-ray being used in the PXRD experiment, θ is the angle the peak appears at and β is the integral breadth (area/height) of the peak. k is related to the shape of the crystal, near the value of 1. For simplicities sake, k will be assumed to equal 1 for all further analysis.[38]

Performing a simple Gaussian fit to the (002) diffraction peak allows a value of β to be obtained. As the value of λ (15.418 nm) and the position of the peak are known, a value of L can be obtained. They are plotted in figure 3.10 for the different deposition temperatures. Although by SEM analysis it was shown 500 °C produced the thickest films (figure 3.12) 450 °C seems to produce the most crystalline layers, 18 nm corresponds to roughly 18 layers.

3.2.4 Analysis of WS_2 on glass and silicon - Raman

Raman spectroscopy showed the presence of the major 2LA (355 cm^{-1}) and A_{1g} (420 cm^{-1}) resonances as well as a peak at 178 cm^{-1} corresponding to bulk WS_2 for all of the films. The films deposited at 500 °C on both substrates and 450 °C on glass also showed resonances at 232, 298, 326, 582 and 702 cm^{-1} consistent with bulk WS_2. Films on the glass substrates exhibited peaks at 523 cm^{-1} corresponding to bulk WS_2 whilst these peaks were covered by the silicon substrate peak (520 cm^{-1}) for the films on silicon. Raman spectra displayed a broad peak at c.a. 1300 cm^{-1} indicating the presence of amorphous carbon. Figure 3.11 displays typical Raman spectra for films grown at 450 °C on glass and silicon.

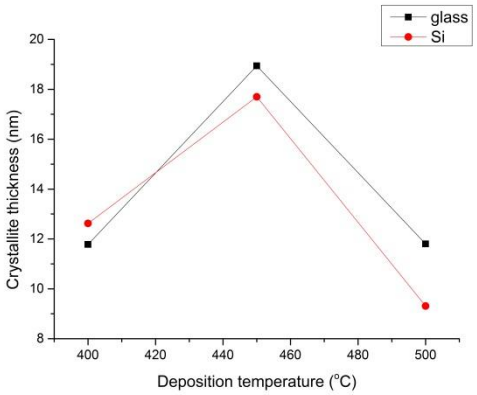

Figure 3.10 Crystallite thickness of WS_2 films deposited on glass and silicon calculated by the Scherrer formula.

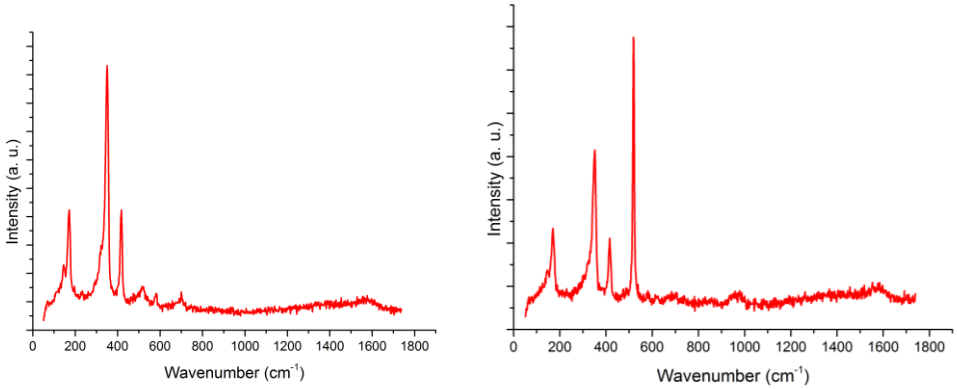

Figure 3.11 Raman spectra of WS_2 on glass (left) and silicon (right).

3.2.5 Analysis of WS_2 on glass and silicon - EDS

EDS spectra were taken for all films, confirming the presence of tungsten and sulphur in close to the desired 1:2 ratio. The stoichiometries of W:S are displayed in table 3.2.The presence of oxygen in the films could not be determined due to it being present in the substrates. It was found a small amount of carbon contamination was present within the films, although this is common for films deposited using AA-CVD.[39] EDS spectra can be found in Supplementary information sulphur.2.

Table 3.2 Stoichiometries of W:S grown on glass and silicon at various temperatures.

Temperature (°C)	Substrate	W:S stoichiometry
400	Glass	$WS_{2.1}$
400	Si	$WS_{1.9}$
450	Glass	$WS_{2.4}$
450	Si	$WS_{2.3}$
500	Glass	$WS_{2.5}$
500	Si	$WS_{1.9}$

3.2.6 Analysis of WS_2 on glass and silicon - Scanning Electron Microscopy (SEM)

SEM images, shown in figure 3.12, revealed some morphological elements of the films. The films appeared to be comprised of crystallite flakes probably on the surface of a continuous film, which indicates Stranski–Krastanov (SK) growth. This could be due to a balance between WS_2 being formed on a hot reactive substrate and the templating effect causing preferential growth on existing WS_2 hexagonal faces. This seems to be particularly evident on silicon, where at 400 °C Volmer–Weber (VW)

growth seems to dominate, whereas at 500 ^{o}C a continuous layer becomes more evident. The difference in growth mechanisms could be partly explained by a templating effect. Although a thin native oxide layer will exist on top of the silicon wafer, some cubic order may still be presented to the reactive species. As PXRD studies have indicated,WS_2 seems to prefer to grow with its hexagonal plane parallel to the substrate, creating a phase mismatch between the cubic silicon and the hexagonal WS_2 leading to WS_2 preferentially grown on already grown layers, creating islands. At higher temperatures, enough energy could be provided to allow a more Frank–van der Merwe (FM)-like growth mechanism to proceed, despite the higher energy barrier. Glass however is amorphous, reducing this energy barrier. Film thickness measured from side on SEM images are shown in figure 3.13. Over all growth temperatures, WS_2 films on glass are thicker than on silicon, further confirming WS_2 preferentially grows on glass over silicon.

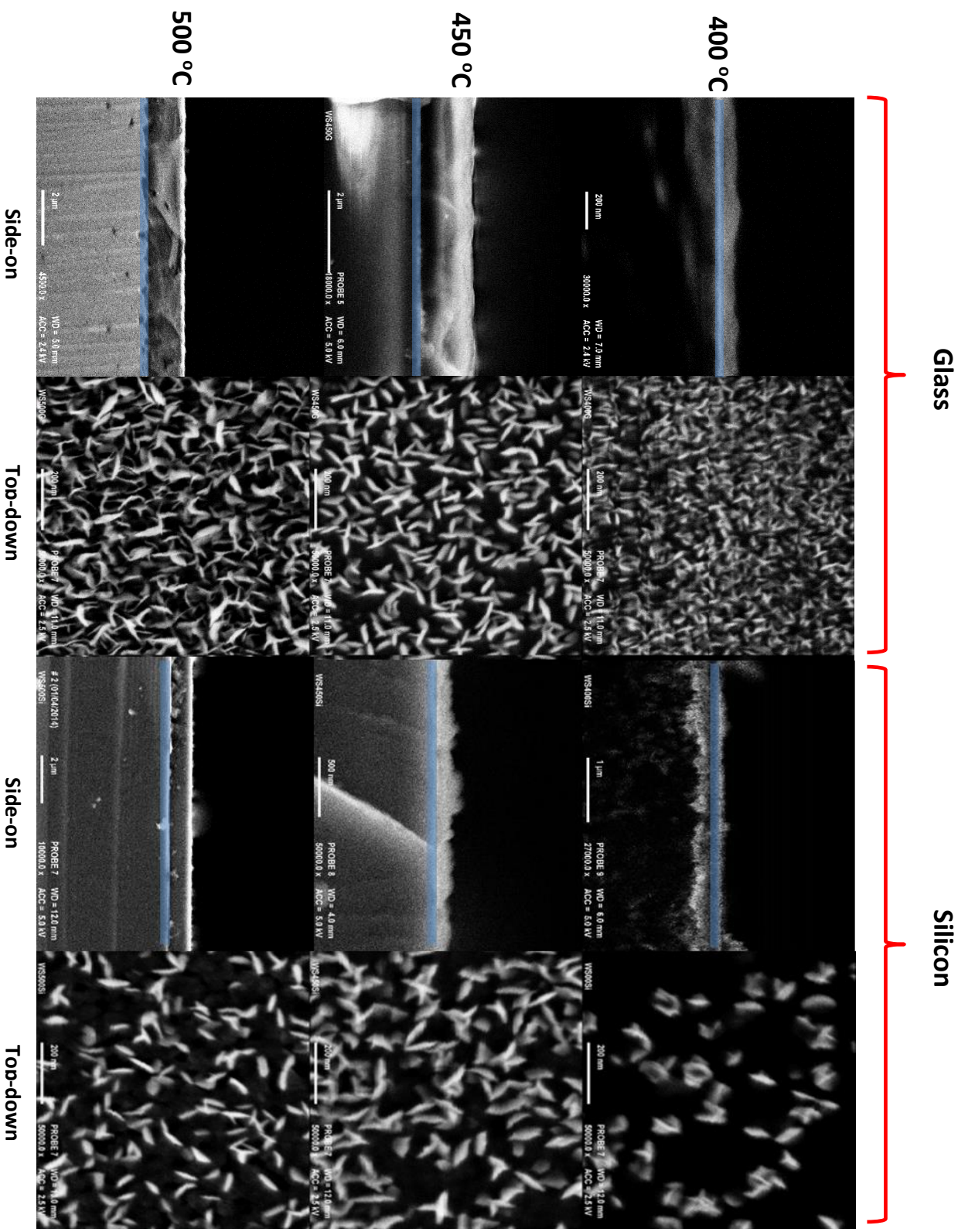

Figure 3.12 Top-down and side on SEM images of WS_2 on glass and silicon. Blue lines highlight boundary between substrate and WS_2.

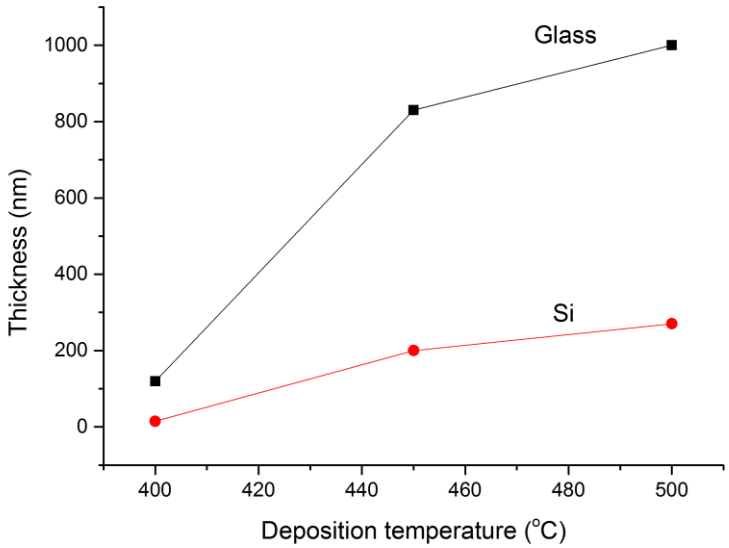

Figure 3.13 Film thicknesses of WS_2 on glass and silicon at various temperatures derived from SEM images.

3.2.7 Analysis of WS_2 on glass and silicon -AFM

AFM images were taken of the WS_2 films. Figure 3.14 shows images taken of WS_2 deposited onto glass and silicon at 400 °C. Individual particles can be seen on the silicon substrate whereas as more continuous film is present on the glass, supporting the results found through SEM analysis.

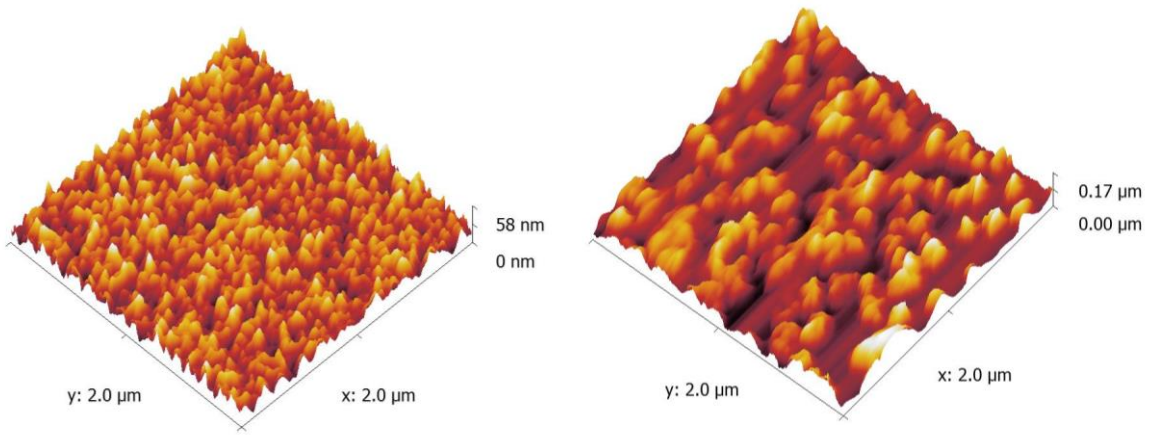

RMS: 7.15 nm

RMS: 29.2 nm

Figure 3.14 AFM images and RMS values of WS_2 grown at 400 °C on glass (left) and silicon (right).

3.2.8 WS_2 depositions on glass and silicon summary

It has been shown through the depositions using $W(S_2CNEt_2)_4$ as the precursor, WS_2 orientated films can be grown on glass and silicon. Due to the degree of orientation of the films, the phase of WS_2 could not be determined, although it is likely to be 2H as this form (as discussed previously) is the most thermodynamically stable phase commonly found when WS_2 is synthetically produced. SEM and AFM analysis reveals a difference in interaction between the growing WS_2 films with the glass and silicon substrates in the temperature range 400-500 ^oC. Lower temperatures seem to support a VW growth mechanism whereas SK growth becomes more important at higher temperatures.

3.3 Results and discussion - AA-CVD of WS_2 on graphene

After depositions of WS_2 on commonly used substrates using $W(S_2CNEt_2)_4$ were analysed, a series of depositions were then carried out on graphene transferred onto SiO_2 substrates using the same precursor. To maximise the chance of observing different growth mechanism occurring, depositions were run at 400 ^oC as on silicon this produced solely VW growth, which was postulated to be due to a templating effect. All the other deposition parameters were kept the same, except time which was varied to explore how much control could be exerted over film thickness. Depositions were run for 5, 10, 15, 30 and 60 mins.

3.3.1 Analysis of WS_2 on graphene - PXRD

The crystallinity and orientation of the WS_2 films deposited onto graphene were analysed by PXRD. Although quantitative analysis can be carried out by on comparing absolute peak intensities between different samples, as the exact conditions of sample collection cannot be replicated, it was immediately apparent the peaks produced from the WS_2 on graphene sample were stronger than WS_2 on glass or silicon. PXRD data for films grown from 10 -60 mins are shown in figure 3.15. Well above variations produced by s collecting conditions. This indicated the WS_2 films produced on graphene were more crystalline than the WS_2 on glass and silicon counterparts. This was found to be even more significant when the WS_2 on graphene films were shown to be much thinner by further analysis. From PXRD it can be seen the films get thinner with decreasing deposition time due to the silicon (001) peak getting proportionally larger. Additionally, unlike for WS_2 films grown on glass and silicon, WS_2 (004) and (006) reflections become apparent, providing further evidence of increased orientation with the substrate.

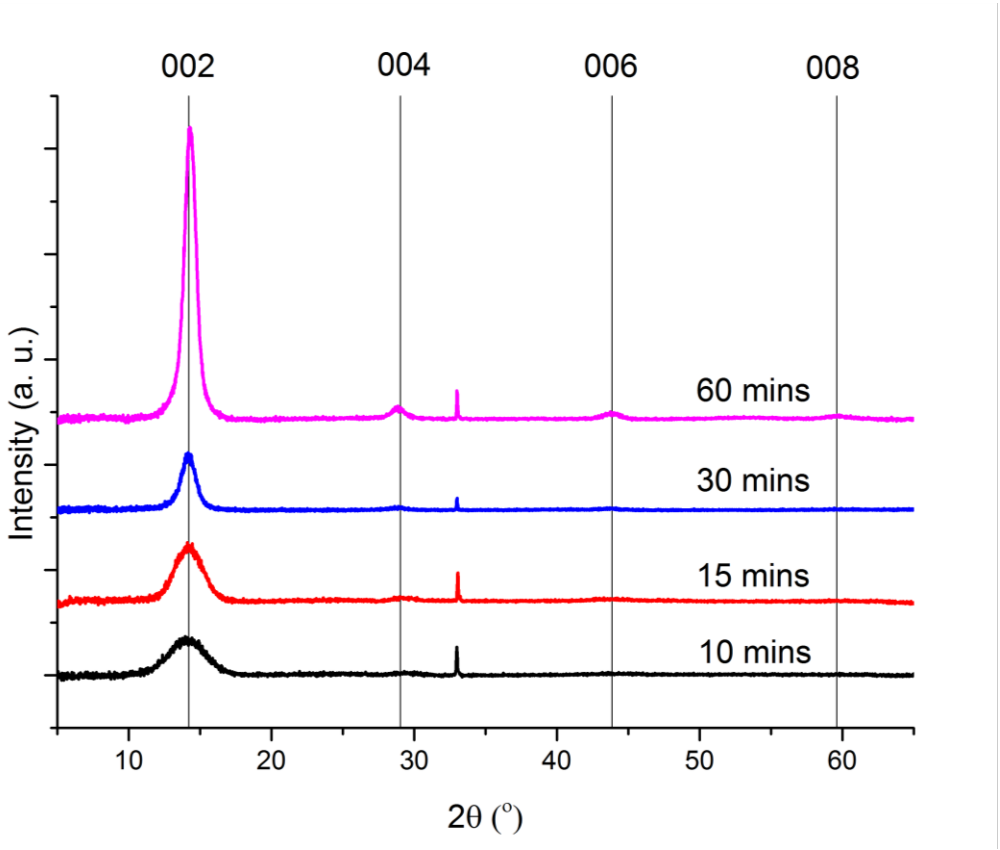

Figure 3.15 PXRD spectra of WS_2 deposited for various lengths of time on graphene.

Using the Scherrer formula the first three deposition times reveal a linear crystal growth rate against time normal to the 002 plane. This fits with the analysis of the WS_2(002) and the (001) silicon peak ratios. Figure 3.16 displays WS_2(002)/Si(001) peak ratios and crystallite thickness normal to the (002) plane against time. However beyond 30 minutes the crystallite size no longer grows linearly with time, indicating an increase in polycrystallinity within the films. Extrapolating to higher deposition times, it appears the maximum average crystal thickness achievable for the deposition conditions used is approximately 15 nm, corresponding to 15 layers of WS_2.[40]

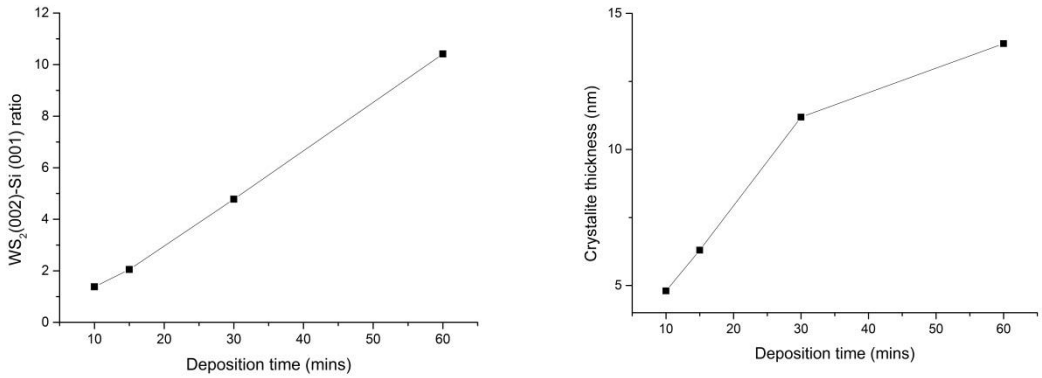

Figure 3.16 WS_2(002)/Si(001) peak ratios (left) and crystallite thickness normal to the (002) plane (right) against time.

3.3.2 Analysis of WS_2 on graphene - Raman

Raman spectroscopy was used to further analyse the WS_2 films deposited onto graphene. For all the deposited films, the peaks corresponding to WS_2 and graphene were present. In agreement with PXRD, the silicon peak decreases in relative intensity with increasing growth time. Figure 3.17 displays a Raman spectrum containing the WS_2 peaks and the G peak for graphene. It also shows the peaks corresponding to the WS_2 films for the various deposition times.

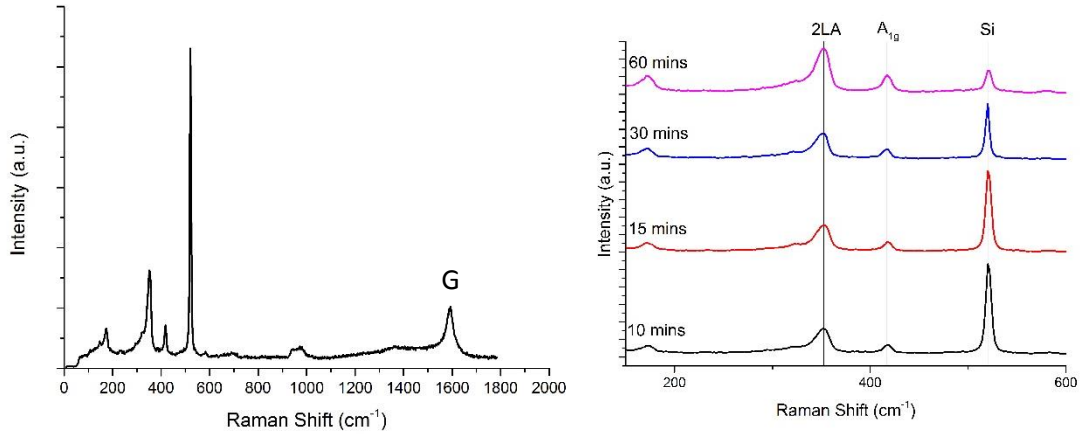

Figure 3.17 Raman spectra of WS_2 on graphene grown for 10 mins displaying WS_2 peaks and graphene G peak (left) and WS_2 and silicon peaks for growth times of 10 – 60 mins.

As discussed in the background section of this chapter, the 2LA peak in particular can experience a shift in wavenumber when the number of layers in the WS_2 film approach 1. The film that was deposited for 10 mins does display an up shift of 2 cm^{-1} from 353 to 351 cm^{-1} for the LA peak compared to all the other depositions. This is in line with the finding of Mauricio Terrones et. al. who show that from bulk as the number of layers is decreased to the limit of 3, there is a decrease in Raman shift of the LA peak. [41] However, this goes against the claims of Goki et. al. who report that for 3,4,and 5 layers, the LA peak it at a higher wavenumber than for bulk WS_2.[42] Figure 3.18 shows how the separate groups reported the 2LA mode shifts with varying number of layers. For the films deposited in this piece of work, no shift was observed in the $A1_g$ peak, where it occurred at 417 cm^{-1} for all deposition times.

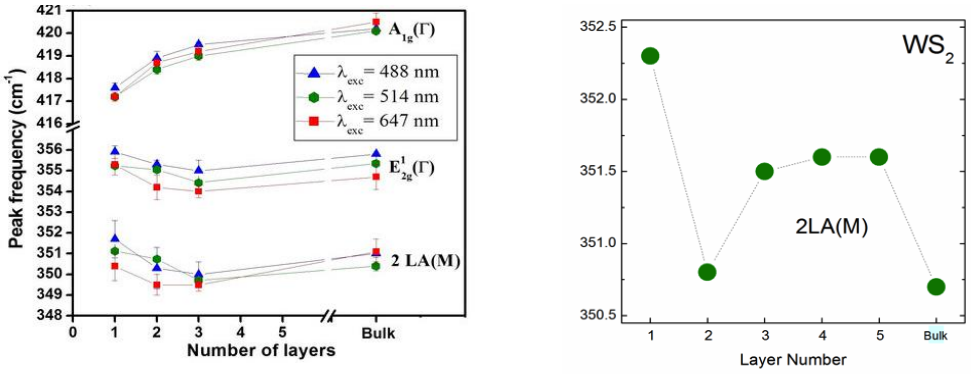

Figure 3.17 Two different reports of how the 2LA mode shifts with varying number of layers. Data on the right obtained using a 532 nm laser. Reproduced from ref 41 (left) and 42 (right).

Although it seems a finite size effect is occurring for the thinnest film, the shifts in the spectra do not shed light on its exact thickness. Reasons for this include, unlike the reports mentioned, the WS_2 films discussed here are continuous, and are not necessarily the same height over the diameter of the laser spot being used in these measurements (ca. 1 µm), there may also be many crystal domains over the scale of the laser spot. The degree of doping from residual oxygen could be different, since even reported single crystals of WS_2 have local variations in doping, defects and strain.[43] Additionally unlike the reports the WS_2 films are grown on a layer of graphene which may influence the Raman results.[44]

Figure 3.18 shows Raman spectra of the films over the range where the key graphene peaks appear. The spectra show the graphene has maintained its mixture of monolayer and bilayer structure and the process does not seem to have introduced defects. However, it can be seen that the process has introduced amorphous carbon into the films which is evident from the growth of the broad peak at 1200-1400 cm^{-1} with increasing deposition time, in line with the Raman results for the films deposited on glass and silicon.

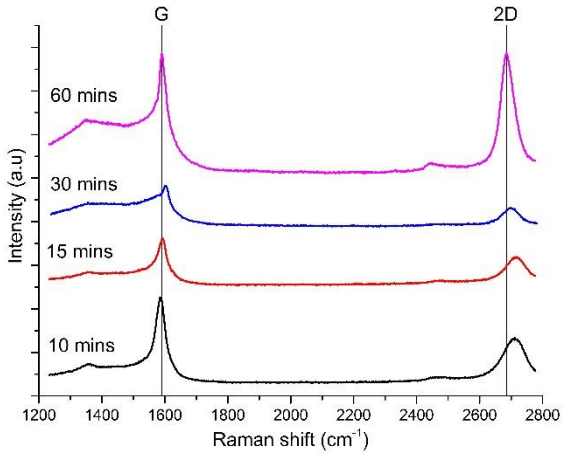

Figure 3.18 Graphene Raman spectra for WS_2 growth times of 10-60 mins.

3.3.3 Analysis of WS_2 on graphene - Optical

Raman analysis of the films also showed that WS_2 films grown at 400 °C selectively grew on graphene for deposition times under 1 h. Figure 3.19 shows optical images of interfaces between the WS_2-graphene film and the SiO_2 substrate for films grown for different lengths of time. The left hand image shows a film grown for 30 minutes. It can be seen there is no deposition in the areas free of graphene. The right hand image shows a WS_2-graphene after an hour of deposition. It can be seen the majority of the WS_2 growth has still occurred on the graphene however a small amount of growth has occurred on the SiO_2 substrate.

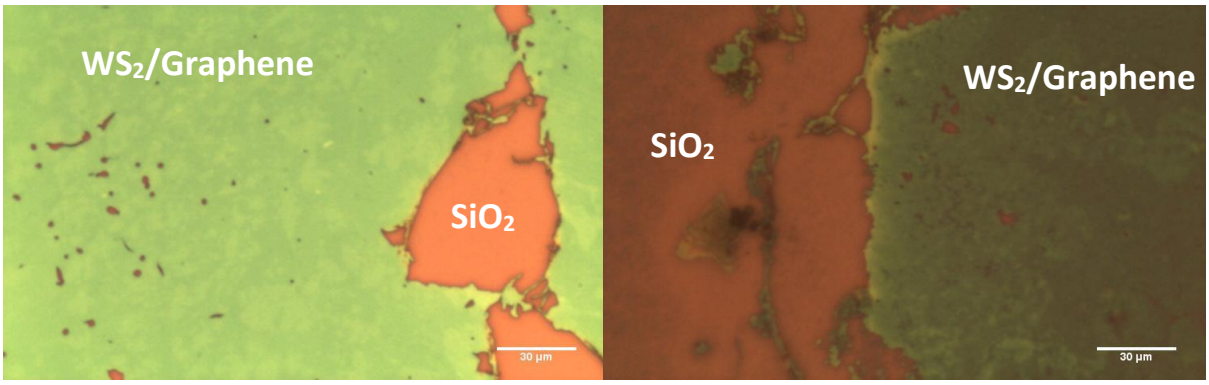

Figure 3.19 Optical images of WS_2 grown on graphene for 30 mins (left) and 60 mins (right) bare SiO_2 is in orange.

To further confirm the greatly increased growth on graphene at 400 °C, a Raman map was taken, shown in figure 3.20. The coverage of the graphene and the WS_2 film is uniform with both closely matching the film that can be seen optically. Defects from the transfer process at the edge of the graphene sheet are also observable. Here it is likely that the graphene and polymer are heavily wrinkled which could limit WS_2 film growth. The change in intensity at the top of the maps is likely due to laser focusing issues, as slight variations in substrate height are picked up over such large maps.

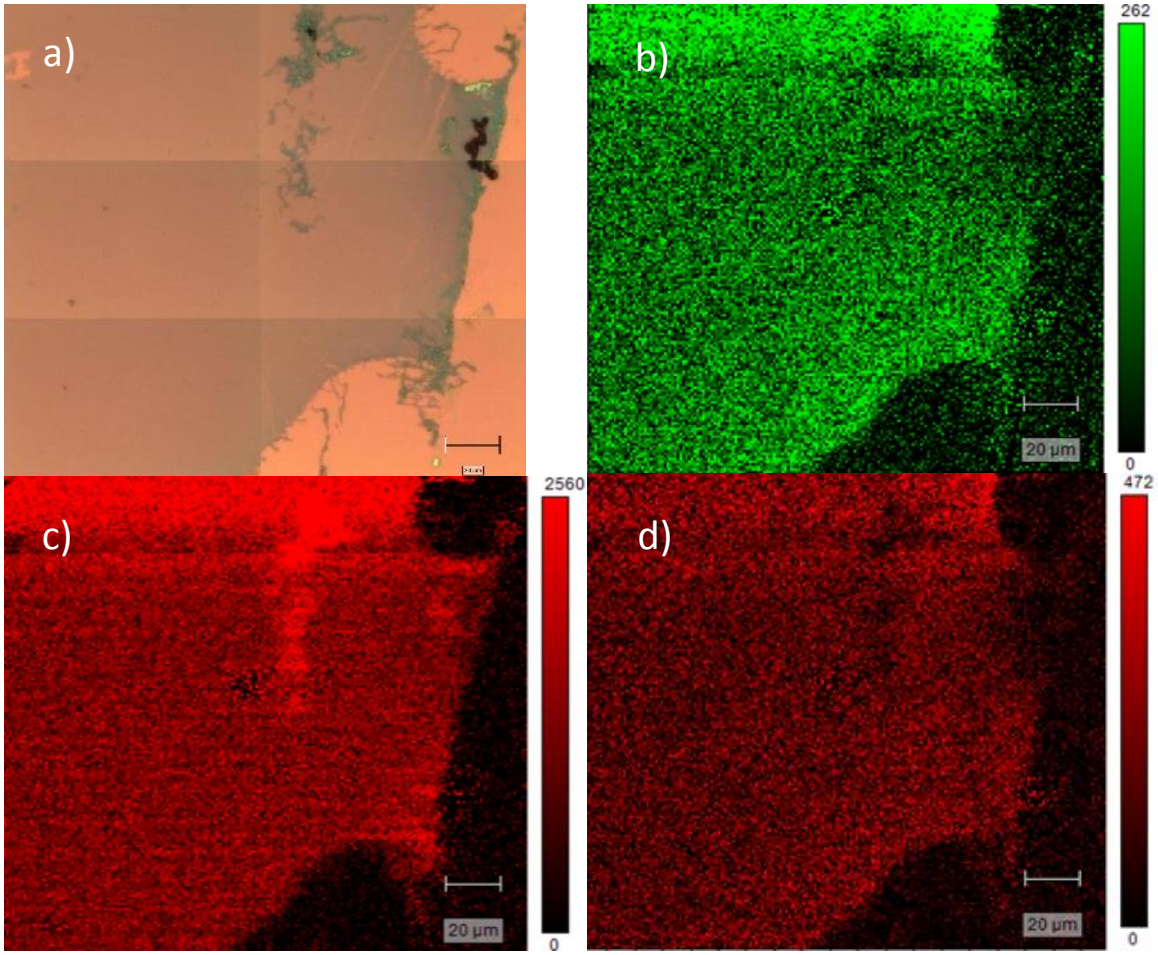

Figure 3.20 a) Optical map. **b)** Intensity of the 2LA WS_2 Raman peak. **c)** Intensity of G graphene Raman peak. **d)** Intensity of the D graphene Raman peak.

If the growth temperature was increased to 450 °C, it could be seen that WS_2 grows well on SiO_2 as well as graphene. This is in line with the results from the study of WS_2 growth on glass and silicon, where at 450 °C WS_2 grew on both. Figure 3.21 shows this in an optical image.

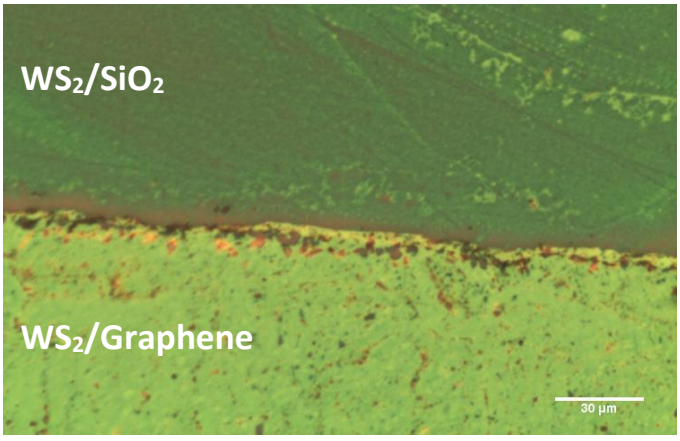

Figure 3.21 Optical image of WS_2 grown on graphene for 30 mins at 450 °C.

3.3.4 Analysis of WS_2 on graphene - SEM

SEM images were taken to further analyse the WS_2-graphene films. It can immediately be seen that the films have far fewer features then those deposited onto glass and silicon. Figure 3.22 shows SEM images for the deposition run for 60 mins. Features in the graphene substrate are in fact more obvious than the WS_2 component of the film. The lighter patches were believed to be thicker patches of WS_2. Later AFM analysis revealed them to be more continuous, flatter areas.

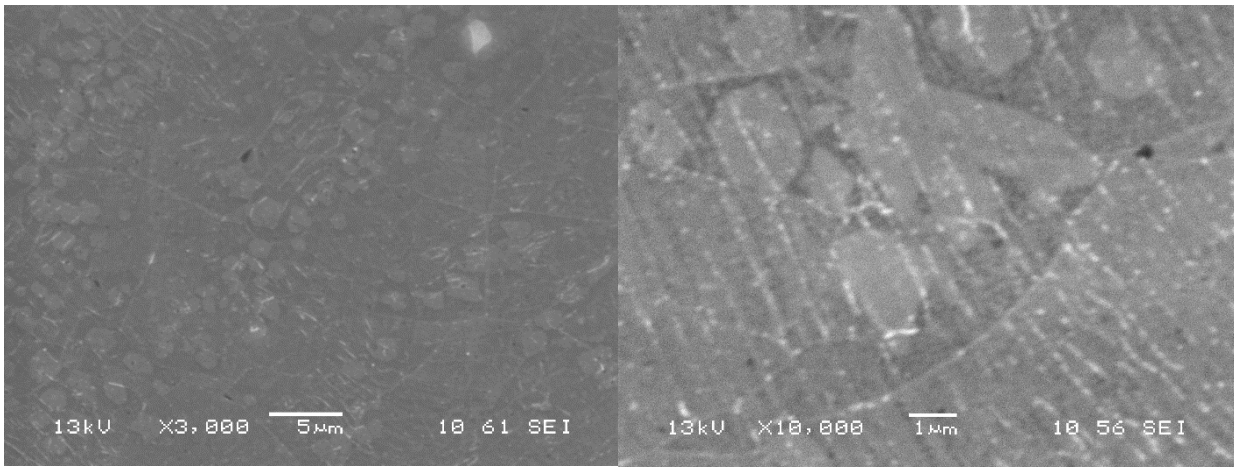

Figure 3.22 SEM images of WS_2 grown on graphene for 60 mins.

Figure 3.23 shows SEM images for a film deposited in 30 mins. Again the WS_2 film appears featureless, with the graphene substrate providing any structure. Wrinkles can again be seen, with some nanoparticles also visible, and these are believed to be impurities from the copper, as discussed in chapter 2.

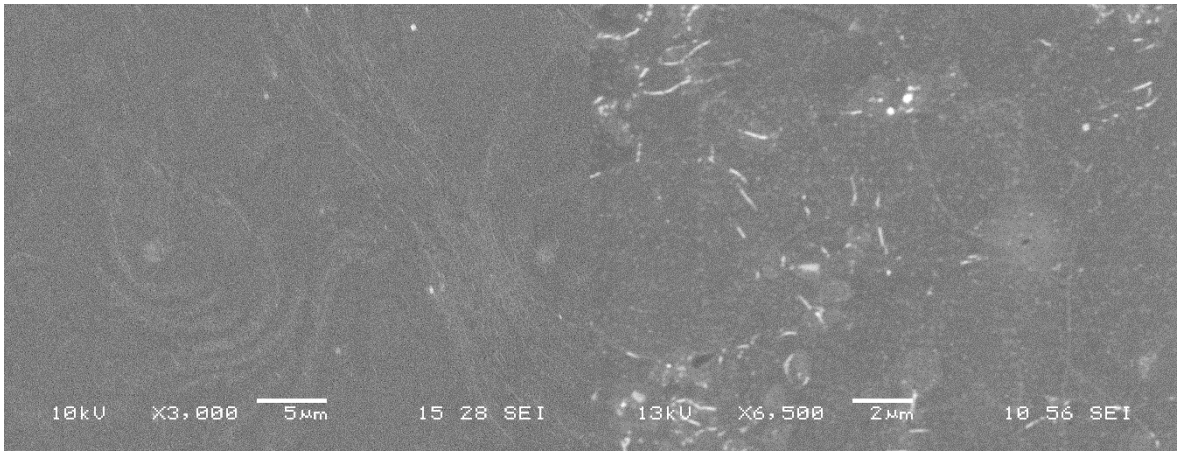

Figure 3.23 SEM images of WS_2 grown on graphene for 30 mins.

Figure 3.24 shows SEM images for films grown in 15 and 10 mins. More nanoparticles can be seen for 15 mins than for 30 mins, this is believed to be because as the films are thinner the nanoparticles, which most likely are copper impurities, become more visible on the graphene substrate. As well as this, the usual features such as wrinkles from the graphene substrate can be seen. Films grown over 10 mins look similar in SEM images as those grown at 15, with the features already mentioned present. One main difference is the greater occurrence of areas like those circled in red in figure 3.24. These are areas of the film where WS_2 coverage seems to be incomplete as graphene is still present. For 10 mins of deposition, the wrinkles in graphene can still be seen without the darker layers of WS_2 on top.

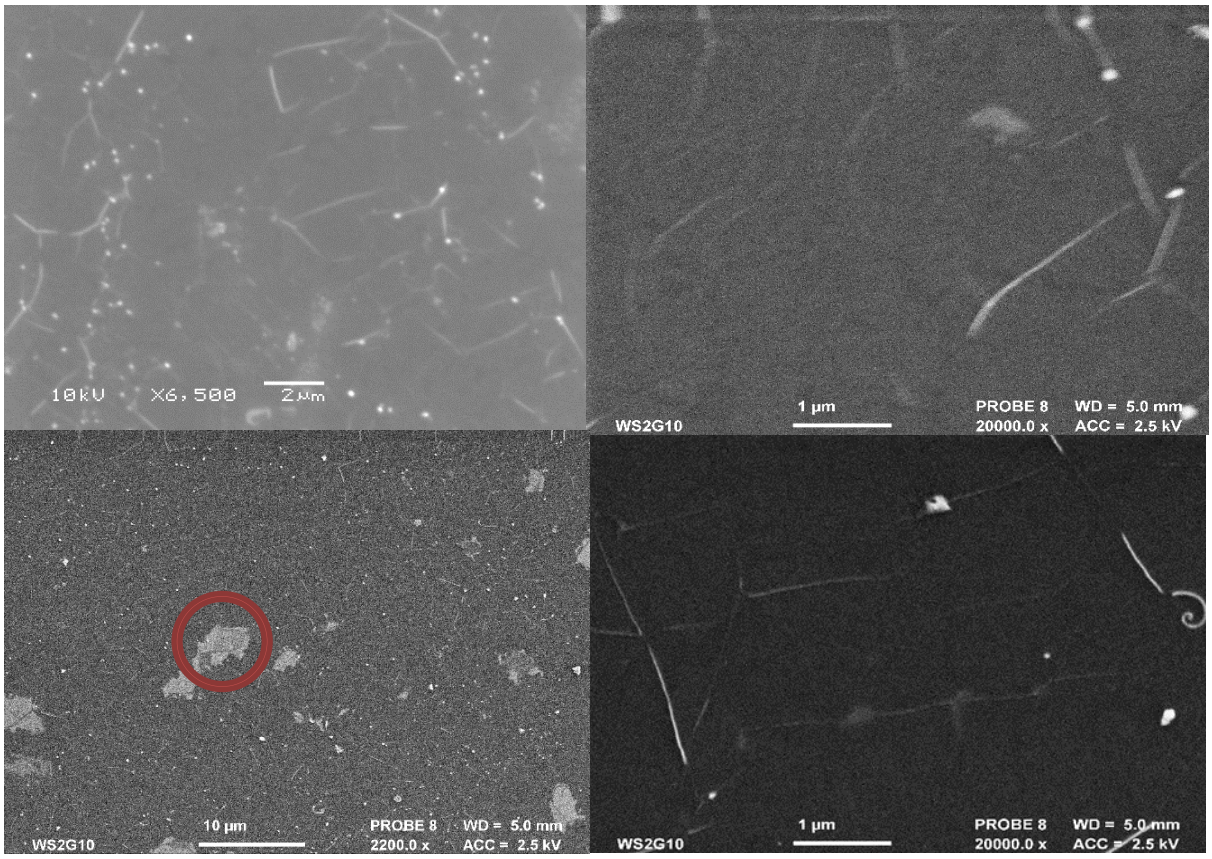

Figure 3.24 SEM images of WS_2 grown on graphene for 15 mins (top) and 10 mins (bottom). Red circle highlights area of incomplete WS_2 coverage.

Figure 3.25 shows in greater detail a variety of features present in the deposited films. The top left picture shows a tear in the graphene substrate, revealing bare SiO_2 underneath where no WS_2 has grown. The top right image shows a mixture of a graphene tear with some WS_2 delamination. A pre-exisiting tear can be seen however areas of bare graphene around the edges of the tear are visible, where the WS_2 film has peeled back. As the WS_2 films are not chemically bound to the graphene, it is understandable that there will be a degree of delamination from the graphene substrate. The bottom left image shows an area of either incomplete WS_2 film growth or WS_2 delamination. The wrinkles in the graphene are clearly visible continuing from the darker patch of WS_2 across to where only graphene is present. The final image shows and area where the WS_2 film is not present on the graphene surface. It is interesting to note that the WS_2 film often leaves straight edges with clearly defined angles. The final image also shows there are many areas, which appear completely featureless, especially at low magnifications.

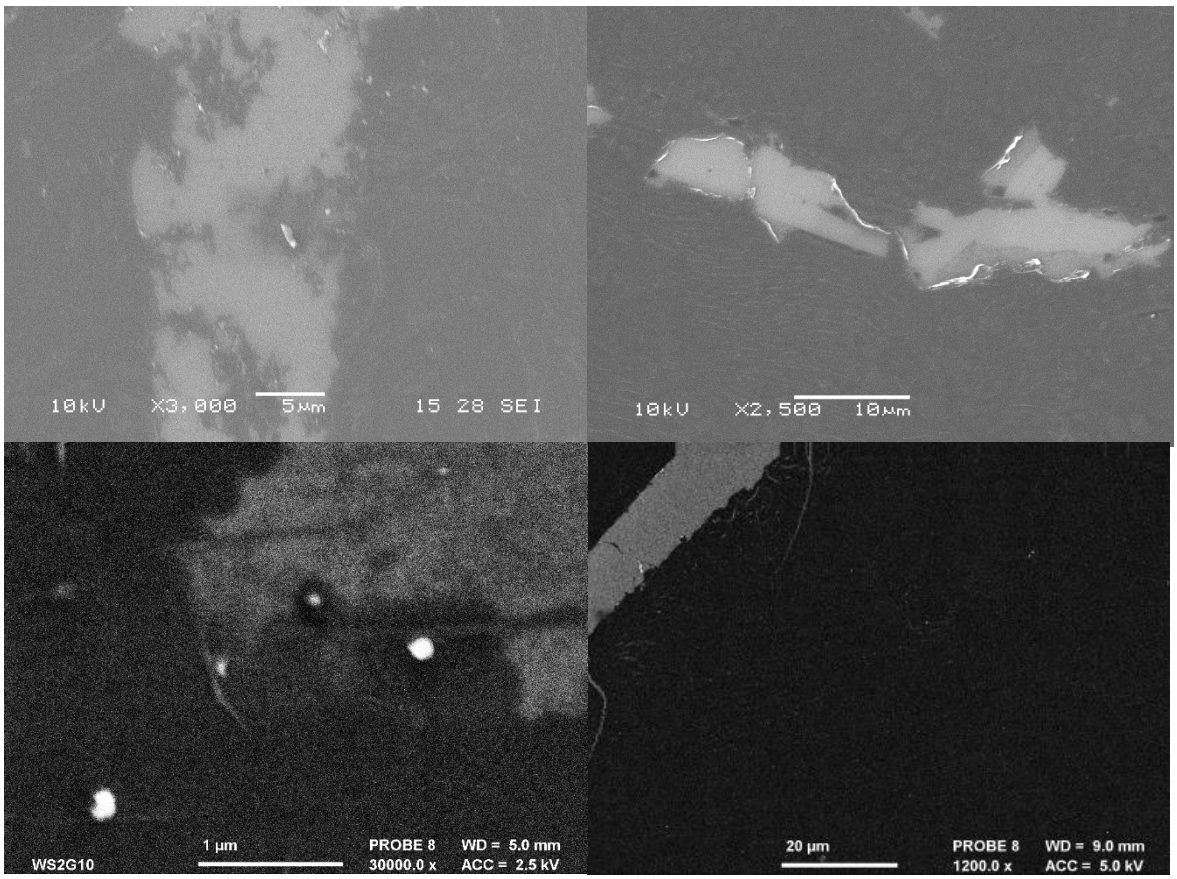

Figure 3.25 SEM images of WS_2 grown on graphene for 10 mins, displaying a variety of features present in the deposited films.

3.3.5 Analysis of WS_2 on graphene - EDS

Meaningful data could only be collected for the WS_2 film grown for 60 mins where tungsten and sulphur were found in the correct ratios. The presence of oxygen could not be determined due to the underlying SiO_2 substrate. All the other films were too thin, so that a large signal from the underlying substrates dominated the spectra.

3.3.6 Analysis of WS_2 on graphene - AFM

The topography of the films was further analysed by AFM. Additionally, film thickness measurements could be carried out using gaps or scratches in the WS_2 films. It was ensured that RMS values were not recorded over areas of bare SiO_2.

An AFM image and film thickness measurement for the WS_2-graphene film grown for 60 mins is shown in figure 3.26.The AFM reveals similar features as those found through SEM analysis. It was found the film did have some surface texture, although it was still far flatter than those grown on glass or silicon. Features from the underlying graphene substrate are still visible and the wrinkles form the highest points of the film. The smoother patches were found to be the same height as the rest of the film by line profile analysis.

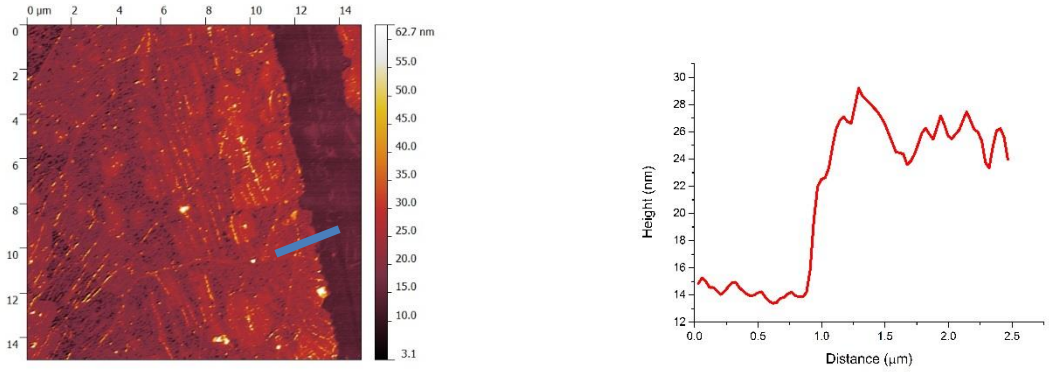

RMS: 2.6 nm

Figure 3.26 AFM image and step height of WS_2 film on graphene grown for 60 mins. The blue bar shows where step height was taken.

An AFM image and step height of the film grown for 30 mins is shown in Figure 3.27. Surface texture is still present, however it is sparser than in the film grown for 60 mins. The RMS of the film also is slightly lower, indicating a flatter film. It is also interesting to note many of the cracks in the film produce geometries with internal angles measured to equal 120 °. Some of these have been highlighted in the figure. These geometries are understandable, as WS_2 has a hexagonal structure and the film is likely to fault along planes related to this.

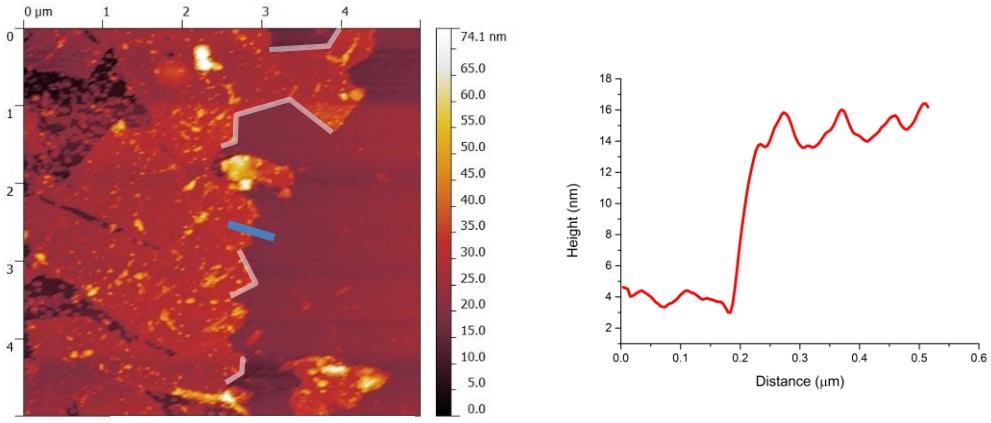

RMS: 2.2 nm

Figure 3.27 AFM image and step height of WS_2 film on graphene grown for 30 mins. The blue bar shows where step height was taken. White bars highlight internal angles of 120 °.

An AFM and step profile of the film grown over 15 mins is shown in figure 3.28. It can be seen the film is far less textured than the previous two, resulting in a lower RMS value. It must be noted this RMS value was taken over areas not including wrinkles, as these dominated the height profile thus heavily affected the resulting RMS values. As the AFM image displayed shows a scratch rather than a crack in the film, fewer hexagonal geometries can be seen.

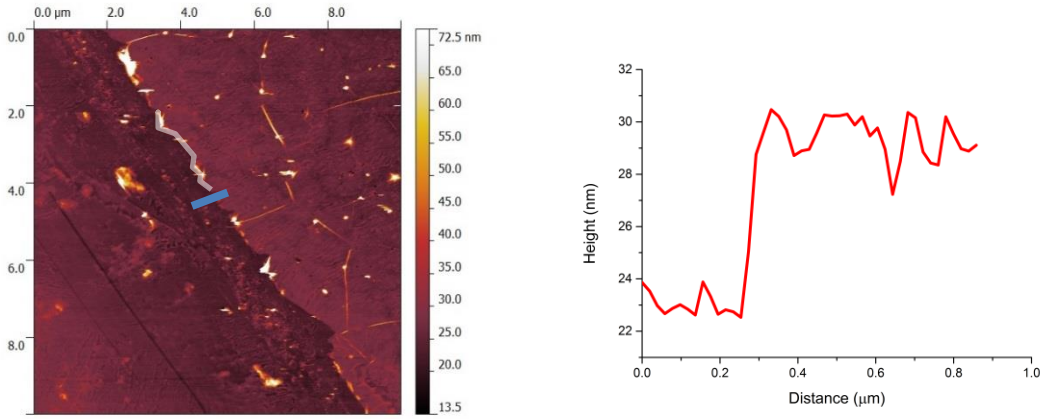

RMS: 0.8 nm

Figure 3.28 AFM image and step height of WS_2 film on graphene grown for 15 mins. The blue bar shows where step height was taken. White bars highlight internal angles of 120 °.

An AFM and step profile of the film grown over 10 mins is shown in figure 3.29. The film is topgraphically very similar to the film grown over 15 mins, featuring the same RMS value. Hexagonal features can again be seen. In the AFM image in the figure, it is easy to see the underlying graphene film where the film has not grown over or delaminated, with wrinkles in the graphene continuing from the WS_2- graphene section to purely graphene.

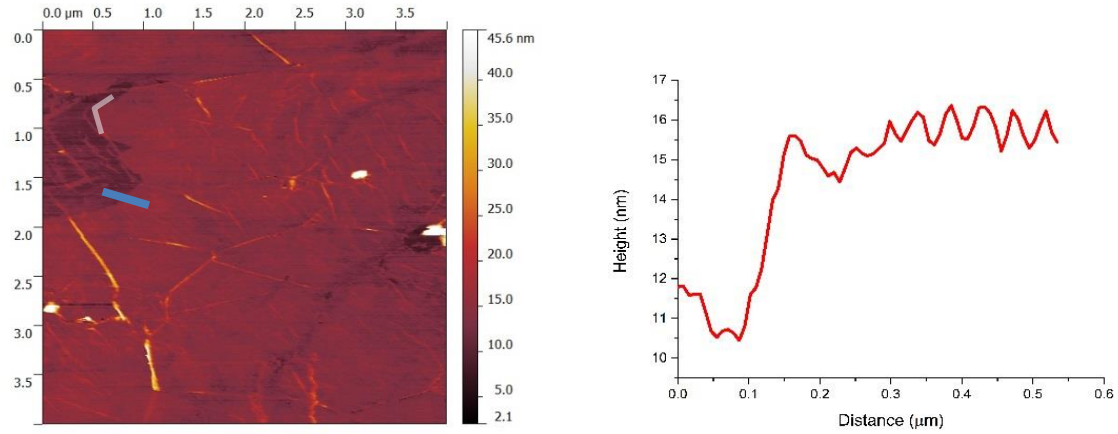

RMS: 0.8 nm

Figure 3.29 AFM image and step height of WS_2 film on graphene grown for 10 mins. The blue bar shows where step height was taken. White bars highlight internal angles of 120 °.

A comparison between the step heights found via AFM and the crystallite thickness found by PXRD is shown in figure 3.30 which are found to be in good agreement. This indicates the films are well ordered parallel to the substrate, with little misalignment between the WS_2 layers. The crystallite thicknesses and step heights are displayed in table 3.3

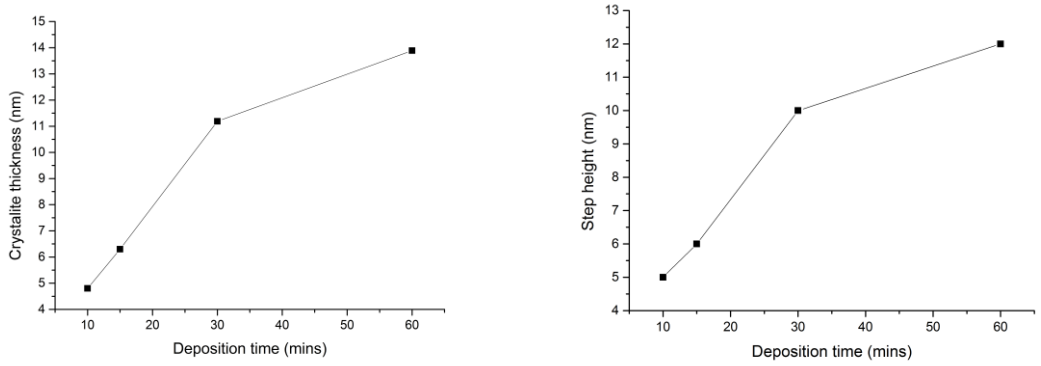

Figure 3.30 Comparison between the step heights found via AFM (left) and the crystallite thickness found by PXRD (right).

Table 3.3 Crystallite thicknesses and step heights of WS_2 grown on graphene over different deposition times.

Deposition time (mins)	Crystallite thickness (nm)	Step height (nm)
10	4.8	5
15	6.3	6
30	11.2	10
60	13.9	12

Overall, AFM results highlight the greatest differences between the WS_2 films grown on glass and silicon and those grown on graphene. WS_2-graphene films are far flatter and it is possibe to grow very thin films. This level of morphological control and the growth of such thin films has never before been achieved by AA-CVD.

3.4 Results and discussion – High temperature CVD of WS_2

As the preceeding section has shown, depositing WS_2 onto graphene via AA-CVD drastically changes the morphology of the resulting WS_2 films. In addition the change to F-M layer by layer growth allowed very thin WS_2 films to be grown. Even so, it did not seem possible to produce WS_2 monolayers by this technique as the thinnest films achieved were 5 nm, or 5 layers, thick.

In the last five years, after it was shown monolayers of graphene could be grown by high temperature CVD, the question has been asked whether other ultra-thin materials can also be grown by this method. This has lead to a large focus by the scientific community on graphene-like materials, such as TMDs.

WS_2 is one of the materials that is being studied. Quickly following on from the related TMD, MoS_2, the first example of monolayer WS_2 via CVD at high temperatures was reported in 2013.[45] [9]

Therefore, the question was asked whether a continuous monolayer WS_2 film could be deposited onto sheet of CVD grown graphene, via a high temperature CVD route? This had not been attempted before.

Synthesis of monolayer TMDs has been notoriously difficult to repeat across different reactor types and conditions, therefore before WS_2 could be grown on graphene, CVD of monolayer WS_2 on SiO_2 had to be achieved. The reactor designed for CVD graphene growth discussed in chapter 2 was used with a few minor modifications to carry out the high temperature CVD studies. A diagram of the modified reactor is shown in figure 3.31.

To try and emulate as closely as possible successful reported growth conditions, the changes to the reactor were:

- The use of Ar as a carrier gas
- The reactor switched to running at atmospheric pressure.
- The second heating zone moved from the liquid precursor pot to adjacent to the furnace on the quartz tube

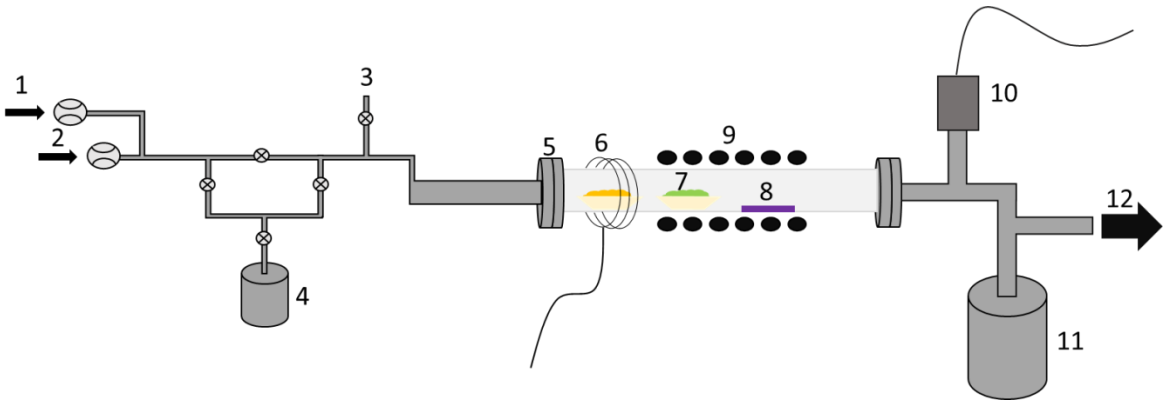

Figure 3.31 Diagram of reactor used for high temperature CVD of WS_2. The numbers in the diagram correspond to- 1: Now provides a flow of Ar to act as a carrier gas. 2: Not used. 3: Not used. 4: Not used 5: Ultra-Torr fitting to 1 " quartz tube. 6: Heating tape around the position where an alumina boat containing elemental sulphur sits. 7: Alumina boat containing WO_3 powder. 8: SiO_2 wafer. 9: Furnace. 10: Pressure sensor. 11: Liquid N_2 trap (not used) 12: To extraction/pump.

The position of the SiO_2 substrate with respect to the WO_3 source varies in different publications. Yu et al. place the wafer physically on top of the WO_3 source,[46] whereas Warner et al. place it downstream.[47] For this study it was decided that the SiO_2 wafer would be consistently placed 5cm downstream from the WO_3 source. Additionally the position of the sulphur source varies between publications. Some report it being placed just within the furnace,[48] others have a separate heating zone.[9] A separate heating zone was chosen to increase the control over the sulfur atmosphere.

3.4.1 Growth mechanisms

The growth mechanism of WS_2 on SiO_2 substrates from WO_3 and sulphur by CVD is not yet well understood. It is known WO_3 decomposes to WS_2 via a reactive oxy-sulphur intermediate, not by the direct reduction of WS_3.[49,50] Yu et al. proposed a reaction mechanism from the sulphurisation of pre-deposited WO_3 particles.[51] They suggest firstly, flakes of WO_xS_{2-x} were formed. Further sulfurisation produces thick WS_{2+x} flakes with a mixture of W_{IV} and W_{VI}, whereupon monolayer WS_2 forms in the middle of the flake and expands outwards. Evidence for this reaction mechanism is shown in figure 3.32.

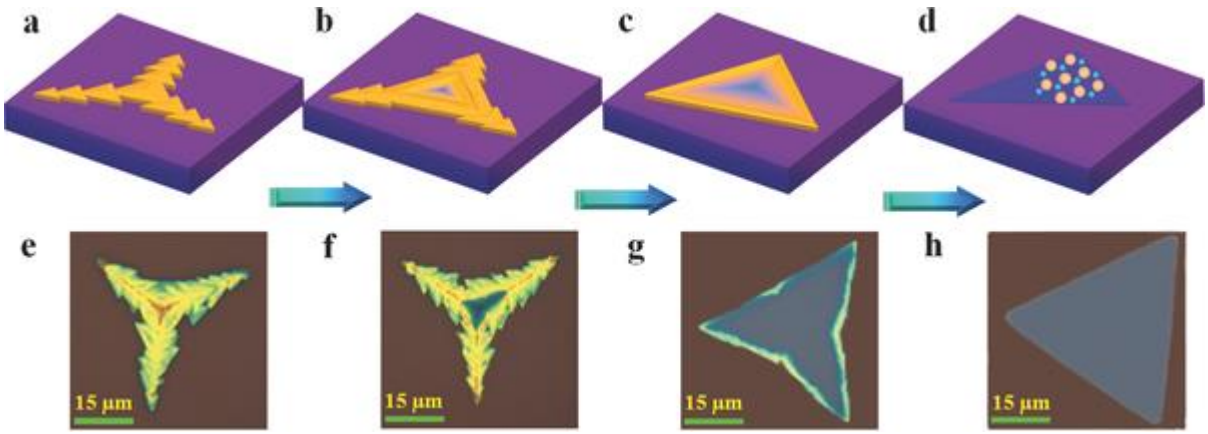

Figure 3.32 Proposed growth mechanism of monolayer CVD WS_2 by Yu et al. Reproduced from ref 51.

However, Shaijumon et al. have found, for pre deposited WO_3, the concentration of initial WO_3 on the substrate determined how WS_2 flakes grow, with monolayers growing from a usually thicker centre.[52] Higher concentrations tend to form stacked or spiral WS_2 flakes. Figure 3.33 shows evidence of these different growth mechanisms.

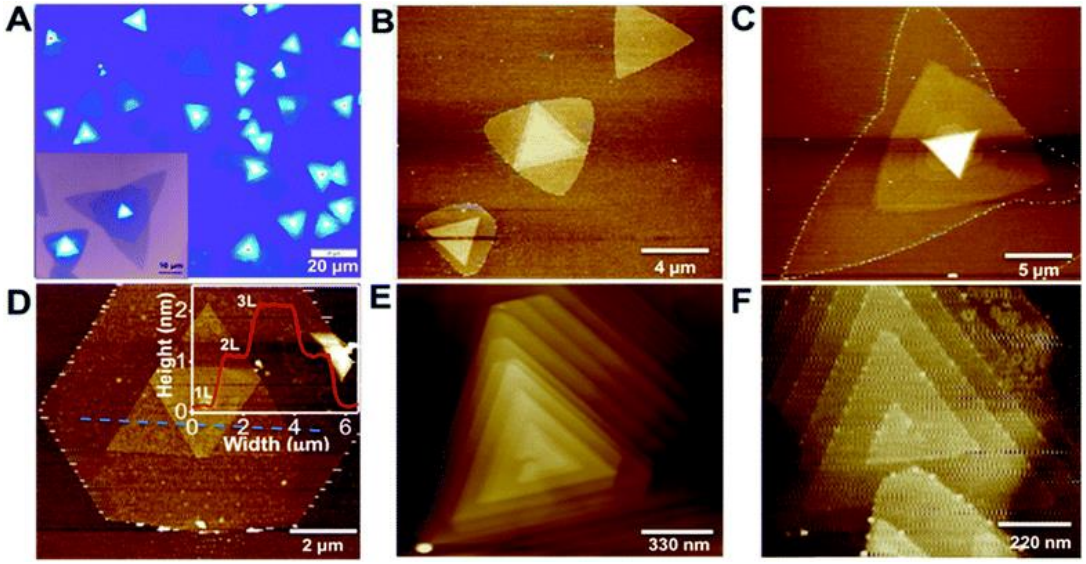

Figure 3.33 Various WS_2 flakes grown by Shaijumon et al.[52]

The growth mechanism becomes even harder to discuss in experiments which involve WO_3 and sulphur simultaneously being deposited onto a substrate. In this case it is generally agreed that it is not WS_2 that is volatilised, but rather WO_3 or an oxy-sulphur species.[53] This species undergoes sulphurisation on the subatrate. A complication is that as well as sulphur reducing WO_3 to WS_2 within the alumina boat, which decreases the volatilisation of WO_3, a sulphur atmosphere is required to form WS_2 on the substrate. So on the one hand, a higher concentration of sulphur slows down deposition, by reducing the WO_3 depostion rate, but on the other speeds it up by sulphurising the WO_3 species on the substrate faster.

3.4.2 Growth parameters

As discussed above, the concentration of the sulphur atmosphere and the time at which it is introduced is very influential on how WS_2 is going to grow. The temperature of the main furnace will also influence the rate of WO_3 and oxy-sulphur deposition as well as its subsequent growth on the substrate. Finally, the carrier gas flow will influence not only the sulphur atmosphere concentration, but residency time of precursor species on the SiO_2, affecting crystal growth.

To find the reactor specific conditions required to produce monolayer WS_2 crystals, these parameters were varied one by one.

3.4.3 Depositions of WS_2 onto SiO_2 by high temperature CVD

Depositions were carried out using the reactor shown in figure 3.31. Before each run, the system was pumped down to ca. $2x10^{-2}$ mbar and held for 30 mins. The system was then flushed with 500 ccm of Ar for 30 mins to ensure residual water and oxygen were removed from the system. To ensure sulphur was not introduced too early, the furnace was initially heated to 600 ^oC and held at that temperature for 10 mins before the furnace was heated up further and the heating tape around the sulphur was heated. The intitial conditions picked matched as closely as possible those reported by Warner et. al. who used a similar experimental setup.[54] The heating tapes were set at 180 ^oC, Ar flow rate at 100 ccm, main furnace temperature of 1070 ^oC and the alumina boats contained 1g of sulphur in the first and 1g WO_3 powder in the second. When the furnace was at 1070 ^oC, it was held at that temperature for 30 mins, after which the heating tapes were turned off and the furnace was allowed to naturally cool to room temperature. The first parameter to be varied was the concentration of sulphur atmosphere.

3.4.4 Varying the sulphur atmosphere

The sulphur atmosphere was varied by changing the temperature of the heating tapes. At tape temperatures below 150 ^oC, only oxide particles could be found on the SiO_2 substrate. Their presence was confirmed by Raman spectroscopy.

At tape temperatures of 150 ^oC, sufficient sulphur is volatilised to produce a mixture of WS_2 and WO_3 particles. There is also a small number of triangular shaped WS_2 particles with a few appearing to be very thin. Figure 3.34 shows optical images of films grown with tape temperatures of 150 ^oC, with triangular WS_2 particles circled in red.

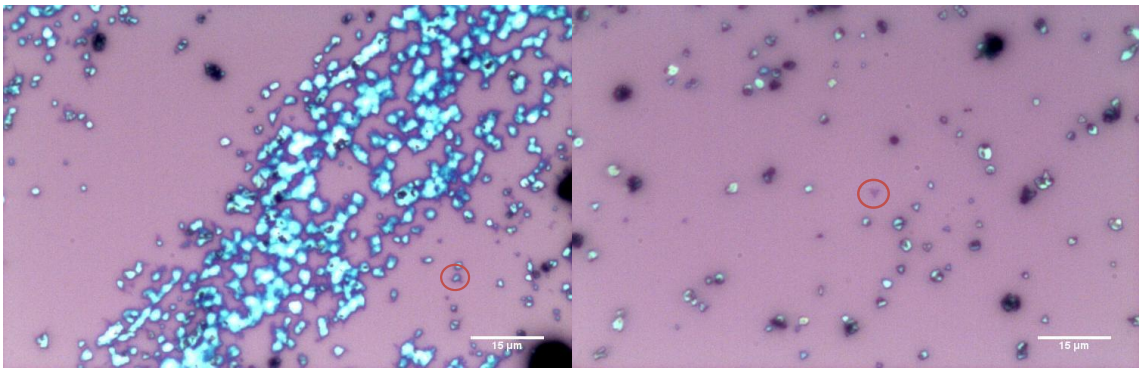

Figure 3.34 Optical images of mixtures of WS_2 and WO_3 particles with heating tape temperatures below 150 ^oC a few small triangular domains are present, circled in red.

At tape temperatures of 200 ^oC, a mixture of materials grows. Furthest downstream on the SiO_2 wafer, a very well defined architecture of nanowires is produced. These are similar in structure to those produced by Warner et. al., where they see nanowires being formed when sulphur is introduced too late into their system.[54] Figure 3.36 shows these nano wires and the ones produced in this study. Warner et. al claim they are WS_2 nanowires, although the nanowires produced in this study create no clear Raman peaks associated with WS_2. However the (002) peak was present in PXRD, where Scherrer analysis produced crystal thicknesses of 23 nm. AFM analysis gave thicknesses ranging from 12 to 80 nm with the vast majority of wires 12 nm thick. It is proposed the wires are a mixture of WS_2 and tungsten oxysulphur species, where an increased sulphur atmosphere promotes their growth on the hottest part of the substrate.

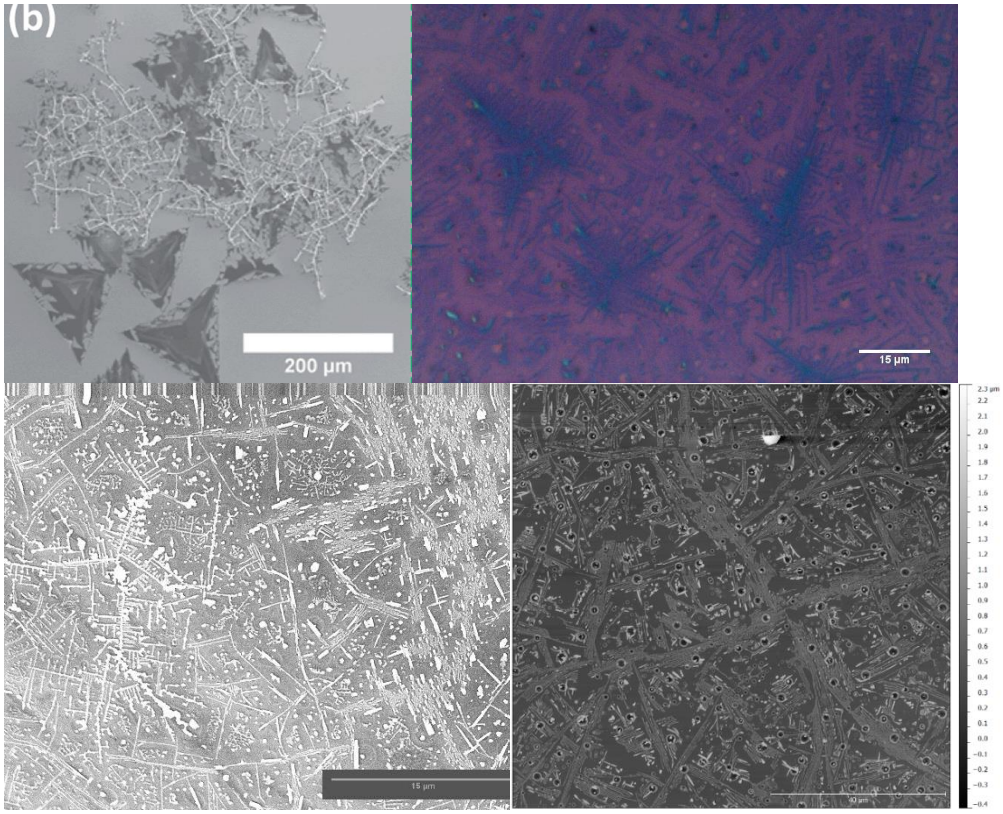

Figure 3.35 Top left, SEM image of nanowires produced by Warner et al. Top right, bottom left and bottom right: optical, SEM and AFM images respectively of nanowires produced in the study.

Further along the substrate, where temperatures are marginally cooler, the growth of WS_2 films can be observed, seeded from WO_3 particles. The edges of the films, although appearing to have some triangular structure and very thin, are not as regular as single crystal WS_2 previously reported. Additionally AFM analysis indicates the films range in the number of layers. Figure 3.37 displays optical images of the triangular structures seeded from WO_3 particles. Although close to the triangular crystals desired, at these reaction conditions WS_2 growth in 2 dimensions lacks control.

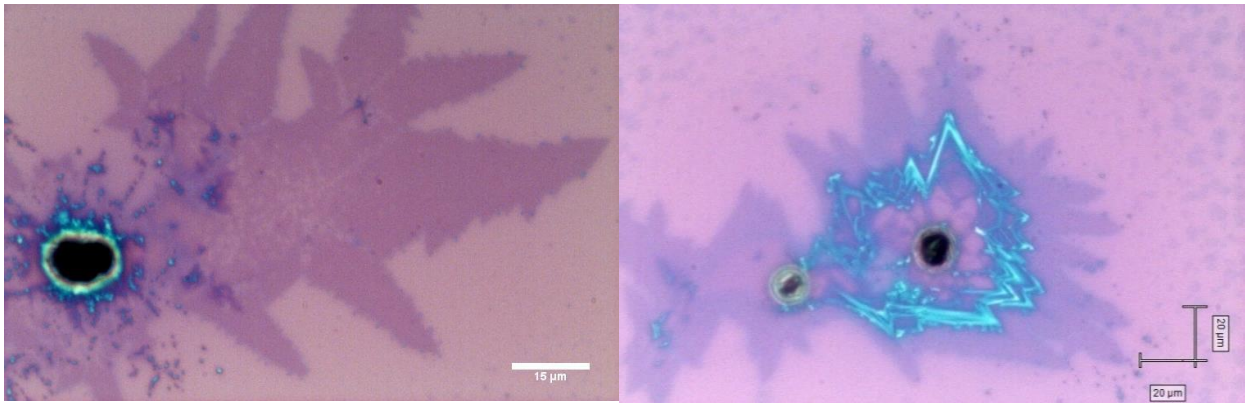

Figure 3.36 Optical images of thin WS_2 films growing from WO_3 particles.

If the tape temperature is increased even further to 300 °C, rapid deposition of thick, relatively uniform films of WS_2 are formed, decreasing in thickness on the down stream and thus hotter end of the substrate. Figure 3.37 shows an optical image of the deposited film. WO_3 particles could also be observed.

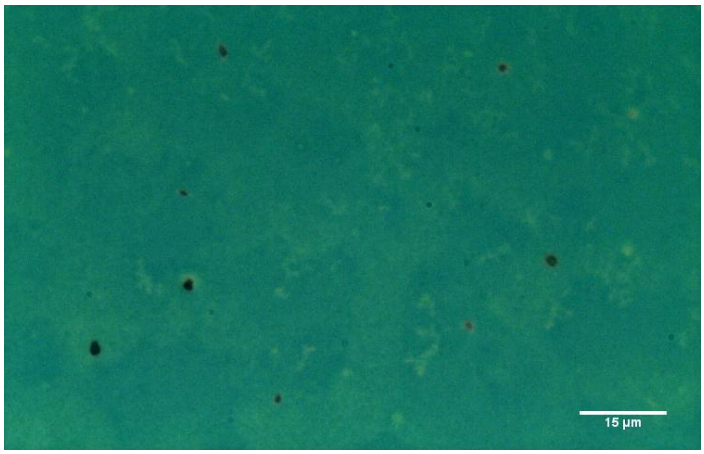

Figure 3.37 Optical image of thick WS_2 film.

3.4.5 Varying the furnace temperature

As heating tape temperatures of 200 °C produced the thinnest WS_2 films, the temperature of the furnace was decreased to 1000 °C to explore whether a potentially slower rate of deposition would increase crystal uniformity. It was found however that the film mainly consisted of 'circular' particles, that produced a Raman spectrum inconsistent with WS_2 or WO_3 and are hypothesised to be a tungsten oxy-sulphide species. It is proposed that the lower furnace temperature must decrease the volatilisation of the tungsten precursor, however not enough energy is provided to the substrate to fully transform it to WS_2. At the hottest end of the substrate, 'chunks' of another tungsten oxy-sulphide species can be observed. Figure 3.38 displays optical images of these species, whilst figure 3.39 displays Raman spectra of them. Not all the Raman peaks could be matched with those found in the literature. Table 3.4 gives values of the Raman peaks found for the particles, with peaks published for oxysulphide species.[55]

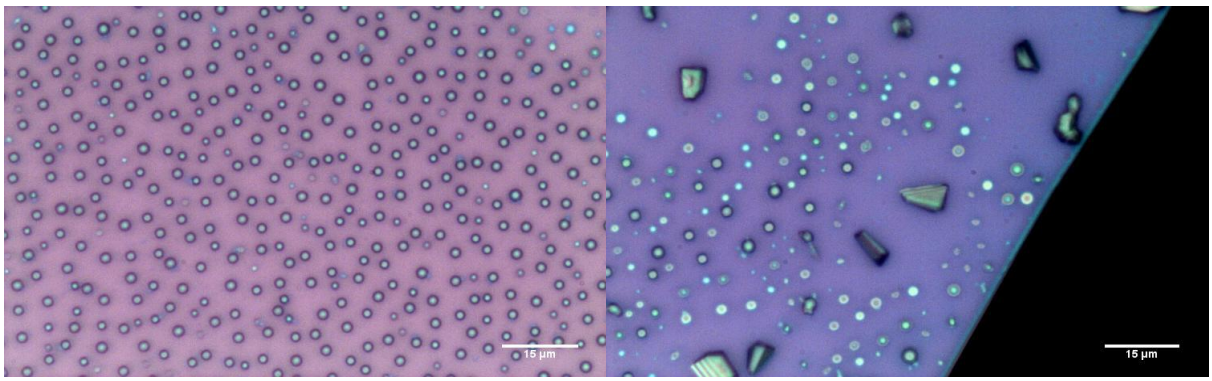

Figure 3.38 Optical images of 'circular' (left) and 'chunk' species (right), proposed to be tungsten oxy-sulphide.

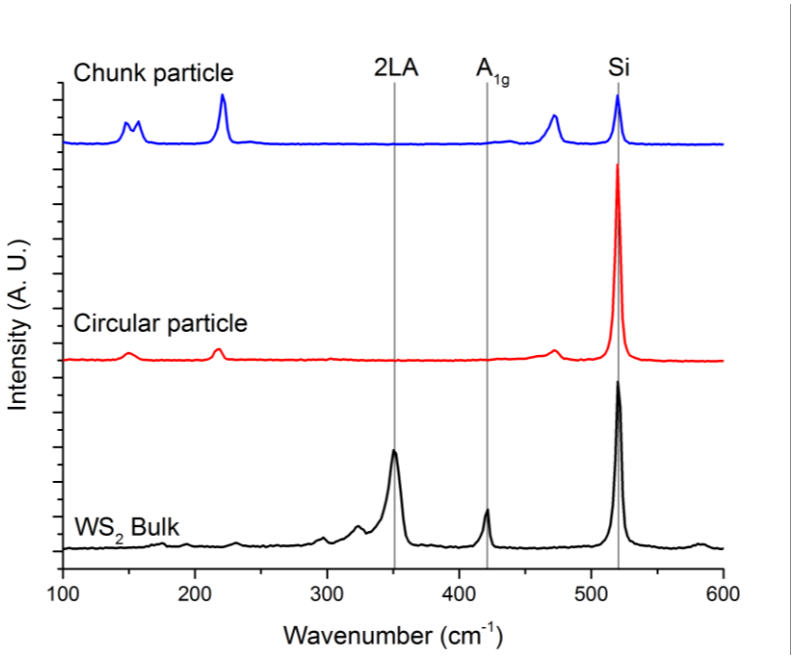

Figure 3.39 Raman spectra of the chunk, circular and WS_2 materials.

Table 2.4 Raman peak values of 'chunk' and 'circular' particles and published values of various tungsten oxy-sulphur species. Values from ref 55.

WS_2 Bulk (cm^{-1})	Spherical particle (cm^{-1})	Chunk particle (cm^{-1})	$W_3S_9^{2-}$ (cm^{-1})	W_3OS_8 (cm^{-1})	$WO_2S_2^{2-}$ (cm^{-1})	WS_3O^{2-} (cm^{-1})	WO_3S^{2-} (cm^{-1})	WS_4^{2-} (cm^{-1})
421	472	472	494			474		479
351		437	442	442	454	451	461	455
323			336	338	453		333	
296					310		315	
231					280	264		
194	217	220			235		239	
174	151	158				182		182
		147						

3.4.6 Varying the carry gas flow rate

It was found if the heating tape was set to 200 °C and the furnace to 1070 °C and the Ar carrier gas flow rate was dropped to 50 ccm from 100 ccm, WS_2 growth was drastically altered. Whereas other groups have concentrated on sulphur atmosphere and substrate heating,[47] it was found that the carrier gas flow rate was also very important. Figure 3.40 shows WS_2 crystals grown using these growth parameters. The crystals contain incomplete triangles, as seen in other reports.[56] The centre of the crystals contain thicker layers of WS_2, figure 3.40 also contains Raman spectra displaying the shift in the 2LA and the A_{1g} peaks from taking a spectrum at the edge and center of the crystals. The values of the peaks are displayed in table 2.5. Additionally, the PL spectra show the transition from an indirect to direct bandgap, shown in figure 3.40. Decreasing the gas flow rate influences two things: firstly, it increases the concentration of the sulphur and tungsten precursor atmosphere, and secondly it increases the residency time of the tungsten precursor over the substrate. This explains the results of depositions run with a carrier gas flow rate of 100 ccm discussed above, where species containing a lack of sulphur were found, and the WS_2 crystals formed seemed to have grown in a fast, uncontrolled manner.

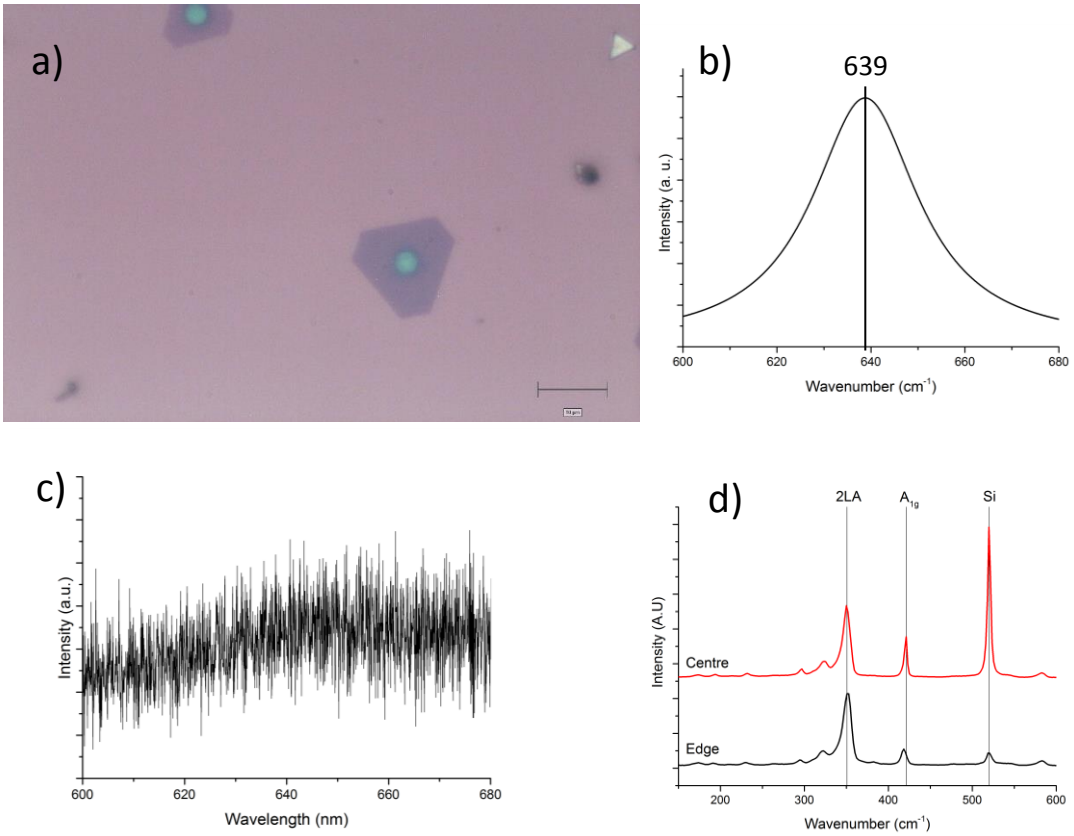

Figure 3.40 a) Optical image of incomplete WS_2 triangles. **b)** PL spectra from edge of incomplete triangle. **c)** PL spectra at centre of incomplete triangle. **d)** Raman spectra at centre and edge of incomplete triangle.

Table 3.5 Values of 2LA and A_{1g} Raman peaks for the centre and edge of incomplete triangle

Raman peak	Centre (cm^{-1})	Edge (cm^{-1})
2LA	351	353
A_{1g}	421	418

If the carrier gas flow rate is increased to 60 ccm, the majority of crystals become complete triangles, as mentioned in other reports not all the triangles are identical, some contain spiral, stacked structures, others contain thicker triangles in their centre and some appear to be comprised of only a monolayer. Example optical images and an AFM of one of these structures is shown in figure 3.41. Line profiles taken from AFM show the outer layer to be c.a. 1 nm, corresponding to a monolayer. The second triangle closer to the center corresponds to 2 layers, whilst the inner triangle is greater than 10. The AFM also reveals particles which are present after some depositions, although they seem to be localised to random areas on the substrate. This could be due to local variations in conditions within the reactor causing condensation of particles.

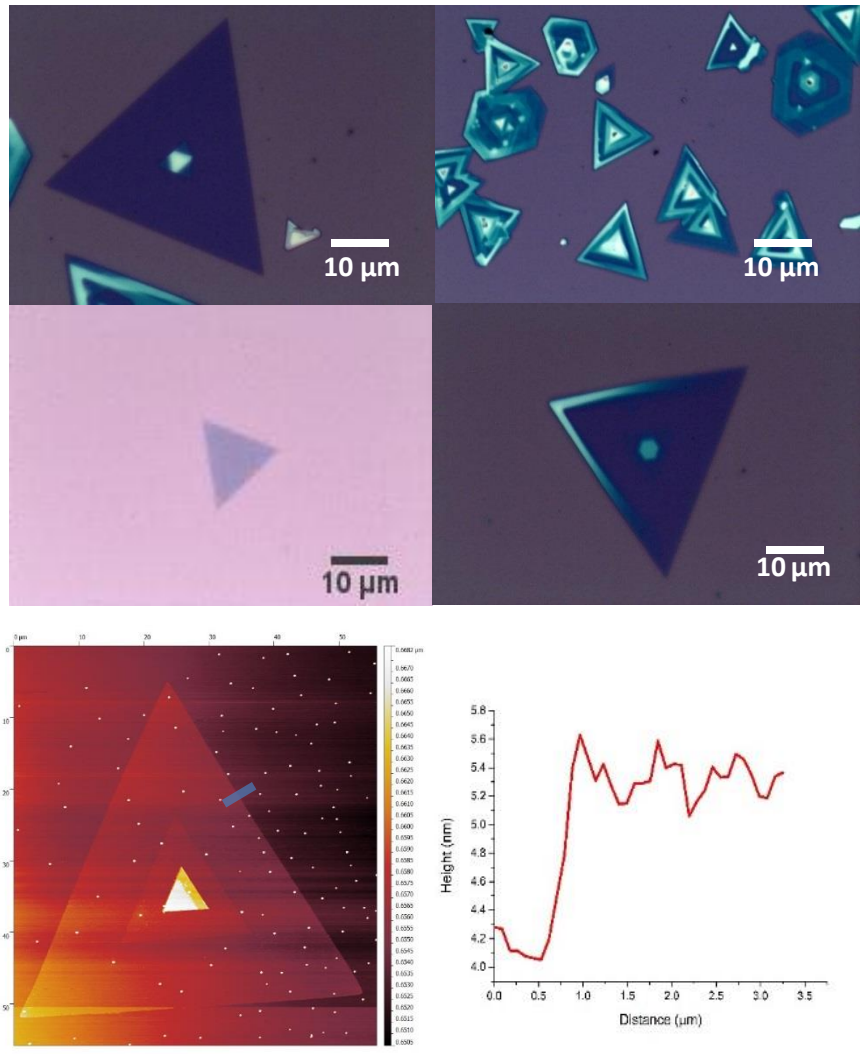

Figure 3.41 Optical images of various triangular morphologies with an AFM with step height, the blue line indicates where step height was taken from.

Figure 3.42 displays SEM images taken of various WS_2 crystals. Multilayer triangles tend to have spherical particles surrounding them, which were not observed optically. These may be smaller versions of the spherical particles found from depositions with furnace temperatures of 1000 °C. Interestingly, there seems to be a depletion zone around the triangles, pointing towards the circular species agglomerating to form them. For monolayer triangles no spherical particles can be observed indicating the rate of agglomeration is far less, leading to monolayer growth.

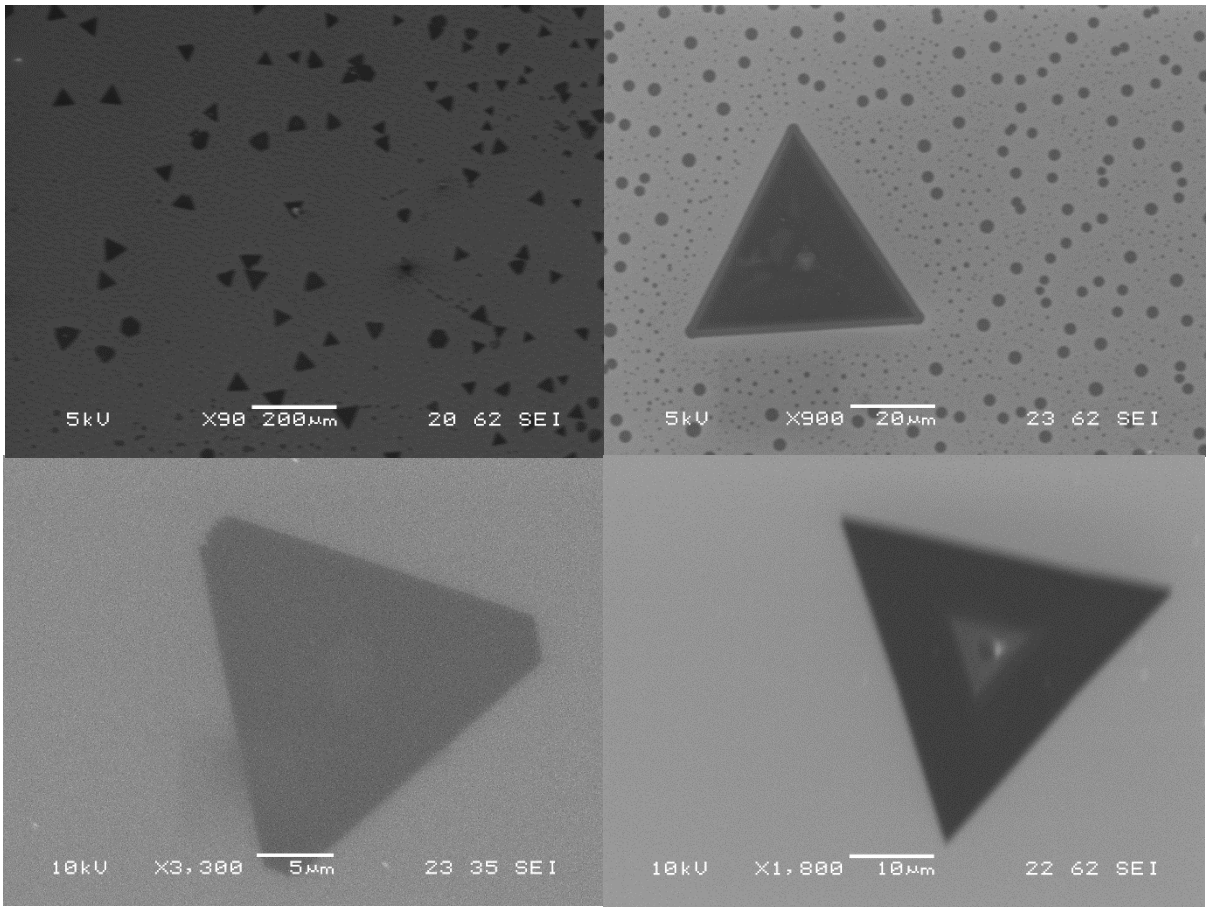

Figure 3.42 SEM images of various WS_2 triangles.

3.4.7 High temperature depositions on SiO_2 summary and comparisons with $W(S_2CNEt_2)_4$.

Even at the highest sulphur atmosphere concentrations, formation of WS_2 from the tungsten oxide was far slower than from $W(S_2CNEt_2)_4$. This is due to two reasons, firstly $W(S_2CNEt_2)_4$ was designed to be thermodynamically unstable with respect to the formation of WS_2 and the activation energy required for this transformation is far less than for the oxide. Secondly as the oxide relied on evaporation, far less of it was transferred to the substrate than $W(S_2CNEt_2)_4$ which was transferred by aerosol.

For high temperature depositions, changes in temperature not only changed the deposition mechanism, but also what material was actually deposited. For depositions from $W(S_2CNEt_2)_4$, only the growth mechanism was affected by temperature. For high temperature growth it was also found the carrier gas flow rate was very important in determining the final morphology of the WS_2 crystals.

3.4.8 High temperature depositions onto graphene

As it had been shown that WS_2 monolayers could be grown using high temperature CVD within the developed reactor, it was of great interest to explore how the substrate would affect its growth. As graphene had been shown to dramatically change the way that $W(S_2CNEt_2)_4$ deposited and heterostructures of monolayer graphene-monolayer WS_2 being of great interest to the scientific community, it was chosen as the substrate.

Initially, the same conditions were chosen that produced the highest proportion of WS_2 monolayers as discussed in the previous section. As expected, this produced triangular WS_2 crystals on regions of SiO_2 not covered by graphene. However, there was continuous coverage on graphene of two or more layers with islands of thicker growth. As the previous study identified a trend between the concentration of the sulphur atmosphere and the thickness of the WS_2 films deposited, the heating tape temperature was varied. It was found by decreasing the tape temperature from 200 ^oC to 175 ^oC, the WS_2 films on graphene remained continuous but large area monolayer regions emerged. Figure 3.43 shows optical images of WS_2 on graphene grown in different concentrations of sulphur atmosphere. It also shows a Raman spectrum of WS_2 on graphene grown at 175 ^oC, displaying the peaks for WS_2, graphene and the strong photoluminescence peak corresponding to monolayer WS_2. It is important to note the lack of a graphene D peak, indicating the high temperature CVD process had not damaged the graphene substrate.

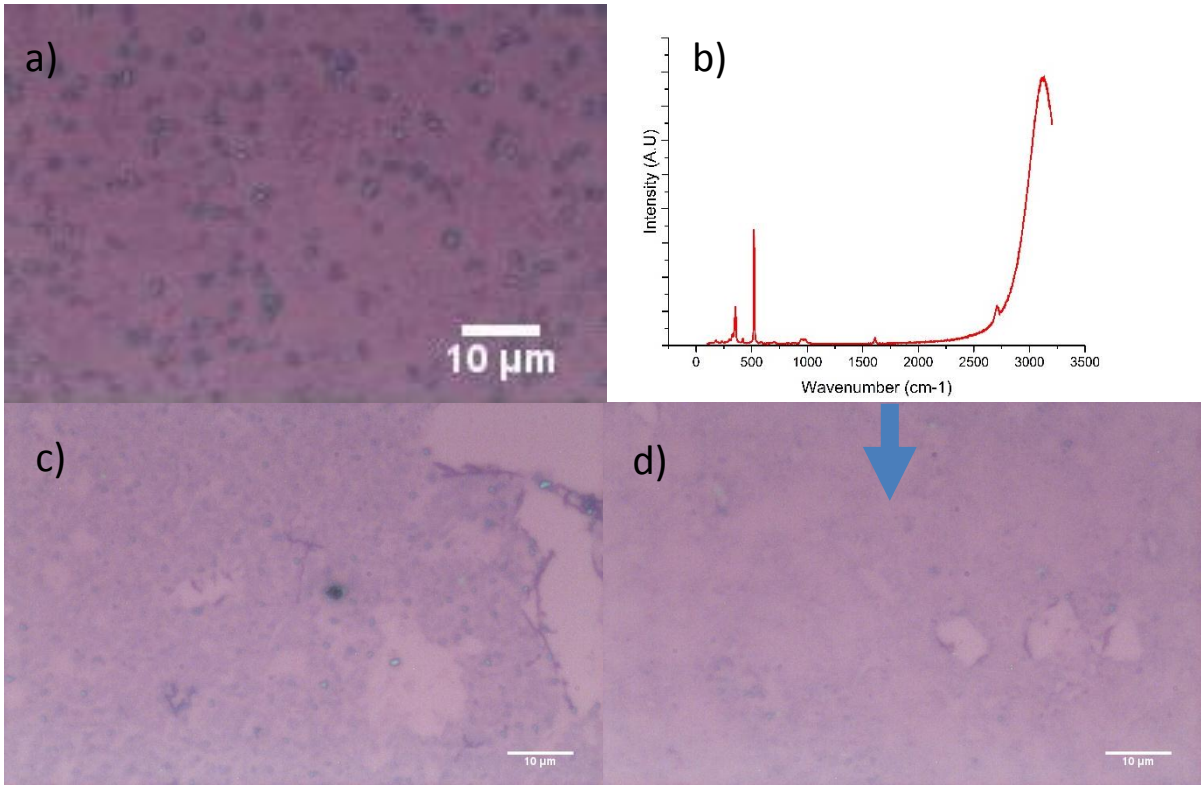

Figure 3.42 a) WS_2 grown on graphene with tape temperature of 200 °C. **b)** extended Raman spectrum taken from d). **c)** WS_2 grown on graphene with tape temperature of 185 °C. **d)** monolayer WS_2 grown on graphene with tape temperatures of 175 °C.

Raman and PL spectra of the WS_2 of varying thickness on graphene and SiO_2 are shown in figure 3.43. It was found there was no shift in the 2LA and A_{1g} peaks for thicker WS_2 on graphene as there was for thicker WS_2 on SiO_2. However, the ratio of the heights of the 2LA and A_{1g} peaks did vary. As of now there has been no direct comparison between Raman spectra of WS_2 grown on SiO_2 and WS_2 grown on graphene. Additionally it was found the A_{1g} peak from monolayer WS_2 experiences quenching when layered on graphene. This has not previously been discussed in the literature, but as the A_{1g} mode is an out of plane vibration,[57] it is likely the graphene substrate hinders this vibration in some way. The relative height of the A_{1g} peak increases for thicker WS_2, however still experiences quenching when layered on graphene. In agreement with literature discussed in the introduction to the chapter, the PL peak for WS_2 is quenched when on graphene and also shifted to higher energies. The PL peak for thicker WS_2 on graphene is shifted to lower energies with respect to monolayer WS_2 on graphene and experiences further quenching. To the best of our knowledge, this is the first example of a continuous film of WS_2 on graphene which has exhibited a PL response indicitive of a monolayer of WS_2.

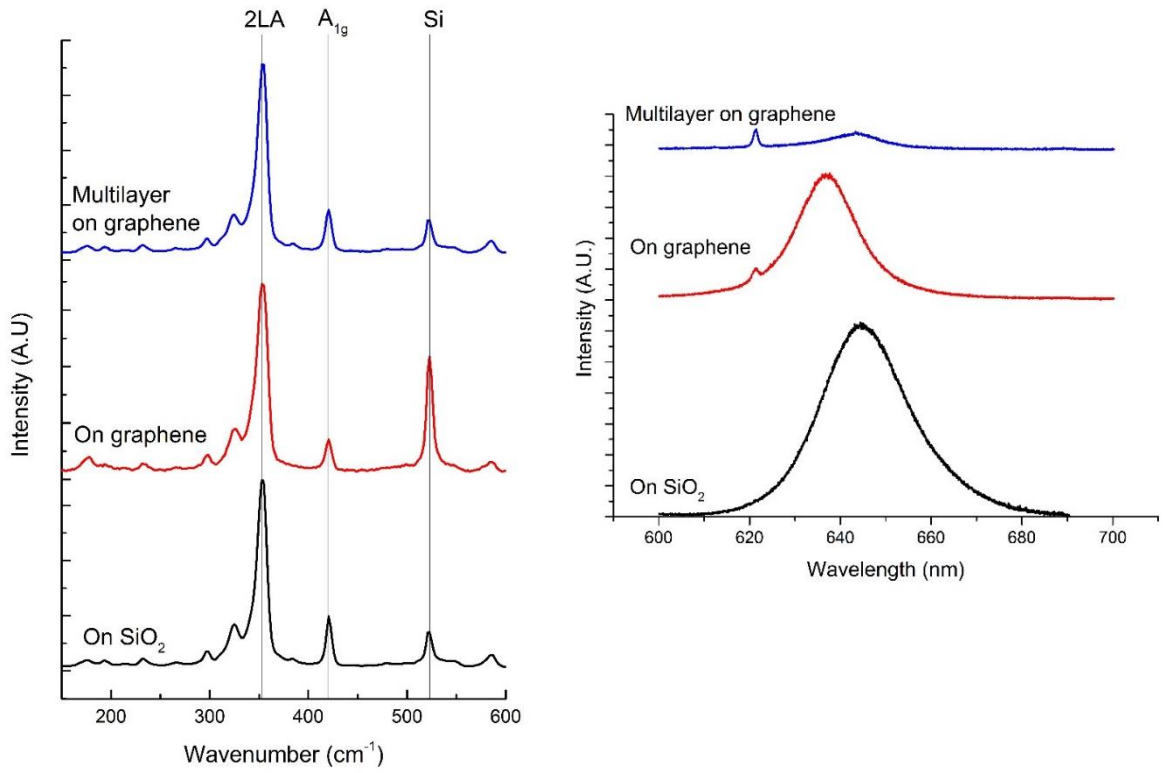

Figure 3.43 Left, Raman spectra of WS_2 on and off graphene. Right, room temperature PL spectra of WS_2 on and off graphene.

AFM was used to confirm the presence of a WS_2 monolayer on graphene. Figure 3.44 shows an AFM image of monolayer WS_2 on monolayer graphene and the step hight showing the film thickness to be

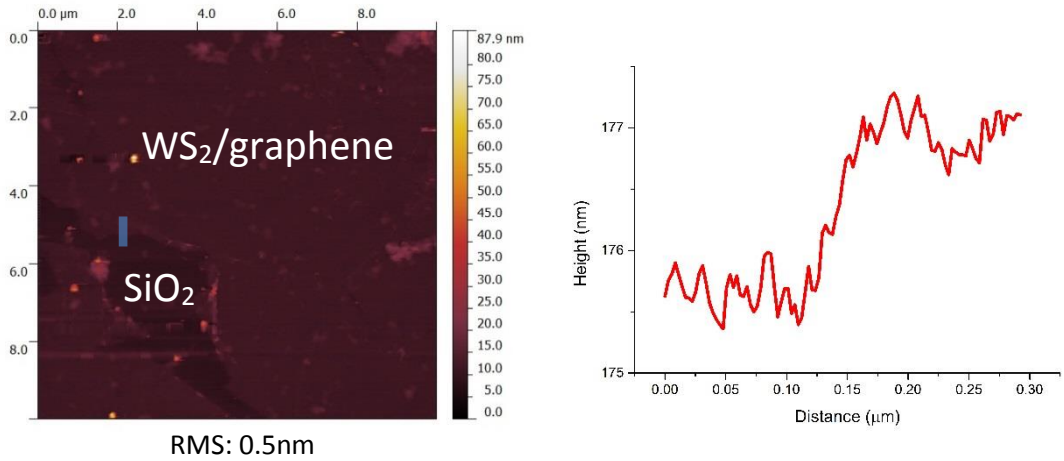

RMS: 0.5nm

Figure 3.44 AFM of monolayer WS_2 on graphene with step height taken at the position of the blue bar.

ca. 1.3 nm, corresponding to a monolayer of WS_2 and a monolayer of graphene. The RMS value of 0.5 nm shows the film is the flatter than those produced by AA-CVD.

3.4.9 Conclusions

It has been shown WS_2 can be successfully deposited by two techniques: AA-CVD and high temperature CVD. Exploring the effect of substrates on AA-CVD has never been a serious focus before and the dramatic changes in the WS_2 films produced when deposited onto graphene rather than more classic AA-CVD substrates has not been seen previously. It has been shown depositing a phase matching material onto graphene gives great control over the thickness of the film deposited, allowing to the best of our knowledge the thinnest continous films ever deposited by AA-CVD to be produced. However, a limit was reached when the films reach ca. 5nm thick. To achieve a further reduction in film thickness a CVD process which involved using temperatures above 1000 ^oC was used. This process allowed continuous sheets of monolayer WS_2 to be grown on graphene. The presence of monloayers was confirmed by AFM, Raman and PL studies.

3.5 References

1. Georgiou, T.; Jalil, R.; Belle, B. D.; Britnell, L.; Gorbachev, R. V.; Morozov, S. V.; Kim, Y.-J.; Gholinia, A.; Haigh, S. J.; Makarovsky, O.; Eaves, L.; Ponomarenko, L. A.; Geim, A. K.; Novoselov, K. S.; Mishchenko, A., Vertical field-effect transistor based on graphene-WS_2 heterostructures for flexible and transparent electronics. *Nature Nanotechnology* **2013,** *8* (2), 100-103.
2. Chen, T. Y.; Chang, Y. H.; Hsu, C. L.; Wei, K. H.; Chiang, C. Y.; Li, L. J., Comparative study on MoS_2 and WS_2 for electrocatalytic water splitting. *Int. J. Hydrog. Energy* **2013,** *38* (28), 12302-12309.
3. Tenne, R.; Margulis, L.; Genut, M.; Hodes, G., Polyhedral and cylindrical Structures of Tungsten Disulfide. *Nature* **1992,** *360* (6403), 444-446.
4. Voiry, D.; Mohite, A.; Chhowalla, M., Phase engineering of transition metal dichalcogenides. *Chemical Society Reviews* **2015,** *44* (9), 2702-2712.
5. Jiang, T.; Liu, H.; Huang, D.; Zhang, S.; Li, Y.; Gong, X.; Shen, Y.-R.; Liu, W.-T.; Wu, S., Valley and band structure engineering of folded MoS2 bilayers. *Nat Nano* **2014,** *9* (10), 825-829.
6. Kim, H.-C.; Kim, H.; Lee, J.-U.; Lee, H.-B.; Choi, D.-H.; Lee, J.-H.; Lee, tungsten. H.; Jhang, S. H.; Park, B. H.; Cheong, H.; Lee, S.-W.; Chung, H.-J., Engineering Optical and Electronic Properties of WS_2 by Varying the Number of Layers. *ACS Nano* **2015,** *9* (7), 6854-6860.
7. Tiwari, A.; Syväjärvi, M., *Advanced 2D Materials*. John Wiley & Sons: 2016.
8. Georgiou, T.; Jalil, R.; Belle, B. D.; Britnell, L.; Gorbachev, R. V.; Morozov, S. V.; Kim, Y.-J.; Gholinia, A.; Haigh, S. J.; Makarovsky, O.; Eaves, L.; Ponomarenko, L. A.; Geim, A. K.; Novoselov, K. S.; Mishchenko, A., Vertical field-effect transistor based on graphene-WS_2 heterostructures for flexible and transparent electronics. *Nat Nano* **2013,** *8* (2), 100-103.
9. Gutiérrez, H. R.; Perea-López, N.; Elías, A. L.; Berkdemir, A.; Wang, B.; Lv, R.; López-Urías, F.; Crespi, V. H.; Terrones, H.; Terrones, M., Extraordinary Room-Temperature Photoluminescence in Triangular WS_2 Monolayers. *Nano Letters* **2013,** *13* (8), 3447-3454.

10. Wang, X. H.; Ning, J. Q.; Zheng, C. C.; Zhu, B. R.; Xie, L.; Wu, H. S.; Xu, S. J., Photoluminescence and Raman mapping characterization of WS_2 monolayers prepared using top-down and bottom-up methods. *Journal of Materials Chemistry C* **2015,** *3* (11), 2589-2592.
11. Bernardi, M.; Palummo, M.; Grossman, J. C., Extraordinary Sunlight Absorption and One Nanometer Thick Photovoltaics Using Two-Dimensional Monolayer Materials. *Nano Letters* **2013,** *13* (8), 3664-3670.
12. Yan, Y.; Xia, B.; Li, N.; Xu, Z.; Fisher, A.; Wang, X., Vertically oriented MoS_2 and WS_2 nanosheets directly grown on carbon cloth as efficient and stable 3-dimensional hydrogen-evolving cathodes. *Journal of Materials Chemistry A* **2015,** *3* (1), 131-135.
13. Zeng, L.; Tao, L.; Tang, C.; Zhou, B.; Long, H.; Chai, Y.; Lau, S. P.; Tsang, Y. H., High-responsivity UV-Vis Photodetector Based on Transferable WS_2 Film Deposited by Magnetron Sputtering. *Scientific Reports* **2016,** *6*, 20343.
14. Ratha, S.; Rout, C. S., Supercapacitor Electrodes Based on Layered Tungsten Disulfide-Reduced Graphene Oxide Hybrids Synthesized by a Facile Hydrothermal Method. *ACS Applied Materials & Interfaces* **2013,** *5* (21), 11427-11433.
15. Voiry, D.; Yamaguchi, H.; Li, J.; Silva, R.; Alves, D. C. B.; Fujita, T.; Chen, M.; Asefa, T.; Shenoy, V. B.; Eda, G.; Chhowalla, M., Enhanced catalytic activity in strained chemically exfoliated WS_2 nanosheets for hydrogen evolution. *Nat Mater* **2013,** *12* (9), 850-855.
16. Cao, S.; Liu, T.; Hussain, S.; Zeng, W.; Peng, X.; Pan, F., Hydrothermal synthesis of variety low dimensional WS2 nanostructures. *Materials Letters* **2014,** *129*, 205-208.
17. Koçak, Y.; Akaltun, Y.; Emre, G., Magnetron sputtered WS_2; optical and structural analysis. *Journal of Physics: Conference Series* **2016,** *707* (1), 012028.
18. Loh, T. A. J.; Chua, D. H. C.; Wee, A. T. S., One-step Synthesis of Few-layer WS_2 by Pulsed Laser Deposition. *Scientific Reports* **2015,** *5*.
19. Lee, Y.-H.; Zhang, X.-Q.; Zhang, W.; Chang, M.-T.; Lin, C.-T.; Chang, K.-D.; Yu, Y.-C.; Wang, J. T.-W.; Chang, C.-S.; Li, L.-J.; Lin, T.-W., Synthesis of Large-Area MoS_2 Atomic Layers with Chemical Vapor Deposition. *Advanced Materials* **2012,** *24* (17), 2320-2325.
20. van der Zande, A. M.; Huang, P. Y.; Chenet, D. A.; Berkelbach, T. C.; You, Y.; Lee, G.-H.; Heinz, T. F.; Reichman, D. R.; Muller, D. A.; Hone, J. C., Grains and grain boundaries in highly crystalline monolayer molybdenum disulphide. *Nat Mater* **2013,** *12* (6), 554-561.
21. Gao, Y.; Liu, Z.; Sun, D.-M.; Huang, L.; Ma, L.-P.; Yin, L.-C.; Ma, T.; Zhang, Z.; Ma, X.-L.; Peng, L.-M.; Cheng, H.-M.; Ren, W., Large-area synthesis of high-quality and uniform monolayer WS_2 on reusable Au foils. *Nature Communications* **2015,** *6*, 8569.
22. Hou, X.; Choy, K.-L., Synthesis of Cr_2O_3-based nanocomposite coatings with incorporation of inorganic fullerene-like nanoparticles. *Thin Solid Films* **2008,** *516* (23), 8620-8624.
23. Ouyang, T.; Loh, K. P.; Zhang, H.; Vittal, J. J.; Vetrichelvan, M.; Chen, W.; Gao, X.; Wee, A. T. S., A Surface Chemistry Route to Molybdenum Sulfide and Germanide Films Using the Single-Source Precursor Tetrakis(diethylaminodithiocarbomato)molybdate(IV). *The Journal of Physical Chemistry B* **2004,** *108* (45), 17537-17545.
24. Kevin, P.; Lewis, D. J.; Raftery, J.; Azad Malik, M.; O'Brien, P., Thin films of tin(II) sulphide (SnS) by aerosol-assisted chemical vapour deposition (AACVD) using tin(II) dithiocarbamates as single-source precursors. *Journal of Crystal Growth* **2015,** *415*, 93-99.
25. Mlowe, S.; Lewis, D. J.; Azad Malik, M.; Raftery, J.; Mubofu, E. B.; O'Brien, P.; Revaprasadu, N., Bis(piperidinedithiocarbamato)pyridinecadmium(ii) as a single-source precursor for the synthesis of CdS nanoparticles and aerosol-assisted chemical vapour deposition (AACVD) of CdS thin films. *New Journal of Chemistry* **2014,** *38* (12), 6073-6080.
26. Mlowe,S.; Lewis, D. J.; Malik, M. A.; Raftery, J.; Mubofu, E. B.; O'Brien, P.; Revaprasadu, N., Heterocyclic dithiocarbamato-iron(III) complexes: single-source precursors for aerosol-assisted chemical vapour deposition (AACVD) of iron sulfide thin films. *Dalton Transactions* **2016,** *45* (6), 2647-2655.

27. Yamaguchi, T.; Moriya, R.; Inoue, Y.; Morikawa, S.; Masubuchi, S.; Watanabe, K.; Taniguchi, T.; Machida, T., Tunneling transport in a few monolayer-thick WS_2/graphene heterojunction. *Applied Physics Letters* **2014,** *105* (22).
28. Britnell, L.; Ribeiro, R. M.; Eckmann, A.; Jalil, R.; Belle, B. D.; Mishchenko, A.; Kim, Y.-J.; Gorbachev, R. V.; Georgiou, T.; Morozov, S. V.; Grigorenko, A. N.; Geim, A. K.; Casiraghi, C.; Neto, A. H. C.; Novoselov, K. S., Strong Light-Matter Interactions in Heterostructures of Atomically Thin Films. *Science* **2013,** *340* (6138), 1311-1314.
29. Kobayashi, Y.; Sasaki, S.; Mori, S.; Hibino, H.; Liu, Z.; Watanabe, K.; Taniguchi, T.; Suenaga, K.; Maniwa, Y.; Miyata, Y., Growth and Optical Properties of High-Quality Monolayer WS_2 on Graphite. *Acs Nano* **2015,** *9* (4), 4056-4063.
30. Yun, tungsten. S.; Han, S. W.; Hong, S. C.; Kim, I. G.; Lee, J. D., TThickness and strain effects on electronic structures of transition metal dichalcogenides: 2H-MX_2 semiconductors (M = Mo, W; X = S, Se, Te). *Physical Review B* **2012,** *85* (3), 033305.
31. Bianco, G. V.; Losurdo, M.; Giangregorio, M. M.; Sacchetti, A.; Prete, P.; Lovergine, N.; Capezzuto, P.; Bruno, G., Direct epitaxial CVD synthesis of tungsten disulfide on epitaxial and CVD graphene. *RSC Advances* **2015,** *5* (119), 98700-98708.
32. Azad Malik, M.; O'Brien, P., Chapter 5 Basic Chemistry of CVD and ALD Precursors. In *Chemical Vapour Deposition: Precursors, Processes and Applications*, The Royal Society of Chemistry: 2009; pp 207-271.
33. Kalikhman, V. L., *Izv. Akad. Nauk SSSR, Neorg. Mater.* **1983,** (19).
34. Schutte, tungsten. J.; De Boer, J. L.; Jellinek, F., Crystal structures of tungsten disulfide and diselenide. *J. Solid State Chem.* **1987,** *70* (2), 207-209.
35. Nguyen, T. P.; Choi, S.; Jeon, J. M.; Kwon, K. C.; Jang, H. W.; Kim, S. Y., Transition Metal Disulfide Nanosheets Synthesized by Facile Sonication Method for the Hydrogen Evolution Reaction. *Journal of Physical Chemistry C* **2016,** *120* (7), 3929-3935.
36. Delabie, A.; Caymax, M.; Groven, B.; Heyne, M.; Haesevoets, K.; Meersschaut, J.; Nuytten, T.; Bender, H.; Conard, T.; Verdonck, P.; Van Elshocht,S.; De Gendt, S.; Heyns, M.; Barla, K.; Radu, I.; Thean, A., Low temperature deposition of 2D WS_2 layers from WF_6 and H_2S precursors: impact of reducing agents. *Chemical Communications* **2015,** *51* (86), 15692-15695.
37. Patterson, A. L., The Scherrer Formula for X-Ray Particle Size Determination. *Physical Review* **1939,** *56* (10), 978-982.
38. Warren, B. E., *X-ray diffraction*. Addison-Wesley Pub. Co.: Reading, Mass., 1969.
39. Marchand, P.; Hassan, I. A.; Parkin, I. P.; Carmalt, C. J., Aerosol-assisted delivery of precursors for chemical vapour deposition: expanding the scope of CVD for materials fabrication. *Dalton Trans.* **2013,** *42* (26), 9406-9422.
40. Berkdemir, A.; Gutiérrez, H. R.; Botello-Méndez, A. R.; Perea-López, N.; Elías, A. L.; Chia, C.-I.; Wang, B.; Crespi, V. H.; López-Urías, F.; Charlier, J.-C.; Terrones, H.; Terrones, M., Identification of individual and few layers of WS_2 using Raman Spectroscopy. *Scientific Reports* **2013,** *3*, 1755.
41. Berkdemir, A.; Gutierrez, H. R.; Botello-Mendez, A. R.; Perea-Lopez, N.; Elias, A. L.; Chia, C. I.; Wang, B.; Crespi, V. H.; Lopez-Urias, F.; Charlier, J. C.; Terrones, H.; Terrones, M., Identification of individual and few layers of WS_2 using Raman Spectroscopy. *Scientific Reports* **2013,** *3*.
42. Zhao, tungsten. J.; Ghorannevis, Z.; Amara, K. K.; Pang, J. R.; Toh, M.; Zhang, X.; Kloc, C.; Tan, P. H.; Eda, G., Lattice dynamics in mono- and few-layer sheets of WS_2 and WSe_2. *Nanoscale* **2013,** *5* (20), 9677-9683.
43. Paradisanos, I.; Pliatsikas, N.; Patsalas, P.; Fotakis, C.; Kymakis, E.; Kioseoglou, G.; Stratakis, E., Spatial non-uniformity in exfoliated WS_2 single layers. *Nanoscale* **2016,** *8* (36), 16197-16203.
44. Buscema, M.; Steele, G. A.; van der Zant, H. S. J.; Castellanos-Gomez, A., The effect of the substrate on the Raman and photoluminescence emission of single-layer MoS_2. *Nano Research* **2014,** *7* (4), 561-571.

45. Lee, Y. H.; Zhang, X. Q.; Zhang, tungsten. J.; Chang, M. T.; Lin, C. T.; Chang, K. D.; Yu, Y. C.; Wang, J. T. W.; Chang, C. S.; Li, L. J.; Lin, T. W., Synthesis of Large-Area MoS_2 Atomic Layers with Chemical Vapor Deposition. *Advanced Materials* **2012,** *24* (17), 2320-2325.
46. Cong, C. X.; Shang, J. Z.; Wu, X.; Cao, B. C.; Peimyoo, N.; Qiu, C.; Sun, L. T.; Yu, T., Synthesis and Optical Properties of Large-Area Single-Crystalline 2D Semiconductor WS_2 Monolayer from Chemical Vapor Deposition. *Advanced Optical Materials* **2014,** *2* (2), 131-136.
47. Rong, Y.; Fan, Y.; Koh, A. L.; Robertson, A. W.; He, K.; Wang, S.; Tan, H.; Sinclair, R.; Warner, J. H., Controlling sulphur precursor addition for large single crystal domains of WS2. *Nanoscale* **2014,** *6* (20), 12096-12103.
48. Peimyoo, N.; Shang, J.; Cong, C.; Shen, X.; Wu, X.; Yeow, E. K. L.; Yu, T., Nonblinking, Intense Two-Dimensional Light Emitter: Monolayer WS2 Triangles. *ACS Nano* **2013,** *7* (12), 10985-10994.
49. van der Vlies, A. J.; Kishan, G.; Niemantsverdriet, J. W.; Prins, R.; Weber, T., Basic reaction steps in the sulfidation of crystalline tungsten oxides. *Journal of Physical Chemistry B* **2002,** *106* (13), 3449-3457.
50. van der Vlies, A. J.; Prins, R.; Weber, T., Chemical principles of the sulfidation of Tungsten oxides. *Journal of Physical Chemistry B* **2002,** *106* (36), 9277-9285.
51. Cong, C.; Shang, J.; Wu, X.; Cao, B.; Peimyoo, N.; Qiu, C.; Sun, L.; Yu, T., Synthesis and Optical Properties of Large-Area Single-Crystalline 2D Semiconductor WS_2 Monolayer from Chemical Vapor Deposition. *Advanced Optical Materials* **2014,** *2* (2), 131-136.
52. Sarma, P. V.; Patil, P. D.; Barman, P. K.; Kini, R. N.; Shaijumon, M. M., Controllable growth of few-layer spiral WS_2. *RSC Advances* **2016,** *6* (1), 376-382.
53. Senthilkumar, R.; Ravi, G.; Sekar, C.; Arivanandhan, M.; Navaneethan, M.; Hayakawa, Y., Determination of gas sensing properties of thermally evaporated WO_3 nanostructures. *Journal of Materials Science-Materials in Electronics* **2015,** *26* (3), 1389-1394.
54. Rong, Y.; Fan, Y.; Leen Koh, A.; Robertson, A. W.; He, K.; Wang,S.; Tan, H.; Sinclair, R.; Warner, J. H., Controlling sulphur precursor addition for large single crystal domains of WS_2. *Nanoscale* **2014,** *6* (20), 12096-12103.
55. Payen, E.; Kasztelan,S.; Grimblot, J.; Bonnelle, J. P., Study of the sulphurization of WO_3/ γ-Al_2O_3 catalysts by in situ laser raman spectroscopy. *Catalysis Today* **1988,** *4* (1), 57-70.
56. Fu, Q.; Wang, W.; Yang, L.; Huang, J.; Zhang, J.; Xiang, B., Controllable synthesis of high quality monolayer WS_2 on a SiO_2/Si substrate by chemical vapor deposition. *RSC Advances* **2015,** *5* (21), 15795-15799.
57. Staiger, M.; Gillen, R.; Scheuschner, N.; Ochedowski, O.; Kampmann, F.; Schleberger, M.; Thomsen, C.; Maultzsch, J., Splitting of monolayer out-of-plane A'(1) Raman mode in few-layer WS_2. *Physical Review B* **2015,** *91* (19).

Chapter 4. Chemical Vapour Deposition of Tin Sulphides

4.1 Introduction

This chapter focuses on the materials SnS and SnS_2, therefore the properties and synthesis of these photoactive materials will be discussed. Current progress on creating heterostructures or devices containing graphene, SnS and/or SnS_2 will also be discussed. The experimental results of depositing SnS and SnS_2 by aerosol assisted chemical vapour deposition (AA-CVD) onto graphene will then be presented and compared to depositions of SnS and SnS_2 deposited onto glass and fluorine doped tin oxide (FTO) previously carried out in the group by Dr Ibbi Ahmet. It will be shown due to the need for an annealing step to deposit orthorhombic SnS onto graphene, damage to the graphene causes a drop in photoelectrochemical performance compared to orthorhombic SnS deposited onto FTO. However, due to the shorter deposition times and the lack of an annealing step SnS_2 on graphene outperforms SnS_2 deposited onto FTO. This is attributed to the reduction in strain of SnS_2 on graphene, which causes a favourable shift in its light absorption profile. Due to the current issues with the quality of SnS produced, high temperature CVD of SnS was explored. It will be shown that orientated single crystals of SnS with dimensions of ca. 50 µm across and 4 µm thick can be synthesised on SiO_2, which are far larger than anything published previously.

4.1.1 SnS properties

As well as the drive to integrate graphene into photovoltaic devices,[1] there is a demand for alternate materials to the ubiquitous silicon for the photovoltaic market today. One of the main problems with silicon is although it has a close to ideal bandgap in terms of energy, it is indirect. This means the silicon absorber layer has to be relatively thick to absorb sufficient sunlight. Additionally, the silicon has to be of very high purity. So far, obtaining enough high purity silicon has been economical due to the electronics industry, which produces large amounts of high purity silicon waste. However, if the silicon solar sector is to continue to grow, this economic benefit will start to be eroded. To create such high purity silicon also requires the handling of some extremely toxic and hazardous chemicals such as silanes, silicon chlorides and hydrogen fluoride. The process is also very energy intensive. Doping of silicon requires chemicals such as phosphine or arsine gas and boron tribromide. Sulphur hexafluoride is used to clean reactors used in silicon production, it is 25000x more potent than CO_2 as a greenhouse gas and accidental or fugitive emissions of this chemical are a serious problem.

In light of this, materials that have direct bandgaps, contain earth abundant elements and have facile synthetic routes are highly sought after. One such material is SnS. With a direct bandgap, it has

a high solar absorption coefficient and orthorhombic SnS (α-SnS) has a near ideal direct bandgap of ca. 1.3eV.[2] Tin and sulphur are also earth abundant elements and thus SnS thin films have the received an increasing amount of attention over the last 5 years as a solar cell absorber layer.

4.1.1.1 SnS structure

SnS most commonly exists in the cubic or orthorhombic phase, as it is thermodynamically the most stable. Until very recently, the cubic phase of SnS (π-SnS) was often mistakenly reported as possessing the zinc-blende structure from miss-assigned PXRD data,[4,5] until more thorough electron diffraction analysis was carried out.[6] Figure 4.1 shows the structures of orthorhombic and cubic SnS. Orthorhombic SnS has a layered structure, with van der Waals forces holding the layers together. SnS also exists in a high temperature form,[7,8] but this phase will not be considered further due to it not existing under the practical conditions used in the experiments reported here.

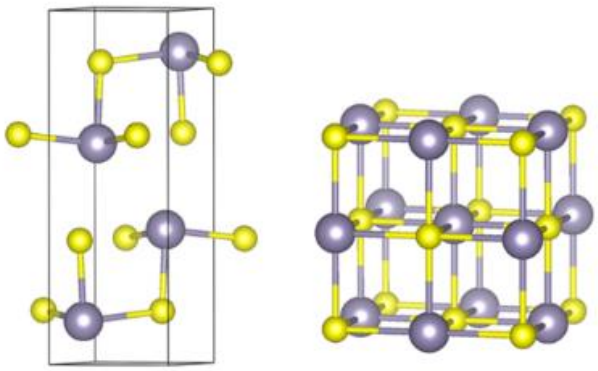

Figure 4.1 Structure of orthorhombic SnS (left) and Cubic SnS (right) adapted from ref 3.

4.1.1.2 SnS optical and electrical properties

Orthorhombic and cubic forms of SnS are both semiconducting and p-type. α-SnS has a direct bandgap of 1.3 eV and an indirect bandgap of 1.07 eV. π-SnS has an indirect bandgap of ca. 1.5 eV.[9] It has been shown the exfoliation of bulk α-SnS into bilayers shifts the bandgap from 1.3 eV to 1.65 eV.[10] α-SnS has an optical absorption coefficient of $>10^4$ cm^{-1} above its band gap which is higher than crystalline silicon and other thin film materials such as CdTe, copper indium selenide (CIS) and copper indium gallium selenide (CIGS).[11,12] Due to the layered structure of α-SnS, the surfaces of the material do not contain any dangling bonds, which make SnS relatively inert and immune to Femi level pinning, which can be an issue in the semiconductor industry.[13] Orthorhombic SnS is naturally p-type due to intrinsic tin vacancies which introduce two holes into the SnS lattice each. However, doping with ions such as Pb^{2+} can switch its behaviour to n-type.[14] The optical and electrical properties of cubic SnS are less well studied, however it has a bandgap of ca. 1.5 eV and seems to exhibit ambipolar behaviour.[2] For a detailed analysis of SnS properties, the reader is referred to a review by Banai et al.[15]

4.1.2 SnS applications

Due to its electrical and optical properties in addition to it being environmentally stable and composed of earth abundant elements, the major proposed application of SnS is as an absorber layer in a solar cell. However, SnS has also received attention as an infra-red detector, battery material and in photoelectrochemical cells.

So far the record efficiency of a solar cell incorporating SnS is 4.4 %, with a short circuit current density of 20.2 mA cm^{-2} and an open-circuit voltage of 0.372 V. This was achieved by Gordon et al. who used a SnS absorber layer deposited by ALD.[16] They attribute the record efficiency to a few factors, which include H_2S annealing of the SnS film to increase grain size to increase carrier mobility, and the fine tuning of the Zn(O,S) buffer layer to align the conduction bands. The addition of a few monolayers of SnO_2 between SnS and Zn(O,S) reduced recombination at the junction. Figure 4.2 shows a diagram and cross-sectional SEM of the solar cell.

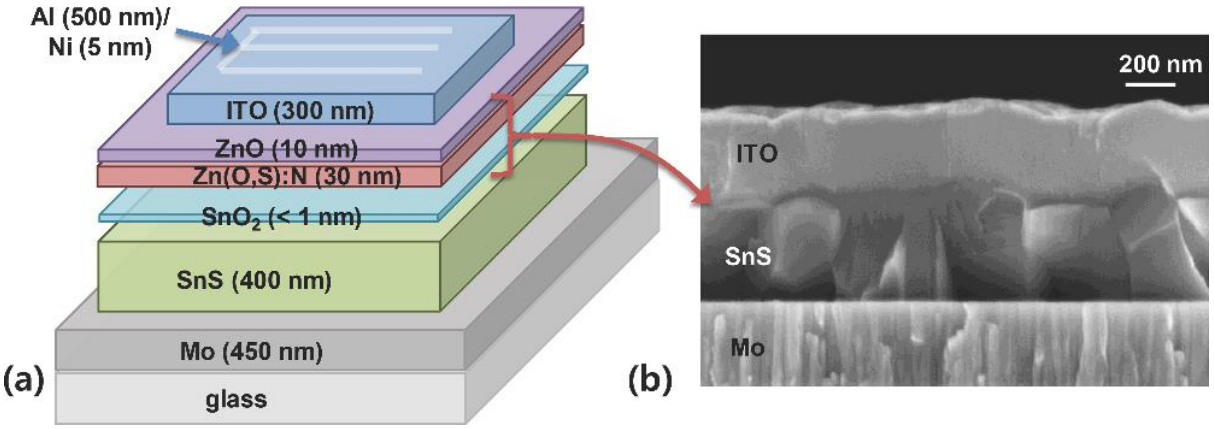

Figure 4.2 a) Diagram of record efficiency SnS solar cell (4.4 %) **b)** Cross-sectional SEM of solar cell. Images reproduced from ref

4.1.3 SnS synthesis

SnS has previously been synthesised in single crystal, nanoparticle and thin film forms. Single crystals can either be synthesised by melt growth (also called the Bridgeman method) or melt mixing. Melt growth involves the transfer of the desired material vapour from a hot zone to a cool zone where it condenses to form a single crystal. Melt mixing involves heating the material above its meting point in a vacuum sealed ampoule which on cooling affords single crystals. SnS single crystals have previously been produced by both techniques, which can then be exfoliated to allow characterisation.[17,18] SnS nanoparticles can be synthesised relatively simply from a tin salt, (often $SnCl_2$) and a sulphur source (such as Na_2S), capping agents such as oleylamine are used to stop agglomeration. The size of the nanoparticles can be tuned by the reaction temperature and precursor injection rates. [19,20] The synthesis of SnS thin films will now be discussed in greater detail.

4.1.3.1 SnS thin film synthesis- wet chemical methods

Wet chemical methods offer the user a simple and economical way of producing SnS thin films. One technique is chemical bath deposition (CBD). This involves SnS nucleating onto the desired substrate from a bath solution where the degree of heating of the bath and the deposition time is controlled by the precursors, although heating is often no hotter than 50 ^{o}C. As with the single crystal techniques, the tin source is very often $SnCl_2$. Examples of the sulphur source include sodium sulphide, thioacetamide, sodium sulphate and thiourea.[21,22,23]

Dip coating involves dipping the desired substrate repeatedly in cold and hot solutions of precursor (often identical to those used in CBD) until the desired thickness is reached, or cycling the substrate between a cold precursor solution and a hot plate.[24] The precursor can be delivered to the substrate by spincoating instead of dipping as this can afford greater control over film uniformity and thickness. Jambor et al. demonstrate single source precursors such as organotin(II) sulfide ((2,6-$(Me_2NCH_2)_2C_6H_3)Sn)_2(\mu$-S) can be spin coated to produce SnS films.[25]

Good control over deposition rates and film composition can be achieved by using electrochemical deposition. A drawback however is that self-limiting growth can limit film thickness. In electrochemical deposition the substrate is the working electrode with a counter and reference electrode also present. Chen et al. also demonstrated the electrochemical deposition of SnS using $SnSO_4$ and $Na_2S_2O_3$, at room temperature.[26]

All these techniques provide low cost, facile routes to thin films of SnS, with reasonably large areas suitable for further study, however film quality, particularly material stoichiometry and morphology have been difficult to control. CVD is a technique that is attempting to address these issues whilst also being scalable, although the equipment required tends to be more complex.

4.1.3.2 SnS thin film synthesis- CVD

Reid et al. have used LP-CVD of a tin thioether, $SnCl_4(o\text{-}C_6H_4(CH_2SMe)_2)$, with a furnace temperature of 650 ^{o}C to produce SnS or SnS_2, depending on the substrate position within the furnace, however due to difficulties in controlling the oxygen content studies using LP-CVD are limited.

The possible range of precursors for AP-CVD of SnS is also limited by their volatility. Therefore precursors that are used in wet chemical techniques and LP-CVD cannot often be used in AP-CVD processes. SnS has been deposited from $SnCl_4$ and toxic H_2S at atmospheric pressure by Parkin et al. onto glass substrates at 545 ^{o}C with good stoichiometric control. [27] It was subsequently shown that the deposition temperature could be reduced to 450 ^{o}C by using tri-n-butyltin trifluoroacetate $Bu^n_3SnO_2CCF_3$.[28] It was later shown that the single source precursor $[Sn(SCH_2CH_2S)_2]_\infty$ eliminated the

need for H_2S. However, due to the low volatility of $[Sn(SCH_2CH_2S)_2]_\infty$ it was necessary to dissolve the precursor in acetone, with subsequent deposition by AA-CVD at 500 °C.[29] In an attempt to further reduce deposition temperatures O'Brien et al. developed a series of tin(II) dithiocarbamate compounds which readily dissolve in THF and can be used for the AA-CVD of SnS at 450°C.[30] The current record for the lowest deposition temperature of SnS using a single source precursor is held by Johnson et al. who reported a tin thiouriate dissolved in THF deposited by AA-CVD at 375 °C. They demonstrated remarkably phase pure and uncontaminated films, often an issue with AA-CVD processes. Additionally they demonstrated at deposition temperatures of 300 °C, π-SnS could be exclusively deposited rather than orthorhombic SnS.[2] Figure 4.3 shows molecular structures of the tin dithiocarbamate and tin thiouriate used by O'Brien and Johnson, respectively.

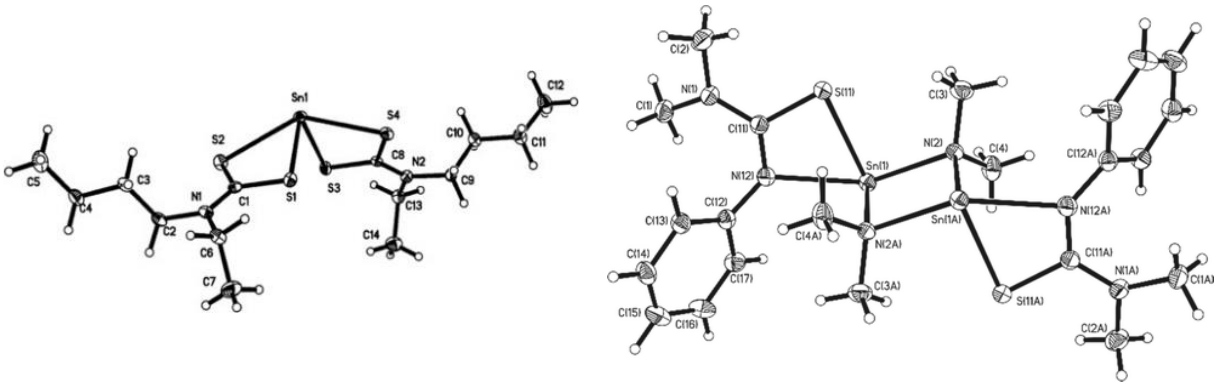

Figure 4.3 Molecular structures of single source precursors used to produce SnS. Left: tindithiocarbamate. Right: tin thiouriate. By O'Brien et al. and Johnson et al. respectively.

Finally, Reddy et al. found by finely tuning the ratios of $SnCl_2$ and n,n-dimethylthiourea dissolved in isopropyl alcohol (IPA) and deionised (DI) water phase pure orthorhombic SnS could be deposited by AA-CVD at 350 °C.[31]

Physical deposition methods have also been used to deposit thin films of SnS. Bulk SnS has been evaporated by resistive evaporation, electron beam evaporation and sputtering.[32,33,34] High quality SnS films can be achieved at temperatures as low as room temperature by this technique, however they require access to high vacuum systems, which is a disadvantage when considering scale up.

4.1.4 SnS_2 properties

Like SnS, SnS_2 also has a direct bandgap however it is larger at ca. 2.2 eV. In the bulk form it appears yellow and is air stable. Unlike SnS, SnS_2 displays n-type behaviour and has potential to be used as a window layer in solar cells, a photodetector and a layered material for batteries.[35,36,37]

4.1.4.1 SnS_2 structure

SnS_2 can be viewed as a graphene-like material due to its layered structure and hexagonal planes of each layer. Side on and top down images of SnS_2 are shown in Figure 4.4.

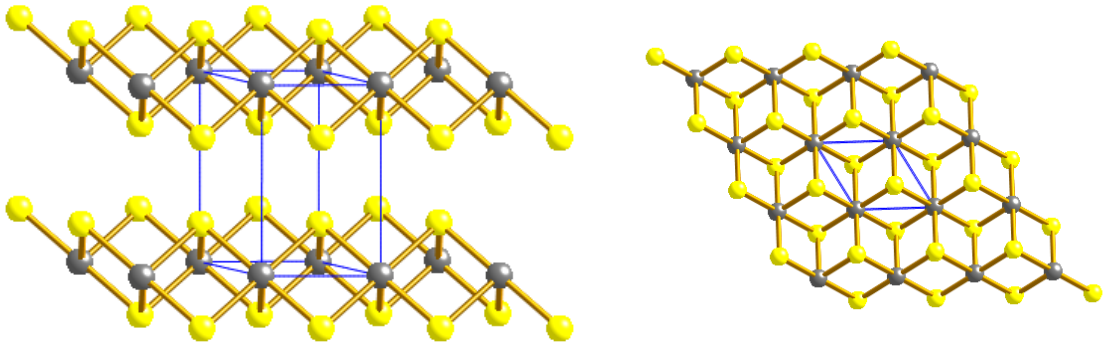

Figure 4.4 Side on and top down images of the SnS_2 structure. Yellow atoms are sulphur and the grey atoms are tin.The unit cell is highlighted in blue.

In SnS_2 the tin atoms exist in a trigonal prismatic environment, similar to the tungsten environment in the most common 1H phase of WS_2. However, there are many different polytypes due to the stacking order of these layers with the mechanism behind their formation remaining unclear.[38,39] it is generally agreed though that the main polytypes encountered are 2H, 18R and 4H and there is evidence that 2H is formed at lower temperatures, 18R at intermediate temperatures and 4H at higher temperatures, although the exact temperatures depend on many experimental factors.[40]

4.1.4.2 SnS_2 optical and electrical properties

As noted previously, SnS_2 has been reported to have a bandgap of 2.18–2.44 eV,[41] and is an intrinsic n-type semiconductor. It has many properties that make it a low-cost candidate for photo catalysed water splitting. Its bandgap lies in the visible region of the solar spectrum and not the UV, unlike TiO_2, where 43 % compared to 4 % in the UV of the solar energy resides.[42] The absence of dangling bonds on its surfaces makes it resistant to degradation and the layered structure gives the potential for a large surface area. Additionally, its valence and conduction bands lie close to the oxidation and reduction potentials for water. On exfoliation to single layers it was found SnS_2 layers undergo significant structural distortion to minimise surface energy.[43] This leads to an increased density of

states near the valence band which increases carrier mobility, leading to enhanced water splitting properties with a conversion efficiency of 38.7 %.[43]

Additionally SnS_2 also has a low lying conduction band which makes is suitable for accepting migrating electrons from a photoabsorber. Although its bandgap is in the visible region, it is rather wide so allows the transmittance of a lot of visible light. This makes it suitable for use as a window layer in a solar cell.[44]

4.1.5 SnS_2 applications

There are four main applications where SnS_2 is being explored; photocatalysis, solar cells, photo detection and energy storage materials.

In the previous section SnS_2 photo catalytic abilities have been mentioned. Wei et al. demonstrated exfoliated monolayers of SnS_2 mounted onto ITO possessed a light conversion efficiency of 38.7 % at 420 nm, which is one of the highest efficiencies recorded to date.[43,45,46] Reddy et al. have reported a solar cell that has a SnS absorber layer and a SnS_2 window layer grown by CBD with an overall efficiency of 0.51 %.[47] Li et al. have shown it can be used as a replacement to the Pt counter electrode in a dye sensitised solar cell, achieving an efficiency of 6.30 % compared to 6.67 % for Pt.[48] Wang et al. continued this work by demonstrating Ag doping of the SnS_2 provided an improvement on the Pt counter electrode with an efficiency of 8.70 %.[49] SnS_2 has also been used as colloidal quantum dots in organic/inorganic hybrid solar cells with efficiencies of 0.31 %.[50] SnS_2 is additionally being explored as a photodetector as it has a very fast current response time. Peng et al. show single crystal SnS_2 grown by CVD has a response time of ca. 5 μs, an order of magnitude faster than any other 2D material measured.[36] Due to its layered structure, SnS_2 can intercalate ions for energy storage applications. This is particularly useful as a replacement for graphite electrodes in Na ion batteries due to graphite's poor performance. It has been shown by Meng et al. that Na can alloy with SnS_2 as the anode to produce Na_2S_2 in a reversible reaction. They report a good performance of 500 mAh g^{-1} for 400 cycles when SnS_2 is deposited by CBD onto r-GO.[51] Again using r-Go, Jiao et al. use exfoliated SnS_2 to report a performance of 610 mA h g^{-1} up to 300 cycles.[52]

4.1.6 SnS_2 synthesis

In a similar manner to SnS, single crystals suitable for exfoliation of SnS_2 can be synthesised by melt mixing or melt growth.[53,54] Additionally SnS_2 nanoparticles can be synthesised in a similar fashion to SnS nanoparticles using a tin salt and a sulphur source, however, the salt is often $SnCl_4$ rather than $SnCl_2$.[55] Sathish et al. have mounted SnS_2 nanoparticles onto graphene nanosheets by heating $SnCl_4$

and thiourea in GO then subsequently reducing the GO. As with SnS, the synthesis of SnS_2 thin films will now be discussed.[56]

4.1.5.1 SnS_2 thin film synthesis- wet chemical methods

CBD is a simple route to producing SnS_2 thin films on a variety of substrates. It usually involves the decomposition of simple tin salts and a sulphur source. SnS and SnS_2 phases can be controlled by the concentration of the sulphur precursor.[57,58] As with SnS, SnS_2 can also be produced by dip coating and electrochemical deposition. As with dip coating, these techniques use simple tin salts and sulphur sources as SnS_2 precursors.[24,55]

4.1.5.2 SnS_2 thin film synthesis- CVD

The LP-CVD of SnS_2 has been reported by Reid et al. who have deposited SnS and SnS_2 from a tin thioether $SnCl_4(o\text{-}C_6H_4(CH_2SMe)_2)$ at 650 ^oC.[59] Again as with SnS, the most probable reason for the lack of reports of LP-CVD of SnS_2 is the difficulty of excluding oxygen from the system. Luo et al. have reported the deposition of SnS_2 nanosheets on carbon cloth at low pressures by the initial deposition of SnO_2 and subsequent sulfurisation. Although the quality of the nanosheets was high, they were produced at temperatures of 850 ^oC and the sheets were < 10 μm across.

Molloy et al. have used AA-CVD of the single source precursor tin(IV) thiolate $(PhS)_4Sn$ in the presence of H_2S to produce SnS_2 films.[60] Liu et al. avoided the use of toxic H_2S by evaporating sulphur, $Na_2S_2O_3$ and $SnCl_4$ in a PECVD process to produce SnS_2 at 550 ^oC. Amalraj et al. have also demonstrated SnS_2 films could be deposited by AA-CVD at the low temperature of 125 ^oC using $SnCl_2$ and thiourea dissolved in H_2O and isopropyl alcohol (IPA) respectively.[61]

4.1.7 SnS and SnS_2 on graphene

Due to the potential applications for SnS and SnS_2, deposition onto graphene is desirable. The properties of graphene discussed in the introduction such as its flexibility, transparency and conductivity make growing SnS and SnS_2 onto graphene an area of current research interest. A popular method for depositing tin sulphide onto graphene is to use CBD to deposit it onto a solution of r-GO. This is useful due to the ease of synthesis and the large surface area created. These composites are often created for use in energy storage and water splitting apllications.[62,63,56] Recently Song et al. reported the growth of SnS_2 crystals on graphene and found deposition onto graphene promoted the orientation of the SnS_2 crystals compared to growth on amorphous substrates.[64] Thus far, there are no examples of large scale continuous films of SnS or SnS_2 on a sheet of graphene. The work discussed in the following section was motivated by the current lack of published data of how SnS and SnS_2 deposits on large area graphene. In addition there is a lack of data on how graphene performs as a transparent conducting electrode (TCE).

4.2 SnS on graphene - Results and discussion

Prior to this work, a single source precursor **(1)** that produces polymorph-selective films was developed by Johnson et al.[2] The molecular structure of which can be seen in figure 4.5.

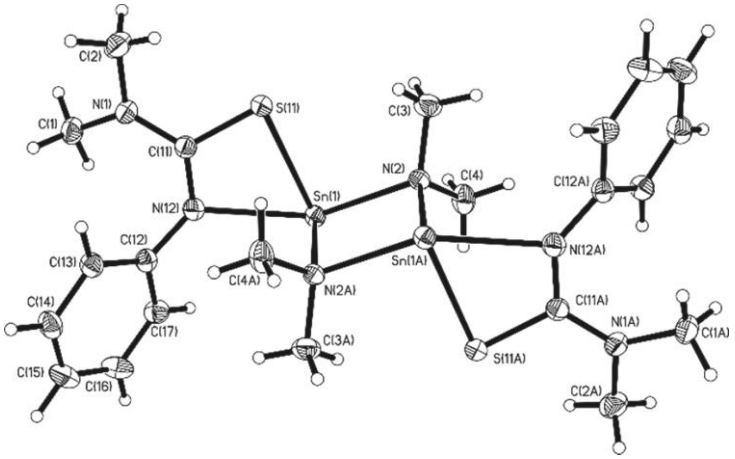

Figure 4.5 Molecular structure of the polymorph selective precursor of SnS developed by Johnson et al.

It was shown the SnS thin films deposited by this precursor were photoactive and could be potentially integrated into a photovoltaic device.[2] This raised the question whether graphene could be used as an alternative conducing layer to the FTO and molybdenum substrates used in the previous work. Three questions will attempted to be answered in the following body of work:

- To what extent is it possible to deposit SnS via AA-CVD onto CVD grown graphene substrates?
- Are the properties of the subsequent SnS/graphene composite desirable for photocurrent generation retained in these films?
- How do resulting photo-electrochemical devices perform compared to SnS films deposited on FTO and molybdenum which have been previously reported?

4.2.1 Depositing graphene-SnS films

Depositions of SnS onto CVD graphene, transferred respectively onto SiO_2 (as discussed in chapter 2), glass, silicon and FTO substrates were carried out via AA-CVD at 375 ^oC using precursor **(1)**. The deposition temperature of 375 ^oC was chosen as it was found to be the optimum growth temperature in a previous study.[2] Black-grey uniform films that adhered well to all the substrates (they were not exfoliated by applying and removing scotch tape) were produced. The films were characterised by a range of techniques as described in the following sections.

4.2.2 Analysis of SnS films - PXRD

PXRD showed all the films were crystalline. Films deposited on glass, silicon and FTO substrates produced diffraction peaks corresponding to α-SnS, however interestingly, SnS films deposited onto graphene produced diffraction peaks corresponding to the cubic phase of π-SnS. Importantly no peaks corresponding to Sn_2S_3, SnS_2, SnO and SnO_2 were present. SnO_2 peaks were only observed in samples in which SnS was deposited onto FTO. Films with graphene as a substrate were diced down to the size of the graphene sheet to ensure no signal was obtained from SnS around the graphene. To obtain the favourable α-SnS phase, π-SnS on graphene was annealed for 2 and 5 hours respectively. The phase change could be followed by PXRD. Figure 4.6 shows the diffraction peaks for an un-annealed glass-graphene-SnS sample, followed by annealing at 375 ^{o}C for 2 hours, then a sample that had been annealed for 5 hours. Finally, the pattern for a SnS sample grown at 375 ^{o}C on bare glass is displayed for comparison.

The π-SnS pattern displays some small peaks corresponding to α-SnS, showing it is not 100 % phase pure. After 2 h of annealing, almost all the peaks corresponding to π-SnS have disappeared, being replaced by peaks corresponding to α-SnS, with the (201) and (102) peaks being the most intense. Only small peaks corresponding to the (111) and (200) reflections of π-SnS remain. After 5 h of annealing only α-SnS remains, with the (111) and (004) peaks being the most intense, as is true with orthorhombic SnS deposited on FTO. π-SnS seems to be a kinetically stable material whereas α-SnS is the most thermodynamically stable. Graphene seems to kinetically stabilise the deposition of π-SnS from AA-CVD relative to glass, silicon and FTO. To deposit π-SnS onto these substrates, a lower reaction temperature of 300 ^{o}C had to be used. From the PXRD data it can be seen α-SnS deposited directly onto glass is highly orientated, whereas α-SnS derived from the annealing of π-SnS on graphene is less orientated.

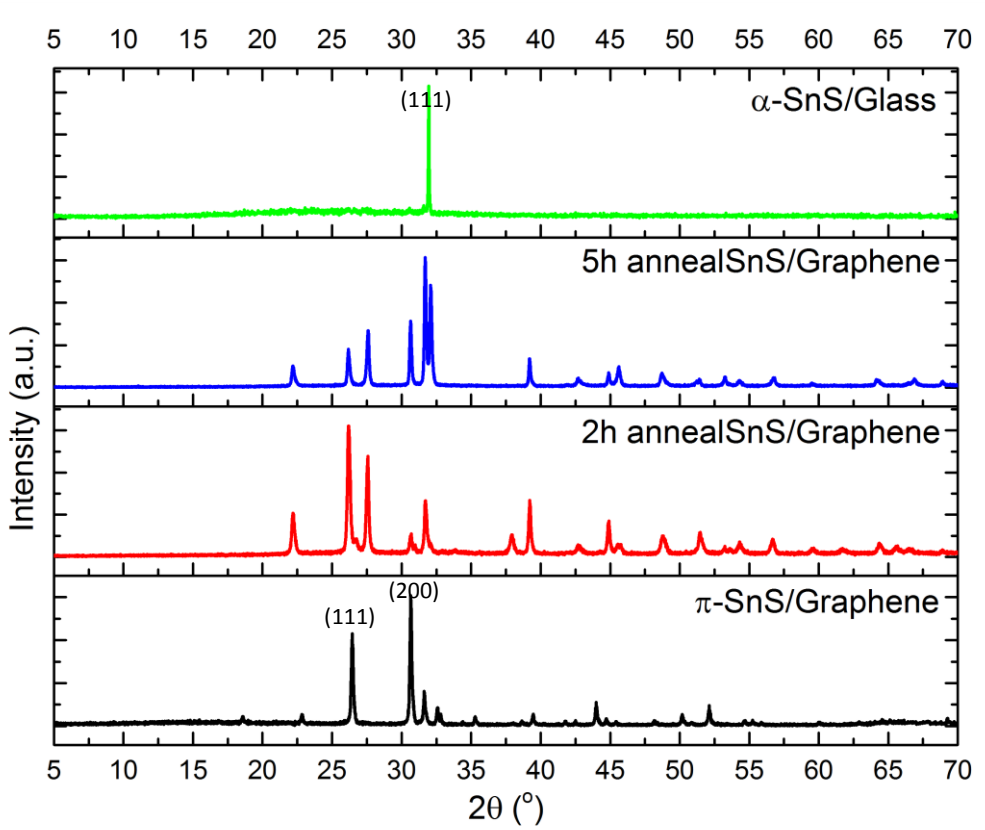

Figure 4.6 PXRD spectra of SnS deposited onto glass and graphene-glass substrates.

Crystallite size was analysed using the Scherrer formula. Table 4.1 displays the results of the analysis. It can be seen for π-SnS, the crystallite size is larger when grown on graphene, particularly normal to the (111) plane. This is in agreement with the observation that π-SnS grows preferentially over α-SnS on graphene compared to amorphous substrates. Scherrer analysis was applied to the (011) and (301) orthorhombic peaks for the samples annealed for 2 and 5 h, respectively. It was found the crystallite size increased with increasing annealing time, the crystallites being larger than those deposited directly onto FTO.

Table 4.1 SnS crystallite thicknesses corresponding to selected PXRD reflections.

	Crystallite thickness normal to reflection plane (nm)		
Peak	SnS cubic		SnS cubic FTO
(111)	102		82.4
(200)	111		119
Peak	2h anneal	5h anneal	SnS ortho FTO
(001)	86.3	115	78.8
(301)	81.4	121	74.6

4.2.3 Analysis of SnS films - Raman

Raman spectroscopy was carried out to study the as deposited π-SnS on graphene as it was annealed. Figure 4.7 shows the Raman spectra of the films and the graphene substrates. As the annealing time increases, the majority of the cubic Raman peaks disappear, to be replaced with peaks corresponding to α-SnS, although unidentified peaks (marked with a star) possibly belonging to π-SnS remain. This indicates a drop in film quality relative to orthorhombic SnS films directly deposited onto amorphous substrates. This is likely to be due to a phase mismatch between the hexagonal graphene substrate and the SnS film as the production of α-SnS on graphene requires annealing π-SnS rather than direct deposition. Raman spectroscopy of the graphene substrate reveals the evolution of the D peak, indicating damage is occurring during the annealing process.

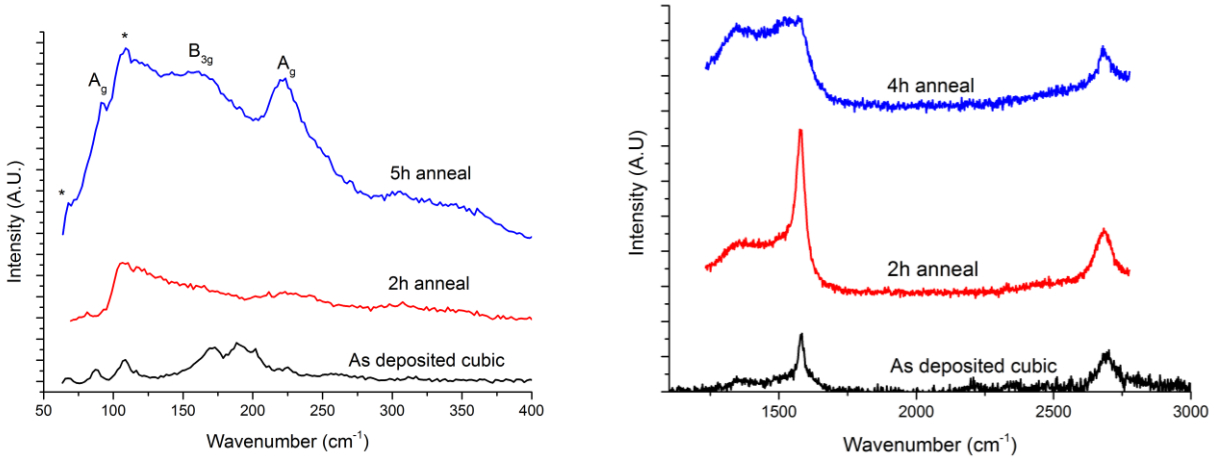

Figure 4.7 Raman spectra of SnS films (left) and graphene substrate (right) after various anneal times.* corresponds to unidentified peaks.

4.2.4 Analysis of SnS films - SEM and AFM

SEM of the films reveals closely packed cubic particles for the π-SnS film deposited on graphene. Upon annealing for 5h, it can be observed these cubic particles have transformed into rough edged platelets with larger lateral dimensions. SEM and AFM images of π-SnS and α-SnS are shown in figure 4.8. As both the films are densely packed they should be suitable for photo electrochemical measurements which require pinholes not to be present. EDS analysis revealed tin and sulphur in the correct ratios for both films, with carbon and oxygen present in quantities of less 2 atomic % for π-SnS and α-SnS. AFM analysis of the SnS films reveals an increase in roughness on annealing for 5h which is supported by SEM images.

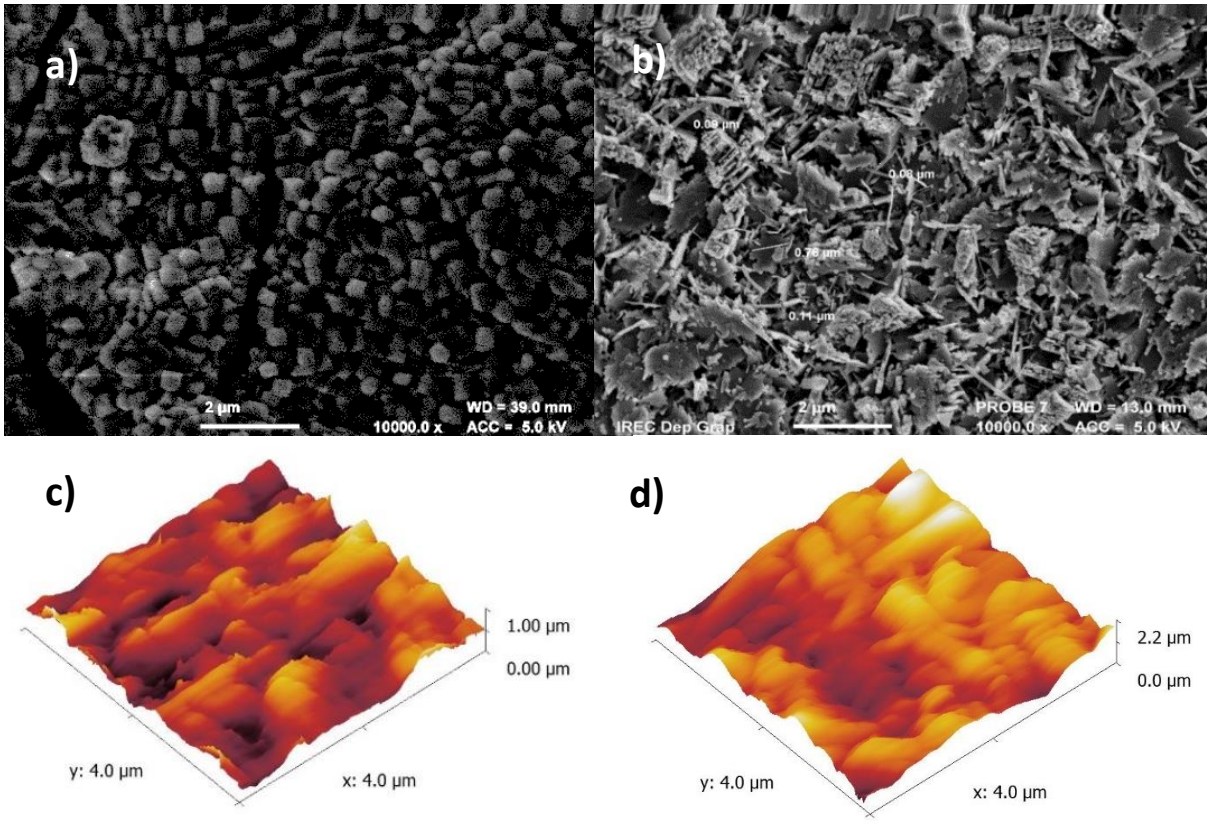

RMS: 0.150 µm RMS: 0.269 µm

Figure 4.8 a)+c): SEM and AFM of π-SnS on graphene. **b)+d)**: SEM and AFM of α-SnS on graphene.

4.2.5 Analysis of SnS films - Photoelectrochemical measurements of SnS Samples

Photoelectrochemical measurements were carried out to characterise the photocurrent generation properties of SnS films deposited onto graphene. Measurements were taken using chopped illumination (470 nm, 2.64 eV) with a frequency of 3 S on and 2 S off. Figure 4.9 presents the photo-electrochemical responses across a potential range of -1.0 to +1.0 V vs Ag|AgCl of π-SnS on graphene, α-SnS on graphene and α-SnS and π-SnS on FTO for comparison. The reductive redox electrolyte used in this experiment consisted of a 0.2 M $Eu(NO_3)_3$ aqueous solution purged with N_2. From figure 4.9 it can be seen α-SnS on both graphene and FTO produce exclusively anodic photocurrents, indicating p-type behaviour. Additionally only anodic photo currents were observed in of 0.1 M $Eu(NO_3)_3$. Large photocurrents are observed at bias potentials greater than +0.3 V and photocurrents are two orders of magnitude greater than the dark currents, an indication that the films do not consist of many pinhole defects.[65] The photocurrents increase with increasing anodic polarisation caused by band bending at the semiconductor-electrolyte interface and resulting in a

larger space charge region. This increases the collection of excited charge carriers, which are generated further from the electrolyte interface. Furthermore evidence of tunnelling or avalanche break down of the semiconductor films are not observed up to +/-1.0 V in all samples. At negative potentials, π-SnS on graphene produces approximately 30 % the current density of π-SnS deposited onto FTO. At positive potentials this is increased to 50 %. This comparative loss of current density can be explained by the lack of phase purity in the π-SnS-graphene. However, as discussed in the previous section, detailed analysis of the PXRD spectrum revealed larger crystallite sizes for π-SnS grown on graphene than FTO. Therefore, it is possible graphene is performing worse than FTO as a TE. The presence of a small defect peak in the graphene Raman spectrum indicates the graphene had been slightly damaged during the deposition process.

α-SnS on graphene generates roughly two orders of magnitude lower photocurrents than α-SnS deposited on FTO. The reasons for this are likely to include film quality of the SnS and the graphene in addition to graphene performing worse that FTO as an electrical contact overall as found for the cubic depositions. From PXRD and Raman it was found that although the crystallites of α-SnS on graphene were larger on graphene than FTO, the films were less phase pure, probably because the material was not α-SnS, reducing photo generation of charge carriers. The graphene substrate was also shown through Raman studies to degrade during the annealing process, further reducing its ability to act as a TE.

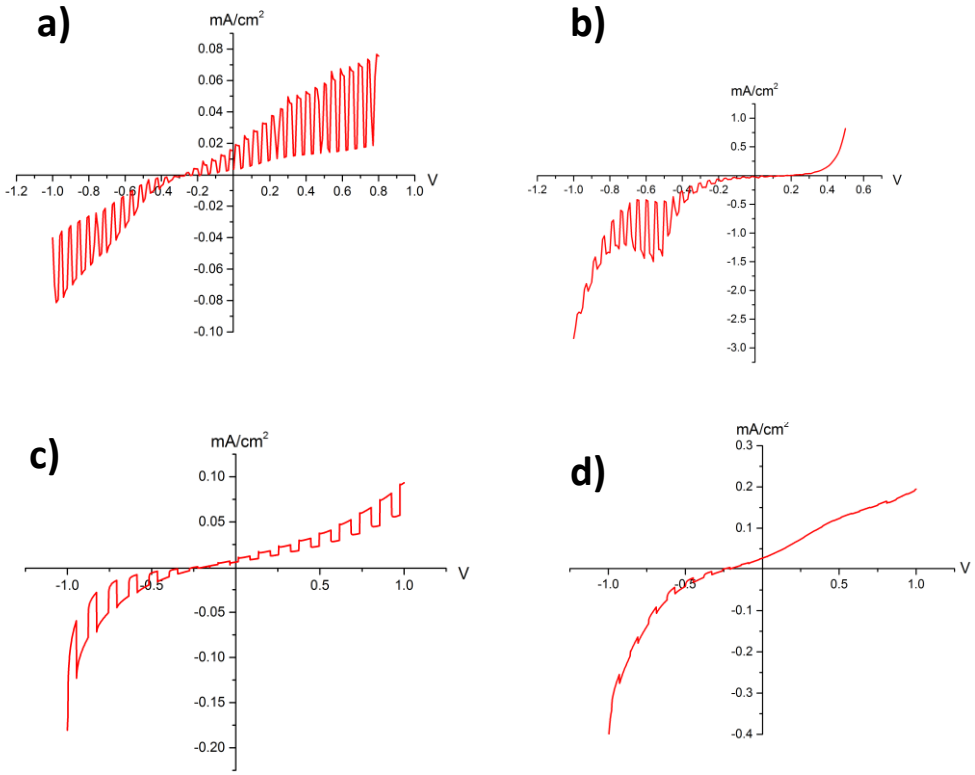

Figure 4.9 a) Photoelectrochemical response of π-SnS on FTO. **b)** Photoelectrochemical response of α-SnS on FTO. **c)** Photoelectrochemical response of π-SnS on graphene. **d)** Photoelectrochemical response of α-SnS on FTO.

The external quantum efficiency (EQE) spectra of π-SnS and α-SnS on graphene are displayed in figure 4.10. At –0.7 V, for π-SnS, there is an onset at 1100 nm (1.13 eV) and a step at 950 nm (1.31 eV), which interestingly correspond to the direct and indirect bandgaps of α-SnS. There is then a sharp onset at 780 nm (1.59 eV) which corresponds to the bandgap of π-SnS. It then peaks at 5.5 % at 700 nm (1.77 eV) whereupon it quickly declines at shorter wavelengths. At + 1.0 V, the EQE spectrum for π-SnS shows a more gradual onset at 760 nm (1.63 eV) which levels out at 680 nm (1.82 eV) which is followed by a gradual increase at shorter wavelengths. The α-SnS component of the EQE spectrum is not present at anodic potentials which is backed up by the photo-electrochemical measurements discussed above, which showed α-SnS does not produce photocurrents at positive potentials.

The EQE spectrum of α-SnS displays a similar shape to π-SnS until 780 nm (1.59 eV), where there is no sharp onset of a peak. This could indicate the continued presence of π-SnS phase in α-SnS after annealing. The spectrum gradually increases to 1% at 700 nm (1.77 eV), whereupon it slowly decreases at shorter wavelengths. At any wavelength, α-SnS has a smaller EQE than π-SnS on graphene, even in the 800-1100 nm region attributed to α-SnS. This again points to damage to the graphene substrate as a higher proportion of α-SnS should produce a larger EQE in the 800-1100 nm region if the graphene substrate remains unchanged.

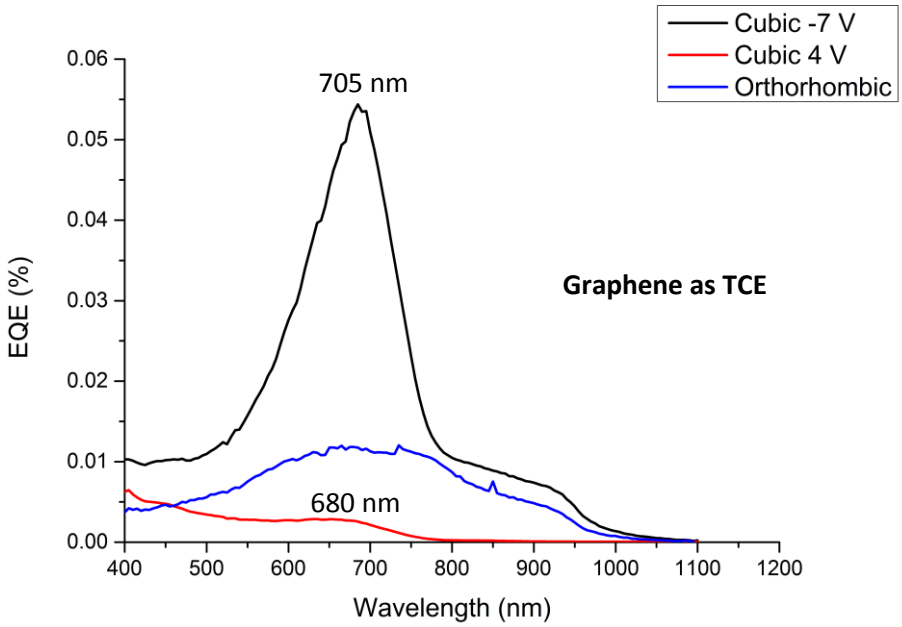

Figure 4.10 EQE spectra of α-SnS and π-SnS on graphene.

Figure 4.11 displays EQE spectra of π-SnS and α-SnS on FTO for comparison. All the spectra have similar shapes to the equivalent spectra with graphene substrates in figure 4.10. The cathodic π-SnS spectrum displays an onset at a shorter wavelength, indicating more pure π-SnS character. Additionally, the anodic cubic spectrum does not flatten out at 680 nm (1.82 eV) but continues to rise. The cathodic π-SnS spectrum peaks at 12 %, slightly over double that of π-SnS on graphene. The anodic spectrum peaks at 18 %, nearly 20 times higher than π-SnS on graphene. Additionally, the orthorhombic spectrum peaks roughly 10 times higher than orthorhombic SnS on graphene.

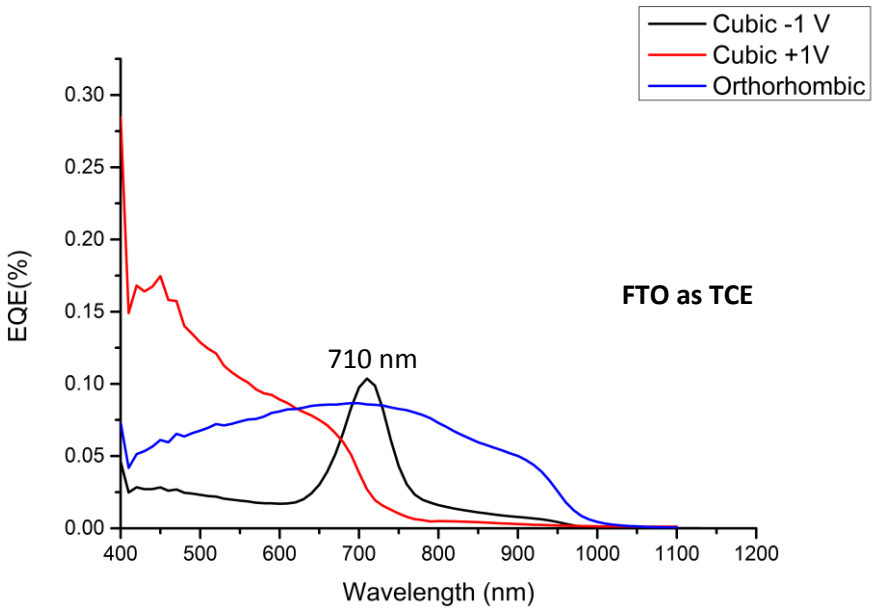

Figure 4.11 EQE spectra of α-SnS and π-SnS on FTO.

By integrating under the entire EQE spectra it is possible to predict the device performance under solar illumination by adjusting for the various proportions of wavelengths that make up the solar spectrum. Table 4.2 displays the calculated short circuit currents for the SnS films on graphene and those on FTO.

Table 4.2 Calculated short circuit currents for SnS on graphene and SnS on FTO.

SnS on graphene		SnS on FTO	
Material	Short circuit current ($mAcm^{-1}$)	Material	Short circuit current ($mAcm^{-1}$)
Cubic -1V	0.737	Cubic -1V	1.94
Cubic +1V	0.0704	Cubic +1V	0.352
Orthorombic -1V	0.283	Orthorombic -1V	2.48

As discussed in the supplementary information chapter, S.3.5, if $[\ln(1-\Phi)]^2$ is plotted against hv and a straight line is drawn close to the onset where the plot becomes linear, the bandgap energy is the value at which the straight line crosses the x axis. Plots for $[\ln(1-\Phi)]^2$ Vs hv for the π-SnS and α-SnS deposited on graphene are displayed in figure 4.12.

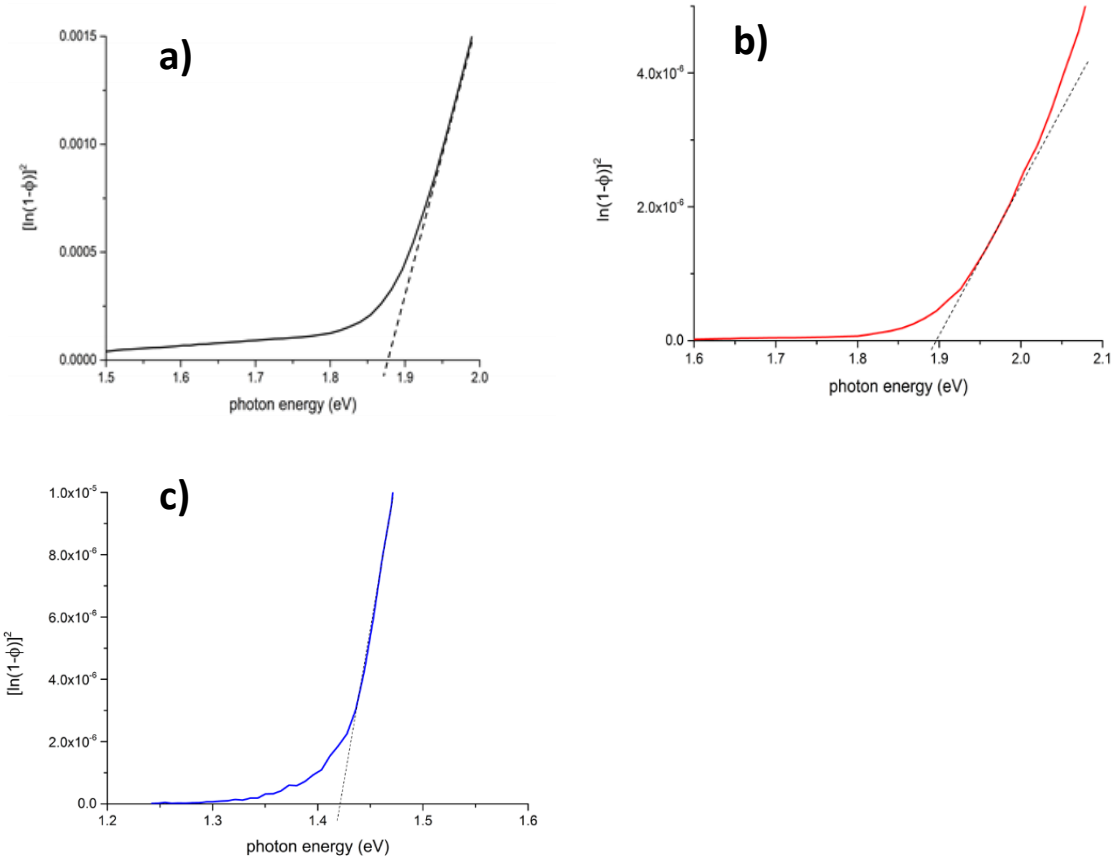

Figure 4.12 Plots to calculate bandgap **a)** π-SnS -1 V **b)** π-SnS +1V **c)** α-SnS.

Bandgaps for SnS on FTO were also calculated in the same way, it was found SnS on graphene has a higher bandgap than on FTO. This is probably because of strain effects, where the strain created by the hexagonal graphene substrate is greater than that produced by rutile FTO. It has be theorised by Efthimios et.al. that the bandgap of SnS increases under strain.[66] Table 4.3 contains the calculated bandaps for SnS on graphene and FTO.

Table 4.3 Calculated bandgaps of SnS on graphene and SnS on FTO.

SnS on graphene		SnS on FTO	
Material	Calculated bandgap (eV)	Material	Calculated bandgap (eV)
Cubic -1 V	1.87	Cubic -1 V	1.63
Cubic +1 V	1.89	Cubic +1 V	1.73
Orthorhombic -1V	1.42	Orthorhombic -1 V	1.25

4.3 SnS on graphene conclusions

It has been shown SnS can successfully be deposited onto graphene. We hypothesised that due to the structure of graphene, at 375 °C SnS grows in the π-SnS polymorph whereas it grows in the α-SnS form on various other substrates. Annealing for 5 h hours transforms π-SnS phase on graphene to α-SnS, however this process introduced damage to the graphene substrate, lowering its performance in photo-electrochemical tests. Although performing worse than SnS deposited onto FTO, it has been demonstrated for the first time that SnS deposited onto graphene can successfully produce a photocurrent when immersed in an electrolyte. As mentioned in previous sections of this work, graphene has a significant effect on the growth of materials deposited by AA-CVD.

4.4 Single crystal SnS from high temperature CVD - Results and discussion

4.4.1 Depositing SnS single crystals

As discussed in the introduction to this chapter, it is widely believed one of the main factors holding back the development of SnS-based solar cell devices from reaching their full potential, is the quality of the SnS, which is in turn, limited by the techniques by which it is deposited. Therefore, it is of great importance that techniques are found which produce higher quality SnS. Very recently there has been a rapidy growing body of literature demonstrating the use of high temperatures and simple oxide or sulfide starting materials to produce single crystals of various materials on a variety of substrates. This technique was used to produce single crystal WS_2 and large area monolayer WS_2 on graphene in the previous chapter.

Therefore a logical question to ask was whether single crystal SnS could be produced by this method? A near identical experimental setup was used to as outlined in section 3.8 of the WS_2 chapter. Figure 4.13 displays a schematic of the reactor used. The only difference between the experimental setup in section 3.8 is the SnO_2 is placed in the boat at 7 rather than WO_3.

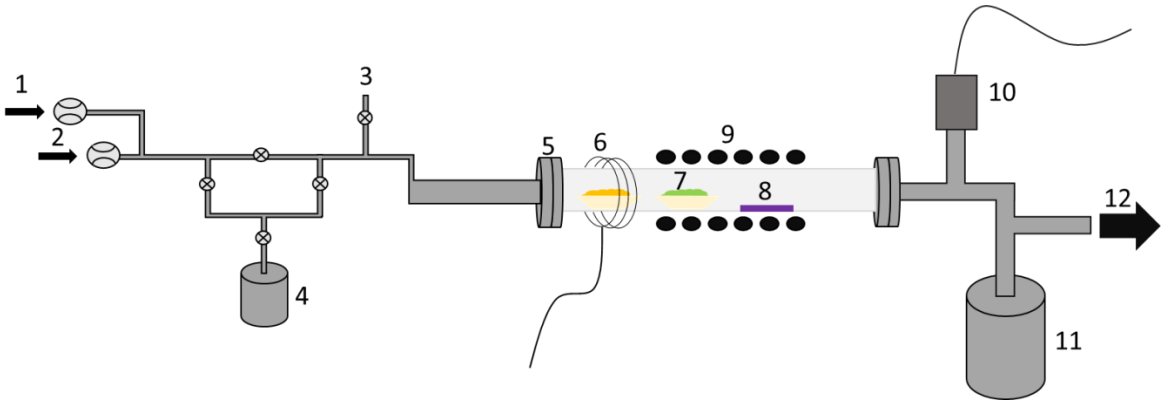

Figure 4.13 Schematic of reactor used to deposit single crystal SnS. The numbers in the diagram correspond to- 1: Provides a flow of Ar to act as a carrier gas. 2: Not used. 3: Not used. 4: Not used 5: Ultra-Torr fitting to 1 " quartz tube. 6: Heating tape around the position where an alumina boat containing elemental sulphur sits. 7: Alumina boat containing SnO_2 powder. 8: SiO_2 wafer. 9: Furnace. 10: Pressure sensor. 11: Liquid N_2 trap (not used) 12: To extraction/pump.

Before each run, the system was pumped down to ca. $2x10^{-2}$ mbar and held for 30 mins. The system was then flushed with 500 ccm of Ar for 30 mins to ensure residual water and oxygen were removed from the system. The furnace was initially heated to 600 ^{o}C and held at that temperature for 10 mins before the furnace was heated up further and the heating tape around the boat containing the sulphur was heated. The heating tapes were set at 180 ^{o}C, Ar flow rate at 100 ccm, main furnace temperature of 1070 ^{o}C and the alumina boats contained 1.0g of sulphur in the first and 1.0g SnO_2 powder in the second. When the furnace was at 1070 ^{o}C, it was held at that temperature for 30 mins, after which the heating tapes were turned off and the furnace was allowed to naturally cool to room temperature. Upon removal from the furnace the SiO_2 substrate appeared to sparkle to the naked eye. On closer inspection under a microscope individual crystals could be identified. It was found increasing the deposition time did not increase the size of the crystals, possibly due to quenching of the SnO_2 precursor over time due to the sulphur atmosphere. To characterise the crystals produced, a range analytical techniques were used, the results of which are disccused below.

4.4.2 Analysis of SnS single crystals - PXRD

The PXRD spectrum of a substrate with the crystals on it is shown in figure 4.14. The very intense peak at 32 ^{o} corresponds to the (400) plane of orthorhombic SnS. Its relative height compared to the (001) silicon substrate peak at 33 ^{o} gives an indication of the crystallinity of the material deposited on the substrate. The small peak at 31.5 ^{o}corresponds to the (111) plane of orthorhombic SnS. As only these two peaks are present, the PXRD pattern indicates the crystals are very highly oriented, with the majority of them having a (400) basal plane. Optical analysis discussed in the following section helps to confirm this.

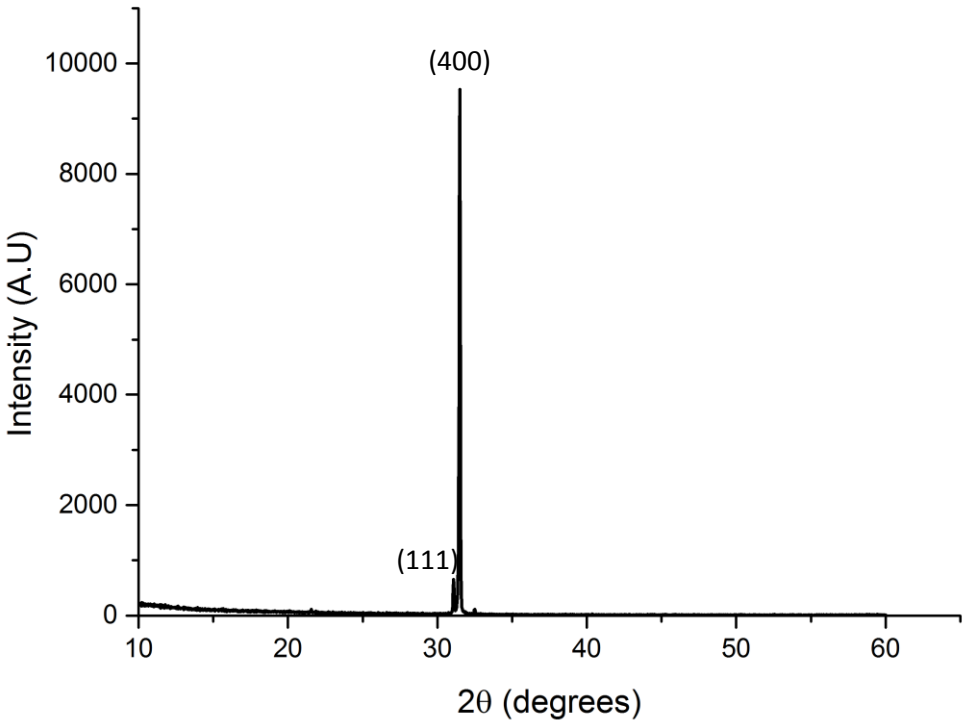

Figure 4.14 PXRD of SnS single crystals on substrate

Figure 4.15 displays the crystal structure for orthorhombic SnS with the planes that produced reflections highlighted. Scherrer analysis could not be carried out as the crystal dimensions were too large to give accurate results.

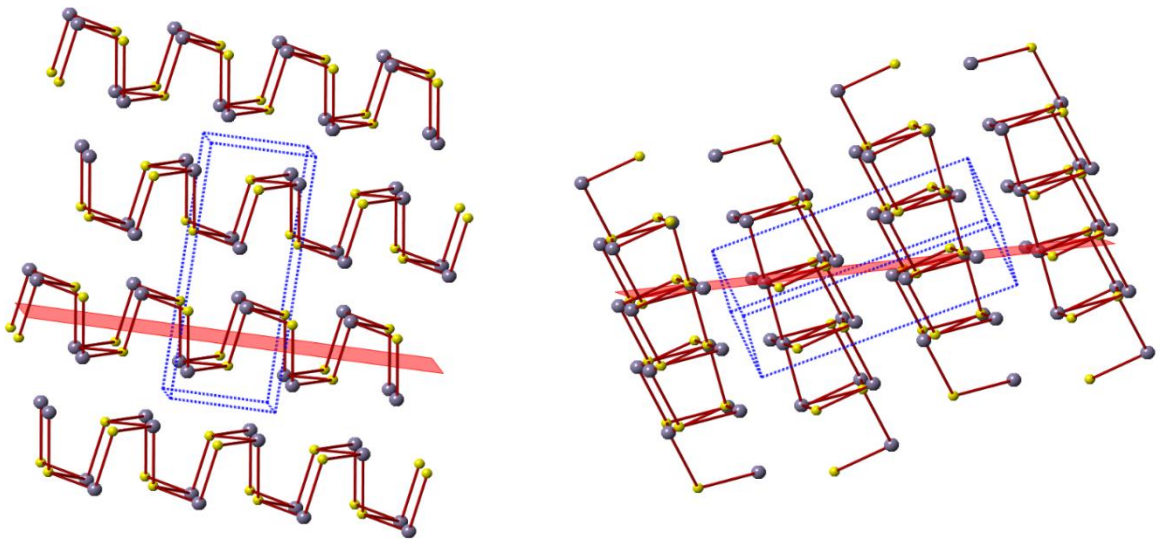

Figure 4.15 Crystal structures of α-SnS with the planes producing reflections in the PXRD spectrum highlighted

4.4.3 Analysis of SnS single crystals - Raman and optical

Optical analysis under a microscope revealed many well defined crystals on the SiO_2 substrate with various morphologies. Figure 4.16 gives three example images representative of many of the crystals formed. The angles highlighted in blue were measured to be 95 °, the angles in green 132.5 ° and the angles highlighted in red were measured to be 85°.This provides evidance that growth proceeds along the 132.5 ° (green) corners until they meet to form a 95 ° (red) corner as shown in picture **iii)**. **iii)** also shows some of the crystals have fractures and are less ordered.

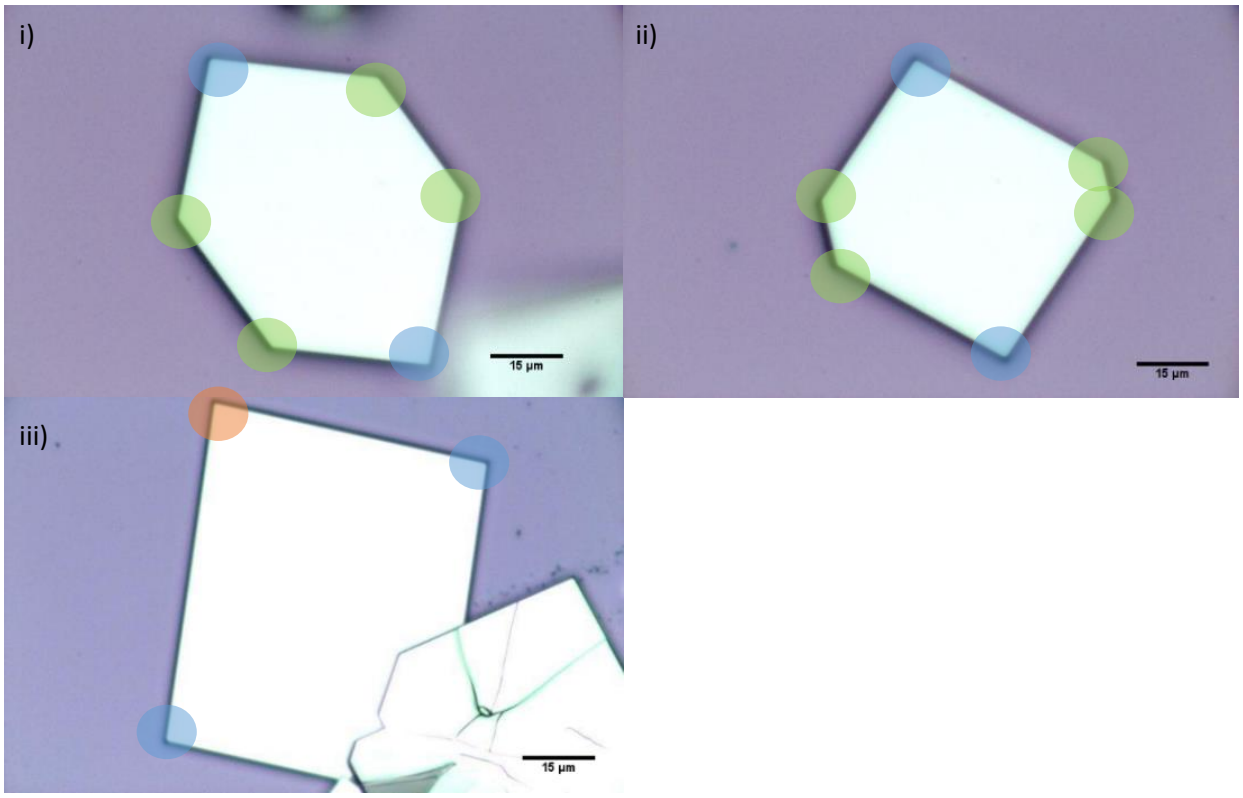

Figure 4.16 Optical images of SnS single crystals.

Raman spectrum recorded on different crystals all displayed peaks only corresponding to orthorhombic SnS. Figure 4.17 displays an example Raman spectra with Raman maps of the crystal **ii)** shown in figure 4.16. These maps demonstrate exclusively orthorhombic SnS is present in the crystal.

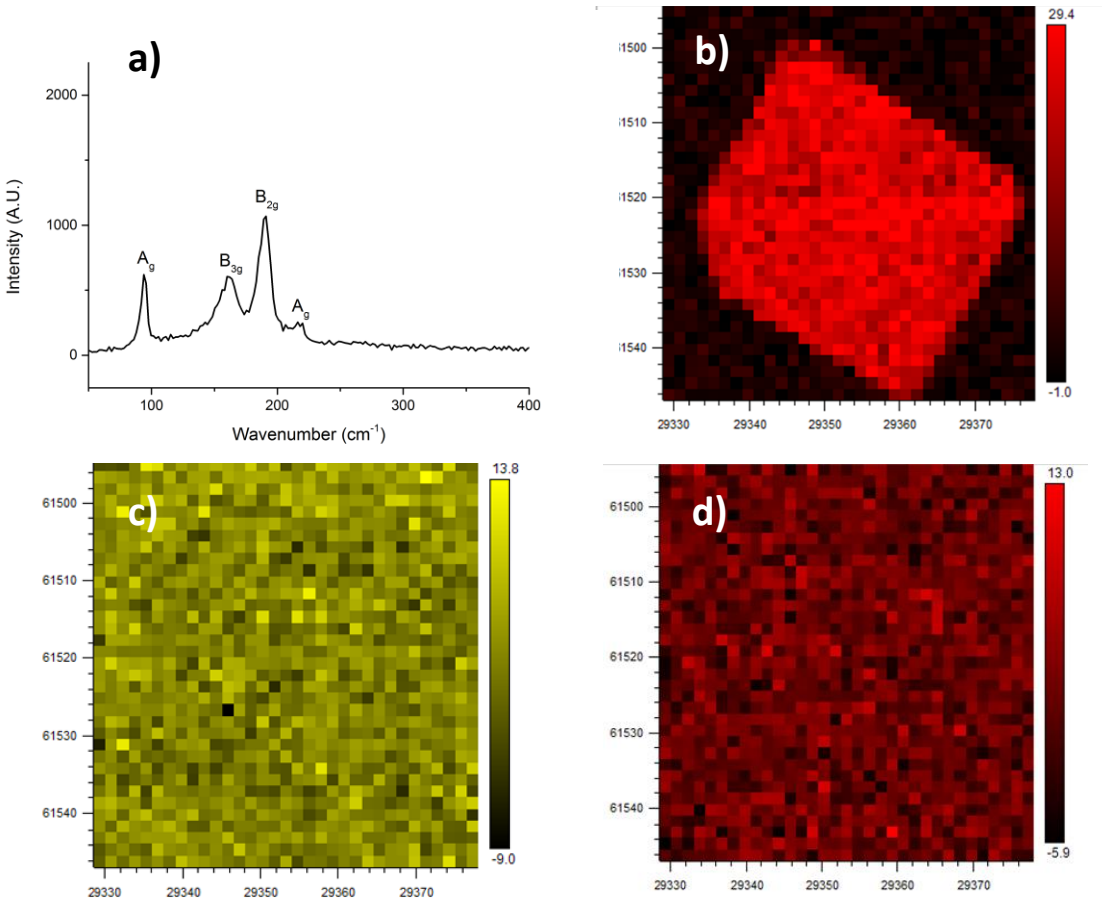

Figure 4.17 a) Example raman spectra of SnS crystal. **b)** Raman map of α-SnS B_{2g} peak intensity. **c)** Raman map of SnS_2 A_{1g} peak intensity. **d)** Raman map of Sn_2S_3 302 cm^{-1} peak intensity.

4.4.4 Analysis of SnS single crystals - SEM and EDS

SEM images of various crystals can be seen in figure 4.18. The SEM images give similar information as the optical images. Image **ii)** in figure 4.18 shows an example of an SnS sheet folding in on itself. This type of orientation out of the plane of the substate could explain the presence of the (111) peak in the PXRD pattern. Image **iii)** is an example of a crystal with multiple domains.

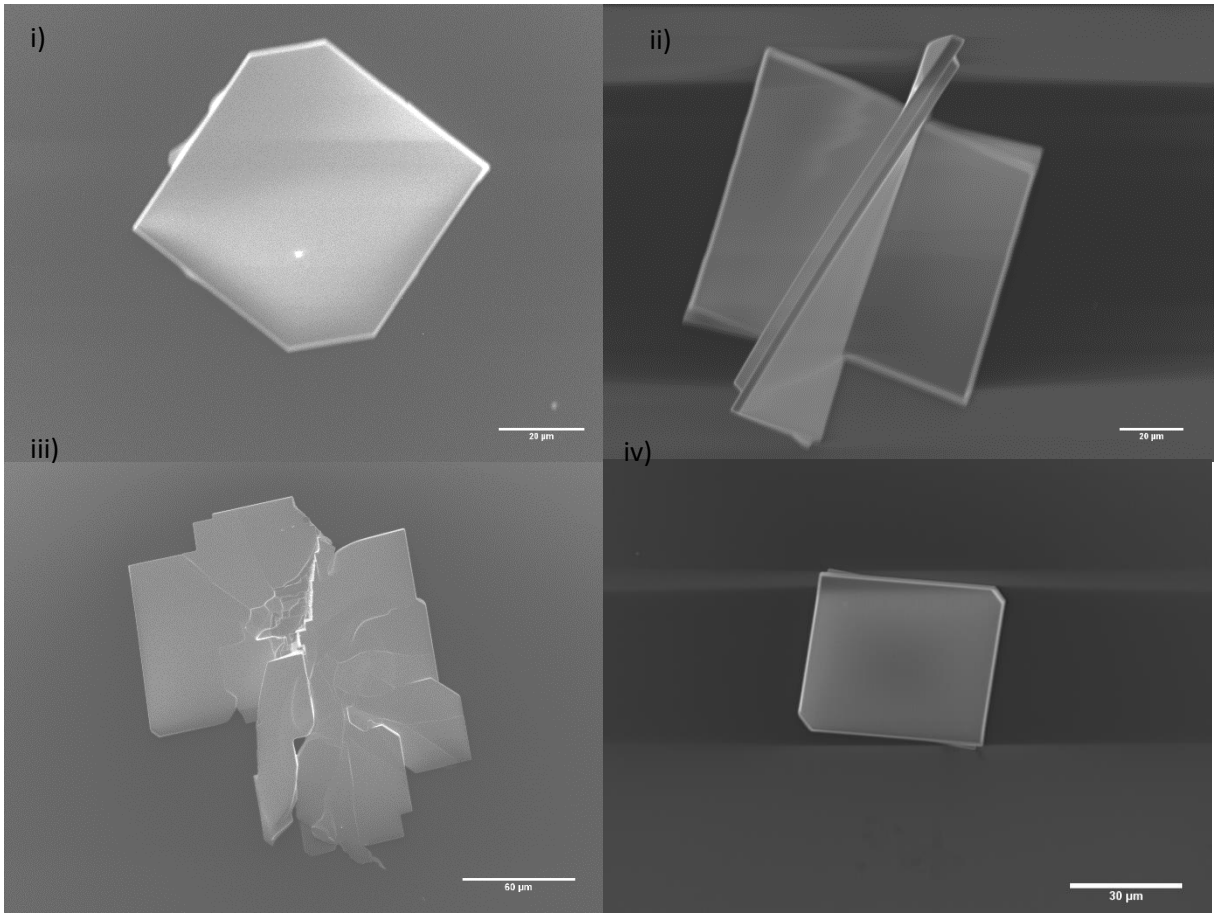

Figure 4.18 SEM images of SnS single crystals

Figure 4.19 shows EDX maps for oxygen, tin and sulphur taken from the crystal in image **iv)** of figure 4.18. It shows the lack of oxygen on the crystal but the presence of tin and sulphur on it. Individual EDX spectra revealed tin and sulphur in a 1:1 ratio within the error of the equipment. Individual EDX spectra can be found in supplementary information.

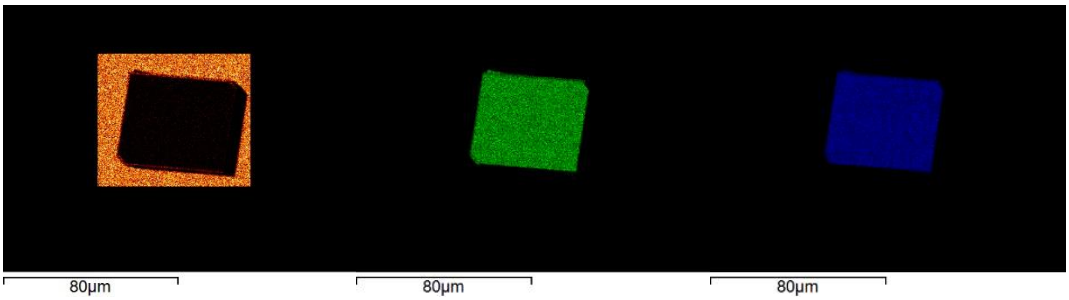

Figure 4.19 Left: EDX map of oxygen. Middle: EDS map of tin.Right: EDS map of S.

4.4.5 Analysis of SnS single crystals - AFM

AFM measurements confirmed the highly ordered nature of the crystals. RMS values range from 1-5nm, comparable with the roughness values of graphene. An example AFM of a crystal and step heights of various crystals are displayed in figure 4.20. The crystals were found to be consistently between 4 μm and 5 μm thick, far thicker than other single crystals for various materials previously published in the literature.

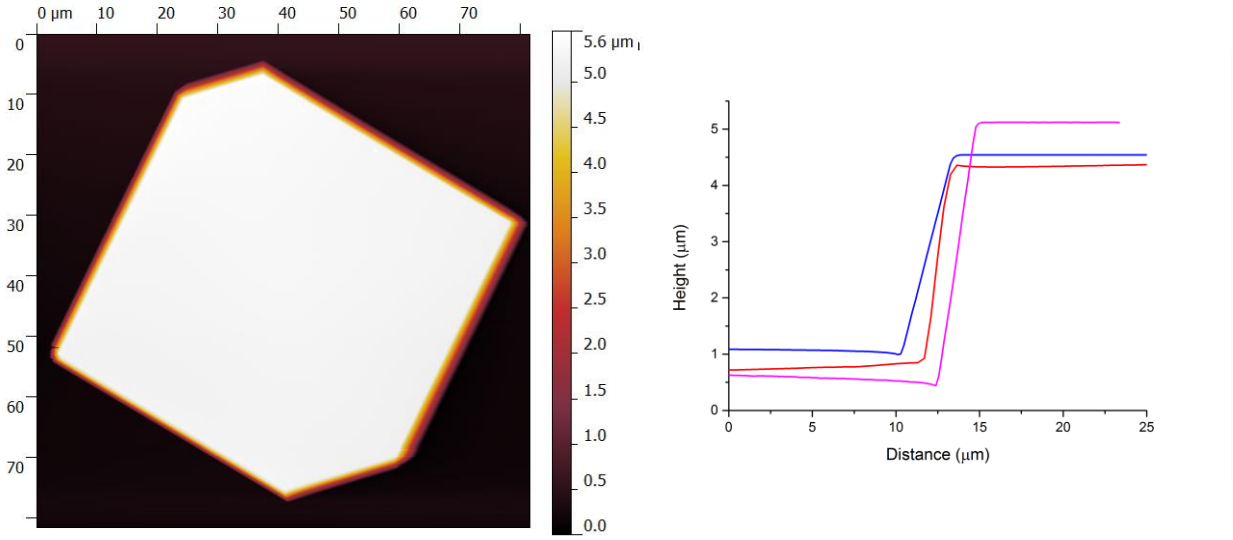

Figure 4.20 AFM of SnS single crystal and step heights of various crystals.

4.5 Single crystal SnS from high temperature CVD conclusions

Using a high temperature CVD technique it has been demonstrated that SnS single crystals large enough to produce devices to test optical and electronic properties can be synthesised. This finding is a step towards producing high quality, large area SnS for solar devices, with the choice of substrate and further tuning of reaction conditions likely to produce even larger single crystals. Since the time of writing this piece of work, Ozkan et al. have reported producing SnS single crystals using a similar experimental technique.[67] Interestingly, although they produce crystals with a similar shape to the ones we report, they are about a quarter of the size and much thinner. The crystals reported by Ozkan et al. are roughly 10 nm in height compared to ca. 4000 nm reported in this work. As they grow their crystals at lower temperatures and higher Ar flow rates, it will be important to elucidate the relationship between these parameters and crystal dimensions in the future.

4.6 SnS_2 on graphene - Results and discussion

'Combustion processing' has proven to be an effective route to creating metal oxide thin films.[68] There is also a growing body of work on the synthesis of metal sulphide by combustion processing.[69,70,71] Combustion processing involves using precursors that upon decomposition produce heat which allows the formation of the desired materials at lower substrate temperatures. Combustion processing requires an oxidiser and a fuel, the oxidiser can be a nitrate anion (NO_3^-), although stronger oxidative anions can be used, such as perchlorates, iodates, bromates or manganates. Nitrates however are often used due to the low toxicity, high volatility, and less contaminating combustion products. For oxide materials, fuels are often urea or acetylacetone, and for sulphide materials, thiourea and thiosemicarbazide have been used. Thus far the combustion processing of SnS_2 has not been explored. The results of this body of work will follow a similar structure to section 4.2, with the deposition of SnS_2 onto different substrates including graphene by AA-CVD will be analysed and their photocatalytic properties explored.

Tin nitrates have been found to be unstable in the solid state,[72] so precursor solutions were prepared following the same protocol set-out by Marks et al,[68] where equimolar solutions of $SnCl_2$ and ammonium nitrate can be an effective substitute to pure tin nitrates. The solvent selected was ethanol which can act as an additional fuel source. Attempts to use water as a solvent caused the rapid formation of SnO_2. Thiourea was selected as the 'sulphur source' and 'fuel'. The thiourea would not completely dissolve into the solution so concentrated nitric acid was added to reach a pH of ca. 2. As well as solubilising the thiourea it contributed additional nitrate ions to the precursor solution.

If the precursor solutions were allowed to evaporate, colourless and yellow crystals were evolved. Single crystal X-ray analysis found the yellow crystals to consist of elemental sulphur and the colourless crystals of α,α- dithiobisformamidinium dinitrate (α-DD) originally characterised by G.B. Jameson et al. obtained from a solution of thiourea nitrate oxidised by H_2O_2.[73] The schematic and molecular structure of α-DD is displayed in figure 4.21

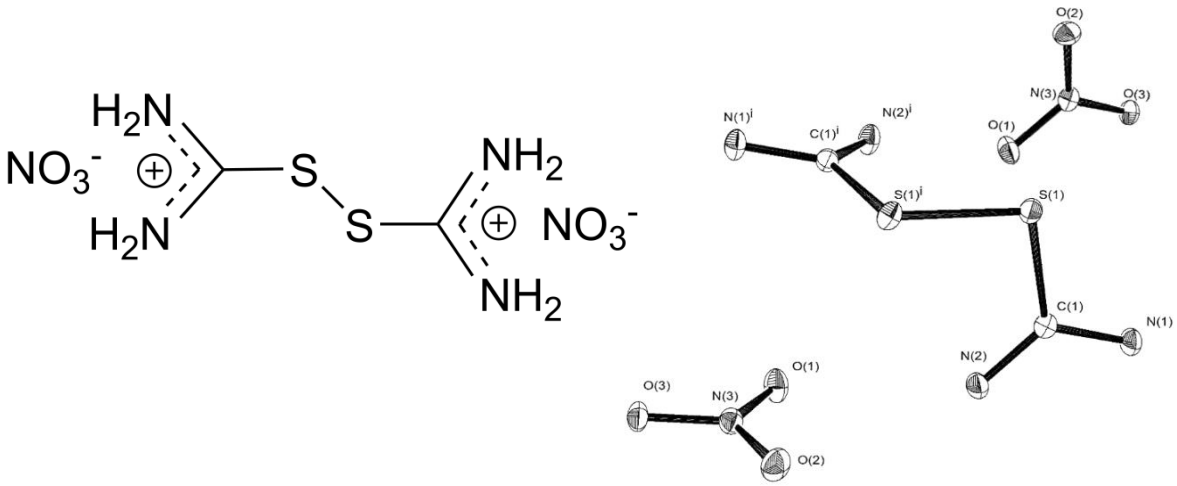

Figure 4.21 Schematic and molecular structure of α-DD, ellipsoids shown at 50% probability.

If α-DD crystals were re-dissolved in ethanol, elemental sulphur would slowly form over a number of days, confirming breakdown of α-DD is the source of the crystals of sulphur originally formed.

A TGA and differential scanning calorimetry (DSC) trace of α-DD is displayed in figure 4.22. At ca. 70 °C there is a rapid exothermic decomposition event with a mass loss of ca. 50 % which likely corresponds to 2 molecules of carbodiimide. The gradual mass loss then likely corresponds to the evaporation of sulphur and organic products.

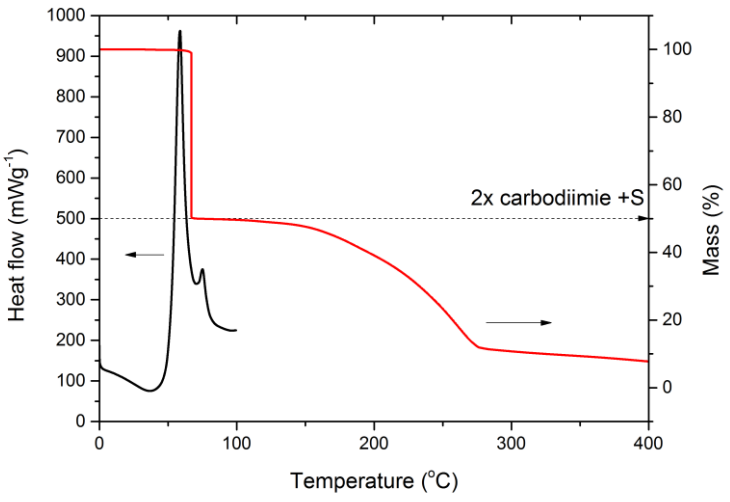

Figure 4.22 TGA and DSC traces of α-DD. TGA ramped at 5 °Cmin^{-1}DSC ramped at 2 °Cmin^{-1}.

4.6.1 Depositing graphene-SnS_2 films

As part of a wider study, outlined in I. Ahmet's thesis, depositions of different concentrations of $SnCl_2$ and thiourea were explored along with different reaction temperatures onto glass and FTO. It was found that the ratio of $SnCl_2$ to thiourea did not affect the phase of the SnS_x produced, although ratios of 1:2 of $SnCl_2$ to thiourea produced the most adherent homogeneous films. It was found temperature had a large effect on the phase of SnS_x. At temperatures ≤375 ^oC, SnS_2 was exclusively formed whereas at higher temperatures α-SnS was additionally formed, although never exclusively or in as high quality as the SnS films discussed in section 4.2. Reaction temperatures of 375 ^oC produced the most homogenous adherent films. Therefore using the same AA-CVD apparatus used in chapter 3, the final deposition parameters chosen to deposit SnS_2 onto graphene, FTO and glass were as follows:

- 1:2 ratio $SnCl_2$ to thiourea in a solution of ammonium hydroxide, nitric acid and ethanol.
- Reactor temperature of 375 ^oC with a deposition time of 30 mins.

Full experimental details can be found in chapter 5.

The deposited films on glass, FTO and graphene were yellow, uniform and well adhered, although the edges of the graphene sheet were visible. Graphene was grown and transferred onto glass by methods outlined in chapter 2.

4.6.2 Analysis of SnS_2 films - PXRD

PXRD analysis found SnS_2 films deposited onto glass, FTO and graphene to be crystalline. All the peaks present either corresponded to SnS_2 or FTO. All the films have a high degree of orientation in the (001) plane, however unlike WS_2 on graphene, all the films display a similar degree of orientation. The differences in intensities of the peaks is also far less significant. Scherrer analysis revealed the crystallite thickness of SnS_2 normal to the (001) plane was ca. 33 nm for all substrates. PXRD traces for SnS_2 on glass, FTO and glass with transferred CVD graphene are displayed in figure 4.23.

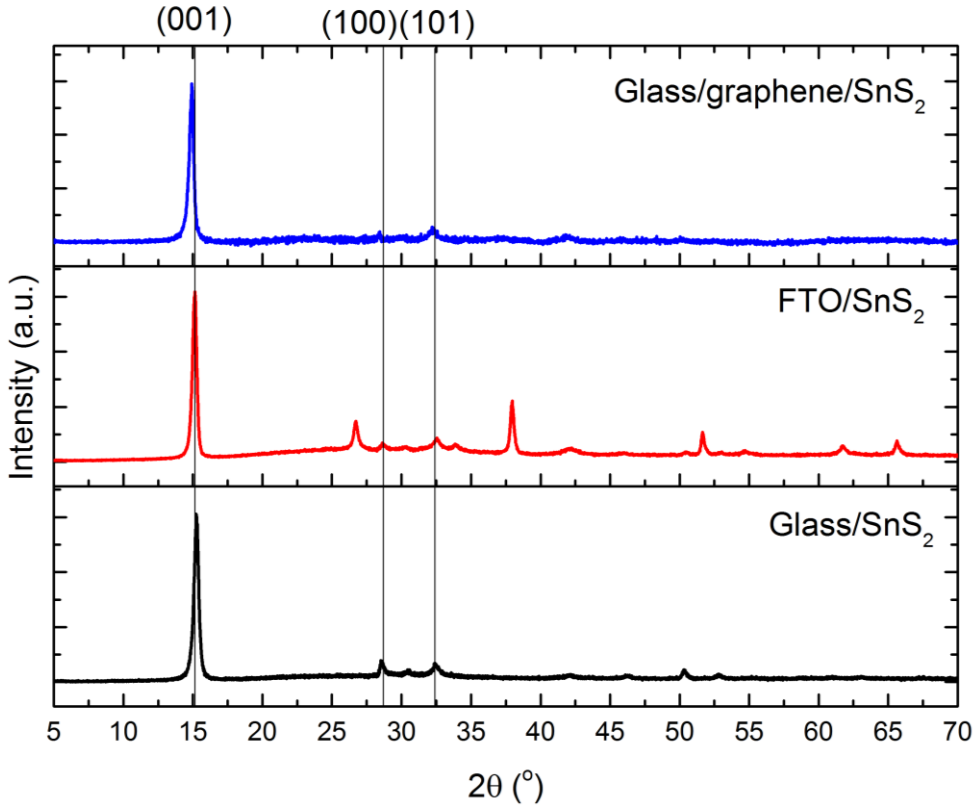

Figure 4.23 PXRD spectrum of SnS_2 on various substrates the most prominent SnS_2 peaks are all labelled the only non-SnS_2 peaks present belong to FTO.

4.6.3 Analysis of SnS_2 films - Raman and optical

Raman analysis was undertaken on SnS_2 films deposited on glass, FTO and graphene. Figure 4.24 shows Raman spectra of SnS_2 deposited on glass and graphene and an optical image of the boundary between the transferred graphene and glass substrates. The A_{1g} peak, consistent with data for single crystal SnS_2 was clearly defined.[74] Additionally, no other peaks corresponding to SnS, Sn_2S_3, SnO, or SnO_2 were present. The broad peak at ca. 500-600 belongs to peaks from 2H or 4H polytypes of SnS_2. The fine structure of the Raman spectra between 0 and 400 wavenumbers most closely match the spectrum for the 2H polytype published by A J Smith et. al.[75] However the 4H polytype has a similar spectrum so the 2H polytype is only tentatively assigned. As single crystals are not being studied, it is possible both polytypes are existing simultaneously. The spectrum of SnS_2 on graphene has the G and 2D peaks present. Importantly the D peak indicating damage to the graphene substrate is not present. This indicates unlike the SnS deposition conditions, the conditions for the deposition of SnS_2 do not damage the graphene substrate. As both SnS and SnS_2 were deposited at 375 °C, it is likely that the shorter deposition time of 30 mins compared to 60 mins for SnS_2 allowed less opportunity

for damage. Additionally SnS_2 could be deposited onto graphene directly whereas orthorhombic SnS required an annealing step which introduced a lot of damage, as discussed earlier in the chapter.

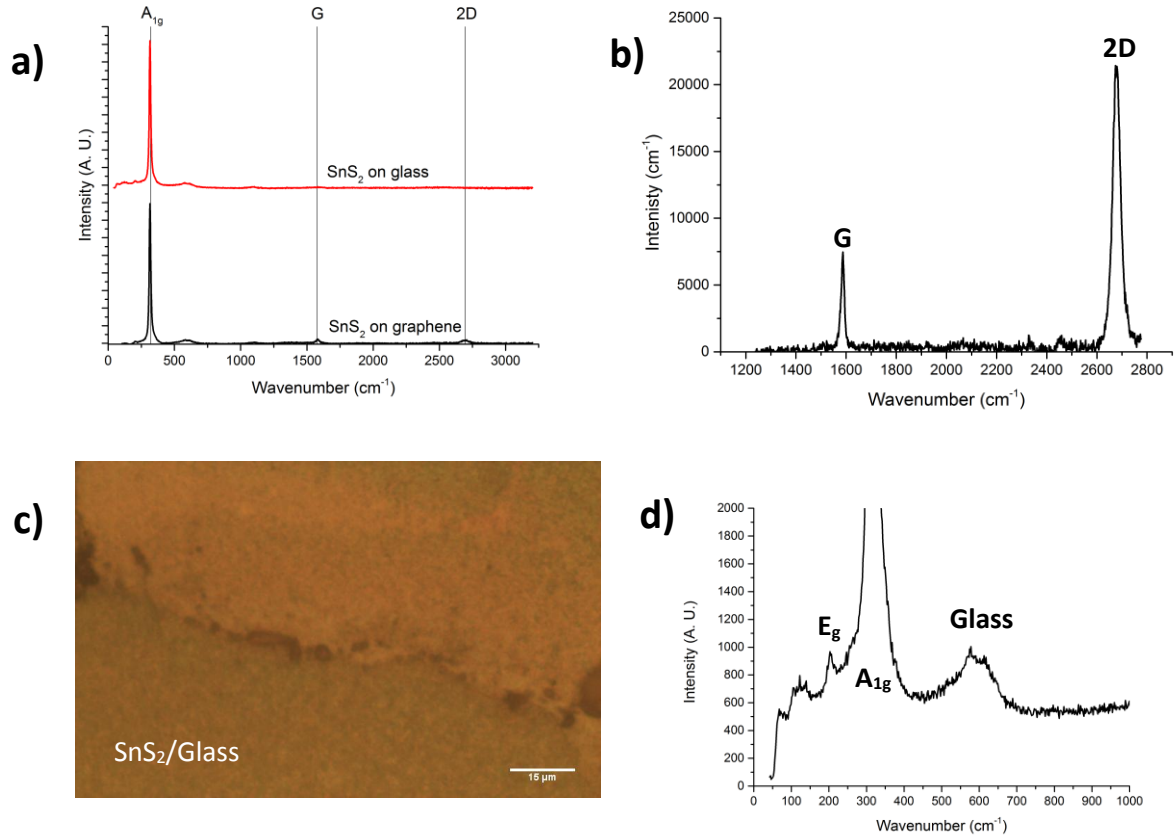

Figure 4.24 a) Raman spectra of SnS_2 on graphene and SnS_2 on glass. **b)** Raman spectrum of undamaged graphene substrate. **c)** Optical image of boundary between glass and graphene substrates with SnS_2 covering both. **d)** Magnified Raman peaks of SnS_2.

4.6.4 Analysis of SnS_2 films - SEM

SEM analysis revealed a change in morphology when SnS_2 was deposited onto glass and FTO compared to graphene. Depositions onto glass and FTO produced crystallite flake morphology, similar to the morphologies found for WS_2 deposited onto glass and silicon in the WS_2 chapter. A reason for this could be the structural similarities between WS_2 and SnS_2. As Raman analysis found SnS_2 to be in its most common 2H polytype, it is likely the mechanistic growth model based on structure discussed for WS_2 still applies. This idea is reinforced by the smoothing of the SnS_2 film that can be observed in figure 4.25 when SnS_2 is deposited on graphene. Although the films have been greatly smoothed there is still some differences compared to the WS_2 films deposited on graphene. It can be seen for SnS_2 on graphene, the films are not as continuous, with individual crystals of

similar structure to SnS_2 on glass and FTO visible. This is backed up by PXRD results which do not display the same dramatic increase in peak intensity as the WS_2 films on graphene displayed.

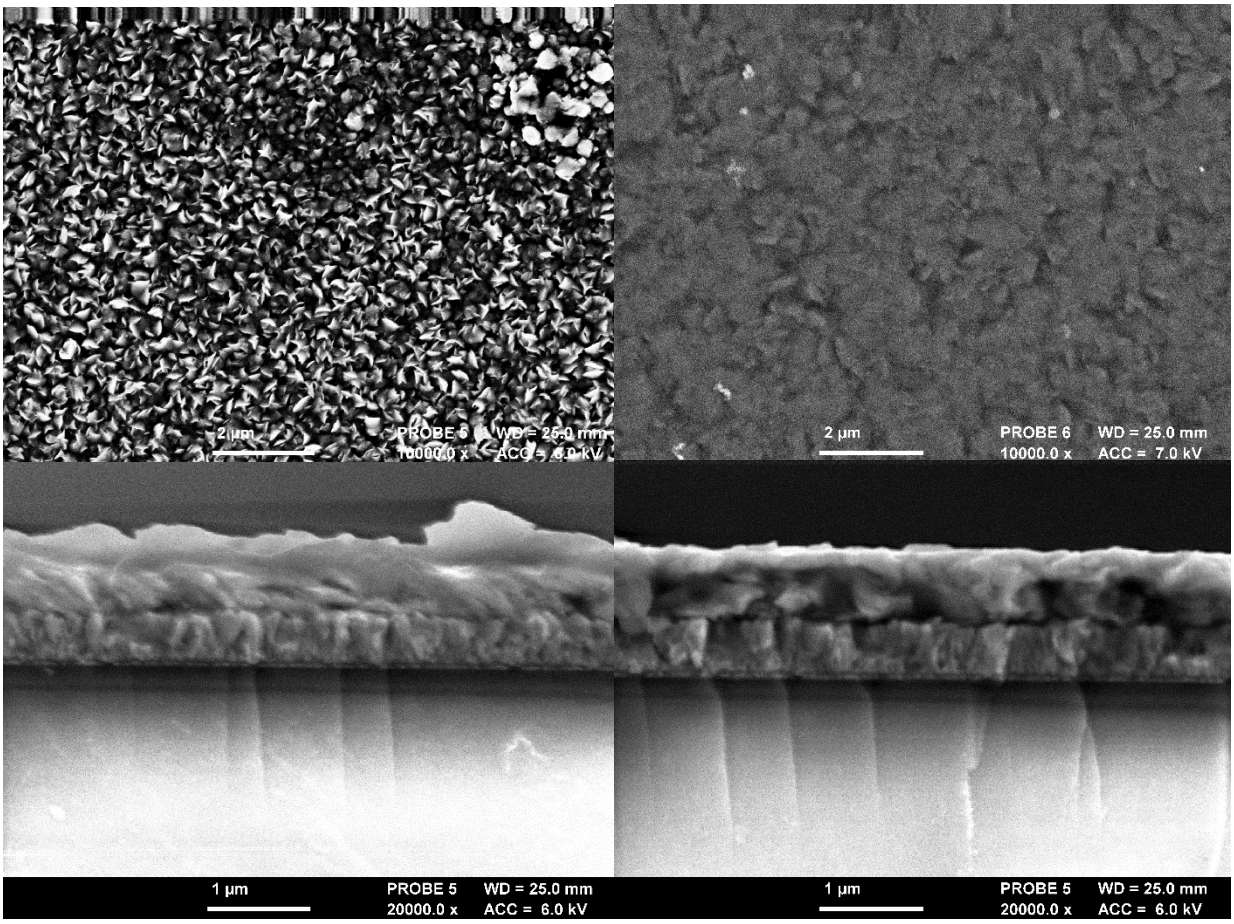

Figure 4.25 Top and bottom left: Top down and side on SEM images of SnS_2 on FTO. Top and bottom right: Top down and side on images of SnS_2 on graphene transferred onto SnS_2.

4.6.5 Analysis of SnS_2 films - AFM

AFM analysis found a change in the morphology of the deposited SnS_2 films on graphene compared to glass and FTO in keeping with the results found by SEM. Figure 4.26 shows AFM images of SnS_2 on glass and on graphene. The SnS_2 grown on graphene is flatter than that grown on glass or FTO, with RMS values roughly halved. However in keeping with PXRD and SEM results, the films are an order or magnitude rougher than the WS_2 films deposited on graphene, with the flattest WS_2 film having an RMS of 0.8 nm and SnS_2 on graphene having an RMS of 26.7 nm.

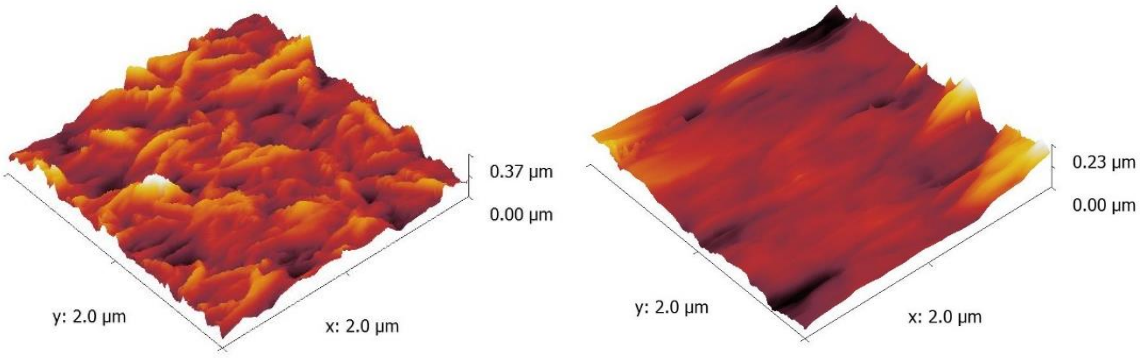

RMS: 45.8 nm

RMS: 26.7 nm

Figure 4.26 3D AFM images of SnS_2 grown on glass (left) and graphene (right).

4.6.6 Analysis of SnS_2 films - Photoelectrochemical measurements of SnS_2 Samples

Photoelectrochemical measurements were carried out to characterise the photocurrent generation within SnS_2 films deposited onto graphene. Measurements were taken using the same conditions as SnS for SnS_2 on graphene, and SnS_2 on FTO for comparison. From figure 4.27 it can be seen SnS_2 on graphene and FTO behaves very similarly. Photocurrents for SnS_2 on graphene are larger. At +1V, the photocurrent for SnS_2 on graphene is roughly double compared to FTO. Dark currents are almost negligible, particularly for SnS_2 on graphene at high voltages. The decrease in dark current for SnS_2 on graphene compared to SnS_2 on FTO could be due to a more continuous film, which is supported by SEM and AFM. Evidence of tunnelling or avalanche break down of the semiconductor films are not observed up to +/-1.0 V in all samples. SnS_2 on graphene and FTO produces exclusively cathodic photocurrents indicating n type behaviour as expected for SnS_2. Unlike for SnS, SnS_2 on graphene outperforms SnS_2 on FTO. A reason for this could be due to the graphene substrate. Raman analysis found the graphene substrate had experienced far less damage during the deposition of SnS_2 compared to SnS, postulated to be due to a shorter deposition time and the lack of need of an annealing step. Another reason could be due to the morphological differences in the SnS_2 between the films. As the SnS_2 film on graphene is smoother, there are likely to be less pinhole defects, which is also shown by photo electrochemical measurements. To elucidate whether graphene is outperforming FTO purely as a conducting substrate, two identical photoactive materials would have to be deposited on graphene and FTO then analysed.

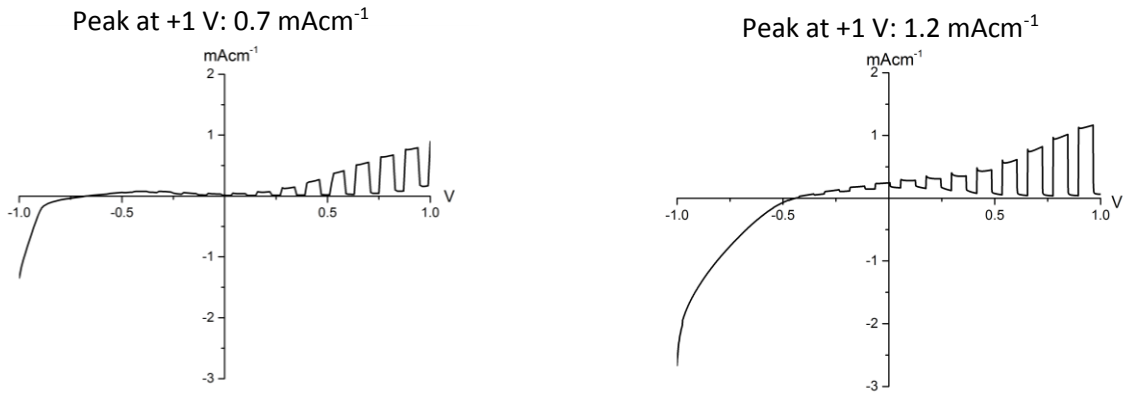

Figure 4.27 Photocurrent responses for blue flashing LED for SnS_2 on FTO (left) and graphene (right).

Figure 4.28 displays the EQE spectra for SnS_2 on graphene and SnS_2 on FTO. Both spectra were taken at + 0.4 V and have an onset at approximately 800 nm where the SnS_2 on graphene spectrum sharply increases at 550 nm and peaks just below 500 nm at 3.5 % EQE before sharply decreasing. The SnS_2 spectrum on FTO sharply increases at 500 nm and is still sharply rising at 400 nm where it reaches 5.8 % EQE. The calculated short circuit current for SnS_2 on FTO at + 0.4 V is 0.160 $mAcm^{-1}$ whereas it is 0.245 $mAcm^{-1}$ for SnS_2 on graphene. The EQE spectra reveal it is likely that SnS_2 on graphene performs better than FTO at 470 nm as the EQE spectrum for SnS_2 on FTO has been blue shifted with respect to the spectrum of SnS_2 on graphene. It can be seen in figure 4.28 at 470 nm the EQE value for SnS_2 on graphene is higher. This blue shift also explains why the calculated short circuit current for SnS_2 on graphene is higher. Even though it does not reach as a high a value as SnS_2 on FTO, it is on average higher for the wavelengths being studied.

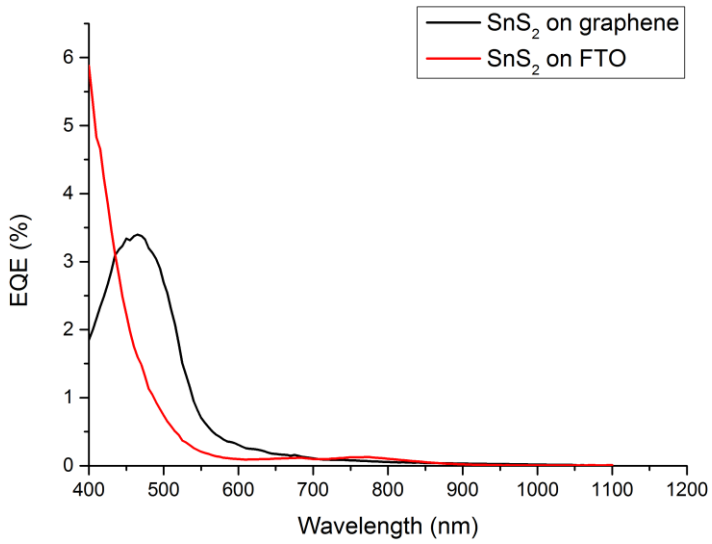

Figure 4.28 EQE spectra for SnS_2 on graphene and FTO.

Figure 4.29 shows $[\ln(1-\Phi)]^2$ plotted against hv for SnS_2 on graphene and SnS_2 on FTO. As for SnS, bandgap values were taken where the straight line crossed the x axis.

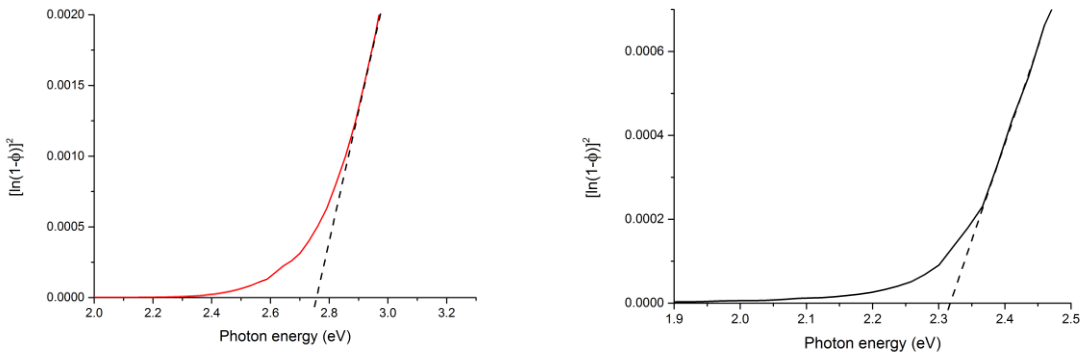

Figure 4.29 Plots to calculate bandgaps of SnS_2 on glass (left) and SnS_2 on graphene (right).

Conversely to SnS, SnS_2 on graphene has a 16 % lower bandgap than on FTO. As well as the bandgap being lower on graphene, the difference in bandgaps is far greater than for SnS. This is attributed to the significant morphological change of SnS_2 deposited on graphene compared to FTO due to the lattice matching of SnS_2 and graphene. This lattice matching introduces far less strain into the material, relaxing the bandgap energy as discussed for SnS. Table 4.4 displays the calculated bandgaps for SnS_2 on FTO and SnS_2 on graphene.

Table 4.4 Calculated bandgaps for SnS_2 on FTO and graphene

Material	Calculated bandgap (eV)
SnS_2 on FTO	2.76
SnS_2 on Graphene	2.32

4.7 SnS_2 on graphene conclusions

It has been shown SnS_2 can be be deposited onto a graphene substrate via AA-CVD. As with WS_2, SnS_2 is a layered material with hexagonally structured atomic planes of sulfur which makes the SnS_2 phase compatible with the graphene substrate. This influences the way SnS_2 grows on graphene compared to amorphous or non hexagonal substrates, producing flatter, more continuous, and less strained films. This results in an increased performance in photoelectrochemial measurements, attributed to a shifting in the band gap of SnS_2 due to reduced strain.

4.8 References

1. Loh, K. P.; Tong, sulphur.W.; Wu, J., Graphene and Graphene-like Molecules: Prospects in Solar Cells. *Journal of the American Chemical Society* **2015**.
2. Ahmet, I. Y.; Hill, M. S.; Johnson, A. L.; Peter, L. M., Polymorph-Selective Deposition of High Purity SnS Thin Films from a Single Source Precursor. *Chemistry of Materials* **2015,** *27* (22), 7680-7688.
3. Burton, L. A.; Walsh, A., Phase Stability of the Earth-Abundant Tin Sulfides SnS, SnS_2, and Sn_2S_3. *Journal of Physical Chemistry C* **2012,** *116* (45), 24262-24267.
4. Greyson, E. C.; Barton, J. E.; Odom, T. W., Tetrahedral Zinc Blende Tin Sulfide Nano- and Microcrystals. *Small* **2006,** *2* (3), 368-371.
5. Avellaneda, D.; Nair, M. T. S.; Nair, P. K., Polymorphic tin sulfide thin films of zinc blende and orthorhombic structures by chemical deposition. *Journal of the Electrochemical Society* **2008,** *155* (7), D517-D525.
6. Rabkin, A.; Samuha, S.; Abutbul, R. E.; Ezersky, V.; Meshi, L.; Golan, Y., New Nanocrystalline Materials: A Previously Unknown Simple Cubic Phase in the SnS Binary System. *Nano Letters* **2015,** *15* (3), 2174-2179.
7. Chattopadhyay, T.; Pannetier, J.; Von Schnering, H. G., Neutron diffraction study of the structural phase transition in SnS and SnSe. *Journal of Physics and Chemistry of Solids* **1986,** *47* (9), 879-885.
8. Sun, B.-Z.; Ma, Z.; He, C.; Wu, K., Enhanced thermoelectric performance of layered SnS crystals: the synergetic effect of temperature and carrier concentration. *RSC Advances* **2015,** *5* (69), 56382-56390.
9. Abutbul, R. E.; Segev, E.; Zeiri, L.; Ezersky, V.; Makov, G.; Golan, Y., Synthesis and properties of nanocrystalline [small pi]-SnS - a new cubic phase of tin sulphide. *RSC Advances* **2016,** *6* (7), 5848-5855.
10. Brent, J. R.; Lewis, D. J.; Lorenz, T.; Lewis, E. A.; Savjani, N.; Haigh, S.J.; Seifert, G.; Derby, B.; O'Brien, P., Tin(II) Sulfide (SnS) Nanosheets by Liquid-Phase Exfoliation of Herzenbergite: IV-VI Main Group Two-Dimensional Atomic Crystals. *Journal of the American Chemical Society* **2015,** *137* (39), 12689-12696.
11. Wang, H.; Liu, X.; Zhang, Z. M., Absorption Coefficients of Crystalline Silicon at Wavelengths from 500 nm to 1000 nm. *International Journal of Thermophysics* **2013,** *34* (2), 213-225.
12. Koteeswara Reddy, N.; Devika, M.; Gopal, E. S.R., Review on Tin (II) Sulfide (SnS) Material: Synthesis, Properties, and Applications. *Critical Reviews in Solid State and Materials Sciences* **2015,** *40* (6), 359-398.
13. Brudnyi, V. N.; Grinyaev, S.N.; Kolin, N. G., The Fermi Level Pinning in Semiconductors (Interphase Boundaries, Clusters, and Radiation Modification). *Russian Physics Journal* **2003,** *46* (6), 594-600.
14. Ran, F.-Y.; Xiao, Z.; Toda, Y.; Hiramatsu, H.; Hosono, H.; Kamiya, T., n-type conversion of SnS by isovalent ion substitution: Geometrical doping as a new doping route. *Scientific Reports* **2015,** *5*, 10428.
15. Banai, R. E.; Horn, M. W.; Brownson, J. R. S., A review of tin (II) monosulfide and its potential as a photovoltaic absorber. *Solar Energy Materials and Solar Cells* **2016,** *150*, 112-129.
16. Sinsermsuksakul, P.; Sun, L. Z.; Lee, S.W.; Park, H. H.; Kim, S.B.; Yang, C. X.; Gordon, R. G., Overcoming Efficiency Limitations of SnS-Based Solar Cells. *Advanced Energy Materials* **2014,** *4* (15).
17. Albers, W.; Haas, C.; van der Maesen, F., The preparation and the electrical and optical properties of SnS crystals. *Journal of Physics and Chemistry of Solids* **1960,** *15* (3), 306-310.
18. Reddy, N. K.; Devika, M.; Prashantha, M.; Ramesh, K.; Gunasekhar, K. R., In situ structural studies on orthorhombic SnS micro-crystals. *European Physical Journal-Applied Physics* **2012,** *60* (1).
19. Sohila, S.; Rajalakshmi, M.; Ghosh, C.; Arora, A. K.; Muthamizhchelvan, C., Optical and Raman scattering studies on SnS nanoparticles. *Journal of Alloys and Compounds* **2011,** *509* (19), 5843-5847.

20. Liu, H.; Liu, Y.; Wang, Z.; He, P., Facile synthesis of monodisperse, size-tunable SnS nanoparticles potentially for solar cell energy conversion. *Nanotechnology* **2010,** *21* (10).
21. Gao, C.; Shen, H.; Sun, L.; Shen, Z., Chemical bath deposition of SnS films with different crystal structures. *Materials Letters* **2011,** *65* (9), 1413-1415.
22. Safonova, M.; Nair, P. K.; Mellikov, E.; Garcia, A. R.; Kerm, K.; Revathi, N.; Romann, T.; Mikli, V.; Volobujeva, O., Chemical bath deposition of SnS thin films on ZnS and CdS substrates. *Journal of Materials Science: Materials in Electronics* **2014,** *25* (7), 3160-3165.
23. Guneri, E.; Gode, F.; Ulutas, C.; Kirmizigul, F.; Altindemir, G.; Gumus, C., Properties of p-type sns thin films prepared by chemical bath deposition. *Chalcogenide Letters* **2010,** *7* (12), 685-694.
24. Ray, sulphur.C.; Karanjai, M. K.; DasGupta, D., Structure and photoconductive properties of dip-deposited SnS and SnS_2 thin films and their conversion to tin dioxide by annealing in air. *Thin Solid Films* **1999,** *350* (1–2), 72-78.
25. Řičica, T.; Střižík, L.; Dostál, L.; Bouška, M.; Vlček, M.; Beneš, L.; Wágner, T.; Jambor, R., SnS and SnS_2thin films deposited using a spin-coating technique from intramolecularly coordinated organotin sulfides. *Applied Organometallic Chemistry* **2015,** *29* (3), 176-180.
26. Cheng, S.; Chen, Y.; Huang, C.; Chen, G., Characterization of SnS films prepared by constant-current electro-deposition. *Thin Solid Films* **2006,** *500* (1–2), 96-100.
27. Price, L. S.; Parkin, I. P.; Hibbert, T. G.; Molloy, K. C., Atmospheric pressure CVD of SnS and SnS_2 on glass. *Chemical Vapor Deposition* **1998,** *4* (6), 222-+.
28. Price, L. S.; Parkin, I. P.; Field, M. N.; Hardy, A. M. E.; Clark, R. J. H.; Hibbert, T. G.; Molloy, K. C., Atmospheric pressure chemical vapour deposition of tin(II) sulfide films on glass substrates from ($Bu_3SnO_2CCF_3$)-Sn-n with hydrogen sulfide. *Journal of Materials Chemistry* **2000,** *10* (2), 527-530.
29. Parkin, I. P.; Price, L. S.; Hibbert, T. G.; Molloy, K. C., The first single source deposition of tin sulfide coatings on glass: aerosol-assisted chemical vapour deposition using [Sn(SCHCHS)]. *Journal of Materials Chemistry* **2001,** *11* (5), 1486-1490.
30. Kevin, P.; Lewis, D. J.; Raftery, J.; Azad Malik, M.; O'Brien, P., Thin films of tin(II) sulphide (SnS) by aerosol-assisted chemical vapour deposition (AA-CVD) using tin(II) dithiocarbamates as single-source precursors. *Journal of Crystal Growth* **2015,** *415*, 93-99.
31. Reddy, N. K.; Reddy, K. T. R., Preparation and characterisation of sprayed tin sulphide films grown at different precursor concentrations. *Materials Chemistry and Physics* **2007,** *102* (1), 13-18.
32. Koteeswara Reddy, N.; Ramesh, K.; Ganesan, R.; Ramakrishna Reddy, K. T.; Gunasekhar, K. R.; Gopal, E. sulphur.R., Synthesis and characterisation of co-evaporated tin sulphide thin films. *Applied Physics A* **2006,** *83* (1), 133-138.
33. Tanuševski, A.; Poelman, D., Optical and photoconductive properties of SnS thin films prepared by electron beam evaporation. *Solar Energy Materials and Solar Cells* **2003,** *80* (3), 297-303.
34. Hartman, K.; Johnson, J. L.; Bertoni, M. I.; Recht, D.; Aziz, M. J.; Scarpulla, M. A.; Buonassisi, T., SnS thin-films by RF sputtering at room temperature. *Thin Solid Films* **2011,** *519* (21), 7421-7424.
35. Yang, Y. B.; Dash, J. K.; Xiang, Y.; Wang, Y.; Shi, J.; Dinolfo, P. H.; Lu, T. M.; Wang, G. C., Tuning the Phase and Optical Properties of Ultrathin SnSx Films. *The Journal of Physical Chemistry C* **2016,** *120* (24), 13199-13214.
36. Su, G.; Hadjiev, V. G.; Loya, P. E.; Zhang, J.; Lei, S.; Maharjan, S.; Dong, P.; M. Ajayan, P.; Lou, J.; Peng, H., Chemical Vapor Deposition of Thin Crystals of Layered Semiconductor SnS_2 for Fast Photodetection Application. *Nano Letters* **2015,** *15* (1), 506-513.
37. Liu, Z.; Deng, H.; Mukherjee, P. P., Evaluating Pristine and Modified SnS_2 as a Lithium-Ion Battery Anode: A First-Principles Study. *ACS Applied Materials & Interfaces* **2015,** *7* (7), 4000-4009.
38. Palosz, B.; Palosz, W.; Gierlotka, S., Structures of 24 new polytypes of tin disulphide. *Acta Crystallographica Section C* **1985,** *41* (10), 1402-1404.
39. Huang, Y.; Sutter, E.; Sadowski, J. T.; Cotlet, M.; Monti, O. L. A.; Racke, D. A.; Neupane, M. R.; Wickramaratne, D.; Lake, R. K.; Parkinson, B. A.; Sutter, P., Tin Disulfide—An Emerging Layered Metal

Dichalcogenide Semiconductor: Materials Properties and Device Characteristics. *ACS Nano* **2014,** *8* (10), 10743-10755.
40. Mitchell, R. S.; Fujiki, Y.; Ishizawa, Y., Structural polytypism of tin disulfide: Its relationship to environments of formation. *Journal of Crystal Growth* **1982,** *57* (2), 273-279.
41. Hu, X.; Song, G.; Li, W.; Peng, Y.; Jiang, L.; Xue, Y.; Liu, Q.; Chen, Z.; Hu, J., Phase-controlled synthesis and photocatalytic properties of SnS, SnS_2 and SnS/SnS_2 heterostructure nanocrystals. *Materials Research Bulletin* **2013,** *48* (6), 2325-2332.
42. Sun, Y.; Gao, S.; Xie, Y., Atomically-thick two-dimensional crystals: electronic structure regulation and energy device construction. *Chemical Society Reviews* **2014,** *43* (2), 530-546.
43. Sun, Y.; Cheng, H.; Gao, S.; Sun, Z.; Liu, Q.; Liu, Q.; Lei, F.; Yao, T.; He, J.; Wei, S.; Xie, Y., Freestanding Tin Disulfide Single-Layers Realizing Efficient Visible-Light Water Splitting. *Angewandte Chemie International Edition* **2012,** *51* (35), 8727-8731.
44. Burton, L. A.; Whittles, T. J.; Hesp, D.; Linhart, W. M.; Skelton, J. M.; Hou, B.; Webster, R. F.; O'Dowd, G.; Reece, C.; Cherns, D.; Fermin, D. J.; Veal, T. D.; Dhanak, V. R.; Walsh, A., Electronic and optical properties of single crystal SnS_2: an earth-abundant disulfide photocatalyst. *Journal of Materials Chemistry A* **2016,** *4* (4), 1312-1318.
45. Su, J.; Guo, L.; Bao, N.; Grimes, C. A., Nanostructured WO_3/$BiVO_4$ Heterojunction Films for Efficient Photoelectrochemical Water Splitting. *Nano Letters* **2011,** *11* (5), 1928-1933.
46. Kim, J. Y.; Magesh, G.; Youn, D. H.; Jang, J.-W.; Kubota, J.; Domen, K.; Lee, J. S., Single-crystalline, wormlike hematite photoanodes for efficient solar water splitting. *Scientific Reports* **2013,** *3*, 2681.
47. Gedi, S.; Minna Reddy, V. R.; Pejjai, B.; Jeon, C.-W.; Park, C.; K.T, R. R., A facile inexpensive route for SnS thin film solar cells with SnS_2 buffer. *Applied Surface Science* **2016,** *372*, 116-124.
48. Yang, B.; Zuo, X.; Xiao, H.; Zhou, L.; Yang, X.; Li, G.; Wu, M.; Ma, Y.; Jin, S.; Chen, X., SnS_2 as low-cost counter-electrode materials for dye-sensitized solar cells. *Materials Letters* **2014,** *133*, 197-199.
49. Cui, X.; Xu, W.; Xie, Z.; Wang, Y., High-performance dye-sensitized solar cells based on Ag-doped SnS_2 counter electrodes. *Journal of Materials Chemistry A* **2016,** *4* (5), 1908-1914.
50. Tan, F.; Qu, S.; Wu, J.; Liu, K.; Zhou, S.; Wang, Z., Preparation of SnS_2 colloidal quantum dots and their application in organic/inorganic hybrid solar cells. *Nanoscale Research Letters* **2011,** *6* (1), 298.
51. Ma, C.; Xu, J.; Alvarado, J.; Qu, B.; Somerville, J.; Lee, J. Y.; Meng, Y. S., Investigating the Energy Storage Mechanism of SnS_2-rGO Composite Anode for Advanced Na-Ion Batteries. *Chemistry of Materials* **2015,** *27* (16), 5633-5640.
52. Liu, Y.; Kang, H.; Jiao, L.; Chen, C.; Cao, K.; Wang, Y.; Yuan, H., Exfoliated-SnS_2 restacked on graphene as a high-capacity, high-rate, and long-cycle life anode for sodium ion batteries. *Nanoscale* **2015,** *7* (4), 1325-1332.
53. Arora, sulphur.K.; Patel, D. H.; Agarwal, M. K., Vapour growth of SnS_2 single crystals. *Journal of Crystal Growth* **1993,** *131* (1), 268-270.
54. Mikkelsen, J. C., Polytype characterization of SnS_2 crystals grown from Sn-rich melts. *Journal of Crystal Growth* **1980,** *49* (2), 253-260.
55. Chaki, sulphur.H.; Deshpande, M. P.; Trivedi, D. P.; Tailor, J. P.; Chaudhary, M. D.; Mahato, K., Wet chemical synthesis and characterization of SnS_2 nanoparticles. *Applied Nanoscience* **2013,** *3* (3), 189-195.
56. Sathish, M.; Mitani, S.; Tomai, T.; Honma, I., Ultrathin SnS_2 Nanoparticles on Graphene Nanosheets: Synthesis, Characterization, and Li-Ion Storage Applications. *The Journal of Physical Chemistry C* **2012,** *116* (23), 12475-12481.
57. Reddy, K. T. R.; Sreedevi, G.; Ramya, K.; Miles, R. W., Physical Properties of Nano-crystalline SnS_2 Layers Grown by Chemical Bath Deposition. In *International Conference on Materials for Advanced Technologies 2011, Symposium O*, Aberle, A., Ed. 2012; Vol. 15, pp 340-346.

58. Gedi, S.; Reddy, V. R. M.; Pejjai, B.; Jeon, C. W.; Park, C.; Reddy, K. T. R., A facile inexpensive route for SnS thin film solar cells with SnS_2 buffer. *Applied Surface Science* **2016,** *372*, 116-124.
59. Reid, sulphur.D.; Hector, A. L.; Levason, W.; Reid, G.; Waller, B. J.; Webster, M., Thio- and seleno-ether complexes with Group 4 tetrahalides and tin tetrachloride: preparation and use in CVD for metal chalcogenide films. *Dalton Transactions* **2007,** (42), 4769-4777.
60. Barone, G.; Hibbert, T. G.; Mahon, M. F.; Molloy, K. C.; Price, L. S.; Parkin, I. P.; Hardy, A. M. E.; Field, M. N., Deposition of tin sulfide thin films from tin(iv) thiolate precursors. *Journal of Materials Chemistry* **2001,** *11* (2), 464-468.
61. Vijayakumar, K.; Sanjeeviraja, C.; Jayachandran, M.; Amalraj, L., Characterization of Tin disulphide thin films prepared at different substrate temperature using spray pyrolysis technique. *Journal of Materials Science: Materials in Electronics* **2011,** *22* (8), 929-935.
62. Zhu, J.; Wang, D.; Liu, T., Preparation of tin sulfide–graphene composites with enhanced lithium storage. *Applied Surface Science* **2013,** *282*, 947-953.
63. Wang, Q.; Nie, Y.-X.; He, B.; Xing, L.-L.; Xue, X.-Y., SnS_2–graphene nanocomposites as anodes of lithium-ion batteries. *Solid State Sciences* **2014,** *31*, 81-84.
64. Yang, D.; Li, B.; Hu, C.; Deng, H.; Dong, D.; Yang, X.; Qiao, K.; Yuan, S.; Song, H., Controllable Growth Orientation of SnS_2 Flakes for Low-Noise, High-Photoswitching Ratio, and Ultrafast Phototransistors. *Advanced Optical Materials* **2016,** *4* (3), 419-426.
65. Alkire, R. C.; Kolb, D. M.; Lipkowski, J.; Ross, P. N., *Photoelectrochemical materials and energy conversion processes*. John Wiley & Sons: 2010; Vol. 12.
66. Tritsaris, G. A.; Malone, B. D.; Kaxiras, E., Optoelectronic properties of single-layer, double-layer, and bulk tin sulfide: A theoretical study. *Journal of Applied Physics* **2013,** *113* (23).
67. Mutlu, Z.; Wu, R. J.; Wickramaratne, D.; Shahrezaei, S.; Liu, C.; Temiz, S.; Patalano, A.; Ozkan, M.; Lake, R. K.; Mkhoyan, K. A.; Ozkan, C. S., Phase Engineering of 2D Tin Sulfides. *Small* **2016,** *12* (22), 2998-3004.
68. Kim, M.-G.; Kanatzidis, M. G.; Facchetti, A.; Marks, T. J., Low-temperature fabrication of high-performance metal oxide thin-film electronics via combustion processing. *Nat Mater* **2011,** *10* (5), 382-388.
69. Liu, J. X.; Pu, X. P.; Zhang, D. F.; Seo, H. J.; Du, K. P.; Cai, P., Combustion synthesis of CdS/reduced graphene oxide composites and their photocatalytic properties. *Materials Research Bulletin* **2014,** *57*, 29-34.
70. Liu, J. X.; Zhang, D. F.; Pu, X. P.; Liu, J. X.; Zhang, R. G., Combustion synthesis of Zn-CdS and its photodegradation performance of methylene blue. *Materials Letters* **2014,** *117*, 158-161.
71. Xu, L. Q.; Zhang, W. Q.; Ding, Y. W.; Yu, W. C.; Xing, J. Y.; Li, F. Q.; Qian, Y. T., Shape-controlled synthesis of PbS microcrystals in large yields via a solvothermal process. *Journal of Crystal Growth* **2004,** *273* (1-2), 213-219.
72. Addison, C. C.; Simpson, W. B., 96. Tin(IV) nitrate: the relation between structure and reactivity of metal nitrates. *Journal of the Chemical Society (Resumed)* **1965,** (0), 598-602.
73. Jameson, G. B.; Blazso, E.; Seferiadis, N.; Oswald, H. R., α,α'-Dithiobisformamidinium dinitrate, $[(NH_2)_2CSSC(NH_2)_2][NO_3]_2$ at 110 K. *Acta Crystallographica Section B* **1982,** *38* (8), 2272-2274.
74. Bialoglowski, M.; Jastrzebski, C.; Podsiadlo, S.; Jastrzebski, D. J.; Gajda, R.; Gebicki, W.; Wrzosek, P. A.; Wozniak, K., Synthesis of tin disulfide single crystals for nano-layer exfoliation. *Crystal Research and Technology* **2015,** *50* (9-10), 695-699.
75. Smith, A. J.; Meek, P. E.; Liang, W. Y., Raman-Scattering Studies of SnS_2 and $SnSe_2$. *Journal of Physics C-Solid State Physics* **1977,** *10* (8), 1321-1333.

Chapter 5. Experimental

5.1 General experimental procedures

5.1.1 Substrate preparation

Glass, FTO and silicon substrates were cleaned using a dilute solution (2%) of Hellmanex™ in 1:1 iso-propanol and deionised water. The films were then cleaned with a 0.3 M solution of acetic acid in isopropanol, then isopropanol and finally dried under a fast flow of N_2. All substrates were wiped with lint free clothes and blown with N_2 before deposition to remove possible dust particles on the surface.

Glass microscope slide were purchased from VWR. Fluorine doped tin oxide (FTO, (101) oriented) on glass substrates was purchased from Pilkington Glass. P-type boron doped 100 oriented silicon wafers were supplied by Element 6. Silicon dioxide wafers were synthesised from thermal treatment p-type boron doped 100 oriented silicon wafers to produce a 300 nm layer of SiO_2. The wafers were purchased from IDB technologies.

5.1.2 Aerosol Assisted Chemical Vapour Deposition (AA-CVD)

The precursor solution is dispensed into the precursor holder in a glovebox under an atmosphere of argon and all the solvents were dried and degassed using standard Schlenck line techniques prior to preparation. The sealed precursor holder is then attached onto the AA-CVD apparatus. Once all substrates were prepared and mounted into the quartz deposition chamber, Ar gas is allowed to flow through the system, by-passing the precursor holder, for 20 minutes to purge the system with argon. Then with continuing gas flow, the furnace is switched on and allowed to reach the target deposition temperature and equilibrate for 20 minutes. The regulator pressure of the Ar cylinder was set between 1 and 2 bar. Next the gas flow is diverted to flow through the precursor container which draws the solution into the TSI 3076 Constant Output Atomiser and thus into the deposition chamber as an Aerosol. Once the desired deposition time has been reached, the argon flow was once again made to by-pass the precursor holder and the furnace was allowed to cool to room temperature. Then the argon flow was stopped and the substrates removed from the reactor.

5.1.3 Scanning Electron Microscopy (SEM)

Samples were stored in a vacuum desiccator for at least 12 h before loading into the SEM vacuum chamber. Images were taken on a Field Emission Scanning Electron Microscope 6301F (FE-SEM), or a JEOL 6480 Low Vacuum large stage SEM platform. Cross sectional images were obtained by briefly immersing a sample in liquid nitrogen before fracturing to obtain a well-defined cleave.

5.1.4 Energy-dispersive X-ray Spectroscopy (EDS)

EDS spectra were captured on an Oxford Instruments Scanning Electron Microscope 6480 LV fitted with a Silicon Drift (SDD) - X-Max^N Detector and processed using INCA Wave software.

5.1.5 Atomic Force Microscopy (AFM)

AFM images were obtained using a Digital Instruments Nanoscope IIIa or a Nanosurf easyScan 2 with contact Al-G tips (resonant frequency 13 kHz, force constant 0.2 N/m). All AFM data were processed by the SPM data visualisation and an analysis tool Gwyddion.

5.1.6 Raman Spectroscopy

Raman spectroscopy was carried out using a Renishaw inVia Raman Microscope with a 532 nm (81.7 W) laser using various spot sizes, exposure times and energy intensities. Raman maps were either carried out using a standard or streamline acquisition mode. Data were processed using the Renishaw WiRE software package.

5.1.7 Thermogravimetric Analysis (TGA)

Thermogravimetric data was obtained using a Perkin Elmer TGA 4000 quartz microbalance. Data were analysed using PYRIS Version 10.1 Instrument managing and analysis software. Atmosphere was excluded using crimped sealed aluminium sample pans. Data was collected using a continuous furnace purge rate of N_2 at 20 mL min^{-1}, where the furnace was heated from 30 ^{o}C to 600 ^{o}C at a ramp rate of 5 ^{o}C min^{-1}and mass measurements were recorded once per second.

5.1.8 Powder X-ray Diffractometry (PXRD)

PXRD data were collected using BRUKER D8-Advance in flat plate mode. Data were collected from 5 to 70 2θ at 2^o min^{-1}. The X-rays were generated from a copper source with λ = 15.4 nm. Diffraction data were processed using EVA PXRD analysis software. Crystalline phases were identified by matching data from databases and published sources.

5.1.9 Differential scanning calorimetry (DSC)

DSC data were collected using a DSC Q20 and analysed on Q-Series DSC analysis software. Before collection the furnace temperature was equilibrated at 0 ^{o}C . The sample purge flow was 18 ccm of N_2 and 18 ccm of Ar and the ramp rate set at 2^{o}C min^{-1}.

5.2 Experimental for Chapter 2

5.2.1 Homebuilt CVD reactor details

Gases were delivered to the reaction chamber via ¼ in. stainless steel tubing. Benzene was contained in a stainless steel pot sealed by a needle valve. Ultra-Torr fittings connected piping to a 1 in quartz tube cut to 70 m in length. A liquid N_2 trap separated the system from a scroll pump. Gas flow rates were controlled by Bronkhorst MASS-VIEW flow meters. Pressures were measured by a Oerlikon DISPLAY ONE pressure gauge. Reactor temperature was provided by an Elite Thermal Systems 1200°C.

5.2.2 Copper pre-treatment

99.8 % purity copper foil was purchased from Alfa Aesar. The foil was immersed in a 10 % solution of concentrated nitric acid for 30s before quickly being immersed in de-ionised (DI) water. The foil was then rinsed with DI water acetone then isopropanol (IPA) before blow-drying with nitrogen. The foil was then cut using scissors into 9 cm x 3 cm sheets. Using the homebuilt CVD reactor, a sheet was placed in the centre of a quartz tube and annealed at 1050 ^{o}C at low pressure with a 25 ccm flow of H_2 to flatten the copper and expand the crystallographic grains. The system was then allowed to cool to room temperature whereupon the flow of H_2 was stopped and the system returned to atmospheric pressure.

5.2.3 Methane CVD of graphene

Low Ethylene Grade N3.5 methane purchased from BOC was used in all experiments. N4.5 Hydrogen purchased from BOC was used in all experiments. The pre-treated copper was cut using scissors into 3 cm x 3 cm sheets and placed in the centre of the quartz tube of the homebuilt CVD reactor. The system was flushed with H_2 and subsequently pumped down 3 times prior to heating. Under various flows of H_2, the furnace was heated to various temperatures. Once the desired furnace temperature had been reached, various flows of methane were introduced for 20 mins. After 20 mins, the methane flow was stopped and the reactor was allowed to cool to room temperature, assisted by a flow of N_2. Once the reactor was at room temperature, the H_2 flow was stopped and the system returned to atmospheric pressure. The copper with the graphene film grown on was then removed from the system.

5.2.4 Benzene CVD of graphene

Anhydrous 99.8 % benzene was purchased from Sigma Aldrich. Prior to loading 25 ml into to a stainless steel pot in a glovebox to be fitted to the CVD reactor, it was degassed by 2 freeze-thaw cycles. Once the stainless steel pot had been attached to the reactor, the following procedures were the same as

in the case for methane CVD of graphene. The only difference was the needle valve to the benzene was opened to the desired value instead of a methane flow being introduced. It was found ca. 0.2 g of benzene was used in each deposition.

5.2.5 Cleaning the reactor

After ca. 10 experiments, a black build-up of carbon was visible in the centre of the quartz tube with evaporated copper closer to the ends. The copper was removed through immersion in nitric acid and the carbon removed by baking the quartz tube at 700 ^{o}C for 3 h.

5.2.6 Optimised transfer process.

Copper sheet with graphene films grown on were first cut into 1 cm x 1 cm sheets. A solution of 25 mg ml^{-1} 350000 mw PMMA (Sigma Aldrich) in chlorobenzene was spin coated on top the sheets at 3500 rpm for 30 s. (Note: the PMMA needs ca. 24 h to fully dissolve in chlorobenzene and reach the correct viscosity) The PMMA was the left to harden for 30 min at R.T. before baking at 120 ^{o}C for 30 min. The copper/graphene/PMMA stack was then flipped upside down and placed in a home built plasma cleaner and subjected to 100 W O_2 plasma for 10 mins. The stack was then flipped to have the PMMA upside again and floated on a solution of 10 mg mL^{-1} sodium persulphate (Sigma Aldrich) in DI water. The copper sheet was completely etched in 24 h whereupon the sodium persulphate solution was carefully replaced by DI water by removing 90 % of the solution and replacing with DI water 10 times. The solution was then replaced by ca. 0.01 M HCl and the graphene/PMMA left to float for 10 mins. The HCl was then then replaced by removing 90 % of the solution and replaced with DI water 10 times. The floating graphene/PMMA stack was held in place by a needle and the desired substrate placed underneath at an angle, slowly drawing the stack out of solution. The substrate was then placed at an angle to allow the water to escape from under the graphene film. The substrate/stack was then allowed to dry for at least 8 h. After this, the substrate/stack was baked at 150 ^{o}C for 30 mins for greater adherence to flatten the PMMA. Once the substrate /stack had cooled (Important) it was then placed in a bath of dichloromethane for 30 mins to remove the PMMA. The substrate/graphene was then immediately gently rinsed with acetone then IPA and dried with a stream of N_2.

5.2.7 ALD of graphitic materials

Prior to deposition, copper substrates were pre-treated in the same way as for the CVD processes except for the annealing step. N4.5 Hydrogen, N4.8 N_2 and N4.8 Ar gas were purchased from BOC. Depositions were run on a Beneq TFS 200 ALD rig. 100 ccm of process gas was running continuously throughout the depositions. Once the reactor has reached the desired temperature, a H_2 plasma was introduced for 10 mins to clean the surface. Benzene was stored in one of the liquid source pots. Benzene pulses were 2 s long, H_2/Ar pulses were 5 s long. The plasma generator was set to 300 W for all experiments with plasma pulses being 2 s long. Purge times were 10 s long. After the desired amount of cycles has been completed, the sample was taken into the load lock and allowed to cool before exposure to atmosphere.

5.3 Experimental for Chapter 3

5.3.1 Chemical reagents

All chemicals used in this chapter were purchased from Sigma Aldrich. Toluene dried under argon using Innovative Technology's solvent purification system, then degassed once using cold vacuum degassing (77 K) and argon. Toluene was then stored over molecular sieves in a Young's ampule.

5.3.2 Synthesis of $W(S_2CNEt_2)_4$

A mixture of $W(CO)_6$ (1.76 g, 5 mmol) and tetraethylthiuram disulfide $Et_2NC(S)SS(S)CNEt_2$ (2.97 g, 10 mmol) in THF (30 ml) was refluxed for 72 hours. Solvent was removed *in vacuo* to provide a purple solid which was washed with hexane. The solid was dissolved in THF and stored at -28 °C to provide 3.18 g of purple crystals. Yield: 82 %

5.3.3 AACVD of WS_2

All the general procedures for AACVD reported in 5.1 were used in the AACVD depositions of WS_2. 0.78 g $W(S_2CNEt_2)_4$ was added to 100 ml toluene. The solution was then filtered into the precursor container.

5.3.4 High temperature synthesis of WS_2

1 g Sulphur (99.98 % purity) and 1 g WO_3 (99.9 % purity) were placed in alumina boats purchased from Sigma Aldrich. The sulphur boat was placed 9 cm from the left end of the quartz tube, the WO_3 boat was placed 34 cm from the left end of the quartz tube and the substrate was placed 49 cm from the left end of the quartz tube. The tube furnace was placed in the centre of the tube and the heating tapes over the sulphur boat end of the quartz tube. The system was pumped down to ca. $2x10^{-2}$ mbar then flushed for 30 mins with 500 ccm of N4.8 Ar gas purchased form BOC. The furnace was then

heated to 600 °C. After this the Ar flow rate was dropped to the desired value, the sulphur heating tapes were set to heat to the desired value and the furnace heated to the desired value. Once the deposition time was reached, the sulphur heating tapes and the furnace were set to cool. Once room temperature had been reached, the Ar flow was switched off and the substrate was removed from the system. The sulphur boat was cleaned by melting the remaining sulphur and pouring it out of the boat followed by a cycle through a NaOH then HCl bath and finally rinsed with IPA and acetone and left to air dry. The WO_3 boat was cleaned by a cycle through a NaOH then HCl bath and finally rinsed with IPA and acetone and left to air dry.

5.4 Experimental for Chapter 4

5.4.1 Chemical reagents

All chemicals used in this chapter were purchased from Sigma Aldrich. Ethanol (absolute, >99.8 %), tin(II) chloride dihydrate (98 %), thiourea/TU (>99.0 %), nitric acid (70 %) and ammonium nitrate (>98 %).

5.4.2 Synthesis of BismonoN-phenyl-*N'*,*N'*dimethyl-thioureide-bis(dimethylamido) ditin(II) [Sn([C_6H_5]NCSN[Me_2])(NMe_2)]

Sn([C_6H_5]NCSN[Me_2])(NMe_2) was prepared following the preparation published by Johnson et al.[1]

Phenyl isothiocyanate (2.40 mL, 2.276 g, 20.10 mmol) was added dropwise, over 10 min, to a cooled (−40 °C) and stirred THF solution (100 mL) of tetrakis(dimethylamido)ditin(II) (4.180 g, 20.10 mmol) resulting in an instantaneous colour change from yellow to colourless. After stirring at room temperature for 2 h, THF was removed *in vacuo*. To the residual solid, 80 mL of hexane was added and stirred for 1 h, whereupon a white precipitate evolved. The hexane was removed from the precipitate by cannula filtration. The precipitate was washed a further two times with fresh hexane. The white precipitate was then dissolved in a THF:hexane mixture (15 mL:30 mL). After filtration through Celite, the solution was stored at −20 °C for 3 days, during which time colourless crystalline needles were formed. The product was subsequently isolated by filtration and dried *in vacuo*. Yield, 5.55 g, 86 % , m.p. 125 °C decomposed to black. Analysis, found (calc. for $C_{11}H_{17}N_3SSn$): C 38.40 (38.63); H 5.35 (5.01); N 12.15 (12.29). ^{1}H NMR (300 MHz, THF-d^8): δ_H 7.20-7.11 (m, 2H, N(C_6H_5)), 6.91-6.72 (m, 3H, N(C_6H_5)), 2.83 (s, 6H, N-(CH_3)), 2.62 (s, 6H, N-(CH_3)).^{13}C NMR (75.5 MHz, THF-d^8): δ_C 129.43 (s, N-C(=S)-N),123.23 (s, N-(C_6H_5)), 45.37 (s, N-(CH_3)), 42.13 (s, N-(CH_3)). ^{119}Sn NMR (75.8 MHz, THF-d^8): δ_{Sn} 38.50 (s).

5.4.3 AACVD of SnS

All the general procedures for AACVD reported in 5.1 were used in the AACVD depositions of SnS. $Sn([C_6H_5]NCSN[Me_2])(NMe_2)$ was dissolved in toluene to make a 0.8 M solution. And 100 ml was added to the precursor container.

5.4.4 High temperature CVD of SnS

1 g Sulphur (99.98 % purity) and 1 g SnO_2 (99.9 % purity) were placed in alumina boats purchased from Sigma Aldrich. The sulphur boat was placed 9 cm from the left end of the quartz tube, the SnO_2 boat was placed 34 cm from the left end of the quartz tube and the substrate was placed 49 cm from the left end of the quartz tube. The tube furnace was placed in the centre of the tube and the heating tapes over the sulphur boat end of the quartz tube. The system was pumped down to ca. $2x10^{-2}$ mbar then flushed for 30 mins with 500 ccm of N4.8 Ar gas purchased form BOC. The furnace was then heated to 600 ^oC. After this the Ar flow rate was set to 55 ccm, the sulphur heating tapes were set to 200^oC and the furnace was set to 800 ^oC. After 30 mins, the sulphur heating tapes and the furnace were set to cool. Once room temperature had been reached, the Ar flow was switched off and the substrate was removed from the system. The sulphur boat was cleaned by melting the remaining sulphur and pouring it out of the boat followed by a cycle through a NaOH then HCl bath and finally rinsed with IPA and acetone and left to air dry. The SnO_2 boat was cleaned by a cycle through a NaOH then HCl bath and finally rinsed with IPA and acetone and left to air dry.

5.4.5 Preparation of $Sn(NO_3)_2$ –Thiourea solution.

5.64 g of $SnCl_2.2H_2O$ (0.025 mol) was added to 250 mL of Ethanol and stirred for 5 mins. 4.00 g of NH_4NO_3 (0.05 mol), and 3.15 mL of 70 % HNO_3 (0.05 mol) was then added and stirred for 5 mins. When the solution turned clear, 3.81 g of thiourea (0.05 mol) was added. The solution quickly turned pale yellow. After 15 mins of stirring, the solution was then filtered, from which ~0.10 g of white precipitate was isolated.). The solution 0.1M concentration with respect to Sn^{2+}.

5.4.6 Synthesis of α,α-Dithiobisformamidinium Dinitrate (α-DD)

A $Sn(NO_3)_2$ – thiourea solution was prepared as outlined above. The ethanol was then allowed to evaporate in air at room temperature until yellow (Sulfur) and colourless (α-DD) crystals were evolved. The colourless crystals were separated by single crystal X-ray diffraction analysis, DSC and TGA.

5.4.7 AACVD of SnS_2

All the general procedures for AACVD reported in 5.1 were used in the AACVD depositions of SnS_2. The 0.1 M solution of $Sn(NO_3)_2$ was used for all depositions. Its loading into the precursor container did not have to be managed air sensitively.

5.5 Photoelectrochemical measurements

5.5.1 Sample Preparation

The films were either deposited onto TEC 7 FTO substrates (1.5 x 3.5 cm) or 1 x 1 cm graphene substrates mounted on SiO_2 using the discussed AACVD precursors and techniques. The SnS film was removed from the end section of samples (c.a. 1 cm by 0.3 cm area) by abrasion with 1 µm alumina paste or the SnS_2 films by using a conc. NaOH 70:30, water:isopropanol solution and cotton bud, to expose the graphene or FTO back contact. This area was then painted with RS Standard Silver contact paint and connected to the Potentiostat with crocodile clips. The edges of the samples were isolated by scribing through the film with a diamond tipped stylus. For FTO sample, a 1 x 1 cm area was isolated using Kapton polyimide tape, for graphene samples a 1 x 0.5 cm was isolated in the same manner.

5.5.2 The Photoelectrochemical Cell

The measurement cell was a glass-sided vessel with approximate volume of 27 cm^3 (3cm x 3cm x 3cm). All photoelectrochemical measurements of deposited films were carried out using an aqueous solution of 0.2 M $Eu(NO_3)_3.6H_2O$ (99.9%, Alfa Aesar) as an electron scavenging redox electrolyte. The photocurrent responses of the films were measured using a Pt wire counter and Ag|AgCl reference electrode.

5.5.3 Photocurrent measurement under single wavelength LED illumination

Photocurrent under single wavelength LED illuminations was measured using the setup shown in figure 5.1. A Faraday cage was used to eliminate external illumination and electromagnetic interference. Photocurrents were generated using a pulsed illumination from a ThorLabs LEDC8-Collimated 470nm LED ca. 10 cm from the sample surface and measured using an Ivium Compactstat potentiostat at a range of potentials against an Ag|AgCl reference electrode. Data was recorded on IviumSoft Software. Flashing Sweep measurements were conducted with the 470 nm LED using a illumination sequence of 3 s on and 2 s off with a sweeping potential from -1 V to 1V and a slew rate of either 10 mVs^{-1} or 20 mVs^{-1}.

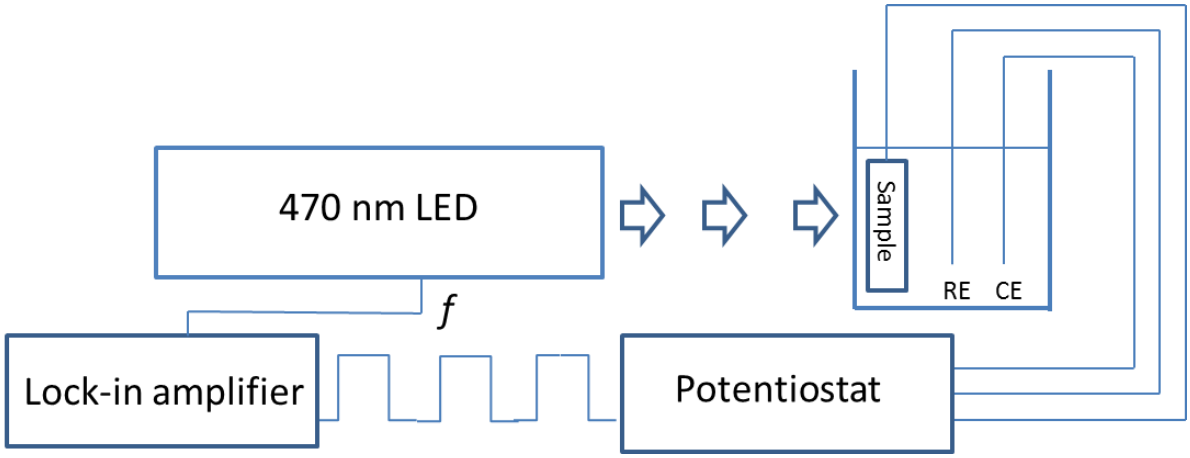

Figure 5.1 Diagram of experimental set up for photocurrent measurements under single wavelength LED illumination RE and CE stand for reference and counter electrode. The LED pulses with frequency *f.* This frequency is known by the lock-in amplifier to allow it to enhance the signal from the background noise.

5.5.4 Measurement of External Quantum Efficiency (EQE)

The sample cell was placed within a Faraday cage to eliminate external illumination and electromagnetic interference. The experimental setup is shown in figure 5.2. Monochromatic light of variable wavelengths was generated by a tungsten argon lamp (IL6S Bentham Illumination), grating monochromator (G312 ROUG grating) and stepper controller (Bentham PCM3B/IEEE), which was controlled using the LabVIEW software. The incident light was chopped at 27 Hz and a current amplifier (Femto DLPCA-200) connected to a lock-in amplifier (Stanford Research Systems ST830 DSP) was used to detect the photocurrent. A yellow filter was used to eliminate second-order harmonics from the monochromatic light at wavelengths above 550 nm. EQE measurements were made at potentials of -0.7 V and +1.0 V vs. Ag|AgCl, using a home built battery powered DC potentiostat. The spectrum was recorded twice in opposite directions of wavelength to confirm that the sample was stable. Then a slower scan was performed to record the final spectrum. Measurements in the range 1100-400 nm were performed with 10 nm intervals. The photon flux was calibrated using a 1 cm^2 Si photodiode In order to obtain the EQE of the SnS or SnS_2 films.

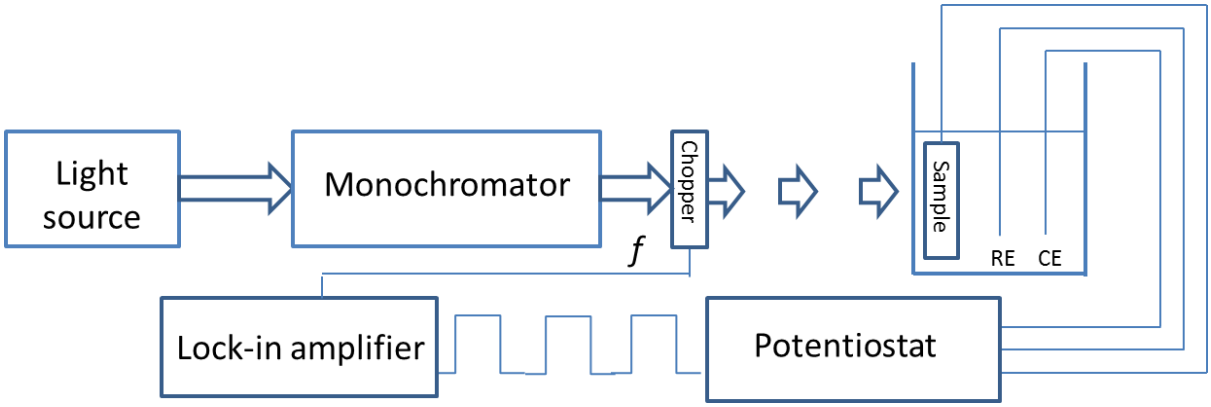

Figure 5.2 Diagram of experimental set up EQE measurements. RE and CE stand for reference and counter electrode. The chopper breaks the monochromatic beam of light into a series of pulses with frequency *f.* This frequency is known by the lock-in amplifier to allow it to enhance the signal from the background noise.

5.6 References

1. Ahmet, I. Y.; Hill, M. S.; Johnson, A. L.; Peter, L. M., Polymorph-Selective Deposition of High Purity SnS Thin Films from a Single Source Precursor. *Chemistry of Materials* **2015,** *27* (22), 7680-7688.